

WL-TR-91-4011
ADA240651

DIRECT IMAGING OF DEFORMATION AND DISORDER
IN EXTENDED-CHAIN POLYMER FIBERS



David C. Martin
Department of Polymer Science and Engineering
University of Massachusetts
Amherst MA 01003

March 1991

Final Report for the Period July 1986 - June 1990

Approved for public release; distribution unlimited

MATERIALS DIRECTORATE
WRIGHT LABORATORY
AIR FORCE SYSTEMS COMMAND
WRIGHT-PATTERSON AIR FORCE BASE OHIO 45433-6533

20040219156

BEST AVAILABLE COPY

NOTICE

When Government drawings, specifications, or other data are used for any purpose other than in connection with a definitely Government-related procurement, the United States Government incurs no responsibility or any obligation whatsoever. The fact that the Government may have formulated or in any way supplied the said drawings, specifications, or other data, is not to be regarded by implication, or otherwise in any manner construed, as licensing the holder, or any other person or corporation; or as conveying any rights or permission to manufacture, use, or sell any patented invention that may in any way be related thereto.

This report is releasable to the National Technical Information Service (NTIS). At NTIS, it will be available to the general public, including foreign nations.

This technical report has been reviewed and is approved for publication.



W. WADE ADAMS, Project Scientist
Hardened Materials Branch
Electromagnetic Mat'ls & Surv Div

FOR THE COMMANDER



GARY K. WAGGONER, Chief
Hardened Materials Branch
Electromagnetic Mat'ls &
Surv Div



WILLIAM R. WOODY, Chief
Electromagnetic Mat'ls & Surv Div

If your address has changed, if you wish to be removed from our mailing list, or if the addressee is no longer employed by your organization, please notify WL/MLPJ, Wright-Patterson AFB OH 45433-6533 to help us maintain a current mailing list.

Copies of this report should not be returned unless return is required by security considerations, contractual obligations, or notice on a specific document.

UNCLASSIFIED

SECURITY CLASSIFICATION OF THIS PAGE

REPORT DOCUMENTATION PAGE				Form Approved OMB No. 0704-0188	
1a. REPORT SECURITY CLASSIFICATION Unclassified			1b. RESTRICTIVE MARKINGS		
2a. SECURITY CLASSIFICATION AUTHORITY			3. DISTRIBUTION/AVAILABILITY OF REPORT Approved for public release; Distribution Unlimited		
2b. DECLASSIFICATION/DOWNGRADING SCHEDULE					
4. PERFORMING ORGANIZATION REPORT NUMBER(S) WL-TR-91-4011			5. MONITORING ORGANIZATION REPORT NUMBER(S)		
6a. NAME OF PERFORMING ORGANIZATION Department of Polymer Science & Engineering		6b. OFFICE SYMBOL (If applicable)	7a. NAME OF MONITORING ORGANIZATION Materials Directorate (WL/MLPJ) Wright Laboratory		
6c. ADDRESS (City, State, and ZIP Code) University of Massachusetts Amherst MA 01003		7b. ADDRESS (City, State, and ZIP Code) WL/MLPJ Wright-Patterson AFB OH 45433-6533			
8a. NAME OF FUNDING/SPONSORING ORGANIZATION Air Force Office of Scientific Research		8b. OFFICE SYMBOL (If applicable) AFOSR/NC	9. PROCUREMENT INSTRUMENT IDENTIFICATION NUMBER AFOSR-85-0275 and F49620-89-C-0073		
8c. ADDRESS (City, State, and ZIP Code) Bolling Air Force Base Washington DC 20332		10. SOURCE OF FUNDING NUMBERS			
		PROGRAM ELEMENT NO. 61102F	PROJECT NO. 2303	TASK NO. A3	WORK UNIT ACCESSION NO. NC
11. TITLE (Include Security Classification) Direct Imaging of Deformation and Disorder in Extended-Chain Polymer Fibers					
12. PERSONAL AUTHOR(S) David C. Martin					
13a. TYPE OF REPORT Final		13b. TIME COVERED FROM Jul 86 TO Jun 90		14. DATE OF REPORT (Year, Month, Day) March 1991	
15. PAGE COUNT 373					
16. SUPPLEMENTARY NOTATION					
17. COSATI CODES			18. SUBJECT TERMS (Continue on reverse if necessary and identify by block number)		
FIELD	GROUP	SUB-GROUP	Rigid-Rod Polymer Ultrastructure PBZT High Resolution Electron Microscopy PBZO Kinking Grain Boundary Compression Disorder Kink Bands		
11	05				
07	04				
19. ABSTRACT (Continue on reverse if necessary and identify by block number)					
<p>The rigid-rod polymers poly (paraphenylene benzobisthiazole) (PBZT) and poly (paraphenylene benzobisoxazole) (PBZO) can be spun from lyotropic liquid-crystalline solutions into solid fibers with extraordinary mechanical properties. However, these fibers are comparatively weak in compression, with deformation occurring by strain localization into kink bands.</p> <p>This report examines the ultrastructure of PBZT and PBZO fibers as a function of processing condition. In particular, High Resolution Electron Microscopy (HREM) is used to directly image structural features such as grain boundaries, dislocations, and the molecular level details of deformation processes. HREM images of PBZT and PBZO enable the quantitative determination of crystallite size, shape, orientation, and internal perfection as a function of processing condition. The nature of the disorder present within and between PBZT and PBZO crystallites is analyzed, modeled, and compared to experimental Wide Angle</p> <p style="text-align: right;">(Cont'd)</p>					
20. DISTRIBUTION/AVAILABILITY OF ABSTRACT <input checked="" type="checkbox"/> UNCLASSIFIED/UNLIMITED <input type="checkbox"/> SAME AS RPT. <input type="checkbox"/> DTIC USERS			21. ABSTRACT SECURITY CLASSIFICATION Unclassified		
22a. NAME OF RESPONSIBLE INDIVIDUAL Dr W. W. Adams			22b. TELEPHONE (Include Area Code) (513) 255-6615		22c. OFFICE SYMBOL WL/MLPJ

Block 19 Cont'd

X-ray Scattering (WAXS) and Selected Area Electron Diffraction (SAED) data. Both PBZT and PBZO exhibit high degrees of orientation on a local scale, yet measurable misorientation does exist.

HREM images in and around PBZT and PBZO kink bands reveal that local, sharp bending and/or breaking of covalently bonded molecules is involved in compressive failure. A model for kinking is proposed which involves the nucleation and growth of a bundle of partial edge dislocations of like sign. A stress analysis using this model is used to correlate systematic morphological features of kinks with local material instabilities. A quantitative analysis of the linear density of kinks within a fiber as a function of applied plastic strain enables the energy required to form a kink to be determined.

The geometry and energetics of grain boundaries in extended chain polymer solids is discussed. Possible mechanisms for grain boundary motion are presented. Comparisons between different grain boundary structural models and experimental HREM data are shown.

FOREWORD

This report was prepared by the Polymer Science and Engineering Department, The University of Massachusetts, Amherst MA. The work was initiated under Project No 2303A3, "Structural Chemistry." It was administered under the direction of the Materials Directorate, Wright Laboratory, Air Force Systems Command, Wright-Patterson Air Force Base Ohio, with Dr W. Wade Adams as the Materials Directorate Project Scientist. The work was funded by the Air Force Office of Scientific Research (AFOSR), Bolling Air Force Base, Washington DC, with Dr Donald R. Ulrich as the program manager for grant number AFOSR-85-0275 and contract number F49620-89-C-0073. The author was Dr David C. Martin of the University of Massachusetts. This report constitutes the basis of the author's Ph.D. dissertation submitted to the University of Massachusetts in February 1990, and covers research conducted from September 1986 to February 1990.

The author acknowledges the help and support of family, friends, and colleagues during the course of this research. In particular, the inspiration and guidance of thesis advisor Edwin L. Thomas made this endeavor a rewarding educational experience. My hope is that I can follow his example and maintain a fresh, curious, yet critical outlook in the future.

I thank the members of my thesis committee for the many conversations and insights which were important in planning, guiding, and interpreting the results from my investigations. In particular, W. Wade Adams was helpful not only for providing samples and discussing avenues of interest, but for critical examination of the intermediate and final versions of this report.

Scientifically, I benefitted greatly from working with the "French Connection": Alain Boudet, Thierry Granier, and Philippe Pradere. I thank each of these gentlemen for their help and for showing me by example how science can and should be done.

I thank the other members of the ELT research group for all the feedback and friendly conversations. Also, I thank Brant Kolb for helping me with laboratory procedures and for just being a great friend.

Finally, I thank Kim for her love, understanding, and support during the completion of this work, and my mother for calling me nearly every week just to keep in touch.

TABLE OF CONTENTS

	<u>Page</u>
ACKNOWLEDGEMENTS.....	iii
ABSTRACT.....	i
LIST OF TABLES.....	Viii
LIST OF FIGURES.....	ix
 CHAPTER:	
I. INTRODUCTION AND OVERVIEW.....	1
A. Outline and Goals of the Dissertation.....	1
B. Rigid-Rod Polymers.....	6
1. Rigid Polymer Synthesis.....	6
2. Chain Symmetry and Chemical Defects.....	8
3. Solution Behavior.....	11
4. Morphology of the Solid State.....	12
C. Questions About Ultrastructure in Rigid-Rod Polymers.....	17
 II. HIGH RESOLUTION ELECTRON MICROSCOPY OF POLYMERS.....	 19
A. Introduction.....	19
B. High Resolution Electron Microscopy (HREM) ..	20
1. HREM Details.....	22
2. Interaction of Incident Wave with Sample.....	25
3. Physics of Image Formation.....	28
4. Image Simulations: Multislice.....	38
5. Simulated HREM Images of Rigid-Rod Polymers.....	40
C. HREM of Polymers.....	52
1. History of Polymer HREM.....	52
2. HREM and Dark Field Imaging.....	60
3. Experimental Details.....	62
a. Sample Preparation.....	62
b. Instrument Operation: Low Dose HREM.....	64
c. Sample Thickness Determination....	69
d. Photographic Details.....	74
e. Optical Bench.....	76
f. Microdensitometry.....	77
D. Summary.....	78

III.	AXIAL SHIFT DISORDER OF PBZT IN THE SOLID STATE.....	80
A.	Introduction.....	81
1.	Previous Work.....	81
2.	Overview of This Study.....	91
B.	Experimental.....	93
C.	Results.....	96
D.	Discussion.....	114
1.	Models for Disorder in Polymer Fibers.....	114
2.	Paracrystalline Lattice Fluctuations..	116
3.	Statistical Disorder.....	122
E.	Conclusions.....	131
IV.	ULTRASTRUCTURE OF CIS-PBZO.....	134
A.	Introduction.....	136
B.	Experimental.....	143
C.	Results.....	146
1.	WAXS and SAED Scattering.....	146
2.	HREM.....	169
3.	Critical Point Dried PBZO Fiber.....	190
D.	Discussion.....	200
E.	Conclusions.....	205
V.	MICROMECHANISMS OF COMPRESSIVE PLASTIC DEFORMATION IN RIGID-ROD POLYMER FIBERS.....	208
A.	Introduction.....	209
B.	Experimental.....	224
C.	Results.....	224
D.	Discussion.....	243
E.	Quantitative Observations of Kinking.....	266
1.	Thermodynamics of Kinking.....	267
2.	Experimental.....	270
3.	Results.....	275
F.	Conclusions.....	279
VI.	GRAIN BOUNDARIES IN EXTENDED CHAIN POLYMERS....	281
A.	Introduction.....	281
B.	Grain Boundary Geometry.....	283
C.	Grain Boundaries in Polymers.....	289
1.	Lateral Chain Invariant (LCI) Boundaries.....	294
2.	Lateral Chain Rotation (LCR) Boundaries.....	297

3. Axial Chain Invariant (ACI)	
Boundaries.....	308
4. Axial Chain Rotation (ACR)	
Boundaries.....	318
D. Conclusions.....	324
 VII. CONCLUDING REMARKS AND FUTURE WORK.....	325
A. Chapter III: PBZT Ultrastructure.....	325
B. Chapter IV: PBZO Ultrastructure.....	327
C. Chapters III and IV: PBZT and PBZO.....	329
D. Chapter V: Kinking.....	330
E. Chapter VI: Grain Boundaries.....	331
F. PBZT and PBZO Thin Films and Crystal Solvates.....	332
 BIBLIOGRAPHY.....	336

LIST OF TABLES

Table 2.1: Imaging Parameters for High Resolution Electron Microscopy using a JEOL 2000 FX Transmission Electron Microscope operating at 200 kV.....	34
Table 2.2: HREM Studies of Polymers.....	56
Table 2.3: Mass Thickness Cross Sections for a JEOL 2000 FX Transmission Electron Microscope.....	75
Table 3.1: Summary of orientation measurements as determined from HREM images for PBZT and PBZO.....	104
Table 3.2: Components of the three Fluctuation Tensors for PBZT Aftech II Fiber based on the Paracrystalline Lattice Model.....	123
Table 4.1: Characteristics of PBZO Fiber as reported by H. Ledbetter of Dow Chemical to W. W. Adams of WPAFB.....	144
Table 4.2: Scattering Intensity on the Meridion calculated from the molecular transform of a single PBZO molecule, as well as a PBZO dimer at a relative axial shift of $1/4$ c, and a PBZO dimer at a relative axial shift of $1/2$ c.....	161
Table 4.3: Scattering Intensity of different hkl reflections calculated with the Multislice formalism.....	166
Table 4.4: Summary of crystallite sizes in both the axial and lateral direction as determined from HREM images for PBZT and PBZO.....	183
Table 4.5: Crystallite size as determined by spreading of reflections in the optical transform of HREM images....	185
Table 4.6: Diameters of critically point dried PBZO fiber before drying, after drying, and after untensioned heat treatment.....	193
Table 5.1: Angle of kink with respect to fiber axis as determined by optical microscopy.....	227
Table 5.2: Possible Deformation Twinning systems to explain the observed geometry of kinking in rigid-rod polymers.....	247
Table 5.3: Results of quantitative study of kink density as a function of plastic strain in rigid-rod polymer fibers.....	278

LIST OF FIGURES

Figure 1.1: Schematic of the stress-strain behavior of a rigid-rod polymer fiber.....	4
Figure 1.2: Synthesis of PBZT and PBZO by condensation polymerization.....	7
Figure 1.3: Bond geometry and partial atomic charges of PBZT and PBZO in equilibrium.....	9
Figure 1.4: Schematic of the processing steps in spinning rigid-rod polymer fiber from solution.....	14
Figure 1.5: Morphology of rigid-rod polymers as a function of processing step.....	15
Figure 2.1: Schematic of the HREM Imaging process...	23
Figure 2.2 a) Projected potential of PBZT in several crystallographic directions. b) Simulated Images of 10 nm thick sections of PBZT for a JEOL 2000 FX at Scherzer focus.....	42
Figure 2.3: PBZT SAED pattern compared with plots of $\sin^2(\chi(k))$ at Scherzer focus for a JEOL 2000 FX (200 kV) and a JEOL 4000 FX (400 kV) Transmission Electron Microscope...	45
Figure 2.4: Projected potential and simulated images of PBZO for a JEOL 2000 FX at Scherzer focus.....	47
Figure 2.5: Effect of limited electron dose on HREM images of PBZO.....	51
Figure 2.6: Schematic of procedures used applying the Minimum Dose System (MDS) to low dose HREM imaging.....	66
Figure 2.7: Effect of sample drift on simulated HREM images of PBZO.....	71
Figure 2.8: Intensity of beam flux under a holey carbon film as compared to vacuum as a function of objective lens defocus.....	73
Figure 3.1: Behavior of the phase contrast transfer function (equation 2.5) as a function of defocus.....	95
Figure 3.2: Simulated HREM images for a PBZT model structure as a function of defocus.....	97

Figure 3.3: SAED pattern of heat treated trans-PBZT fiber.....	98
Figure 3.4: HREM image of PBZT taken near the Scherzer focus.....	101
Figure 3.5: Plot of the crystallite orientation of rigid-rod polymer fibers as determined by HREM.....	102
Figure 3.6: Plot of the maximum axial size of PBZT crystallites as a function of the maximum lateral size as determined from HREM images.....	105
Figure 3.7: HREM image of PBZT fiber fragment using an underfocused objective lens.....	108
Figure 3.8: Higher magnification view of PBZT 1.24 nm (001) fringes showing an area where the (001) fringes meet with a large amount of local misfit, confirming the validity of model which considers a statistical probability of encountering complete axial disorder between adjacent molecules.....	111
Figure 3.9: Models of PBZT structure showing the effect in real space of a higher and higher probability of encountering complete axial disorder between molecules.....	112
Figure 3.10: a) Schematic of the fluctuation tensors associated with each unit cell vector in the paracrystalline lattice model. b) The size of the principal components of the fluctuations tensors determined for PBZT are drawn to scale. c) Geometry of the triclinic unit cell which fits the scattering data.....	124
Figure 3.11: Simulated SAED patterns for PBZT using a triclinic unit cell and a higher and higher probability of encountering complete axial disorder between molecules.....	126
Figure 3.12: Comparison between SAED data for the sixth layer line in heat treated PBZT and theoretical predictions using a triclinic unit cell and a disorder model with different probabilities of encountering complete axial disorder between adjacent molecules.....	128
Figure 4.1: WAXS of PBZO fiber bundles as a function of heat treatment.....	148

Figure 4.2: Densitometer scans of the WAXS data presented in Figure 4.1. a) Meridional scan showing the average WAXS intensity in a rectangular window of width 0.8 nm^{-1} oriented along the fiber axis, plotted as a function of magnitude of the scattering vector k . b) Scan of the second order layer line, again using a rectangular window of width 0.8 nm^{-1} centered about the layer line, plotted as a function of the cylindrical reciprocal lattice coordinate R150

Figure 4.3: Schematic SAED patterns of PBZO from thick (a) and thin (b) fiber fragments.....152

Figure 4.4: Models of different types of regular axial registry between PBZO molecules in the a direction. a) Axial shift of 0 c ; b) Axial shift of $1/2 \text{ c}$; c) Axial shifts of $+1/4 \text{ c}$ and $-1/4 \text{ c}$; and d) Axial shift of $+1/4 \text{ c}$155

Figure 4.5: Reciprocal lattices corresponding to the axial shift models of Figure 4.4. a) Axial shift of 0 c ; b) Axial shift of $1/2 \text{ c}$, c) Axial shifts of $+1/4 \text{ c}$ and $-1/4 \text{ c}$; and d) Axial shift of $+1/4 \text{ c}$157

Figure 4.6: Combined pattern using both models C and D.....158

Figure 4.7: Comparison of model calculations of meridional scattering intensity for PBZO and that obtained experimentally by WAXS.....163

Figure 4.8: a) Molecular transform of a single PBZO chain and a PBZO dimer with a relative axial shift of $1/4 \text{ c}$ on layer lines 1 and 2.....164

Figure 4.9: HREM image of As-Spun PBZO.....172

Figure 4.10: HREM image of PBZO HT 600.....174

Figure 4.11: HREM image of a PBZO HT 600 fiber fragment showing a region with a high population of (200) fringes.....176

Figure 4.12: HREM image of PBZO HT 665 showing a domain which has grown quite large in the lateral direction.....178

Figure 4.13: a) Crystallite size and shape distribution in as spun PBZO as determined by HREM and DF. b) Crystallite size and shape distribution in heat treated PBZO as determined by HREM and DF.....181

Figure 4.14: High Magnification view of an HREM image of PBZO HT 600 showing a region containing an edge dislocation.....	188
Figure 4.15: Model of an extra (100) plane which would explain the image in Figure 4.14.....	189
Figure 4.16: Optical micrographs of a) wet PBZO fiber, b) Critically Point Dried PBZO fiber, and c) Critically Point Dried and Heat Treated PBZO fiber.....	192
Figure 4.17: DF image of CPD HT fiber.....	196
Figure 4.18: HREM image of CPD HT fiber.....	198
Figure 4.19: Model to explain the origin of the four-point SAXS pattern in terms of crystallites with axial chain invariant boundaries.....	203
Figure 5.1: Schematic of the geometry of twinning...	217
Figure 5.2: Optical micrographs of kinks in PBZO fibers: (A) As Spun, (B) HT 600, and (C) HT 665.....	226
Figure 5.3: Equatorial Dark Field image of a Kink in a PBZO HT 600 fiber fragment.....	230
Figure 5.4: Equatorial Dark Field image of a Kink in PBZO HT 600 in which a kink has not propagated all of the way across the fiber fragment.....	233
Figure 5.5: Equatorial Dark Field image of an S-shaped kink in PBZO HT 600.....	236
Figure 5.6: Fibrillated kink in PBZO HT 665.....	238
Figure 5.7: Sketch of an HREM image of PBZT showing the orientation of 0.59 (100) or 0.36 (010) lattice fringes as a function of position.....	240
Figure 5.8: HREM image of a kink in PBZO HT 665.....	242
Figure 5.9: Histogram of the frequency of observation of a kink of a given axial size in DF images of PBZO.....	244
Figure 5.10: Schematic diagram illustrating the geometry of kinking.....	249
Figure 5.11: Schematic of the partial dislocation model of kink formation and propagation.....	251

Figure 5.12: Dislocation Stress Model. (a) Detail from Figure 5.4 showing the isolated kink which had not propagated completely across the fiber. (b) Positions of the dislocations determined using $b=6$ nm. (c) The hydrostatic component of the stress field around the kink using the dislocation model. (d) Iso-stress contour lines.....	255
Figure 5.13: Schematic of an assymetric intermolecular potential well.....	259
Figure 5.14: Fiber in compression: energy balance....	268
Figure 5.15: Experimental configuration used by DeTeresa (1985) to study the critical strain necessary for kink initiation.....	272
Figure 5.16: Typical plot of the total number of kinks N_t seen in the optical microscope vs. position x along the fiber.....	274
Figure 5.17: Plots of the density of kinks $\rho(\epsilon)$ vs. strain ϵ for PBZO as a function of heat treatment and for PPTA.....	276
Figure 6.1: The four different types of grain boundaries which are possible between crystals which have a well defined direction cl	293
Figure 6.2 Schematic diagram of a cross section of an individual microfibril in a rigid-rod polymer fiber projected down the chain axis.....	295
Figure 6.3: Schematic diagram of a plausible mechanism for grain growth by LCI boundary migration.....	298
Figure 6.4: Schematic diagram of a lateral chain rotation (LCR) boundary between neighboring polymer crystallites.....	300
Figure 6.5: Enlargement of an HREM image of a LCR boundary in critically point dried PBZO fiber.....	302
Figure 6.6: Molecular interpretation consistent with the contrast seen in Figure 6.5.....	303
Figure 6.7: Possible mechanism for grain growth at an LCR boundary involving the propagation an internal molecular kink along the boundary and the cooperative lateral motion of a segment of the molecule.....	305

Figure 6.8: OM and SEM views of a region from an isotropic thin film of PBZT which deposited on a deformable substrate and then deformed in uniaxial tension.....307

Figure 6.9: Microfibril consisting of three crystallites in axial registry separated by ACI grain boundaries.....310

Figure 6.10: View of a specific ACI boundary in PBZT as seen from the top.....312

Figure 6.11: HREM Image showing 0.59 nm (100) fringes meeting 0.36 nm (010) fringes in the axial direction (Boudet et al., 1987).....314

Figure 6.12: Molecular interpretation of Figure 6.13 showing both the two crystallites in axial registry with one crystallite oriented so the molecules are seen "edge-to-edge" and the other "face-to-face".....315

Figure 6.13: HREM Image from a kink in PBZO showing an ACR boundary.....320

Figure 6.15: Molecular interpretation of Figure 6.13 which is consistent with the experimental HREM contrast...322

Figure 7.1: Lacy film of PBZT prepared by floating a 0.135 weight percent solution of IV=2.5 dl/gm onto water..333

CHAPTER I: INTRODUCTION AND OVERVIEW

A. Outline and Goals of the Dissertation

Rigid-rod polymers are those in which easy conformational rotations occur only about the chain axis. Typical examples include poly(paraphenylene benzobisthiazole) (PBZT) and poly(paraphenylene benzobisoxazole) (PBZO). Rigid-rod polymers represent an extreme example of a "stiff" chain molecule. Other, more common polymers such as poly(paraphenylene terephthalamide) (PPTA), poly(benzl-L-glutamate) (PBLG), DNA, and cellulose are "stiff" under certain conditions of environment and temperature, but since these molecules have access to low energy conformational states which are non-linear, they are not truly "rigid-rods".

Rigid-rod polymers can be spun from solution into fibers and films with extraordinary mechanical properties, and therefore are of considerable technological importance. However, these fibers and films are comparatively weak in compression, with post-failure deformation occurring by strain localization into kink bands. This low compressive strength severely limits the potential of these materials for structural components, particularly for high performance applications where strength to weight ratios are critical. A schematic of the stress-strain response of a rigid-rod poly-

mer fiber is shown in Figure 1.1. The fibers have excellent tensile strength (4 GPa) and tensile modulus (400 GPa), but the compressive strength is much lower (0.4 GPa).

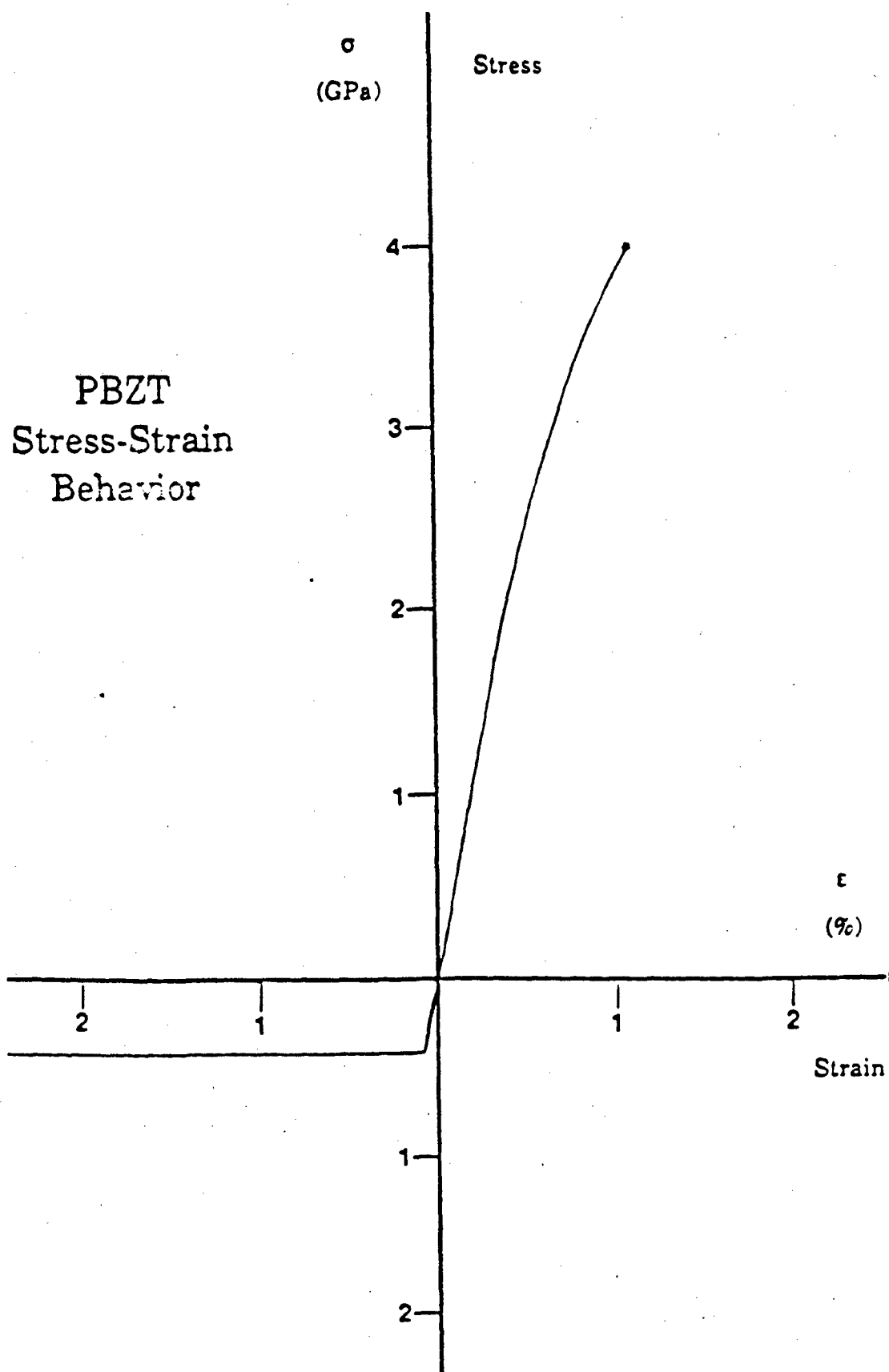
The broad goal of the research described in this dissertation was to provide a fundamental understanding of the solid-state morphology of rigid-rod polymers. In particular, we hoped to find out new information by systematic application of High Resolution Electron Microscopy (HREM) techniques to PBZT and PBZO microstructures. By characterizing the specific types of defect structures present in these novel polymer solids and rationalizing these observations in terms of the known chemical structure, we hoped to understand how these defects affect structure-property relationships. Also, it was hoped that information about the molecular motions involved in the plastic deformation accompanying compressive instability would be obtained.

Normally, a flexible polymer in dilute solution might be envisioned as an isolated strand of "cooked spaghetti", wiggling and twisting about in a loosely coiled conformation. A comparable physical picture of a rigid-rod molecule is that of a stiff strand of "uncooked linguine". The linguine analogy is particularly appropriate because it illustrates the non-circular cross section of the PBZT and PBZO molecules. In general terms, our interest was in understanding what happens when these "linguine-like" molecules

pack together in the solid state. Also, we wished to understand how supposedly completely stiff molecules were able to slip and bend during deformation of a solid fiber.

The second part of this chapter is a general discussion and overview of the chemical structure of rigid-rod polymers and their morphology in the solid state. Chapter II presents experimental and theoretical details of High Resolution Electron Microscopy (HREM), a technique used extensively in this study and not commonly applied to electron beam sensitive materials. Chapter III details an investigation of the structure of PBZT fiber, and Chapter IV concentrates on the structure of PBZO. Chapter V is an in-depth look at the morphology and thermodynamics of compressive deformation zones (kink bands) in rigid-rod polymers. Chapter VI is a theoretical prelude which provides a framework for cataloging different types of grain boundaries in extended chain polymer solids. Experimental confirmation of the different types of polymer grain boundaries will be summarized. Chapter VII contains concluding remarks and suggestions for future work.

Figure 1.1: Schematic of the stress-strain behavior of a rigid-rod polymer fiber. The fiber is extremely strong and stiff in tension, but is comparatively weak in compression with failure occurring by strain localization in kink bands.



B. Rigid-Rod Polymers

1. Rigid-Rod Polymer Synthesis

The synthetic routes to and structural formulas of PBZT and PBZO are presented in Figure 1.2. Both materials are prepared by condensation polymerization in strong acid (typically poly(phosphoric) acid (PPA)). The solubility of the polymers depends on the ability of a solvent to protonate or complex with the chain backbone, and therefore is limited to strong protic or Lewis acids (Jenekhe and Johnson, 1989). The intrinsic viscosity of PBZO and PBZT in Methane Sulfonic Acid (MSA) depends on molecular weight to the power 1.85 (Wong, Ohnuma, and Berry, 1983) and 1.80 respectively (Lee, Chu, and Berry, 1983), indicating that the molecules behave very much like "rigid-rods" in dilute solution.

It is important to note that both PBZT and PBZO can be polymerized into either the trans or cis forms, defined in terms of whether the nitrogens are either on opposite sides of the heterocyclic group (trans) or both on the same side (cis). Historically, PBZT has been made predominantly in the trans form, whereas PBZO has been synthesized in the cis form. In the discussion that follows and throughout the remainder of this thesis, all references to PBZT will be for the trans form and all references to PBZO will be for the cis form, unless otherwise specified.

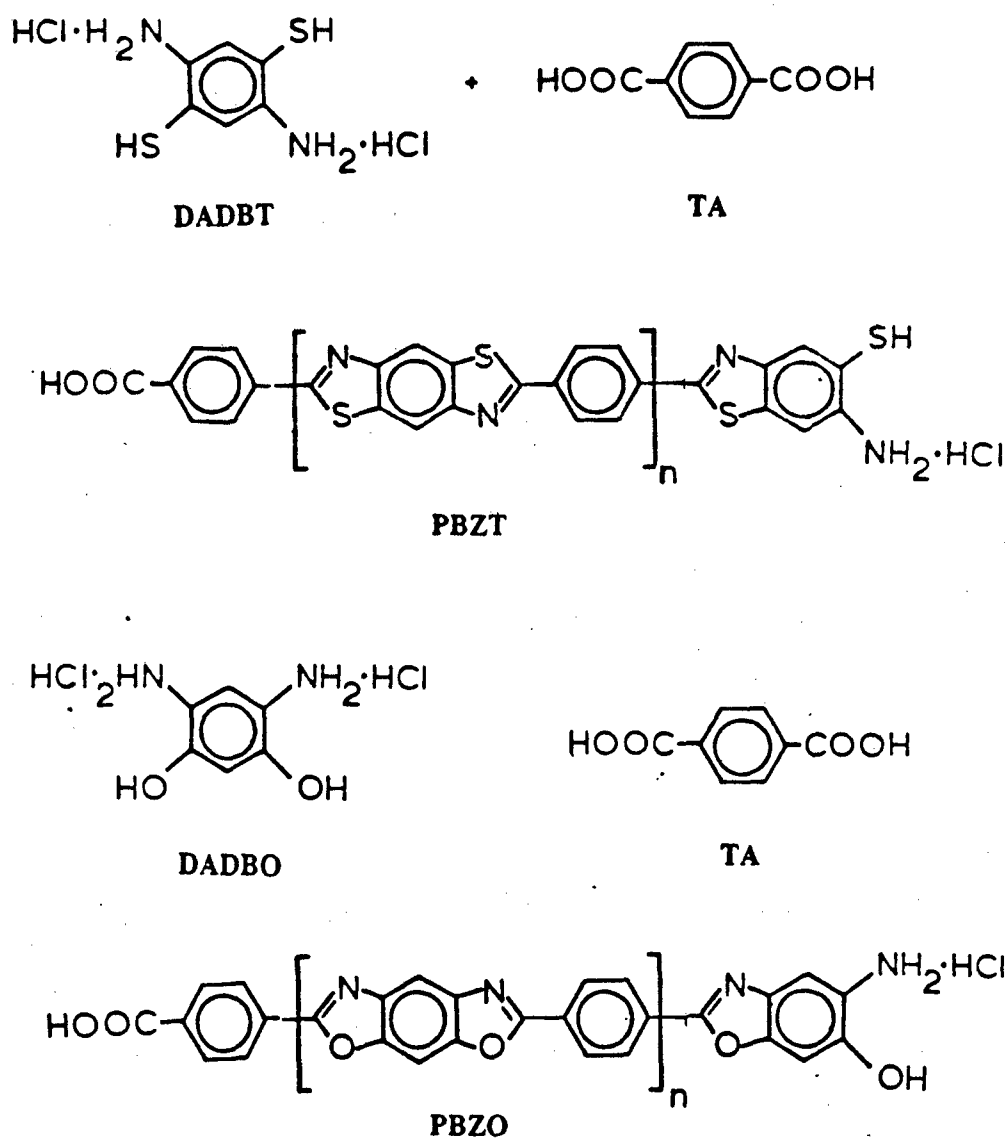


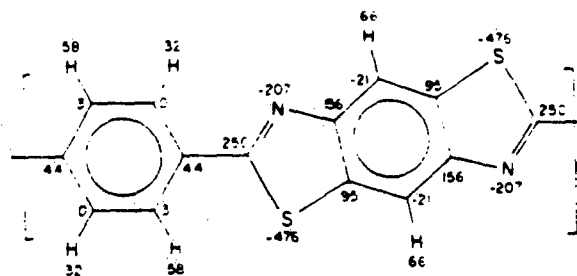
Figure 1.2: Synthesis of PBZT and PBZO by condensation polymerization. Solubility of the polymers depends on protonation of the chain backbone and therefore is restricted to strong protic or Lewis acids. Adapted from Minter (1982).

2. Chain Symmetry and Chemical Defects

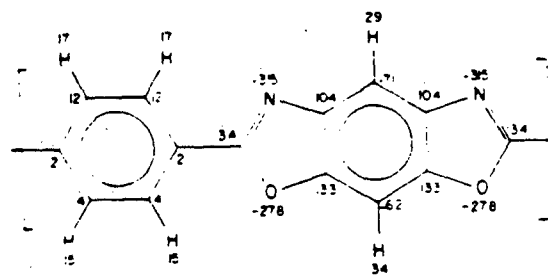
Figure 1.3 shows the cis-PBZO and trans-PBZT repeat units drawn with atomic positions and the partial charge of each atom in equilibrium as determined for isolated molecules by the CNDO/2 method by Bhaumik, Welsh, Jaffe, and Mark (1981). It is apparent that the bond geometry of both PBZT and PBZO is such that easy conformational changes are only those which involve simple rotations of the phenyl or heterocyclic group about the chain axis. Let us now examine how rotations such as these might affect local packing energetics.

First consider the change in local chemical environment induced by a rotation of the heterocyclic group about the chain backbone. The symmetry of either the cis or trans forms is such that the relative positions of nitrogens on neighboring monomers will be changed by such a rotation. This alteration in the specific contacts between molecules will influence the intermolecular potential energy.

The second aspect is the linearity between the bonds at either end of the heterocyclic group. Since the phenyl group-heterocycle bonds are predicted to be colinear with the chain axis for cis-PBZO, this rotation can occur without disrupting the molecular orientation. Notice from Figure 1.3 that the



PBZT



PBZO

Figure 1.3: Bond geometry and partial atomic charges of PBZT and PBZO in equilibrium calculated by the CNDO/2 method (Welsh, et al., 1981). Units are in 10^{-3} of an electron charge. Note that the heterocycle-phenyl ring bonds are colinear with the chain axis for PBZO but not for PBZT. This implies that a rotation of the heterocyclic group about the chain axis will require a local reorientation of the chain for PBZT, but not for PBZO. The symmetries of both the "cis" and "trans" forms mean that such rotations will change the specific nature of intermolecular contacts.

neighboring phenyl group-heterocycle bonds along the backbone are not parallel to the molecular axis in PBZT. Hence, in this case rotations of the heterocyclic group about the chain axis will require a change in the local orientation of the chain.

A chemical defect internal to the chain may occur if the polymerization of PBZT or PBZO is not complete. It is conceivable that during the polymerization the TA acid group does not completely eliminate the DABDT monomer. Such an incomplete reaction of the TA acid with the DABDT monomer might result in the formation of a local flexible linkage in the otherwise rigid backbone. Other types of chain defects might occur due to the presence of impurities in the reaction medium, giving rise to a certain percentage of bonds which allow for flexibility within the chain. The presence of such a flexible "swivel" in the chemical structure has been predicted to have important consequences on phase behavior of rigid polymers (Matheson and Flory, 1981), and might cause major packing problems in the solid state.

Because these polymers are prepared by condensation polymerization, the molecular weight distributions are expected to be reasonably broad. Indeed, this has been experimentally observed (Cotts and Berry, 1981). Experiments indicate a deviation from the "most-probable" distribution with depletion of both short and long chain lengths. This

was rationalized in terms of a rate constant for polymerization which was dependent on the chain length. The polydispersity ratios M_w/M_n are less than the most probable value of 2.0 during the most of the reaction, approaching 2.0 only at high conversion (98% or more).

For typical molecular weights (30,000-60,000), the degree of polymerization is on the order of 100-200. This means that one out of every 50 to 100 units is expected to be a chain end. If the size of the chain end is assumed to be the same as a repeat unit, then in the final fiber 1 to 2% of the material by volume may be chain ends. If there is a tendency for chain ends to segregate out of crystalline regions, then the local density of ends may be higher.

3. Solution Behavior

Dilute solutions of PBZT and PBZO are isotropic, but as the concentration increases the solution becomes anisotropic (Wolfe et al., 1981, Choe and Kim, 1981). Fibers and films are typically prepared by dry-jet wet spinning techniques, involving extrusion of this nematic solution through an air gap into a coagulating bath. These "as-spun" fibers and films are subsequently heat treated under tension for the highest moduli and tensile strengths (Allen, 1983). For PBZT tensile moduli of 330 GPa and tensile strengths of 4.2 GPa have been reported, for PBZO these values are 365 GPa and 5.8

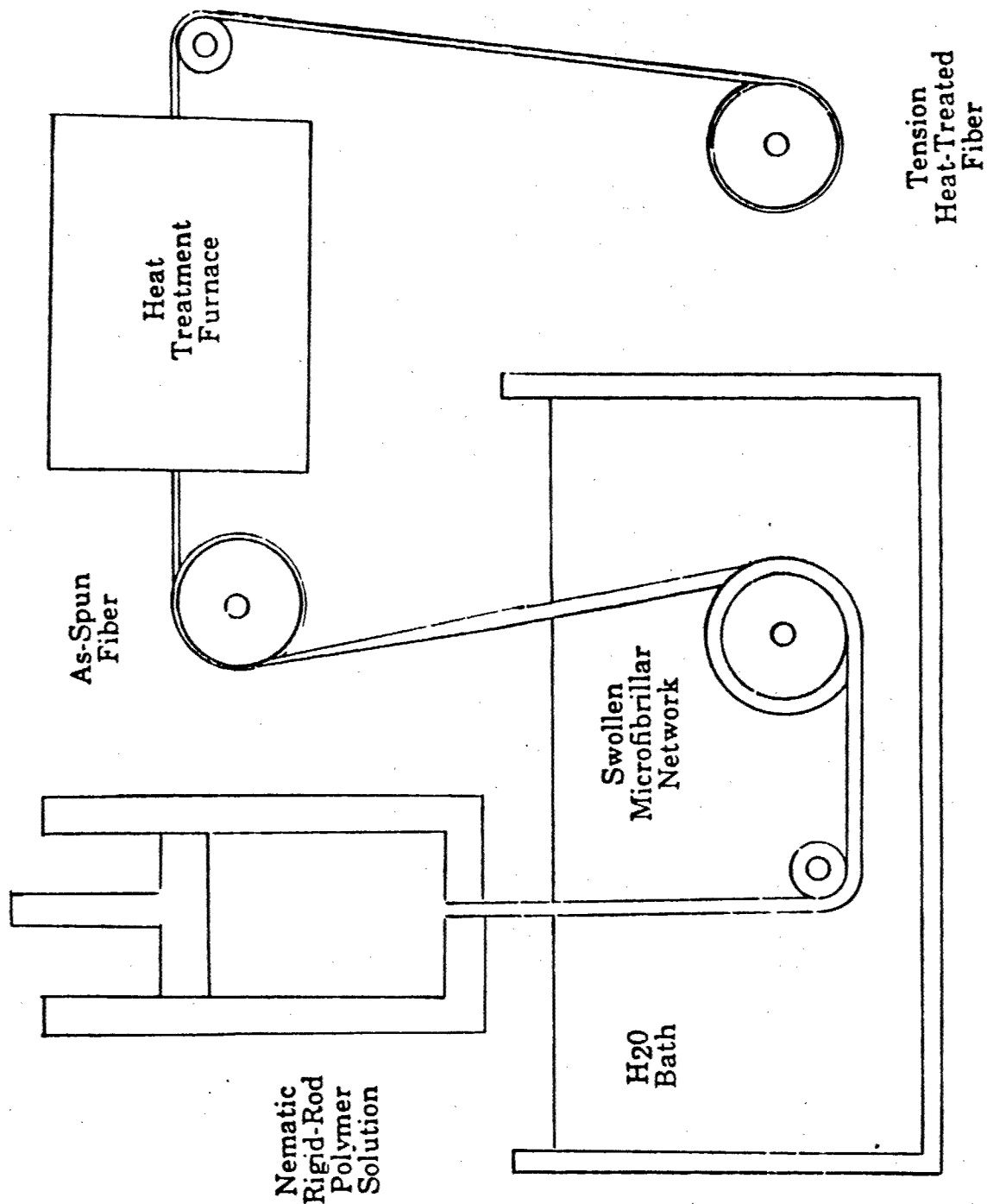
GPa, respectively (Adams and Eby, 1988). A schematic of the fiber processing steps is shown in Figure 1.4.

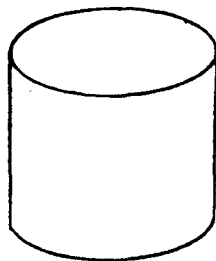
4. Morphology of the Solid State

The structure of fibers and films of PBZT and PBZO has been studied by several techniques including Optical Microscopy (OM), Wide Angle X-Ray Scattering (WAXS), Small Angle X-Ray Scattering (SAXS), Small Angle Neutron Scattering (SANS), Scanning Electron Microscopy (SEM), Conventional Transmission Electron Microscopy (CTEM) using both Bright Field (BF) and Dark Field (DF) Imaging, and High Resolution Electron Microscopy (HREM). From these studies we now have a relatively detailed understanding of the morphology of rigid-rod polymers. The major findings are summarized below and elaborated in detail in the introductions to Chapters III and IV.

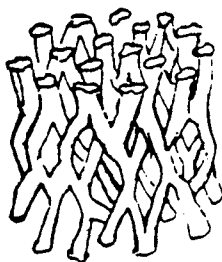
The structure of rigid-rod polymer fibers as a function of processing step is shown schematically in Figure 1.5. In concentrated acid solution, the rigid-rod polymer solution is in the nematic state. During dry-jet wet fiber spinning the acidic solution is extruded through a die and oriented by an elongational stretch in an air gap (Figure 1.5a). This oriented solution is then coagulated forming an interconnected microfibrillar network (Cohen, 1987) (Figure 1.5b). During drying, the network is collapsed

Figure 1.4: Schematic of the processing steps in spinning rigid-rod polymer fiber from solution. The nematic solution is forced through a die under pressure through an air gap and is coagulated in a water bath. The wet fiber is a swollen microfibrillar network. When removed from the water the fiber shrinks into the "as-spun" state. The best properties are obtained after heat treatment under tension.





Nematic
Rigid-Rod
Polymer
Solution



Swollen
Microfibrillar
Network



As-Spun
Fiber



Tension
Heat-Treated
Fiber

Figure 1.5: Morphology of rigid-rod polymers as a function of processing step. The nematic polymer solution undergoes a phase transition to a swollen microfibrillar network upon coagulation in water. After drying the microfibrils collapse yielding the "as-spun" fiber. Heat treatment under tension gives better orientation and larger crystallites.

yielding the "as spun" fiber (Pottick, 1986) (Figure 1.5c). Heat treating under tension allows further perfection of the orientation and increase of the crystallite size (Minter, 1982; Allen, 1983) (Figure 1.5d).

WAXS and SAED patterns of heat treated PBZT and PBZO fiber show strong equatorial reflections with pronounced continuous streaking on layer lines along the fiber axis, indicating the molecules pack well in two dimensions but exhibit disorder along the orientation direction (Roche, Takahashi, and Thomas, 1980). PBZO exhibits more local 3-D crystal texturing than PBZT as evidenced in WAXS by the development of localized scattering on the second order layer line and in SAED by the non-uniform relative intensities of equatorial reflections from different regions of the fiber (Adams et al., 1986; Krause et al., 1988).

SAXS scattering of spun fibers of PBZT and PBZO shows strong equatorial scattering due to voids (Minter, 1982). The voids are elongated in the direction of the fiber axis. The diameter of the microfibrils has been characterized by SAXS of water-coagulated PBZT giving a size of 7 nm (Cohen, 1987). This compares with the 5-15 nm lateral crystallite size seen in heat-treated PBZT by DF imaging and with direct equatorial lattice fringe observations by HREM (Shimamura, Minter, and Thomas, 1983; Boudet et al., 1987). Unlike PBZT, SAXS of heat-treated PBZO shows a four-point pattern

indicative of the development of a periodic fluctuation in the electron density at specific angles to the fiber axis. The periodicity of the structural fluctuations giving rise to this SAXS scattering is approximately 8 nm and is oriented at about 57 degrees to the fiber axis.

The size and shape of the crystallites may be determined by DF imaging and by direct imaging of the lattice by HREM. From DF tilt studies it is known that the crystallites are not long and "twisting" but instead are short, equiaxed, and randomly oriented about the fiber axis (Martin, 1989). The differences in the axial and transverse size of crystallites in different high performance polymers measured by DF has been compared by Krause et al. (1988). PBZO crystallites increase in size in the lateral dimension during heat treatment, whereas PBZT increases size more in the axial direction. In both PBZT and PBZO the size of the crystallites in the axial direction (5-20 nm) is much smaller than the length of each molecule (100-200 nm).

C. Questions About Ultrastructure in Rigid-Rod Polymers

While much has been done to develop a detailed understanding of the morphology of rigid-rod polymers, there are several key issues which remain unanswered. For example:

* What is the detailed nature and extent of limited three-dimensional ordering in PBZT? What types of defect models are appropriate for modeling and characterizing this disorder?

* What is the nature of the three-dimensional crystallinity which develops in PBZO?

* What are the specific defect structures representative of the disorder within and boundaries between PBZT and PBZO crystallites?

* What mechanisms of molecular motion are involved in the compressive deformation process? Is it possible to quantify as a function of strain the nature and number of kinks involved in the plastic deformation behavior of rigid-rod polymers in compression?

This thesis provides answers to some of these questions and points out additional avenues of further investigation for others. The development of our understanding of these details is central to a full appreciation of the relationship between the microstructure of these unique materials and their outstanding mechanical properties. With this insight it may be possible to design novel synthetic and processing routes to tailor properties for even better performance in the future.

CHAPTER II: HIGH RESOLUTION ELECTRON MICROSCOPY OF POLYMERS

A. Introduction

High resolution structural studies are of interest for determining the detailed arrangement of molecules and atoms in a material. The amount of information obtained by an imaging technique can be quite large, and there is a strong tendency to literally interpret images as a direct indication of detailed sample structure. Unfortunately, for samples imaged by phase contrast it is not always possible to directly interpret sample structure from an image due to the strong influence of the microscope optics. This lack of fundamental understanding in image interpretation has led to controversy and misunderstanding of polymer ultrastructure in the past (Thomas and Roche, 1979). A knowledge of the optics of electron imaging and a simulation of model images for a presumed structure are both necessary for valid interpretation of images taken near the ultimate resolution of a microscope.

In this chapter the fundamental physics of high resolution electron imaging is reviewed. A familiarity with the idiosyncrasies associated with proper HREM technique is an important prerequisite for interpretation of much of the data presented in the later chapters of this thesis. Particular

attention will be paid to aspects of HREM relevant for imaging beam sensitive materials.

B. High Resolution Electron Microscopy (HREM)

HREM describes imaging with electrons at a resolution sufficient to resolve the important spacings corresponding to local packing of atoms and molecules into a crystalline lattice. At this resolution (nominally less than 2 nm), image contrast can sometimes be directly related to the projected electron potential of the sample. HREM can therefore be a powerful tool for local structural characterization. Because the spacings corresponding to the crystalline lattice are a common feature in HREM images, these micrographs are also often referred to as "lattice images".

Although HREM investigations of inorganic materials have become common, the use of this technique for organic materials (like most polymers) has been limited by the rapid degradation of the material in the electron beam. However, the careful use of minimum dose exposure techniques as well as particular attention to sample preparation has made it possible to apply HREM to a number of polymers.

In the following section the details of HREM will be briefly reviewed and the relationship between intensity distribution in an HREM image and the original sample struc-

ture will be shown. It will be seen that while the relative intensities of different frequencies originally present in the sample may be altered in the image, the periodicities or "spacings" are not changed. Hence, it is possible to unequivocally associate regions of well-defined periodic fringes observed in HREM images as arising from similar well-ordered regions present in the original sample.

We will explore these points in more detail by examining the relationship between sample structure and HREM image for rigid-rod polymers. These image simulations use the multislice approach to solve the dynamic electron scattering from different projections of the PBZT and PBZO crystal structures determined from scattering techniques. These simulations will illustrate clearly the relationship between the postulated sample structure and the expected HREM image.

Next, the history of HREM imaging of polymers and some highlights of these previous studies will be discussed. Then experimental details pertinent to the HREM studies in this dissertation will be presented including sample preparation, instrument operation, and sample thickness determinations. We will also examine the obscuring effect of limited electron dose and sample drift on simulated images.

1. HREM Details

HREM has become an important tool for structural studies in materials science. Detailed reviews of the procedure are available (e.g., Spence, 1980; Amelinckx, 1986; Fujita and Hirabayashi, 1986; Buseck, Cowley, and Eyring, 1989). The possibilities of using HREM for studying defects in crystalline polymers have been discussed by Martin and Thomas (1987). The following is a condensation of the essentials of HREM imaging necessary to understand the technique with emphasis on the important way in which the microscope influences the final image.

Figure 2.1 is a schematic of the HREM imaging process. We take the electron potential function of our sample as $\phi(x_1, x_2, x_3, t)$, where x_1, x_2, x_3 are positions in real space and t is time. Often, we are interested in the static structure only, and therefore we will restrict this discussion to $\phi(x_1, x_2, x_3)$. Radiation damage will cause changes to ϕ as t increases, but usually the primary interest is in the undamaged specimen structure $\phi(x_1, x_2, x_3, t=0)$.

Impinging upon this sample is the electron beam with its own characteristic wave function ψ_0 traveling in the direction x_3 . The beam interacts with the sample to give rise to an exit wave ψ_x . The Fourier transform of ψ_x is ψ_k , where k is the scattering vector. With the microscope

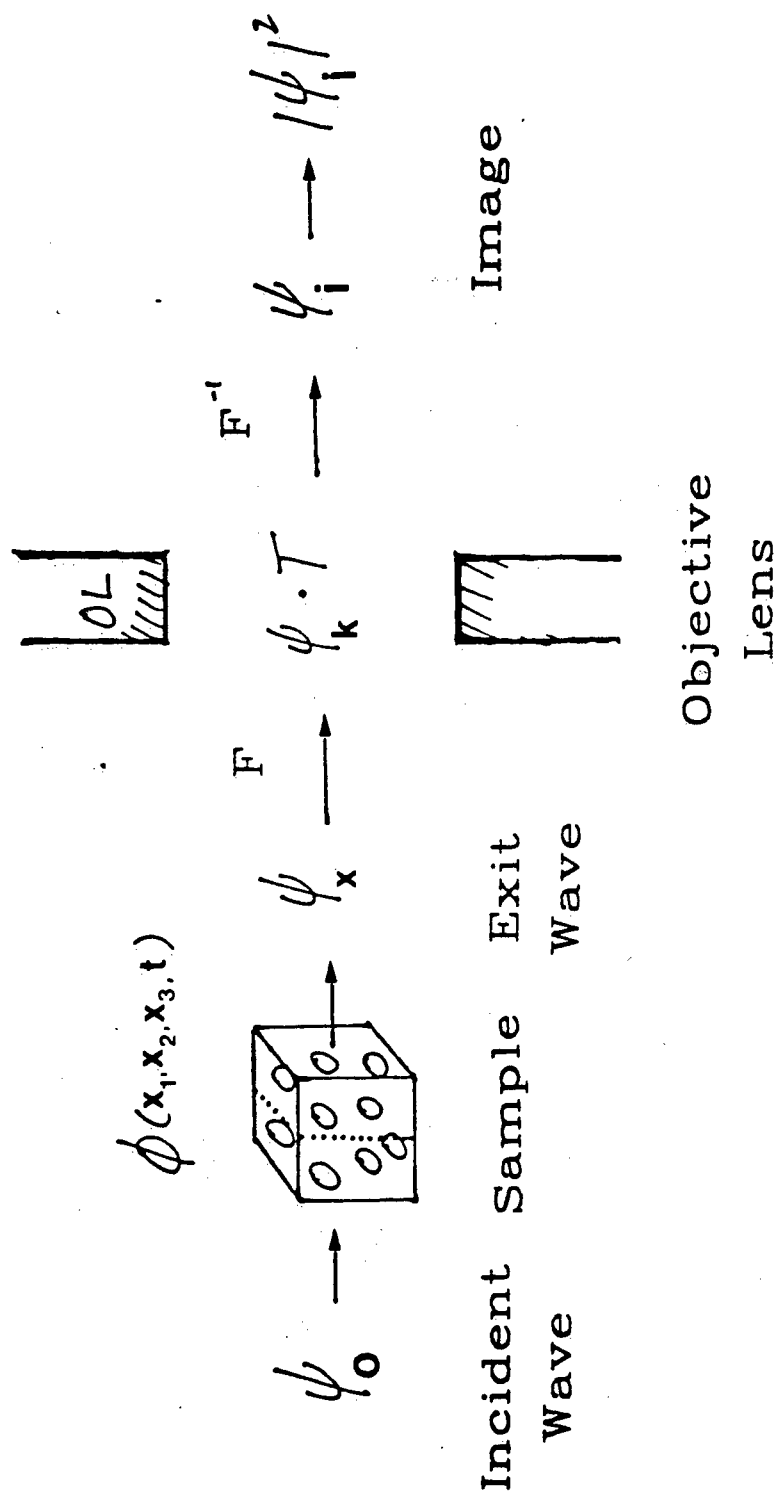


Figure 2.1: Schematic of the HREM imaging process.
See text for details.

objective lens off the experimentally observed quantity is the scattering pattern $I(\mathbf{k})$ which is proportional to the squared amplitude of $\psi_{\mathbf{k}}$. The effect of the objective lens is to multiply $\psi_{\mathbf{k}}$ by a Transfer function T (which depends sensitively on the operating conditions of the microscope), and then to inverse Fourier transform $\psi_{\mathbf{k}} T$ to give $\psi_{\mathbf{i}}$, the image wave. The intensity of the final image is recorded as a two-dimensional array of darkening on the photographic film $I(x_1, x_2)$ which is proportional to the squared amplitude of $\psi_{\mathbf{i}}$.

The goal of HREM imaging is to relate the 2D image intensity $I(x_1, x_2)$ to the 3D sample structure $\phi(x_1, x_2, x_3)$. In order to reconstruct $\phi(x_1, x_2, x_3)$ from $I(x_1, x_2)$ three problems must be solved. First, it is necessary to determine how the structure scatters the incident wave ψ_0 to give rise to an exit wave $\psi_{\mathbf{x}}$. Second, it is necessary to know the effect of the microscope on taking this exit wave and producing an image wave $\psi_{\mathbf{i}}$. This requires an understanding of the transfer function T . Third, since the sample structure is three-dimensional and the image is two-dimensional, it is necessary to reconstruct the three-dimensional structure by taking a series of images about some tilt axis (DeRosier and Klug, 1968).

2. Interaction of Incident Wave with Sample

In general, the scattering from an arbitrary arrangement of atoms requires the solution of the three-dimensional Schrodinger equation for the entire sample-incident wave system. However, in certain limiting cases the relationship between the sample structure and the exit wave is simply related.

The effect of the positive potential distribution ϕ of the sample on an incident plane wave ψ_0 is to cause an acceleration of the electron, causing a small reduction in wavelength. This gives rise to a local phase shift for an electron passing through an area of the sample of higher potential. The amount of phase shift relative to vacuum for an electron passing through a region of uniform potential ϕ of thickness t is $\sigma \phi t$, where σ is given by $\sigma = \pi/\lambda V_0 = 2 \pi m e \lambda/h$. λ is the wavelength of the electron, V_0 the accelerating voltage, m the electron mass, and e the electronic charge.

For high accelerating voltages, the wavelength of the electron calculated from the de Broglie relationship must be corrected for relativistic effects. The algebraic relationship between λ (nm) and V_0 (volts) is (Hirsch et al., 1965):

$$\lambda = 1.22639 / (V_0 + 0.97845 \times 10^{-6} V_0^2)^{1/2} \quad (2.1)$$

Hence, for an accelerating voltage V_0 of 200 kV, the wavelength of the electron λ will be 0.00251 nm, and therefore σ will equal $0.00626 \text{ (nm volt)}^{-1}$. This means a typical sample of thickness t of 10 nm with a constant inner potential ϕ of 10 eV would cause a phase shift of 0.626 radians (35.8 degrees) relative to vacuum.

For a thickness over which focus variation is negligible, the sample acts as a pure phase object and the exit wave ψ_x is related to the incident wave ψ_0 as follows:

$$\psi_x = \psi_0 \exp(-i \sigma \phi(x_1, x_2)) \quad (2.2)$$

where $\phi(x_1, x_2)$ (volt nm) is the total projection of ϕ along the beam direction x_3 , given simply by integrating ϕ in the x_3 direction. This is known as the strong-phase object approximation (SPOA). The SPOA represents the correct dynamical solution to the scattering problem when the voltage is infinite (Moodie, 1972).

If the amount of phase shift is small, the exponential in (2.2) may be expanded and higher order terms neglected, giving

$$\psi_x = \psi_o (1 - i \sigma \phi(x_1, x_2))$$

(2.3)

which is the weak phase object approximation (WPOA). In the WPOA case there is a simple, linear relationship between the projected potential of the sample and the exit wave. For samples of higher atomic weight, significant dynamical (multiple scattering) effects are seen in thicknesses as small as 1 nm (Lynch, Moodie, and O'Keefe; 1975). For lower atomic number samples $\phi(x_1, x_2)$ is smaller so that the WPOA holds for thicker samples.

The solution of the dynamical scattering problem for a thick sample can be calculated by the "multislice" method of Cowley and Moodie (1957). In this approach the sample is treated as a series of N thin slices along the beam direction. The slice thicknesses are chosen so that the defocus variation within each of them is negligible, and therefore the SPOA holds. The smearing of the wave through the vacuum between slices is treated by a spherical Fresnel propagator. In the limit of large N, the results obtained by this technique are equivalent to the rigorous dynamical scattering calculation (Cowley and Moodie, 1957). The multislice approach can be easily adapted for numerical calculations and FORTRAN source code is now widely distributed by the National

Centers for High Resolution Electron Microscopy at Arizona State University and the Lawrence Berkeley Laboratory.

3. Physics of Image Formation

If the exit wave is allowed to propagate in a uniform potential field, then at large distances away from the sample the resulting wave is ψ_k , the scattered wave. ψ_k is the Fourier transform of ψ_x . Without the action of the objective lens the squared amplitude of ψ_k may be collected on film as the electron diffraction pattern.

The effect of the objective lens of the microscope on the propagating wave can be represented as a multiplication of ψ_k by a function T known as the transfer function of instrument and an inverse Fourier transform of $\psi_k T$ to give the image wave ψ_i . Ideally, it would be best to have a transfer function $T=1$ for all frequencies; then the intensity in the image could be directly related to intensities in the exit wave. However, T is a sensitive function of the optics of the microscope and in fact may even be zero or negative. Thus some frequencies may be lost completely or passed in reverse contrast. T approaches zero for low frequencies, is nearly equal to +1 or -1 for a "pass band" of intermediate frequencies which depend sensitively on defocus, oscillates

strongly at higher frequencies, and then approaches zero again at the very highest frequencies.

The functional form of T is (Cowley, 1989):

$$T = \exp(i \chi(k, df)) D_1(k) D_2(k, df) D_3(k, M) A_1(k) \quad (2.4)$$

where df is defocus, M is magnification, $\exp(i \chi(k))$ is the objective lens propagator function, D_1 is the damping envelope due to focus spread, D_2 is the damping due to beam divergence, D_3 is the damping due to the film response, and A_1 is an aperture function.

The first term in equation 2.4 is the objective lens propagator function $\exp(i \chi(k))$ which plays a critical role in determining the phase contrast of a high resolution electron micrograph. The specific form of $\chi(k)$ is

$$\chi(k) = 2 \pi / \lambda (df k^2 \lambda^2 / 2 + C_s \lambda^4 k^4 / 4) \quad (2.5)$$

where C_s is the spherical aberration coefficient of the objective lens. For a JEOL 2000 FX with a side entry goniometer and high resolution pole piece, $C_s = 2.3$ mm. Negative values of df mean an underfocused objective lens. The term $\exp(i \chi(k))$ is sometimes called the coherent phase

contrast transfer function (Cowley, 1989) because it represents the expected objective lens phase shifts for a perfectly coherent source. In reality, electron sources are not coherent; their finite chromatic aberration and beam divergence both serve to dampen high resolution information. Before we discuss the role of the function $\exp(i \chi(k))$, we will first discuss these damping functions.

The first damping function D_1 is due to focal spread and is given as

$$D_1 = \exp[-\pi^2 \sigma_d^2 U^4 / 2] \quad (2.6)$$

where σ_d is the dimensionless spread of focus given in reduced units as $\sigma_d = \sigma_d' / (C_s \lambda)^{1/2}$, with σ_d' the standard deviation of focus in nm. Here, U is a reduced scattering vector $U = k (C_s \lambda^3)^{1/4}$. Likewise, D_2 is given by:

$$D_2 = \exp[-\pi^2 \theta^2 U^2 (U^2 + df')] \quad (2.7)$$

with $\theta = a (C_s / \lambda)^{1/4}$ the reduced semiangular divergence for the beam divergence a in radians, and $df' = df / (C_s \lambda)^{1/2}$ the reduced defocus.

The film damping term D_3 is described well by a Lorentzian (Tsuji and Manley, 1983):

$$D_3 = 1/(1 + A k^2/M^2)$$

(2.8)

where A is a constant which depends on the grain size of the film and developing conditions and M is the magnification. This damping term represents the inability of the film to record incident periodic signals with very small spacings between peaks (high frequencies). The response of a photographic emulsion as a function of signal frequency is called the Modulation Transfer Function (MTF) (Dainty and Shaw, 1974; Shepp, 1989). For beam resistant samples the magnification M can be increased to a point where the effect of D_3 on the recorded image is negligible ($D_3=1$). This is not the case with beam sensitive materials such as those studied in this thesis, where low magnifications are important to reduce the incident electron dose. At low magnifications D_3 becomes the dominant damping term.

Each of the functions D_1 , D_2 , and D_3 damp high frequencies and therefore each may determine the practical limit for information transfer in the microscope. In order to evaluate the different damping functions D_1 , D_2 , and D_3 it is necessary to define some level of intensity necessary for frequencies to make an important contribution to the image.

A convenient value is 14% (Cowley, 1989), representing $\exp(-2)$. This level of the image intensity gives $\exp(-1)$ in the image amplitude (37%). Let us define the maximum resolution (largest important scattering vector k) as k_{\max} . From equation (2.6), we then find the relation:

$$\sigma_d' = 0.45 / (k_{\max}^2 \lambda) \quad (2.9)$$

Likewise, from 2.7 we obtain the requirement:

$$a < 0.32 / (k_{\max} (k_{\max}^2 C_s \lambda^2 + df)) \quad (2.10)$$

as the limiting value of beam divergence necessary to avoid damping due to D_2 . Experimentally, the best information resolution thus far obtained by our research group on the JEOL 2000 FX is the 0.17 nm (840) reflection in poly(paraxylylene) (PPX) (Pradere, 1988), corresponding to a k_{\max} of 5.88 nm^{-1} . From the equations above and the physical characteristics of the microscope ($C_s = 2.3 \text{ mm}$, $\lambda = .00251 \text{ nm}$), this corresponds to a maximum defocus spread σ_d' of 5.2 nm and a limiting semi-angle of illumination a of about 0.1 mrad.

Experimentally, the parameter Λ in D_3 may be determined by measuring the response of the film to a beam stable object of known periodicity. This involves taking a series of

lattice images as a function of magnification and determining the smallest magnification at which it is still possible to detect Fourier peaks of the appropriate frequency in the optical transform of the image. On the JEOL 2000 FX, it was found that a 1.4 nm lattice image of an oxide sample could not be resolved below 10,000x on Kodak SO-163 Electron Image Film developed in full strength D-19 developer for 12 minutes. This corresponds to a peak-to-peak distance on the film of 14 microns. Using a value of D_3 equal to 0.14 as the limit of reasonable detection, this gives a value for A of $1.2 \times 10^9 \text{ nm}^2$. For a HREM micrograph of a 0.55 nm lattice (corresponding to the PBZO (200) first equatorial spacing) taken at 130,000x, the film damping term $D_3=0.81$.

These values are quite reasonable for obtaining good, high resolution images. The following Table 2.1 summarizes the experimental parameters governing HREM imaging with a JEOL 2000 FX and Kodak SO-163 film.

Let us now examine the expected HREM image intensity in the case of the WPOA (Cowley, 1989). In the following discussion the role of the damping functions D_1 , D_2 , and D_3 will be assumed unimportant. The WPOA gives us the normalized transmission function $q(x_1, x_2)$:

Table 2.1
HREM Imaging Parameters
for a JEOL 2000 FX with
Side-Entry Goniometer and
High Resolution Pole Piece

Parameter	Symbol	Value	Units
Voltage	E_0	200	kV
Wavelength	L	0.00251	nm
Spherical Aberration	C_s	2.3	mm
Defocus Spread	$\sigma d'$	5.0	nm
Beam Divergence	α	0.1	mrad
Film Damping	A	1.2×10^9	nm^2

$$q(x_1, x_2) = \psi_x / \psi_0 = 1 - \sigma \phi(x_1, x_2) \quad (2.11)$$

The image plane wave is then given by

$$\psi_i = q(x_1, x_2) * tf(x_1, x_2) \quad (2.12)$$

where $*$ is the convolution operator and $Tf(x_1, x_2)$ is the Fourier transform of $\exp(i \chi(k))$. $tf(x_1, x_2)$ is a complex function which can be written in terms of its real and imaginary parts $s(x_1, x_2) + i c(x_1, x_2)$. The intensity at the image plane is then:

$$I(x_1, x_2) = \{1 + \sigma \phi(x_1, x_2) * s(x_1, x_2) - i \sigma \phi(x_1, x_2) c(x_1, x_2)\} \\ \times \{1 + \sigma \phi(x_1, x_2) * s(x_1, x_2) + i \sigma \phi(x_1, x_2) c(x_1, x_2)\} \quad (2.13)$$

Dropping terms of second order in $\sigma \phi(x_1, x_2)$ gives

$$I(x_1, x_2) = 1 + 2 \sigma \phi(x_1, x_2) * s(x_1, x_2) \quad (2.14)$$

$\exp(-i \chi(k))$ may be written as $\cos(\chi(k)) - i \sin(\chi(k))$, therefore $s(x_1, x_2)$ is the Fourier transform of $\sin(\chi(k))$.

The function $\sin(\chi(k))$ modulates the amplitude of the scattered frequencies for weak phase objects. For optimum

imaging, it would be ideal to have $\sin(\chi(k)) = 1$ or -1 for all important frequencies k . However, examination of equation 2.5 shows that in general $\sin(\chi(k))$ may vary widely and is a sensitive function of the operating conditions (C_s and Δf). At a slight underfocus of the objective lens, there is a focus condition in which $\sin(\chi(k))$ is nearly equal to $-\pi/2$ over a broad range of frequencies. This focus setting, which gives rise to optimum contrast for samples with a broad range of scattered frequencies is called the Scherzer focus, after Otto Scherzer who was the first to describe it (1949). The Scherzer focus is given by $-1.2(C_s \lambda)^{1/2}$. At the Scherzer focus the first zero in the transfer function occurs at a frequency of $k_s = 1.51/(C_s \lambda^3)^{1/4}$ which is a measure of the optimum point resolution of the microscope. For the JEOL 2000 FX the Scherzer focus is -91 nm and $1/k_s = d_s = 0.29$ nm.

For an ideal objective lens, $\chi(k) = -\pi/2$ for all frequencies, giving $\sin(\chi(k)) = -1$ for all k . In this optimal case, equation 2.14 becomes:

$$I(x_1, x_2) = 1 - 2 \sigma \phi(x_1, x_2) \quad (2.15)$$

Equation 2.15 shows that for a sample obeying the WPOA in the limit of an ideal lens, the HREM image intensity distribution will be linearly related to the projected specimen structure $\phi(x_1, x_2)$. Equation 2.15 shows that atoms (high potential)

will appear dark (less intensity) than neighboring vacuum ($\phi=0$). Under these stringent conditions, image interpretation is intuitive. For other defocus settings dark areas are not necessarily a direct mapping of regions in the sample with a high projected potential. The maximum amount of contrast in the image under optimum conditions is given by $2\sigma \phi_{\max}(x_1, x_2)$.

Note that in a real image the amount of contrast will never be this high; oscillations in $\sin(\chi(k))$ and the damping functions D_1, D_2 , and D_3 will all serve to damp the intensity of different frequencies in an actual experimental image. However, the equation represents a lower bound for the minimum $\phi(x_1, x_2)$ necessary to give the observed contrast in a micrograph. Hence, by measuring the experimentally obtained HREM image contrast one can estimate a lower bound on the minimum amount of local variations in ϕ necessary to give rise the observed contrast. Quantitative measurements such as these are of interest in detailed comparison of structural models with experimental images, particularly for highly disordered systems where models might predict a smaller amount of variation in ϕ than could be explained by the observed HREM contrast.

The actual contrast for a known sample and microscope configuration can be calculated if the full dynamic scattering of the material is known. As mentioned earlier, a con-

venient method of calculating the dynamic scattering problem is the "multislice" formalism.

4. Image Simulations: Multislice

If the dynamic scattering of a crystal structure of a given thickness is known, then it is possible to calculate experimental HREM images if the operating conditions of the microscope are also known. A comparison of calculated images with those experimentally obtained is further confirmation of the validity of a given structural model. Such comparisons are now routinely performed in HREM studies of inorganic materials.

Multislice image calculations are useful for providing the experimenter with a good "feel" for what is expected in an attempt to use HREM on a new sample. However, because of the computationally intensive nature of these calculations and the number of parameters which are involved, caution must be employed in detailed interpretation of results obtained. Recently, in the study of oxygen ordering in superconductors, Ourmazd and Spence (1987) used image calculations to suggest that certain "white rows" seen in HREM images could be interpreted in terms of different types of ordering on the oxygen deficient planes. However, Huxford, Eaglesham and Humphreys (1987) showed with similar calculations that

variations in Debye-Waller factors could also lead to image predictions which were similar to those seen with vacancy ordering.

There are other deficiencies in the multislice calculation which may lead to errors and therefore deserve mention. Most of the multislice programs in use rely on the Mott formula for approximating the electron scattering factor (Mott and Massey, 1965). Peng and Cowley (1988) have shown that the Mott formula can lead to serious errors in simulated images and potential distributions, particularly for large objects (small frequencies). This is not a problem for small unit cells, but becomes critical for simulations of large objects and for extended cells containing defects. Also, the scattering factors which are incorporated are all assumed to be spherically symmetric about the atomic center. The deviations from local symmetry which arise from hybridization of the electrons into molecular orbitals have not yet been incorporated into the multislice approach. These effects might be particularly significant in low atomic number materials with strong molecular orbital hybridization and aromaticity.

Another limitation in the current formulations of the multislice approach is in determining image contrast for small deviations off the Bragg angle. Such predictions are important for understanding the "rocking curve" behavior of

HREM images. As currently written, multislice packages recalculate a two-dimensional unit cell which describes the periodic projection of the structure in a given crystallographic direction. For small deviations from a Bragg reflection, the projection may be along a non-crystallographic direction. In such a case, the program calculates a slice thickness which is prohibitively large (often over 100 nm). This method of creating "periodic slices" also limits the ability to easily determine the effect of thin sections through samples with large unit cells.

Finally, it is important to consider memory requirements and sampling problems in the multislice formulation. When simulating images of non-periodic objects (like lattice defects), it is necessary to use an artificially large unit cell which is periodically continued in order to perform the multislice calculation in Fourier space. It has been noted (O'Keefe, 1984; Self and O'Keefe, 1989) that for 128x128 sampling nets (determined by array sizes in multislice formulations), the supercell size should be less than 4 x 4 nm for sufficient sampling in both real and Fourier space.

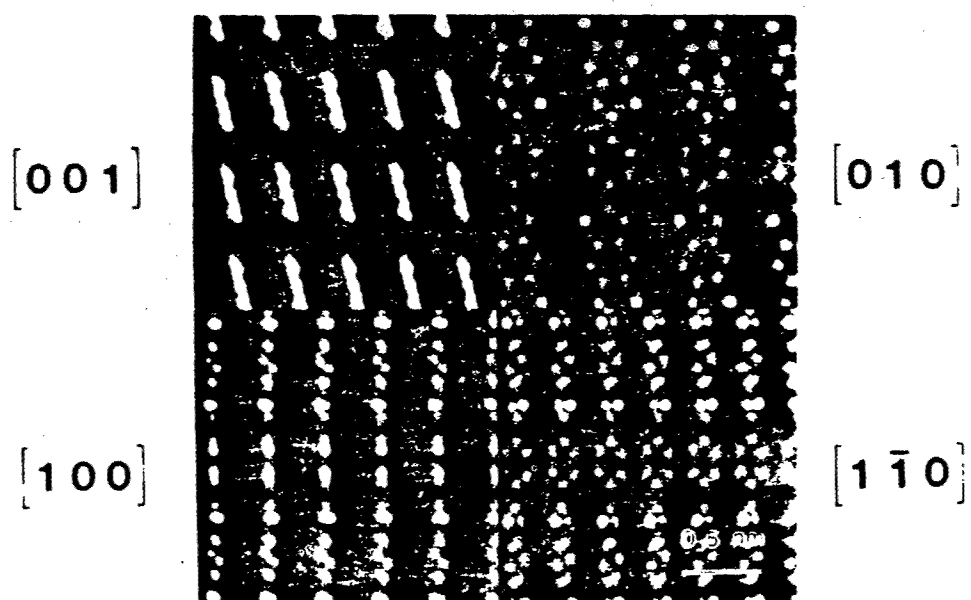
5. Simulated HREM Images of Rigid-Rod Polymers

The following section presents results of multislice calculations for the expected HREM images of PBZT and PBZO.

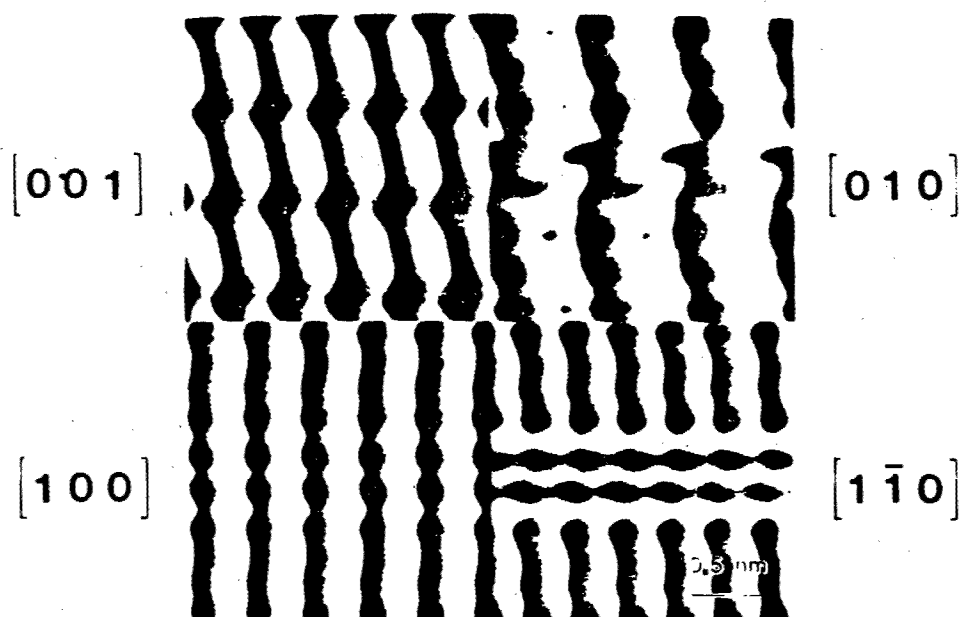
The coordinates of the atoms used in these calculations were provided by W. W. Adams and A. Fratini. For PBZT, the monoclinic primitive unit cell was used with $a=0.595$ nm, $b=0.362$ nm, $c=1.249$ nm, $\alpha=90$, $\beta=90$, and $\gamma=95.47$ degrees. For PBZO, the unit cell used was monoclinic and nonprimitive, with $a=1.1039$ nm, $b=0.3458$ nm, $c=1.2061$ nm, $\alpha=90$, $\beta=90$, and $\gamma=91.50$ degrees. Placement of the second chain in this non-primitive unit cell has been suggested at the position $(1/2, 0, 1/2)$ (Fratini and Adams, private communication), but we have found that a placement of $(1/2, 0, 1/4)$ is more consistent with experimental WAXS and SAED data. The positioning of the second chain in the PBZO unit cell and its influence on SAED and WAXS scattering patterns will be discussed in more detail in Chapter IV.

Figure 2.2a shows the crystal structure of PBZT projected in several different crystallographic directions. The general shape of the PBZT molecule can be easily seen. In PBZT, the planes of highest electron density are the 0.59 nm (100) and 0.36 nm (010) planes parallel to the chain axis. These planes correspond to lateral close packing between molecules "side-to-side" and "face-to-face" respectively. Projections of the crystal structure in the $[010]$ and $[100]$ directions enables these spacings to be seen clearly.

The structure shown has the neighboring PBZT molecules aligned with no axial shift. Because of the uniform cross



(a)



(b)

Figure 2.2 a) Projected potential of PBZT in several crystallographic directions. b) Simulated Images of 10 nm thick sections of PBZT for a JEOL 2000 FX at Scherzer focus. While the high resolution details about the hydrogen atoms and internal structure of the phenyl and heterocyclic group cannot be resolved, it is possible to determine the positions of the stacks of polymer chains. At Scherzer focus, the stacks of molecules are in reverse contrast, with the image predicted to be dark where the projected potential is high, and light where the projected potential is low.

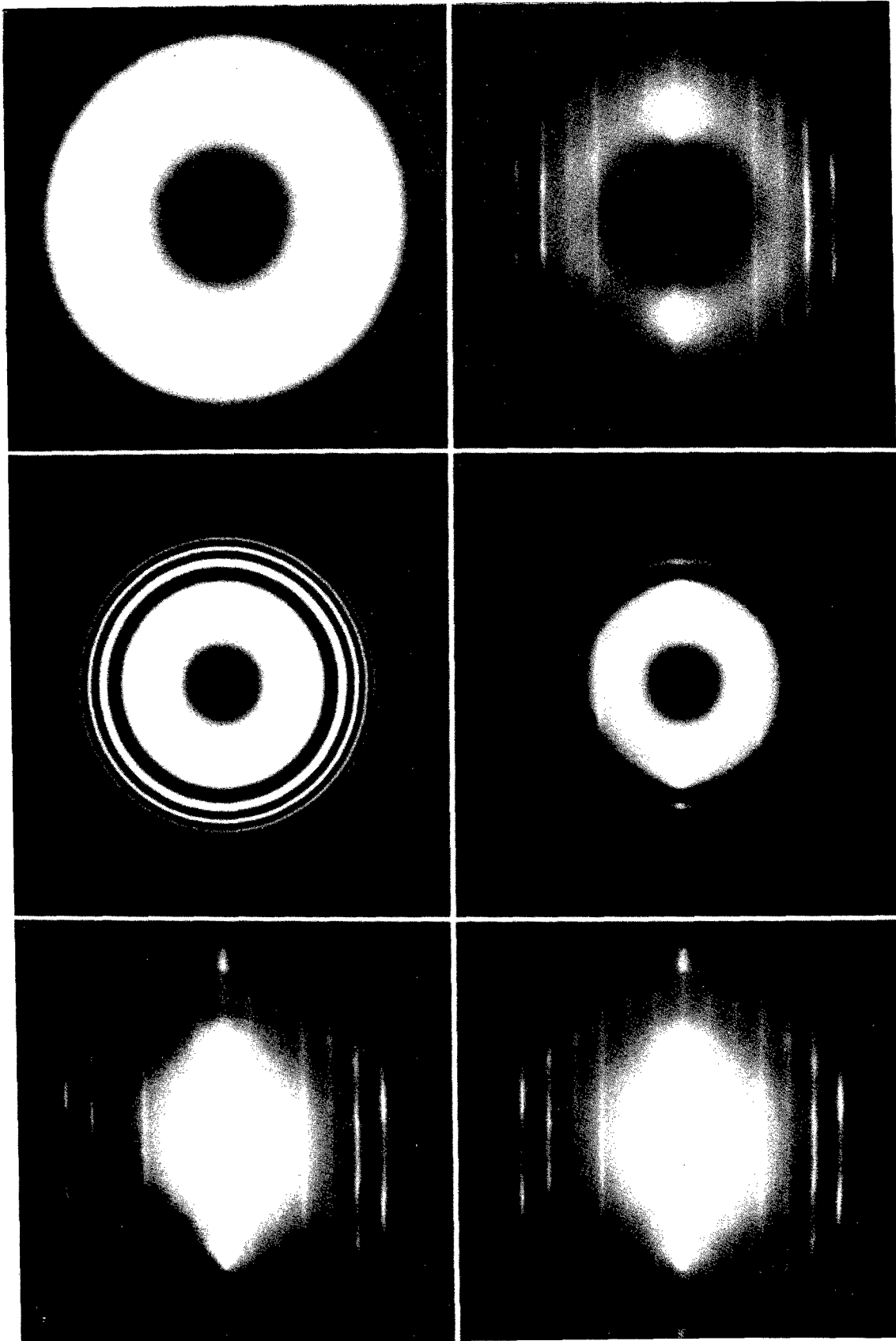
section of the PBZT molecule (seen clearly in the [001] projection down the chain axis) and the weak lateral bonding, PBZT exhibits axial shift disorder in the solid state. In Chapter II the nature of axial shift disorder in PBZT will be studied with both imaging and scattering experiments.

Figure 2.3a shows an electron diffraction pattern of PBZT. On the same scale in Figure 2.3b is shown the square of the function $\sin(\chi(k))$. This function represents what would be observed in an optical diffraction pattern of a hypothetical sample with uniform scattering power imaged in the JEOL 2000 FX at the Scherzer condition. As discussed earlier, the first zero occurs at a frequency of $k_s = 3.44 \text{ nm}^{-1}$, corresponding to a resolution d_s of 0.29 nm. Figure 2.3c shows the product of 2.3a and 2.3b. Note that the first zero in $\sin^2(\chi(k))$ occurs just after the second equatorial reflection. Also, the third order layer line is the last meridional reflection within the band pass zone.

For comparison, Figure 2.3d and Figure 2.3e show the corresponding amplitude of the CTF at Scherzer for a microscope with $C_s = 0.7 \text{ mm}$ and $\lambda = 0.00164 \text{ nm}$, corresponding to values for a JEOL 4000 FX microscope operating at 400 kV. Note the extra resolution expected at this higher operating voltage and superior C_s . Here, the first zero occurs at a frequency corresponding to a resolution of 0.16 nm.

Figure 2.3: PBZT SAED pattern compared with plots of $\sin^2(\chi(k))$ at Scherzer focus for a JEOL 2000 FX (200 kV) and a JEOL 4000 FX (400 kV) Transmission Electron Microscope.

For a 2000 FX the first zero occurs at $k=3.45 \text{ nm}^{-1}$ ($d=0.29 \text{ nm}$), for a JEOL 4000 FX the first zero is at $k=6.25 \text{ nm}^{-1}$ ($d=0.16 \text{ nm}$).



The expected HREM images of PBZT at Scherzer focus (Figure 2.2b) were calculated using the Multislice formalism with the characteristic operating conditions listed in Table 2.1 . The sample thickness was assumed to be 10 nm. The simulated images show that the details of the molecules such as the exact position of the hydrogen atoms and the shape of the phenyl and heterocyclic group cannot be resolved by HREM with a JEOL 2000 FX. Nevertheless, the images confirm that if there is a region of the sample which exhibits crystalline order and is oriented such that densely packed planes are parallel to the electron beam, the HREM image of this region will show a periodic modulation in intensity at a frequency corresponding to the structural modulation within the sample. Near the Scherzer focus, the strong 0.59 and 0.36 nm fringes are predicted to be in reverse contrast. This is reflected in the simulated image as dark bands where the projected potential is highest (under stacks of molecules).

Figure 2.4 shows the projected potential for PBZO using the unit cell discussed in Chapter 4 as well as the simulated images at Scherzer focus. Again, the images indicate that the spacings between molecules can be easily resolved, but the detailed structure along the chain cannot. In PBZO, the strong Fourier components have spacings of 0.55 nm (200) and 0.33 nm (010), again corresponding to the "side-to-side" and "face-to-face" lateral close packing of the PBZO molecule.

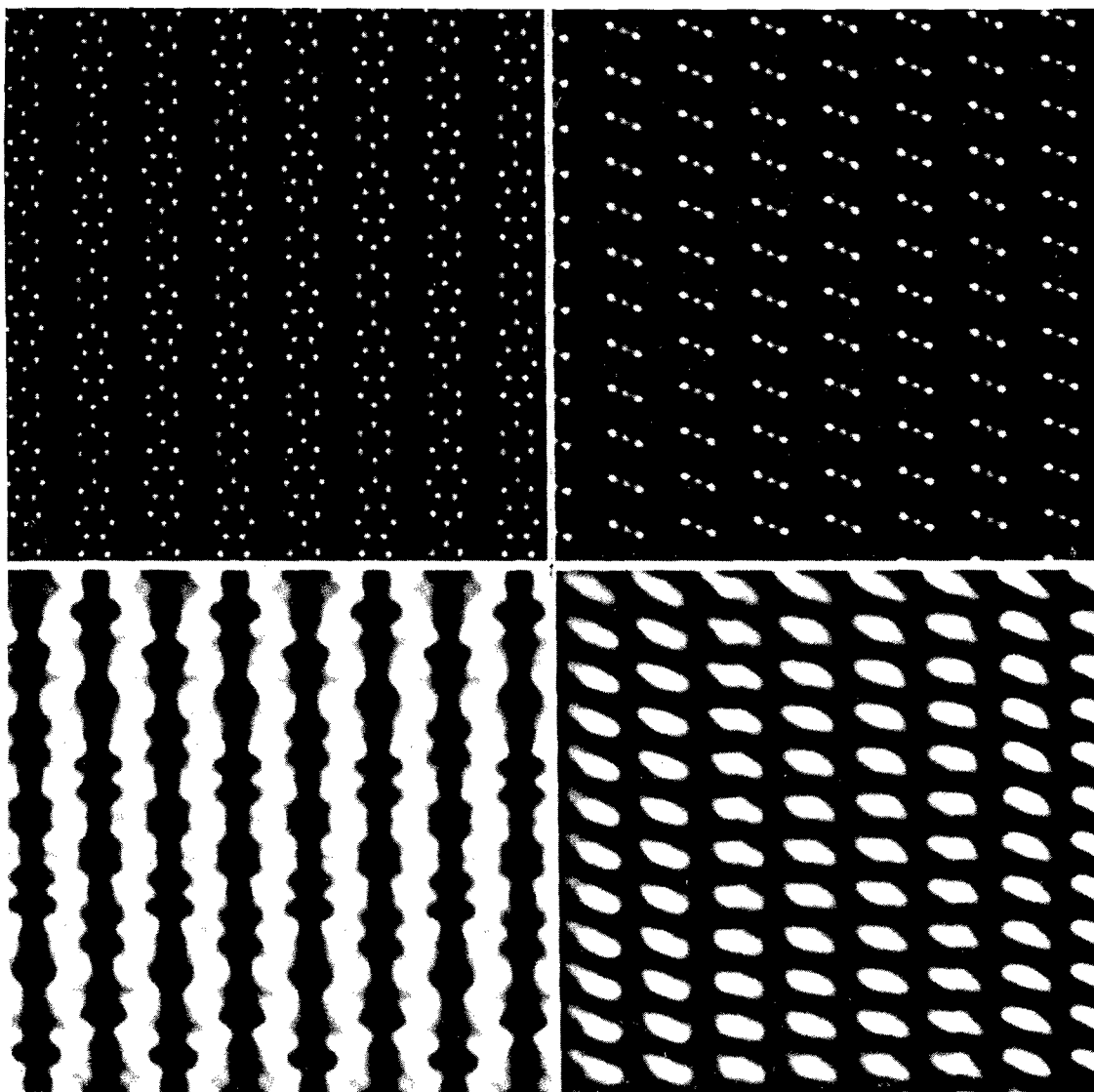


Figure 2.4: Projected potential and simulated images of PBZO for a JEOL 2000 FX at Scherzer focus. As for PBZT, the images lack high resolution detail but serve to unambiguously reveal the local orientation of the polymer chain.

In Figure 2.4 the PBZO molecules are positioned at strictly alternating $+1/4 c$ and $-1/4 c$ axial registry between molecules close-packed in the a direction. A regular axial registry of $1/4 c$ is consistent with localized reflections (indexed as (302) with a non-primitive unit cell) which develop on the second layer line in the PBZO diffraction pattern. More details about the type and extent of regular axial registry in PBZO will be presented in Chapter IV.

In summary, we find that while it is not possible to obtain information about the internal details of PBZT and PBZO molecules, it is possible to image the regular packing between these molecules. Equatorial fringes with spacings of approximately 0.55 nm and 0.35 nm show regions of good lateral packing, and therefore serve to precisely characterize the local molecular orientation. Images of the 1.2 nm meridional fringes are indicative of axial registry between neighboring chains. The extent, perfection, and contrast of the fringes experimentally observed will be sensitive to the specific details of local molecular organization.

These images were simulated using an infinite incident beam dose. In HREM of beam sensitive materials the dose required to form the image is an important constraint on the experiment. The effect of limited dose is to cause a local

fluctuation in the experimentally observed intensity. The effect of limited dose on images can be assessed by electron counting statistics. The parameter indicative of the expected image quality of an object of size d is Q , the number of electrons incident in an area of d^2 . Q is determined simply from J , the total electron dose, and d , the size of the object, by:

$$Q = J d^2 \quad (2.16)$$

This relation emphasizes that for uniform incident radiation the quality of the data (determined by Q) will be dependent on the size of the object of interest d . For beam sensitive materials, there is a limiting amount of radiation which the sample can withstand called the total end point dose (TEPD) J_e . The best expected image quality for an object of size d_1 in a material with $TEPD=J_e$ is given by $Q = J_e d_1^2$. The standard deviation in the intensity of an object illuminated with Q electrons is given by $Q^{1/2}$, hence the relative error e associated with incident electron statistics of Q is given by:

$$e = Q^{1/2}/Q = Q^{-1/2} \quad (2.17)$$

For PBZT at 200 kV, $J_e=2.3 \text{ C/cm}^2$ ($144,000 \text{ electrons/nm}^2$) and $d_{100}=0.59 \text{ nm}$. This gives the best estimate of $Q=50,000$, corresponding to an error e of 0.4%. For PE at 200 kV,

$J_e = 0.015 \text{ C/cm}^2$ (900 electrons/nm²) and $d_{110} = 0.41 \text{ nm}$, hence the maximum value of $Q = 150$, and the expected error \bullet is 8%.

It is possible to simulate the effects of limited dose on HREM images with commercially available routines in software packages such as SEMPER (Synoptics, 1989). These routines use simulate dose limited images by using the image as a probability map for incident electrons. Pradere and Thomas (1989) have used such an approach to investigate the predictions of limited dose on theoretical and filtered images and find results which appear very similar to experimentally obtained low dose HREM images. This supports the contention that sampling statistics play an important role in practical HREM of beam sensitive materials.

The effect of limited dose on HREM images of PBZO is presented in Figure 2.5. Images are shown for the $J = 0.1$, 0.25 , and $1.0 J_e$, where $J_e = 0.8 \text{ C/cm}^2$ (50,000 electrons/nm²) for PBZO at 200 kV (Chapter IV). Since the primary spacing in this image is $d_{200} = 0.55 \text{ nm}$, these images correspond to $Q = 1500$, 3750 , and 15000 , with relative errors of $\bullet = 2.3\%$, 1.6% , and 0.8% . It is apparent that while the positions of the fringe maxima can be interpreted with confidence, the detailed nature of local intensity variation is lost, particularly at the lowest doses. In practice, it is necessary to restrict images to doses of no more than $J_e/3$ in order to

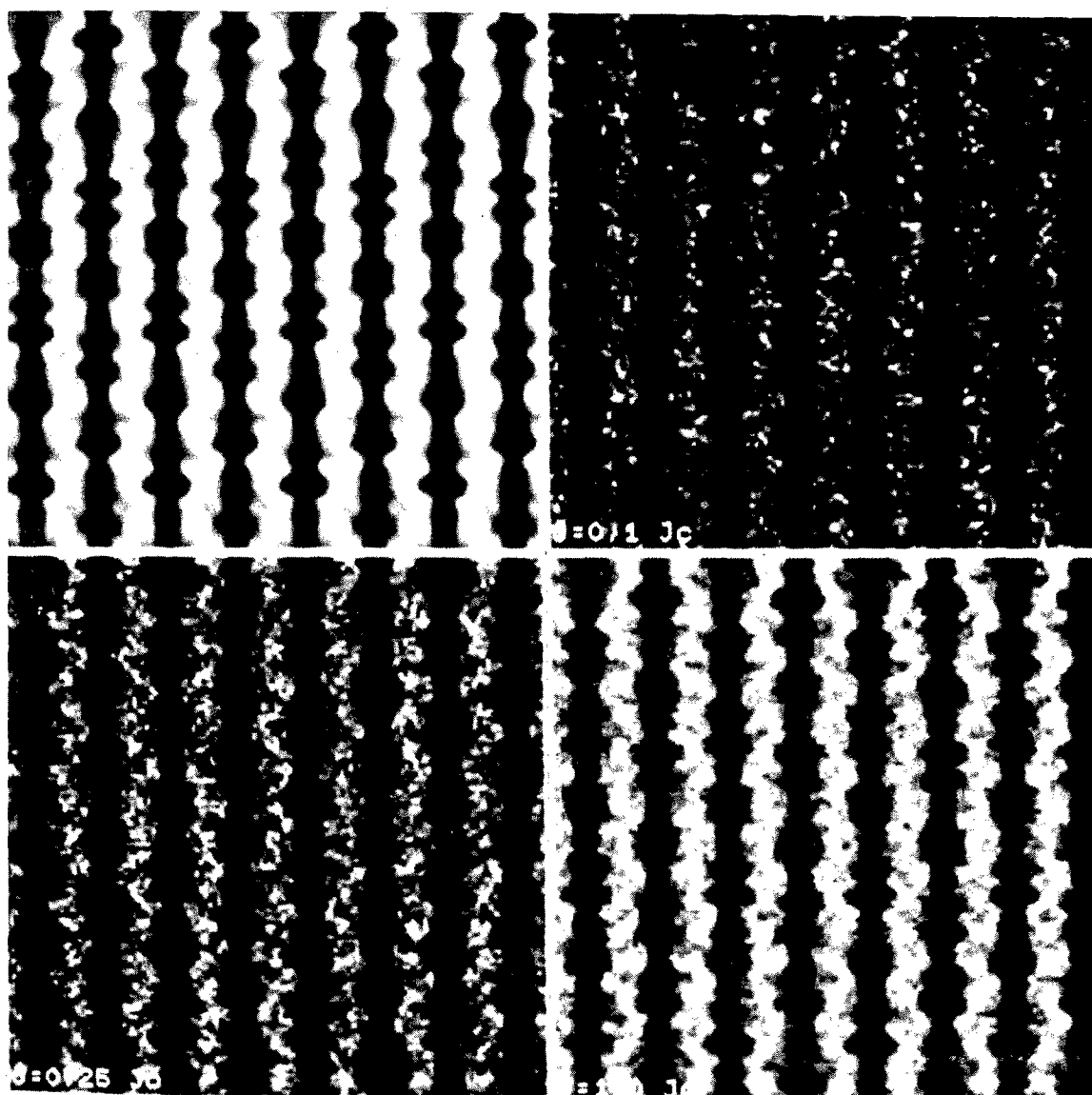


Figure 2.5: Effect of limited electron dose on HREM images of PBZO. As the amount of dose increase, the statistics improve and the apparent "noisiness" decreases. The amount of electrons which pass through a given area of the sample provides a useful measure for assessing the image quality of a dose-limited object.

avoid using electrons scattered from partially damaged crystals.

C. HREM of polymers

1. History of Polymer HREM

The first published image with lattice resolution of a polymer was a two-beam DF image of the 1.8 nm (10.0) spacing in beta-PPX by Bassett and Keller in 1968. Although the image is noisy and the contrast is low, the 1.8 nm spacings can be clearly seen over an area approximately 25 x 75 nm. The lattice is straight and apparently free of defects over the area imaged, although the quality and limited extent of the image makes a detailed interpretation difficult.

In 1975 the 0.64 nm (002) meridional and 0.43 nm (110) equatorial reflections of PPTA fiber were successfully imaged in BF by Dobb, Hindeleh, Johnson, and Saville. These pioneering results showed clearly the intermolecular spacings corresponding to lateral packing and intermolecular registry between PPTA molecules. The appearance of high contrast, straight meridional (002) fringes indicates true three-dimensional crystallinity in this system and confirms the extended-chain structure. Although the general features of the images are consistent with the psuedo-orthorhombic unit

cell for PPTA proposed by Northolt (1974), close examination of the data indicates regions where the (002) and (110) fringes coexist and make a relative angle of 85 degrees, which conflicts with the proposed unit cell angles of $\alpha = \beta = 90$ degrees.

The size and shape of crystalline domains in PPTA as well as their relative orientation could be discerned and were compared with those determined by X-ray diffraction line broadening studies (Bennett, Dobb, Johnson, Murray, and Saville, 1975). It was noted that HREM results gave crystallite sizes that were consistent with but slightly larger than those determined by WAXS and SAED. The crystallites were small (8.6-22.5 nm) and typically free of internal defects, although some regions of more disordered lattices including curved (002) planes were seen. These results were used to rationalize the high tensile strength and relatively weak shear modulus and compressive strength of these fibers in terms of a possible delamination between the relatively weakly laterally bonded, highly oriented PPTA molecules (Dobb, Johnson, and Saville, 1979).

Read and Young (1981) obtained HREM images of large plate-like crystals of poly(diacetylene). Evidence was shown for edge dislocations involving Burger's vectors perpendicular to the chain axis. Yeung and Young (1985) were able to obtain HREM images of polydiacetylenes corresponding

to projections of individual polymer molecules along their chain axis.

Tsuji (1981) obtained HREM images of both the alpha (monoclinic) and beta (hexagonal) polymorphs of PPX, and was able to visualize directly down individual chains in a flexible chain-folded single crystal. Again, evidence was shown for dislocations with Burger's vector perpendicular to the chain axis.

Fryer has studied low-dose HREM of crystals of several low molar mass organic molecules including paraffins (1982) and monolayer Langmuir-Blodgett films of phthalocyanines (1985). It has been possible to characterize the structure of grain boundaries between phthalocyanine domains and to study the high concentration of defects and misorientation in the thin monolayer films. Fryer and Dorset (1987) have investigated the structure of certain lipid systems exhibiting a lamellar texture and have imaged crystal boundaries and edges as well as local fluctuations of the lamellar orientation.

Durst and Voight-Martin (1986, 1989) have investigated the structure of main and side-chain thermotropic smectic liquid crystalline polymers by HREM. They have found defect structures including edge dislocations of different magnitude Burgers vectors. More recently, they have also investigated

discotic liquid crystalline polymers and have obtained projections of the ordered packing of stacks of disk-shaped mesogens (1989).

The PBZT lattice was first imaged by Shimamura, Minter, and Thomas (1983). Evidence for the (100) lateral packing and faint, meandering (001) lines were shown. Lattice images in PBZO have been obtained by Adams et al. (1989) and show similar evidence for good lateral ordering. More detailed comments and criticism about these results will be presented in Chapters III and IV.

Encouraged by these initial successes, more effort has been expended in attempting HREM of polymer ultrastructures. With advances in instrument stability and control, sample preparation techniques, and increased sophistication in image analysis and simulation capabilities, it has now been possible to obtain HREM information in an ever-growing number of polymer systems. A current summary of HREM investigations of polymer microstructures is presented in Table 2.2.

As discussed earlier, the characteristic of a beam sensitive sample which is most important in determining the possible success of HREM imaging is the total end point dose (TEPD) J_e , the incident electron dose required to destroy most of the crystalline order within the sample. The measurement of J_e can be done by measuring several quantities

Table 2.2

HREM Images of Crystalline Polymers

Polymer	hkl	d_{hkl} nm	J C/cm ²	kV	Mag kX	Year	Group
PPX	10.0	1.8		100		1968	Bassett & Keller
	44.0	0.26	0.4	500	100	1982	Tsuji et al.
	84.0	0.19				1988	Pradere & Thomas
PPTA	002	0.64		100		1975	Dobb et al.
	110	0.43	0.4	200		1984	Katayama et al.
PDCH	010	1.2		100	100	1981	Read and Young
		0.9	20	100	100	1984	Read and Young
	210	0.6	20	200	100	1985	Yeung and Young
(SN) x	100	0.39	0.75	200	100	1984	Kawaguchi et al.
	110	0.29					
PE	110	0.41	0.24	100	300	1984	Giorgio & Kern
		0.37				1986	Revol & Manley
	110	0.41				1987	Chanzy et al.
iso-PS		1.10		120		1985	Tsuji et al.
		0.63	0.03	200	41	1985	Tsuji et al.
syn-PS	330	0.44	0.02	200	41	1988	Pradere and Thomas
PBZT	001	1.24	1.6	100	100	1985	Shimamura et al.
	100	0.59		200	100	1986	Boudet et al.
	010	0.36					
	003	0.41	2.3	200	130	1988	Martin and Thomas
PBZO	001	1.2	0.2	200	100	1989	Adams et al.
	200	0.55	0.8	200	100	1989	Martin and Thomas
	010	0.33					
PTFE	100	0.49		100	46	1985	Chanzy et al.
PPCG	100	1.3		100		1985	Zhou et al.
Cellulose	220	0.54		200		1984	Sugiyama et al.
	040	0.39		120	36	1985	Revol
		0.4		120	25	1987	Kuga and Brown
PPV	100	0.43	0.1	200	100	1988	Masse et al.
	001	0.62					

Table 2.2 (cont.)

HREM Images of Crystalline Polymers

Polymer	hkl	d_{hkl} nm	J C/cm ²	kV	Mag kX	Year	Group
PPS	110 200	0.47 0.43	0.2	200	100	1988	Uemura et al.
TLCP's		2.6 3.6				1986 1989	Durst and Voight-Martin
TLCP's		2.9 0.6				1987	Martin et al.

including mass loss, diffraction behavior, or spectroscopic changes. Most often, J_e is characterized by observing the decay in intensity of sharp reflections in the SAED pattern of the originally crystalline material.

A related quantity which is also used to measure beam damage is the critical end point dose J_c , which is obtained by a fit of the intensity of a Bragg reflection as a function of dose to an exponential decay function:

$$I = I_d \exp (-J/J_c) + I_b \quad (2.18)$$

Either J_e or J_c is an adequate measure of the sensitivity of a sample for HREM imaging. Kumar, Krause, and Adams (1985) have found a rough correlation between J_c and the melting (or degradation) temperature T_m of the polymer.

For successful HREM of beam sensitive materials it is important to illuminate with as few electrons as possible to avoid imaging damaged material. Also, it is useful if samples with large characteristic periodicities can be found. As shown previously, the expected image quality is $Q = J d^2$, where d is the size of the feature of interest.

HREM studies of polymer microstructures have provided several new and important insights for solid state polymer physics. It has been established that as for low molecular

weight solids, polymer crystals contain classical lattice defects such as dislocations and grain boundaries. The size, shape, relative orientation, and internal perfection of certain polymer crystals has now been determined. In Chapter V we will present HREM observations of rigid-rod polymers which have undergone plastic deformation in compression, giving insight into the molecular origins of deformation processes and confirming that covalent bond bending in rigid-rod macromolecules is possible at room temperature. As the quality and amount of information of this type increases, we may expect to see further development of theoretical models to help explain these observations. With experimental images of actual defect structures in hand, it will be encouraging to explore in more detail the role such defects play in determining material properties.

2. HREM and Dark Field Imaging

As we discussed in the previous sections, HREM lattice "fringes" can be interpreted in terms of projections of regular molecular packing within the sample. However, it is possible to use DF imaging to provide much the same sort of information by forming an image with only certain parts of the scattered radiation. In general, HREM and DF are complementary techniques and therefore should be both be used to answer local microstructural questions.

One of the primary advantages of HREM is that of the electron dose necessary to form the micrograph. In DF only that part of the radiation scattered into the aperture is used to form an image. Therefore, for the same optical density from a single crystal region on the final negative, DF will always require much more radiation. This means that DF will typically have to be performed at lower magnifications, and therefore will give poorer resolution. Accordingly, HREM is a fine detail technique, giving information about "ultra"structure of the material at or below the molecular level. DF is more of a "micro"structure technique, and is relevant for determining crystal size and shape and general orientation, but is not as sensitive to the possible disorder within these crystals or to small angle boundaries between adjacent crystals.

A second advantage is the fact that one HREM image of a sample contains information about all of the relative orientations of observable fringes simultaneously. In DF, small relative orientations cannot be easily resolved by a finite size aperture. Likewise, it is not simple to resolve small relative variations in lattice spacing by DF. The selectivity for orientation and spacing in DF becomes better with smaller apertures, but with very small apertures high frequency information such as detailed crystal shapes is lost. With optical bench filtering techniques it is possible to use

selective apertures to reconstruct images using only certain reflections (Tomita, et al., 1985). In this way, the HREM image serves as a template for subsequent analysis by "optical DF imaging" with the laser beam.

However, HREM is not without its disadvantages. In HREM imaging, there is an effective aperture function which acts to damp the response of high frequency beams contributing to image. Hence, it is not possible to use HREM to provide information using these higher order reflections since they will not be resolved in the final image. Also, because HREM images are formed with the low angle unscattered, forward scattered, and inelastically scattered electrons, there is a large DC level signal which reduces the image contrast. In DF, only those beams which scatter into the aperture are used to form the image so that the DC level is zero and therefore the final contrast is much higher. Another drawback of HREM is that it is time-consuming and experimentally demanding, and therefore an often unsuccessful technique. It requires careful sample preparation, microscope operation, and operator patience. Also, because of the problems of beam damage, it cannot be applied with success to all systems.

3. Experimental Details

a. Sample Preparation

In this study the materials of interest were high performance fibers of PBZO and PBZT. The sample preparation procedure used was typically "detachment replication". This technique has been used with success in the past to prepare thin sections of high performance fibers (Shimamura, 1983; Krause et al., 1988). The following outlines in detail this method of sample preparation. This approach should be useful for samples with a relatively weak lateral strength.

A solution of collodion in ether (obtained from Ted Pella, Inc.) is spread onto a glass slide. After exposure to air, solvent evaporates making a tacky substrate. Next, the fiber samples are placed on the collodion. Before placing them in collodion the fibers may be lightly scraped with a razor blade to assist in subsequent fibrillation. Scraping should in general be avoided because of the possibility of introducing mechanical damage. Scraping was usually not necessary for the PBZO and PBZT fibers investigated in this study.

The samples are allowed to dry for at least 24 hours in a open petri dish covered with a filter paper, during which time the collodion hardens as the solvent completely evapo-

rates. The fibers are removed from the collodion by lifting with tweezers and the sample is examined in a stereo microscope. With close inspection it is possible to see regions of faint color in the collodion from thin fragments of fiber left behind. Areas of interest are sectioned from the collodion using a razor blade.

The squares of collodion containing thin pieces of fiber are placed face down on previously prepared holey carbon grids supported on a metal screen in a petri dish. Amyl acetate is then slowly poured into the petri dish until it just wets the holey carbon grids. The dish is placed aside where it will not be bumped and the collodion is allowed to dissolve in the amyl acetate for at least 24 hours.

After dissolution the screen with the grids is lifted from the amyl acetate. Some of the fiber samples are now suspended directly over the holes in the holey grid. An additional thin coating of carbon may be used to stabilize the sample and possibly increase radiation resistance (Fryer, 1985), but this overlayer may obscure features in HREM. In this work carbon coating was not used.

b. Instrument Operation: Low Dose HREM

The primary instrument used in this study was a JEOL 2000 FX Transmission Electron Microscope operating at 200 kV. The microscope is equipped with a high-resolution objective lens pole piece (spherical aberration coefficient $C_s = 2.3$ mm), and has a Minimum Dose System (MDS) that allows the operating conditions of the microscope to be changed quickly during operation. Also, a beam blanking device was installed which could be used to manually deflect the beam away from the sample at the condenser lens level in the column.

HREM operation requires careful alignment and astigmatism corrections (Saxton et al, 1983). It has been noted by Spence (1980) that the astigmatism of the objective lens depends critically on the exact position of the objective lens aperture if one is used. In the HREM studies reported here no objective aperture was used.

The procedure used for low dose imaging of a sample was as follows: First, the microscope was carefully aligned and stigmated using high magnification (250kX or more) of the grain of a carbon film on a Gatan video screen using an image intensifier system. Then, the conditions appropriate for imaging were selected. Typically, imaging was done at a screen current of 10 pA/cm^2 and an exposure time of 0.5-1.0 secs. For PBZO, a magnification of 100,000-170,000 could

be used. This corresponds to a sample exposure of 0.05-0.3 C/cm², well below the measured J_e of 0.8 C/cm² for the PBZO (200) equatorial reflection. As mentioned earlier, it is important to restrict exposure to less than $J_e/3$ to avoid imaging the damaged lattice. For PBZT, the higher radiation resistance (2.3 C/cm² for the (100) equatorial) meant that images at magnifications as high as 250,000 (sample dose of 0.6-1.2 C/cm²) could be obtained.

Figure 2.6 shows a schematic of the imaging conditions used during low dose HREM observation (Pradere, 1989). First, the operating conditions were prepared for the final photograph including astigmatism and beam alignment (voltage centering). Typically, this would involve an intermediate setting of the first condenser lens (spot size 4) with a screen current of 5 pA/cm² and exposure time of 1 second. This exposure would result in an average optical density of 0.5 on Kodak SO-163 film developed for 12 minutes in straight D-19. For a magnification of 130,000 this corresponds to a dose rate of 0.08 C/cm²/sec at the sample. Then, the MDS system was initiated causing these lens conditions to be recorded as PHOTO mode. Next, the system was switched to SEARCH mode and the microscope placed in diffraction conditions. The condenser lens was adjusted to reduce the beam flux (spot size 6) causing a large decrease in the intensity (two orders of magnitude). Defocusing the diffraction pattern provided sufficient contrast in the (000)

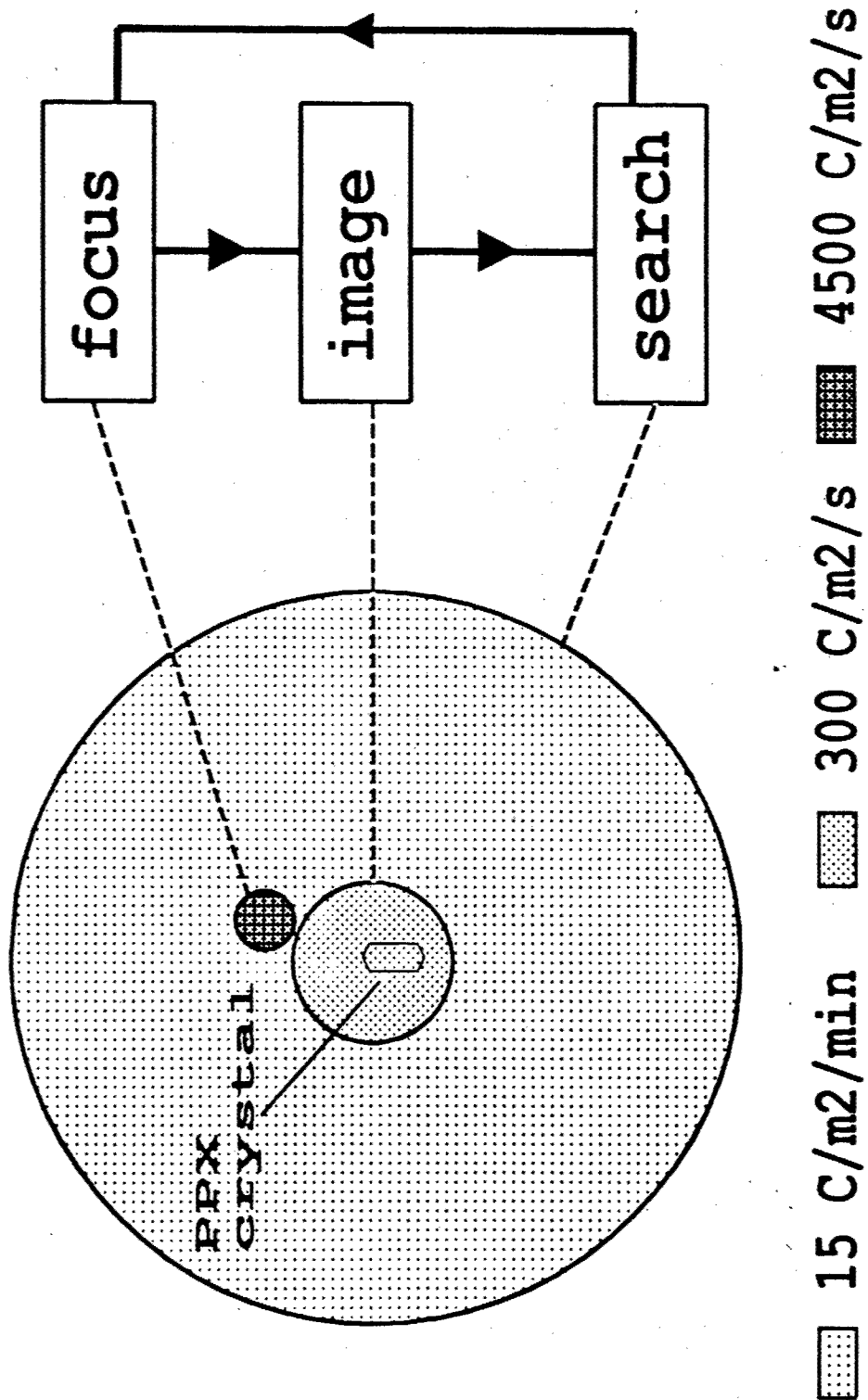


Figure 2.6: Schematic of procedures used when applying the Minimum Dose System (MDS) to low dose HREM imaging. Figure courtesy of Philippe Pradere.

beam for this to low magnification BF image be used to search the sample for an appropriate area for HREM imaging. The magnification of this image can be controlled with the diffraction focus, and it is a simple matter to check for proper sample thickness and orientation by focusing back to the diffraction pattern. Once a suitable place was found, the beam was translated to an adjacent region for focusing. The microscope was then switched to FOCUS mode and the IMAGE SHIFT controls were used to move the beam back to the center of the screen.

With practice and at high operating magnification (100-250 kX), it was possible to focus on an area adjacent to the sample at the same magnification as originally set in PHOTO mode. This is not possible at lower magnifications, in which case it is important to calibrate any possible shift in focus which occurs after a magnification change between FOCUS and PHOTO modes. Scherzer focus was obtained by defocusing a known number (16) of fine objective lens clicks (4 nm/step) from the minimum contrast which occurs at the Gaussian focus. This position of minimum contrast occurs at 0.3 Sch (O. L. Krivanek, 1989), where Sch is the Scherzer focus. For a JEOL 2000 FX, the Scherzer focus is -91 nm and the Gaussian focus is -27 nm. At high magnification, Scherzer can be seen as a local maximum in the contrast variation of a beam stable amorphous film.

After focusing, the beam blanking device was turned on and the sample stage mechanism given 5 minutes to relax, damping out residual mechanical drift. Finally, the PHOTO button was pressed using a second beam blanking time of 10 seconds to avoid vibrations from the motion of the phosphorous screen and advancing film. After exposure, a second image was typically taken of the same region with somewhat longer exposure for better determination of the sample position as well as for defocus and sample thickness calibration.

HREM imaging of fibrous materials such as those used in this study provide is more complicated than for polymer films or of single crystals supported on a carbon substrate. The problem is that a suitable area for focusing must be found every time a new region of the sample is imaged. This means that the FOCUS conditions must be adjusted every time an image is taken. Further, it is important to focus on an area as near as possible to the region of interest because of the possible non-planarity of the sample over large distances. Durst and Voight-Martin use a sprinkling of carbon particles to assist in proper focusing of the microscope (1988, private communication), but this technique met with limited success in our case since the particles did not adhere well to the fibrous samples.

One of the more insidious problems encountered during this study was the effect of sample drift. A drift of more

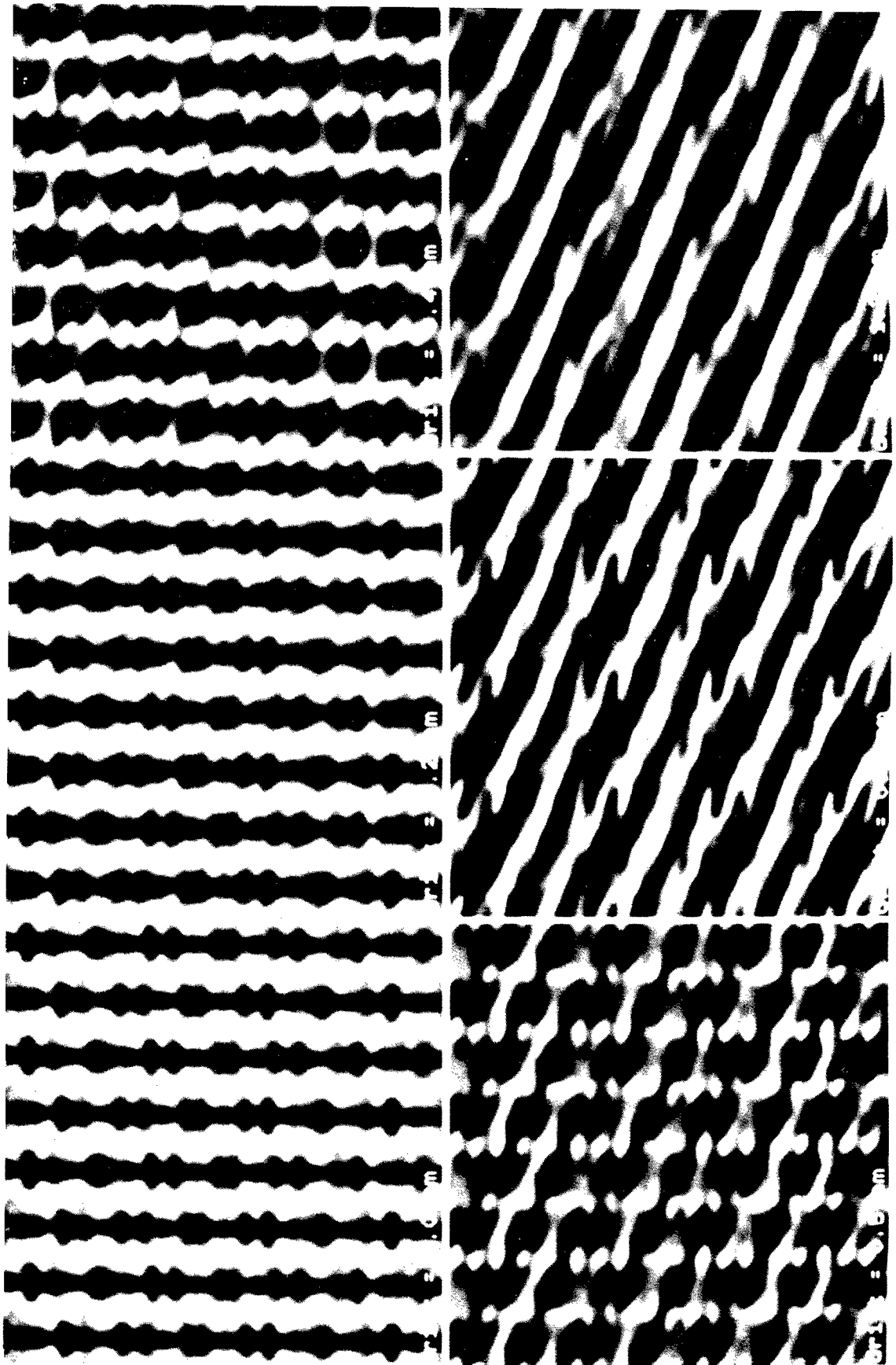
than 0.2 nm during the exposure could easily ruin a micrograph. The obscuring effect of drift is shown via the simulations in Figure 2.7 which predict the effect of uniform drift on an HREM image of PBZO. Image features due to drift can easily be distinguished from actual features characteristic of sample structure by examination of the optical diffraction pattern of the HREM image. Samples which have drifted during exposure show a loss in the intensity of the $\sin^2(\chi(k))$ defocus rings at higher frequencies in the direction of drift. The amount of drift can be estimated from the width of the intensity attenuation.

c. Sample Thickness Determination

An important parameter in interpreting HREM images is the sample thickness. An estimate of the thickness is necessary to determine whether features which are observed to be close to each other in projection are actually close together in the film, or perhaps arise from regions as far apart as the top or bottom of the film. As the sample thickness increases, the likelihood of feature superposition becomes large and the images become uninterpretable.

It is possible to estimate the thickness of a sample made of organic material by mass thickness contrast (Misell and Burdett, 1977). In mass thickness contrast, the trans-

Figure 2.7: Effect of sample drift on simulated images. Note that even for reasonably large sample drifts, the proper orientation of the primary fringes is still preserved. Only when the drift becomes greater than that of the primary periodicities is are the features completely obscured.



mitted electron intensity I is related to the incident electron intensity I_0 by the relationship

$$I/I_0 = \exp(-S_p \rho t) \quad (2.19)$$

where S_p is the effective mass thickness cross section, ρ is the density, and t is the thickness. The effective mass thickness cross section S_p describes the amount of scattering outside of the field limiting aperture and depends only on the size of the aperture A_1 and the operating voltage E_0 . S_p for a given A_1 and E_0 may be determined by measuring I and I_0 for a sample of known t and ρ .

It should be noted that this relationship is valid only for a nearly focused objective lens. This is because at zero focus there is no phase contrast for large objects (T in equation 2.4 goes to 0 for small k). Experimentally, we found that for a focus range of ± 4000 nm near Scherzer focus the ratio of transmitted beam intensity at a sample to that of vacuum varied by only 5% (Figure 2.8). This is well within the range of focusing used in typical HREM imaging (typically less than ± 400 nm). However, it should be noted that significant errors (25% or more) can occur for highly defocused images.

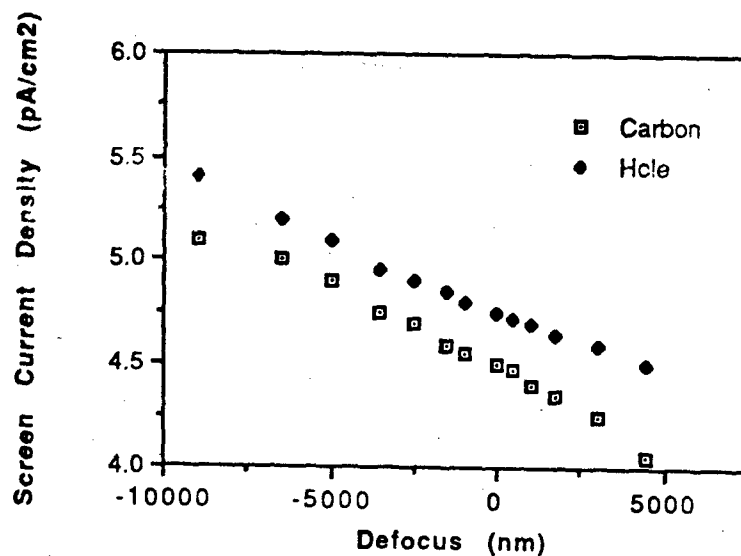


Figure 2.8: Beam intensity of a holey carbon film compared to vacuum as a function of objective lens defocus. For defocus ranges near zero the intensity difference between sample and vacuum varies by only 5%. For larger defocus the error can be more than 25%.

The S_p values for the JEOL 2000 FX were determined by using calibrated polystyrene spheres of diameter 109 nm on a thin (approximately 10 nm) polystyrene support film. The photographic film used was Kodak SO-163, developed in straight D-19 for 12 minutes at room temperature. Optical densities were measured using a plate microdensitometer calibrated with an optical density step wedge.

Table 2.3 lists the effective mass thickness cross sections for different objective apertures in the JEOL 2000 FX using 200 kV electrons. From this calibration the thickness of an unknown sample may be determined by comparing the optical density of the sample to that of a hole. Using $\rho=1.6$ gm/cm³, the density of PBZT, it is seen that under these imaging conditions it would require 240 nm of PBZT to cause a factor of 2 (100%) decrease in the optical density.

The optical density of a typical substrate free sample on an HREM image is only 7% less than the neighboring vacuum using no objective aperture. This corresponds to a sample thickness of 24 nm.

d. Photographic Details

The images obtained in this work typically involved spacings from 0.35 nm to 1.25 nm obtained at magnifications

Table 2.3

Mass Thickness Cross Sections for a
JEOL 2000 FX Transmission Electron Microscope at 200 kV

Aperture Diameter (nm-1)	Sp m^2/mg
column bore (HREM conditions)	0.0018
6.1	0.0020
4.3	0.0024
2.6	0.0031

from 80 kX to 250 kX. This corresponds to distances on the film from 25 to 300 microns. An optical density on the negative of 0.5-1.0 was typically used. For Kodak SO-163 electron image film, it was experimentally determined that an optical density of 1.0 required an illumination dose of 10 pC/cm².

Because of the small size of features on low dose micrographs, it was not simple to examine the negatives directly and see "fringes". Even with a 10x eyepiece, it is a difficult matter to see fringes on low dose micrographs. For assessing whether an HREM negative has fringes or not, it is quickest and easiest to examine the negative by laser light scattering on an optical bench.

e. Optical Bench

The optical bench provides a quick and simple way of analyzing micrographs by light scattering techniques. Illumination of the negative with a laser beam enables the scattering pattern of the image to be obtained. Essentially, this technique is a quick and easy way to take a Fourier transform a local area of the micrograph. The optical transform can be calibrated by using a micrograph of an object with a known d-spacing. A convenient sample for this purpose is the 0.34 nm reflection of turbostratic graphite.

Once an area of interest was located on a negative, the optical diffraction pattern was recorded on T-55 Polaroid film. Enlargement of the interesting area was performed using a standard film enlarger, typically with a 50 mm lens. Large f-stops (f22) were used in order to have the best possible depth of focus. This might involve an exposure time on the print paper of up to 5 minutes or more. Precise focusing of the enlarger was accomplished with a high-quality periscope device which enabled focusing directly on the film grain.

Often, the capabilities of the enlarger (maximum of 20x) were insufficient or a microdensitometer scan of the image was desired. In these cases, an intermediate negative was used to provide a magnified negative image suitable for further enlargement or for scanning on the densitometer. The intermediate negative was prepared using Kodak SO-163 electron image film. Careful focusing using a large f-stop was again critical to insure a high quality intermediate.

f. Microdensitometry

An Optronics P-1000 Photoscan drum scan microdensitometer was used to provide optical density information as a function of position for both images and diffraction

patterns. The instrument has scan sizes from 25 to 100 microns. A 25 micron resolution corresponds to 0.25 nm on a micrograph taken at 100kX. Hence, it is not possible to scan low magnification HREM negatives directly for use in digital analysis.

The output of the densitometer is an 8 bit accuracy integer array of numbers on 800 bpi magnetic tape ranging in value from 0 to 255. These numbers correspond to the optical density of the film. The densitometer was calibrated using an optical density step wedge. It was found that the relationship between optical density and bit number in the digitized image was very nearly linear:

$$OD = (B + 10)/135$$

(2.20)

where OD is the optical density (0-2) and B is an integer in the range 0-255.

D. Summary

We have discussed in detail the physics of HREM image formation and have shown what is to be expected when imaging the rigid-rod polymers PBZT and PBZO. We found that while the specific details corresponding to intramolecular struc-

ture could not be faithfully interpreted, it was possible to associate regions of well-defined periodic fringes as arising from well-ordered areas of molecular packing in the sample. For rigid polymers, equatorial fringes correspond to a direct mapping of the local molecular orientation. Axial registry between molecules should be visible as fringes more or less perpendicular to the fiber axis, depending on the registry between molecules. The perfection, extent, and contrast of these fringes will depend on the local molecular order.

In addition, we have described practical information which should be helpful for those wishing to attempt low dose HREM on systems of their own interest. Such studies have only just begun, but already new information about the details of solid state polymer architecture has been obtained. Similar success is no doubt possible for other interesting systems.

CHAPTER III: AXIAL SHIFT DISORDER OF PBZT IN THE SOLID STATE

This chapter examines the details of axial shift disorder in heat treated trans-PBZT fiber, utilizing SAED and HREM imaging to precisely determine the type and amount of disorder. HREM data has enabled quantification of the detailed size, shape, and mutual orientation of PBZT crystallites. Also, we will show images which illustrate clearly the fluctuating nature of the intermolecular packing of PBZT molecules in real space. This data confirms that a structural model involving local, large amounts of axial disorder with good lateral order is appropriate for PBZT.

The HREM images suggest models for grain boundaries between PBZT crystallites. A more detailed discussion of the structure and energetics of grain boundaries in rigid-rod polymers is presented in Chapter VI, where we will discuss the implications of such grain boundaries in controlling properties of PBZT and PBZO fibers.

Scattering provides a better means of determining average structure because it can sample a large volume of material, whereas imaging provides specific information about the particular types of defects present. The direct observation of significant, local axial shift disorder by imaging provides an impetus for a detailed study of models of the PBZT unit cell using various types and amounts of structural

defects to simulate the observed scattering pattern. It will be shown that a structural model consistent with experimental scattering data for heat-treated trans-PBZT is one involving a triclinic unit cell and a high (80%) probability of complete axial misregistry between neighboring PBZT molecules.

A. Introduction

1. Previous Work

Welsh, Bhaumik and Mark (1978, 1981) calculated the intermolecular interactions between PBZT monomers by an empirical molecular mechanics method. The molecular geometry and partial charges on each atom were determined for the trans-PBZT monomer by the CNDO/2 method. The intermolecular interaction energy was estimated by taking the first chain as one repeat unit long and varying the length of the other until consistent results were obtained. It was found that four neighboring units were required for this purpose. The lateral "face-to-face" interaction energies were found to be -29.4 kcal/mole of monomer repeat unit. This energy is well above the thermal energy at room temperature (0.6 kcal/mole) and approaches that of typical covalent bond dissociation energies (100 kcal/mole). A minimum in energy was found for a relative translation along the chain axis of 0.15 nm for

chains close-packed face-to-face at 0.37 nm, and at a relative translation of 0.1 nm along the chain axis for chain close-packed side-to-side at 0.61 nm (Bhaumik, Welsh, Jaffe, and Mark, 1981). They also explored changes in the interaction energy as one PBZT monomer unit was translated with respect to another, although the energy surface is relatively flat (3 kcal/mole; 5 kT). The intermolecular energies determined for face-to-face and side-to-side packing both show at least five local minima (W. Welsh, 1989, private communication).

A more detailed understanding of the subtleties of chain packing behavior is not warranted by these results, which were referred to by the authors as "very approximate". Besides the obvious problems with limited chain size, the possible importance of different relative internal conformations possible between neighboring PBZT polymers was not investigated. As discussed in Chapter I, the rotation of the heterocyclic group about the backbone changes the symmetry of the repeat unit and therefore affects the interactions between neighboring molecules. The interaction energy between PBZT molecules might be significantly affected by the specific positions of the nitrogen or sulfur atoms on neighboring chains (W. Welsh, 1989, private communication).

The structure of as-spun PBZT was first investigated by WAXS by Adams, Azaroff, and Kulshreshtha (1980). It was

found that the WAXS patterns exhibited broad equatorial reflections, streaks on the meridian along the fiber axis ("layer lines"), and a notable absence of other discrete (hkl) reflections. These results suggested a structural model in which there was a "frozen nematic" arrangement of rigid PBZT molecules. The intensity of the equatorial reflections was rationalized in terms of Bessel functions arising from a limited number of close-packed cylindrically symmetric molecules.

Roche, Takahashi, and Thomas (1980) investigated the structure of as-spun PBZT with SAED. The PBZT used was prepared from 9.85 weight % solution into MSA and coagulated in 50/50 methanol/sulfolane. The intrinsic viscosity of the PBZT was not reported. Again, the scattering patterns exhibited sharp equatorial reflections and diffuse scattering on layer lines, indicating a large amount of shift disorder between molecules. They found that the equatorial scattering could be fit well with a monoclinic unit cell ($a=0.583$ nm, $b=0.354$ nm, $c=1.25$ nm, $\alpha=90$, $\beta=90$, $\gamma=96$ degrees). This unit cell explains the primary equatorial reflections in terms of the (100) and (010) planes, corresponding to "side-to-side" and "face-to-face" packings of PBZT molecules. The high amount of shift disorder did not make it possible to draw further conclusions about axial registry between adjacent chains.

DF images of the PBZT fiber showed discrete regions of coherent diffracting "crystallites" on the order of 4 nm to 15 nm in diameter (Roche et al., 1980). It was also observed that the fibers exhibited a banded structure with a periodicity of 100 nm to 200 nm. However, it was mentioned that such features may have been due to the tendency of the fiber to kink during the ultrasonication step used in sample preparation. Similar features have not been seen in more recent studies of PBZT morphology (Minter et al, 1981; Martin 1989), therefore it appears the sonication used by Roche et al. to disperse the fibers did indeed cause the observed banded structure. Nevertheless, the observation of coherently diffracting regions within kinks was the first observation that crystallinity was maintained during kinking of rigid-rod polymer fibers. The morphology of kinking in PBZT and PBZO will be studied in more detail in Chapter V.

The effect of heat treatment on PBZT ribbons was studied by Minter, Shimamura, and Thomas (1981) with WAXS, SAXS, SAED, and DF. The PBZT used was of intrinsic viscosity 14-18 dl/gm and was formed into ribbons by extruding 12 weight % solution in MSA through a rectangular die into a MSA-water coagulation bath followed by a water wash. PBZT was found to be relatively resistant to electron irradiation, with a critical dose for fading of the equatorial reflections of 1.6 C/cm^2 at 100kV and room temperature. DF imaging using the equatorial reflections indicated an increase of lateral

crystallite size from about 2 nm for as-spun film to 15 nm for film heat treated under tension at 475 C for 32 seconds. It was also observed that after heat treatment the equatorial reflections sharpened, while the molecular orientation remained essentially unchanged.

Odell, Keller, Atkins, and Miles (1981) investigated PBZT structure with WAXS and SAED. The PBZT used had an intrinsic viscosity of 16 dl/gm. Odell et al. used tapes prepared by orienting a nematic solution by shear followed by coagulation. These investigators suggested the use of a non-primitive monoclinic unit cell ($a=1.196$ nm, $b=0.325$ nm, $\gamma=100.9$ degrees) or a primitive unit cell with ($a=0.655$, $b=0.356$, $\gamma=116$ degrees). The non-primitive cell provided a means of explaining the occurrence of a weak diffraction peak at 1.15 nm, a distance twice that of (100) spacing in the primitive cell. This 1.15 nm peak was often seen within a streak on the equator and therefore it was suggested that it could be due to non-Bragg scattering from a limited lattice effect. Odell et al. (1981) also calculated the expected scattering intensity on layer lines and found that the observed variation in intensity on the layer lines could be rationalized in terms of the molecular transform; hence the structure could be considered as two-dimensionally crystalline with virtually complete axial disorder between molecules.

Minter also investigated the theoretically predicted scattering in the PBZT molecular transform (1982) using coordinates determined from the bond angles, lengths, and rotation angles found in model compounds by Wellman et al. (1981). Here, it was also found that the predicted scattering on upper layer lines was consistent with the molecular transform calculations, suggesting that complete axial misregistry was a reasonable model for the PBZT structure.

Allen (1983) correlated crystallite size and heat treatment in PBZT fibers by examining the width of WAXS equatorial reflections. The PBZT fiber used was spun from 10 weight % solution in MSA and had an intrinsic viscosity of 19 dl/gm. The fibers were heat treated under tension at 430 C and 600 C. It was observed that the extent of lateral order increased with increasing heat treatment temperature, with the apparent crystallite size increasing from 3 nm for as-spun to 9 nm and 12 nm for the 430 C and 600 C heat treatments, respectively. Indications were also seen for the 1.2 equatorial reflection originally observed by Odell et al. (1981). Allen also observed a weak modulation of intensity on the second order layer line and postulated this as arising from a (102) reflection from a larger, non-primitive unit cell. The placement of the second PBZT chain within this extended unit cell was not discussed. It was not possible to show even reasonable agreement of this variation in intensity

on the second layer line with the molecular transform calculations by Minter (1982).

Adams and Price (as reported by Allen, 1983) also studied the increase in molecular orientation with heat treatment by using flat-film WAXS on individual PBZT fibers. This study showed that a significant amount (5-10 degrees) of the misorientation seen in WAXS studies of fiber bundles can be simply due to misorientation resulting from the wrapping of the fiber onto the sample holder. The azimuthal spread of the first equatorial reflection was seen to decrease with increasing tensile stress for fiber heat treated at 600 C.

Shimamura, Minter and Thomas obtained the first HREM images of PBZT (1983). The PBZT used was of intrinsic viscosity 31 dl/gm, spun from a 5.6% solution in poly(phosphoric acid) (PPA). The fibers were tension heat-treated at 475 C for 60 seconds with a 4% stretch. The images obtained showed 0.59 nm (100) fringes roughly parallel to the fiber corresponding to the spacing between molecules, and faint, meandering (001) fringes corresponding to the development of local three-dimensional crystallinity. The size of the 0.59 nm (100) fringe patches seen in HREM were about 8 nm in the lateral direction and 15 nm in the direction of the fiber. The (001) fringes were seen to occur in groups of 3 to 10 with limited (5 nm or less) lateral extent. The optical transform of the micrograph indicates streaking on

the first layer line (001) consistent with the axial disorder between molecules.

Further interpretation of the HREM images obtained by Shimamura et al. were frustrated by the limited resolution (0.59 nm), which did not enable both of the strong equatorial reflections to be simultaneously imaged. This limitation was imposed by experimental constraints including the lower wavelength electrons (100 kV), tungsten filament, and lack of a dedicated minimum dose system. Also, the focusing conditions used (near the Scherzer focus) did not allow for the contrast of the 1.24 nm (001) fringes to be properly enhanced for clear visualization.

Feldman, Farris, and Thomas (1985) reported WAXS data obtained by W. Wade Adams of PBZT film as spun, hot dried at 305 C in air, and tension heat treated at 525 C (1985). The PBZT used was of intrinsic viscosity 14 dl/gm. Samples 4 to 9 mm wide and 5 to 10 microns thick were prepared by extrusion of a PBZT/PPA solution through a flat die into a water bath. It was found that hot drying improved the lateral ordering but did not significantly affect orientation, whereas tensioned heat treatment improved the orientation as well as the lateral crystallite size. Also evident in the data but not discussed was the development of more localized scattering intensity on the second layer line after heat treatment, similar to that noted by Allen (1983).

Cohen (1988) investigated the structure of PBZT formed during the coagulation step. The PBZT used was of intrinsic viscosity 18 dl/gm, coagulated from 5.5 weight % solution in PPA into either water or 85% phosphoric acid. The coagulant was exchanged with epoxy resin, preserving the structure. That the structure was not disturbed by polymerization of the epoxy resin was confirmed by SAXS scattering. BF imaging of thin sections of the resulting PBZT-epoxy composite showed that the morphology consisted of an interconnected network of highly oriented microfibrils (Cohen and Thomas, 1988a). SAXS measurements gave an average microfibrillar diameter of 7.1 nm, and a volume fraction of 0.18 in the final film (Cohen and Thomas, 1988b). Since the original weight fraction of PBZT in solution was 0.055, this indicates a slight collapse of the PBZT network after the coagulation and epoxy impregnation steps.

From WAXS diffractometer data, Fratini and coworkers are currently conducting a refinement of the unit cell of PBZT. From several equatorial reflections they found best fit to a primitive unit cell with $a=0.595$ nm, $b=0.362$ nm, $c=1.249$ nm, and $\alpha=90$, $\beta=90$, $\gamma=95.49$ degrees (Fratini and Adams, 1987, private communication). More recent work using the Linked Atom Least Squares (LALS) refinement procedure has shown best fit to a non-primitive unit cell with $a=1.223$ nm, $b=0.365$ nm, $c=1.251$ nm, $\alpha=90$, $\beta=90$, $\gamma=106.2$ degrees (Fratini, Lenhert,

Resch, and Adams, 1989). Non-primitive unit cells apparently have three advantages (Fratini et al., 1989) : 1) different types of axial registry between chains can be considered, 2) close contacts between molecules can be more easily eliminated, and 3) the presence of weak scattering on the equator at a scattering angle corresponding to an intermolecular spacing of 1.15 nm is not explained by a primitive unit cell. The calculated density of the non-primitive unit cell is 1.66 gms/cm^3 , which compares with the 1.57 gms/cm^3 density of PBZT observed experimentally.

The detailed refinement of the unit cell of PBZT is complicated by the large amount of axial shift disorder present in this system. The LALS approach is intended for refinement of crystal structures from materials which show true three-dimensional crystallinity. In order to apply the LALS technique to the refinement of PBZT fiber patterns, it is necessary to make assumptions about the position and intensity of off-meridion "reflections" from the highly streaked layer lines in the PBZT diffraction pattern. As the amount of lateral shift disorder increases, a transition from localized Bragg reflections to highly streaked layer lines is expected. A more complete approach would be to investigate the expected scattering of PBZT over the entire profile of each layer line profile using different choices for the PBZT unit cell and specific models for the type and amount of axial shift disorder.

2. Overview of this Study

With this extensive background of knowledge about the structure of PBZT at hand, it is possible to begin to ask detailed questions about the ultrastructure of PBZT in the solid state. Is it possible to obtain HREM images of both of the strong PBZT equatorial reflections? What extra insight is obtained by such images? Can the (001) reflection be imaged better by using proper focusing techniques? If so, what do such these images imply about the nature of the shift disorder which is present? Is it possible to rationalize a particular model for the disorder present in these fibers? Finally, given support for a disorder model, is it possible to use this model to predict and compare with the experimentally obtained diffraction behavior of the fiber?

We have obtained HREM images of heat treated PBZT fiber which exhibit both the 0.59 nm (100) as well as the 0.36 nm (010) equatorial fringes, allowing the size, shape, and local orientation of PBZT crystallites to be deduced. Observation of 0.59 nm (100) fringes meeting another crystallite exhibiting 0.36 nm fringes provides direct evidence for an axial twist boundary between neighboring polymer crystallites. Such a boundary would necessarily involve both the translation and twisting of the long PBZT molecules as they thread their way from one crystallite to another.

Also, by using proper focusing conditions we have obtained images of the 1.25 nm (001) axial fringes over large regions of the fiber which show clearly the fluctuating nature of intermolecular packing in this system. The optical transform indicates that information up to the (003) 0.41 nm reflection is included in these images. These results confirm the validity of considering very local, large variations in registry between the PBZT molecules.

We examined the applicability of the paracrystalline lattice model (Hosemann and Bagchi, 1962) to describe the disorder present in PBZT. The major components of fluctuation tensors corresponding to the locus of unit-cell edge statistics were determined. Our analysis is patterned after that originally presented by Granier, Thomas, and Karasz (1989) for the description of the paracrystalline nature of molecular packing in poly(paraphenylene vinylene).

We have also examined a disorder model which involves a statistical probability of complete axial misregistry between locally ordered PBZT molecules. The predictions obtained by this disorder model are compared with experimentally obtained SAED data. Best fit of model to data is obtained by using a triclinic unit cell with a high probability of encountering complete axial misregistry between adjacent, uniformly oriented molecules.

B. Experimental

In this study we investigated the morphology of Aftech II, a heat-treated PBZT fiber. Aftech II fiber was prepared from a concentrated nematic solution (approximately 15% by weight) of IV=22 dl/gm PBZT in PPA. The fiber was tension heat treated at 700 C for approximately 30 seconds (W. Wade Adams, private communication).

Both HREM and SAED were used in this work. Samples were prepared by the "detachment replication" procedures detailed in Chapter II.

The total end point dose J_e required to cause fading of the first equatorial reflection was determined to be 2.3 C/cm^2 at 200 kV and room temperature. The sharp layer line reflections were visible on the meridian for a substantially higher dose (5.0 C/cm^2), indicative of the higher stability of bonding along the aromatic PBZT backbone.

In order to more clearly image the nature of the axial shift disorder, an underfocused objective lens focus setting was used to selectively enhance the 1.25 nm (001) spacing corresponding to the repeat distance along the chain. The phase contrast as a function of defocus for feature of a

given size is discussed in detail in Chapter II. From equation (2.5), we find that the maximum contrast is when the $\sin \chi$ term of $T=+1$ or -1 . The $\sin \chi$ term in equation 2.5 is

$$\sin \left\{ (2\pi/\lambda) \left(df \lambda^2 k^2/2 + c_s \lambda^4 k^4/4 \right) \right\}$$

For large features, k is small. Hence, the second term in $\sin \chi$ (with k^4 dependence) will be much smaller than the first. In this case the optimum focus for imaging a feature of size $d=1/k$ with phase contrast is approximately $df=d^2/2\lambda$. To obtain information about shift disorder along the axis of the chain it is necessary to image the 1.25 nm (001) spacing corresponding to the monomer repeat distance along the chain backbone. The amount of underdefocus necessary to image a feature of characteristic size $d=1.25$ nm with $\lambda=.00251$ nm is $df=311$ nm.

Figure 3.1 shows the behavior of the phase contrast transfer function (equation 2.5) as a function of defocus. The position of the strong PBZT lattice periodicities are indicated. Note that at Scherzer focus the 0.59 nm (100) and 0.36 nm (010) reflections are passed strongly and in reverse contrast. The 1.25 nm (001) reflection is not passed strongly. At the larger underfocus of 311 nm, the expected intensity and contrast of the (001) reflection is increased dramatically.

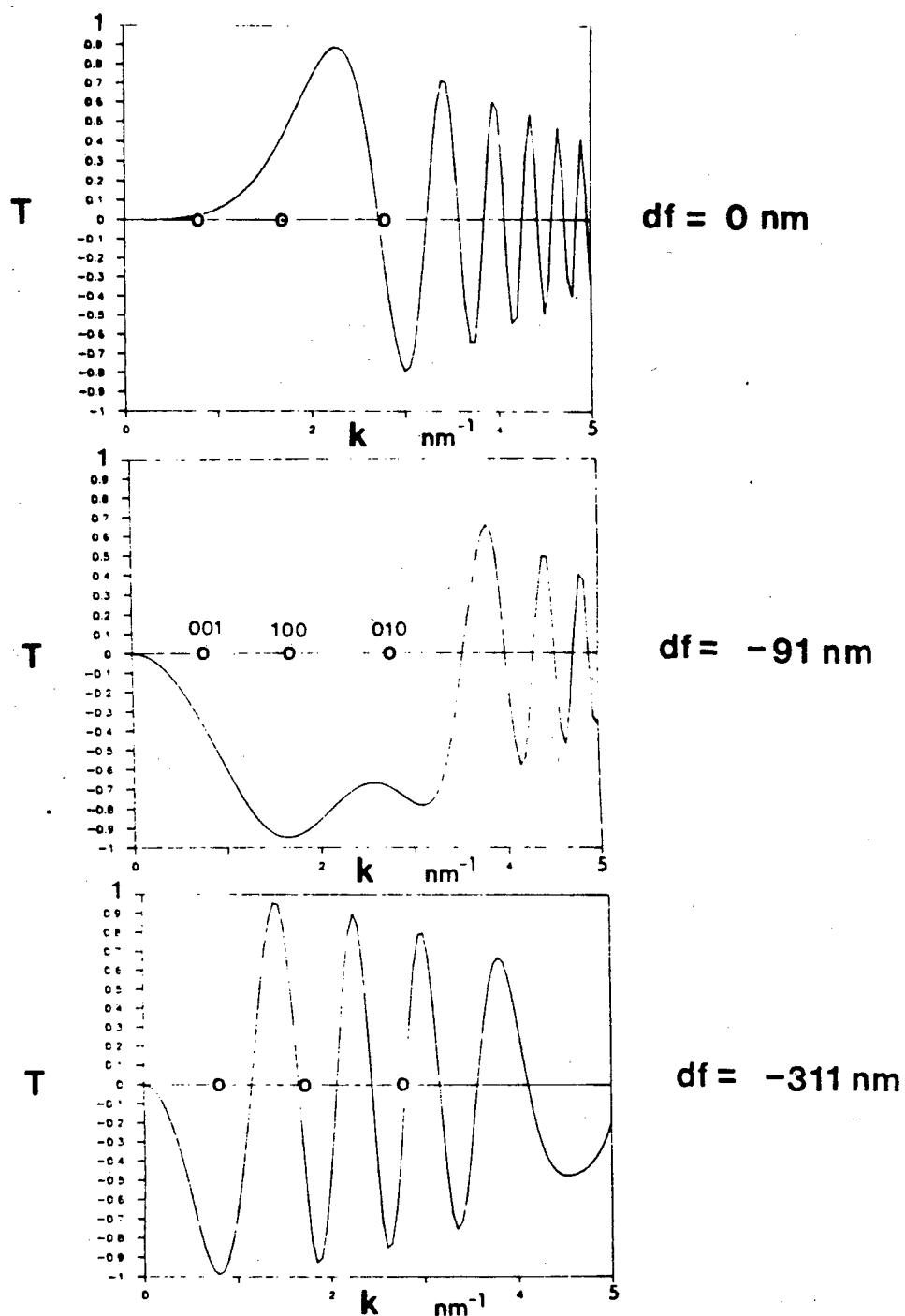


Figure 3.1: Behavior of the phase contrast transfer function (equation 2.5) as a function of defocus. The position of the strong PBZT lattice periodicities (1.25 nm (001), 0.59 nm (100), 0.36 nm (010)) are indicated. At Scherzer focus, the (100) and (010) reflections are passed strongly in reverse contrast, but the (001) is passed only weakly. At large underfocus, the (001) is significantly enhanced but now the higher frequencies are nearly lost.

Figure 3.2 shows simulated images for a PBZT model structure as a function of defocus. These images illustrate clearly how different settings of the objective lens defocus affect the appearance of the HREM images.

C. Results

A SAED pattern of PBZT Aftech II fiber is shown in Figure 3.3. The diffuse layer lines along the fiber axis signify a large amount of axial disorder between neighboring molecules. On the other hand, the strong, sharp reflections on the equator indicate that the lateral packing between molecules is well developed. Hence, to a first approximation the PBZT structure is a one-dimensionally disordered solid.

Dark Field imaging of PBZT using the equatorial reflections shows abbreviated, discrete crystallites similar to that seen by Roche et al. (1981) and Minter et al. (1983). Tilting a PBZT fiber fragment about the fiber axis during DF examination shows that the crystallites are randomly oriented about the orientation direction. In particular, the diffracting crystallites do not move up or down along the fiber axis but come in and out of the Bragg condition in an uncorrelated manner. This experiment indicates that the crystallites are not "twisting" about the fiber axis in a regular manner. Rather, the morphology is a arrangement of

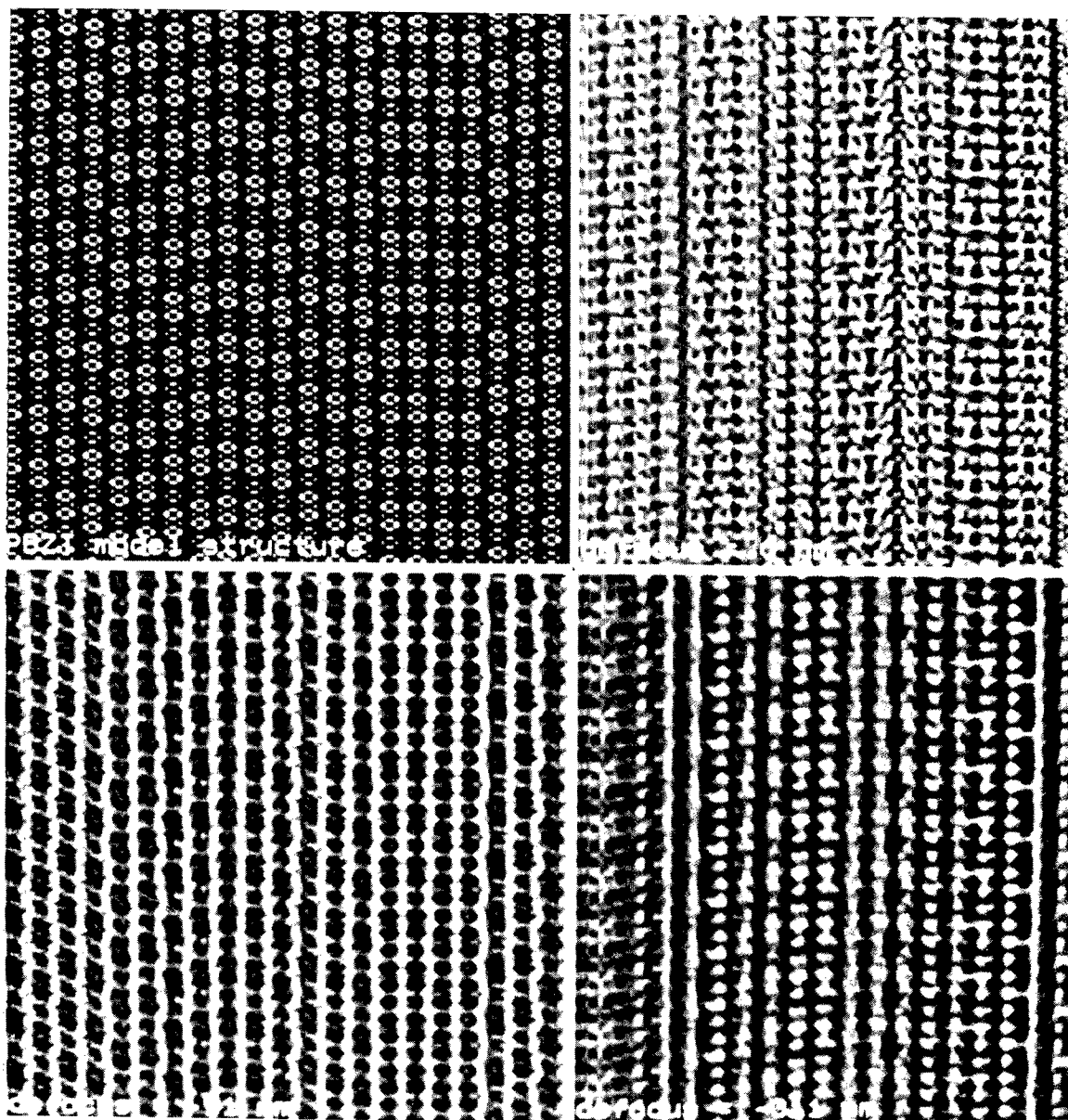


Figure 3.2: Simulated HREM images for a PBZT model structure as a function of defocus. Note how underfocusing enhances the contrast of the 1.25 nm (001) reflections corresponding to the repeat distance along the chain.

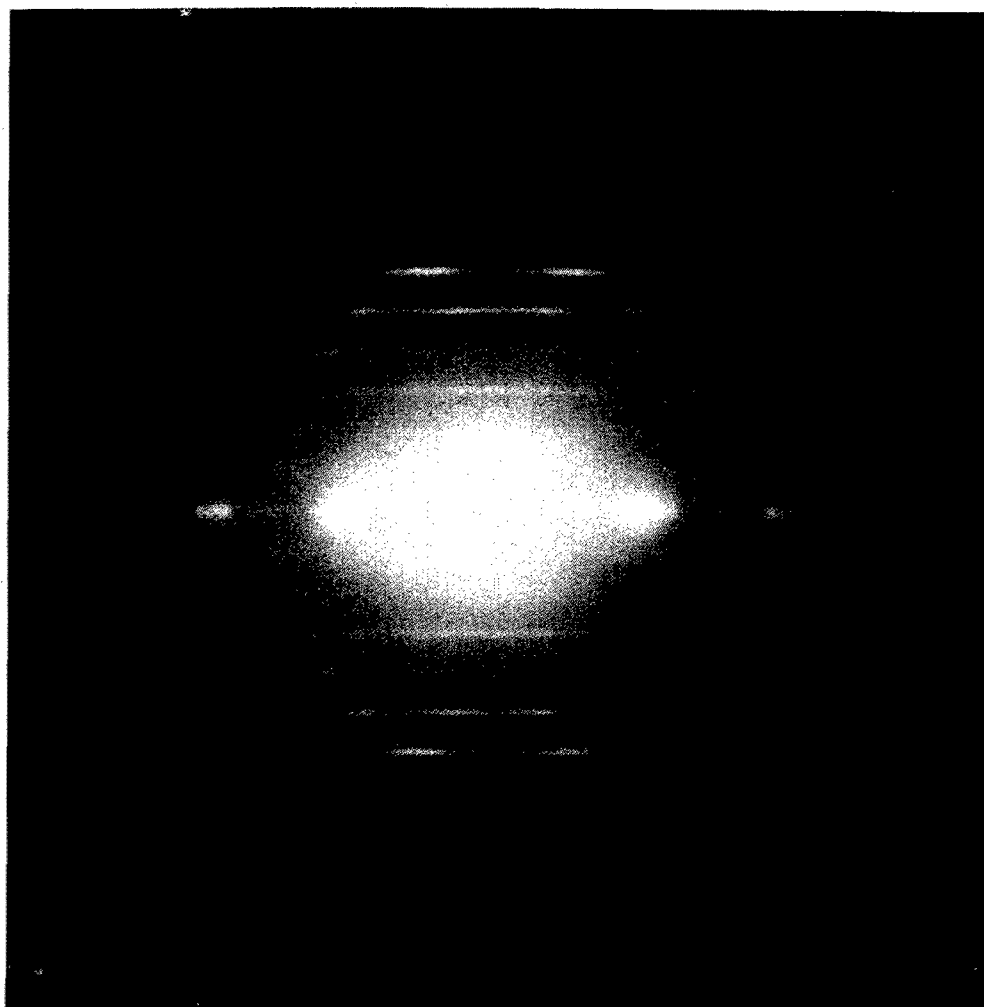


Figure 3.3: SAED pattern of heat treated trans-PBZT fiber. The strong equatorial reflections are indicative of the good lateral packing and the diffuse layer lines are indicative of the large amount of axial lateral disorder.

abbreviated, axially oriented crystallites with more or less random orientations perpendicular to the fiber axis.

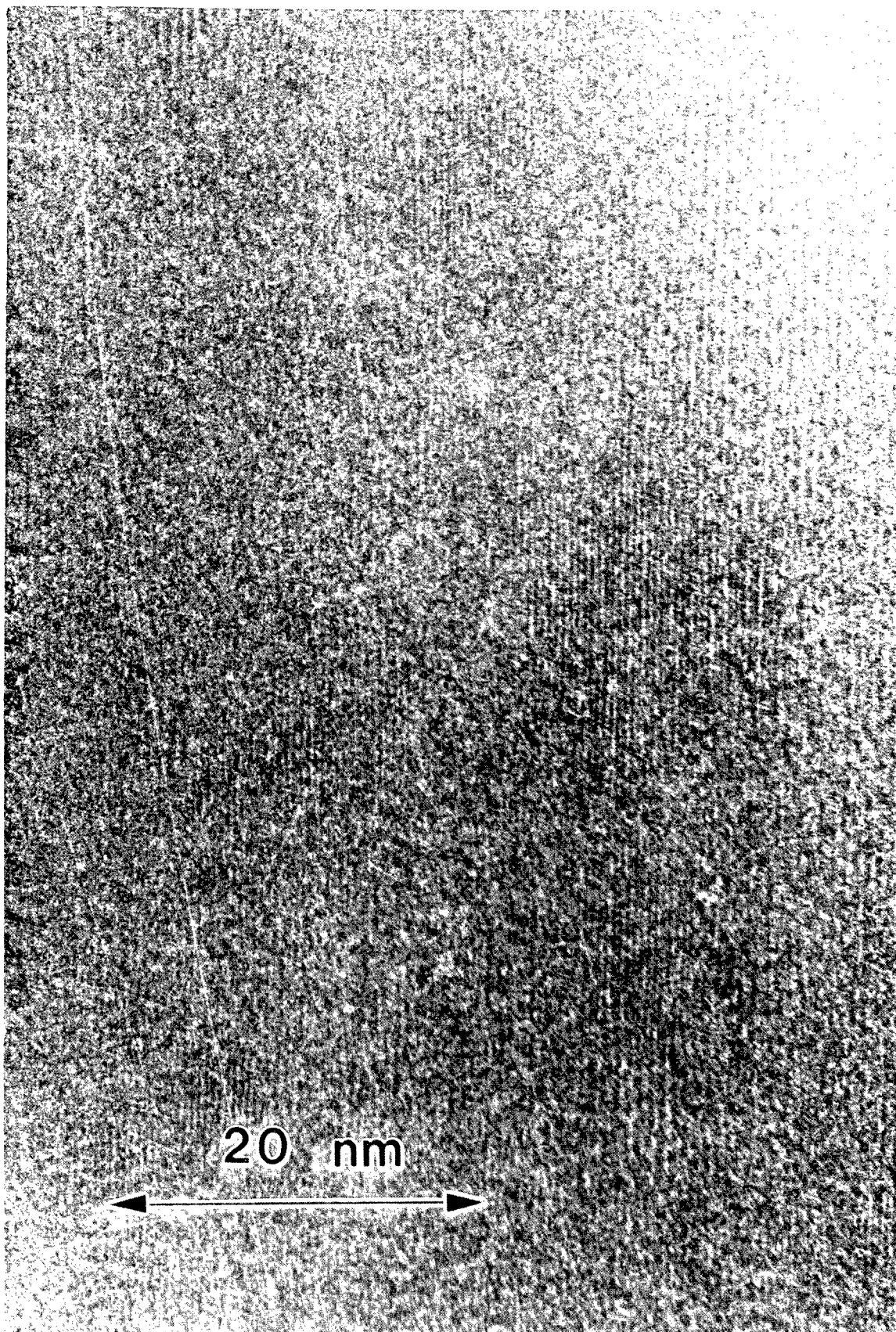
Figure 3.4 is an HREM image of PBZT taken near the Scherzer focus which shows clearly the 0.59 nm (100) and 0.36 nm (010) equatorial spacings (Boudet et al, 1987). From the multislice calculations in the last chapter we know that these fringes arise from the lateral packing between molecules and therefore serve to characterize the local orientation of the molecular axis. Hence, from this and similar HREM images it is possible to measure the precise orientation distribution of the chain axis with respect to the edge of the fiber.

Figure 3.5 shows the results of such measurements for PBZT, as well as for the PBZO fiber discussed in Chapter IV. Note that the axial crystallite orientation is high and uniform for all of the fibers studied. The distributions are all centered about the primary orientation axis.

The standard deviation of the observed misorientation angle determined by HREM for PBZT measured over a 200 nm x 300 nm region containing 85 crystallites was 1.26 degrees. The shape of the orientation distribution was the same regardless of whether angles were measured from 0.59 nm (100) or 0.36 nm (010) fringe patches. The maximum amount of

41

Figure 3.4: HREM image of PBZT taken near the Scherzer focus. The 0.59 nm (100) and 0.36 nm (010) equatorial spacings corresponding to lateral packing side-to-side and face-to-face can be clearly seen. (Boudet et al., 1987).



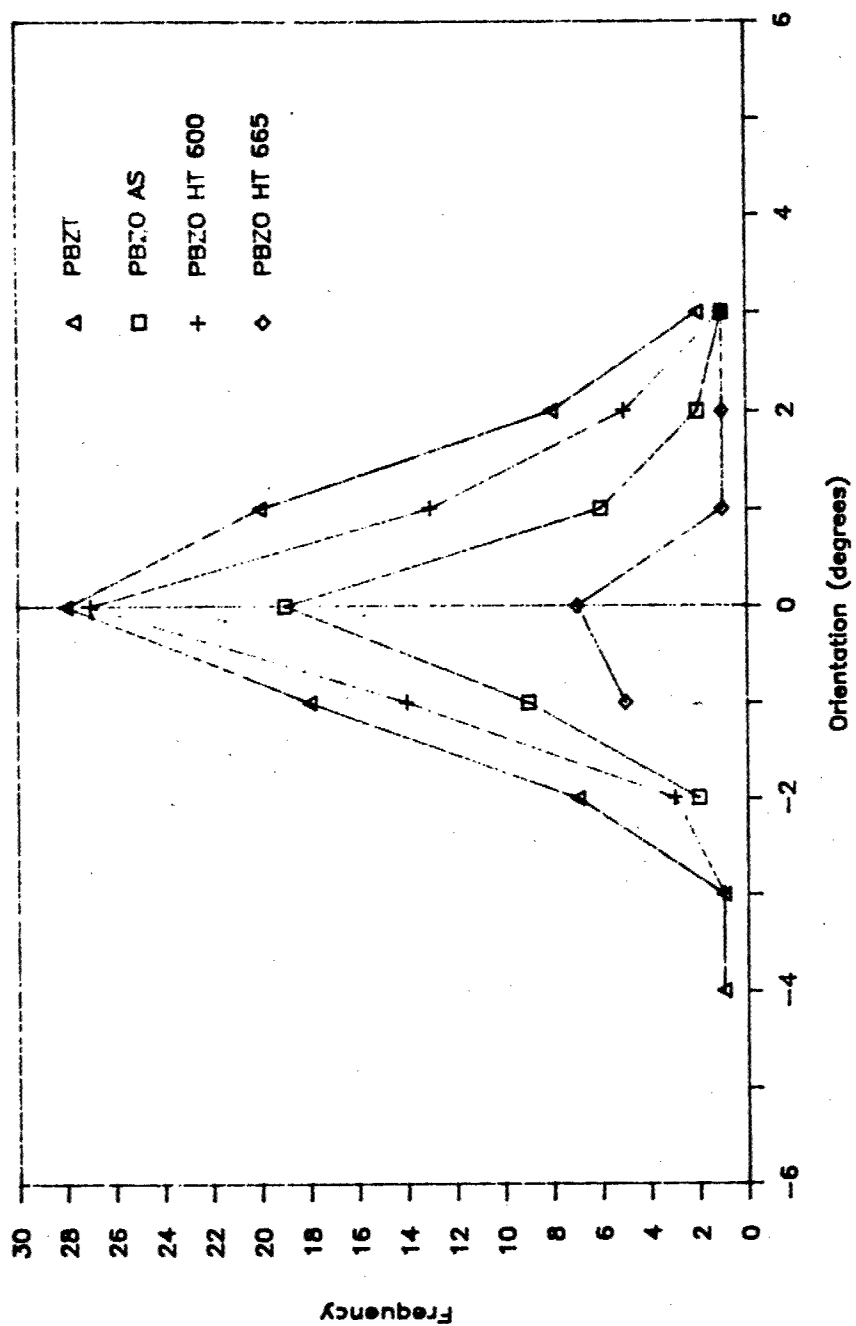


Figure 3.5: Plot of the crystallite orientation of rigid-rod polymer fibers as determined by HREM. The fibers are all very highly oriented, but a certain amount of misorientation does exist.

misorientation between two crystallites in this region was 7 degrees.

A parameter which is often used to describe an orientation distribution is the Hermans-Stein parameter $f = 1/2(3\langle \cos^2(\theta) \rangle - 1)$ where θ is the misorientation angle of a chain with respect to the primary orientation axis (Alexander, 1969). The orientation parameter determined from the data shown was $f = 0.99927$. For heat treated PBZT, and for all of the PBZO fibers studied as well (Table 3.1), the Hermans-Stein orientation parameter measured from HREM images is greater than $f = 0.999$. This emphasizes that subtle changes in the orientation distribution for highly oriented systems such as these do not significantly affect the value of the Hermans-Stein parameter.

From careful analysis of HREM images it is possible to obtain detailed information about the size and shape of PBZT crystallites. The crystallites were generally compact in shape and did not exhibit "rhombohedral" or other unique shapes which might indicate a tendency to form certain types of low-energy grain boundaries. Figure 3.6 shows a plot of the maximum axial size of crystallites as a function of the maximum lateral size. These data were determined by drawing boundaries around fringe patches on HREM enlargements by eye and then measuring the largest dimension of the resulting crystallites in both the axial and lateral directions. It is

Table 3.1

Orientation Measurements from HREM Images

Fiber	Standard Deviation (degrees)	Number of Observations	Hermans-Stein Orientation Parameter
PBZT	1.26	85	.99927
PBZO AS	1.33	39	.99920
PBZO HT 600	1.43	65	.99930
PBZO HT 665	1.25	16	.99929
PBZO CPD	7.86	39	.97254

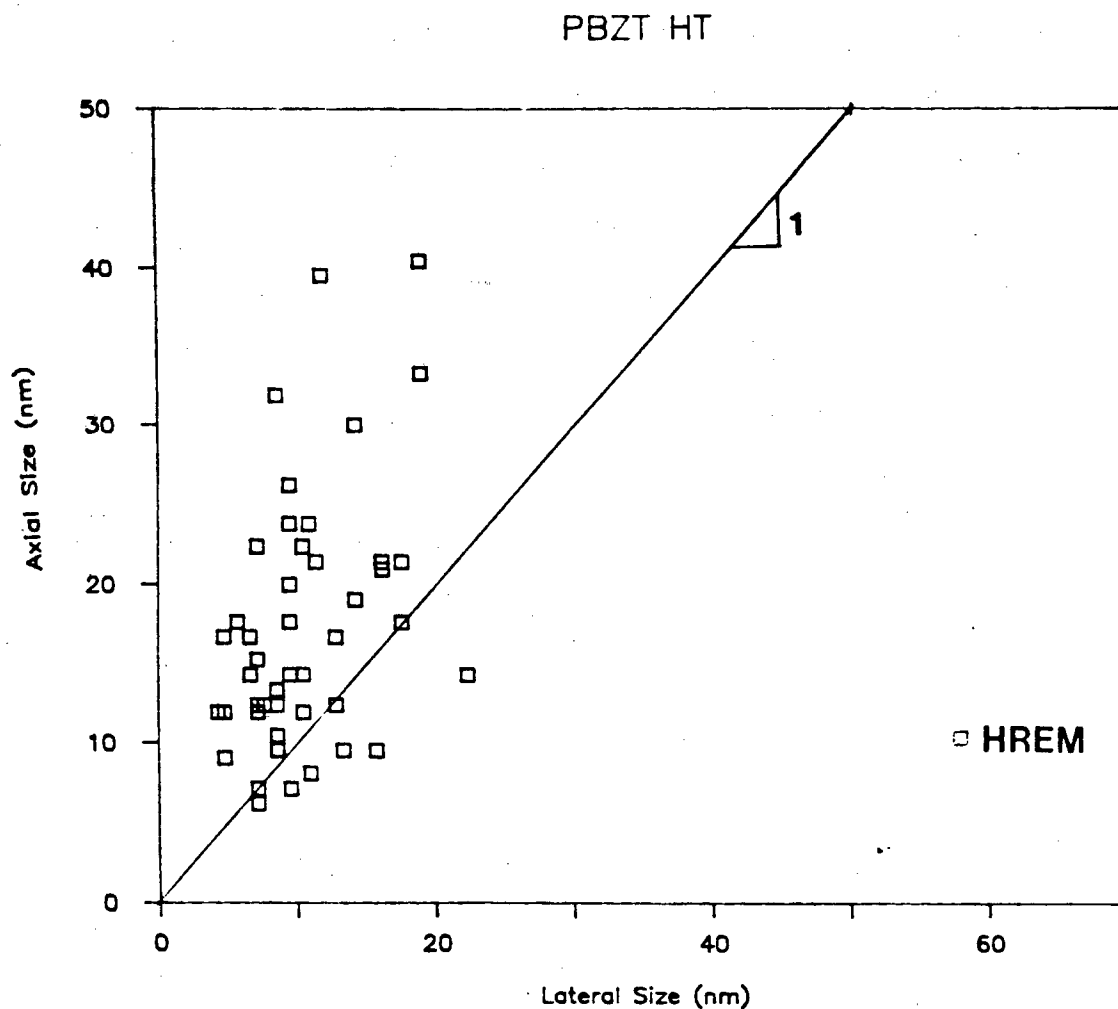


Figure 3.6: Plot of the maximum axial size of PBZT crystallites as a function of the maximum lateral size as determined from HREM images. These data were determined by measuring the size of patches of 0.59 nm (100) and 0.36 nm (010) fringes. Note that there is a reasonably broad distribution in crystallite size and shape.

evident that a relatively broad range of crystallite sizes occur. Note that the dimensions of PBZT crystallites are slightly extended in the axial direction as compared to the lateral direction. Crystals were noted as small as 4 nm and as large as 22 nm in the lateral direction, and as small as 5 nm and as large as 40 nm in the axial direction. The average size of the crystallites observed was 10.4 nm in the lateral direction with a standard deviation of 4.3 nm and 17.2 nm in the axial direction with a standard deviation of 8.0 nm. Because small misorientations of the crystallite may cause the fringes to lose contrast (Chapter II), the size of the fringe patch observed in HREM represents a lower bound on the actual crystallite size.

Figure 3.7 is an HREM image of a PBZT fiber using a highly underfocused objective lens in order to better image the axial fringes corresponding the monomer repeat distance along the PBZT backbone. The undulating (001) lines can be clearly seen over much of the image. They are approximately perpendicular to the fiber axis but their precise orientation varies from region to region. It is apparent from the image that the dimensions of the (001) fringe patches are larger along the fiber axis than in the lateral direction. This is confirmed in the optical transform of the micrographs where we find streaking on the first and third layer lines. From the breadth of the optical diffraction peaks the char-

Figure 3.7: HREM image of PBZT fiber fragment using an underfocused objective lens to enhance the 1.24 nm (001) spacing corresponding to the monomer repeat distance along the PBZT chain backbone. The fluctuating nature of the 1.24 nm (001) spacings can be seen over much of the image. Some areas of lateral ordering with 0.59 nm (100) fringes can also be seen. The edge of the fragment is seen on the right.

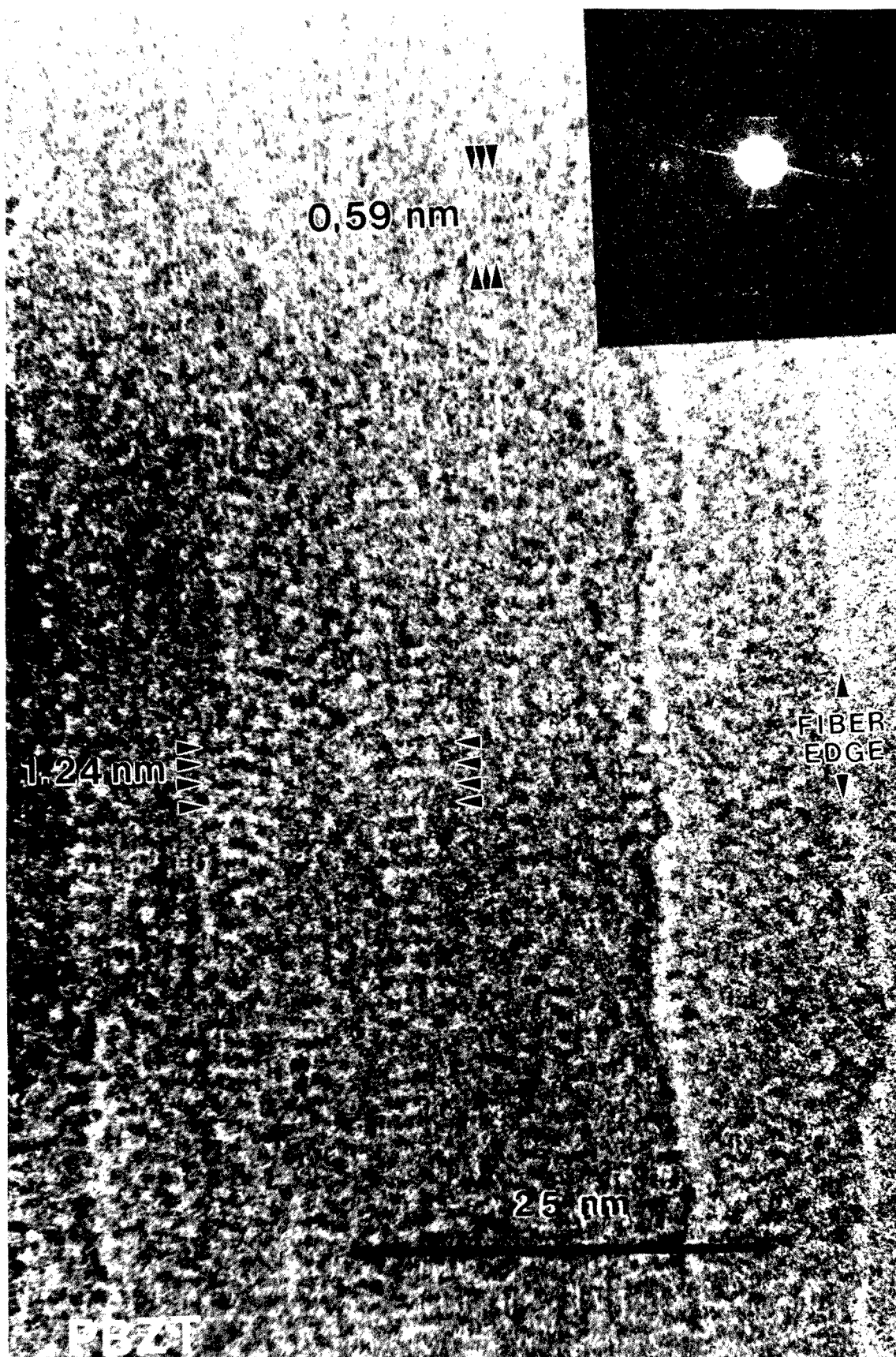


acteristic dimensions of the regions of (001) ordering are 15 nm along the chain axis and 1.0 nm perpendicular to the axis.

Figure 3.8 is a higher magnification view of an area with two sets of (001) fringes meeting laterally at a sharp boundary. This image shows that it is possible to have large, local shifts in axial registry between adjacent domains of PBZT molecules in the solid state.

These results suggest a model which involves variable local axial disorder between laterally well ordered PBZT molecules. From the images shown, it can be seen that the amount of axial misregistry can be quite large (approaching the chain repeat distance of 1.2 nm). To estimate the necessary probability of encountering axial misregistry in these images, we show in Figure 3.9 a simulated PBZT structure with an increasing probability of encountering axial disorder between adjacent PBZT molecules. In this figure only one layer of molecules is shown. The experimental image of course corresponds to a projection through a stack of these disordered layers on top of one another. The effect of finite sample thickness can also be simulated by superposing several disordered layers. A rough comparison of such computer models with the experimental HREM data (Figures 3.7 and 3.8) shows that a probability of axial misregistry somewhere between 30% and 100% is necessary to explain the images obtained.

Figure 3.8: Higher magnification view of PBZT 1.24 nm (001) fringes showing an area where the (001) fringes meet with a large amount of local misfit, confirming the validity of disorder model which considers a statistical probability of encountering complete axial misregistry between laterally adjacent molecules. The optical diffraction pattern is inset.



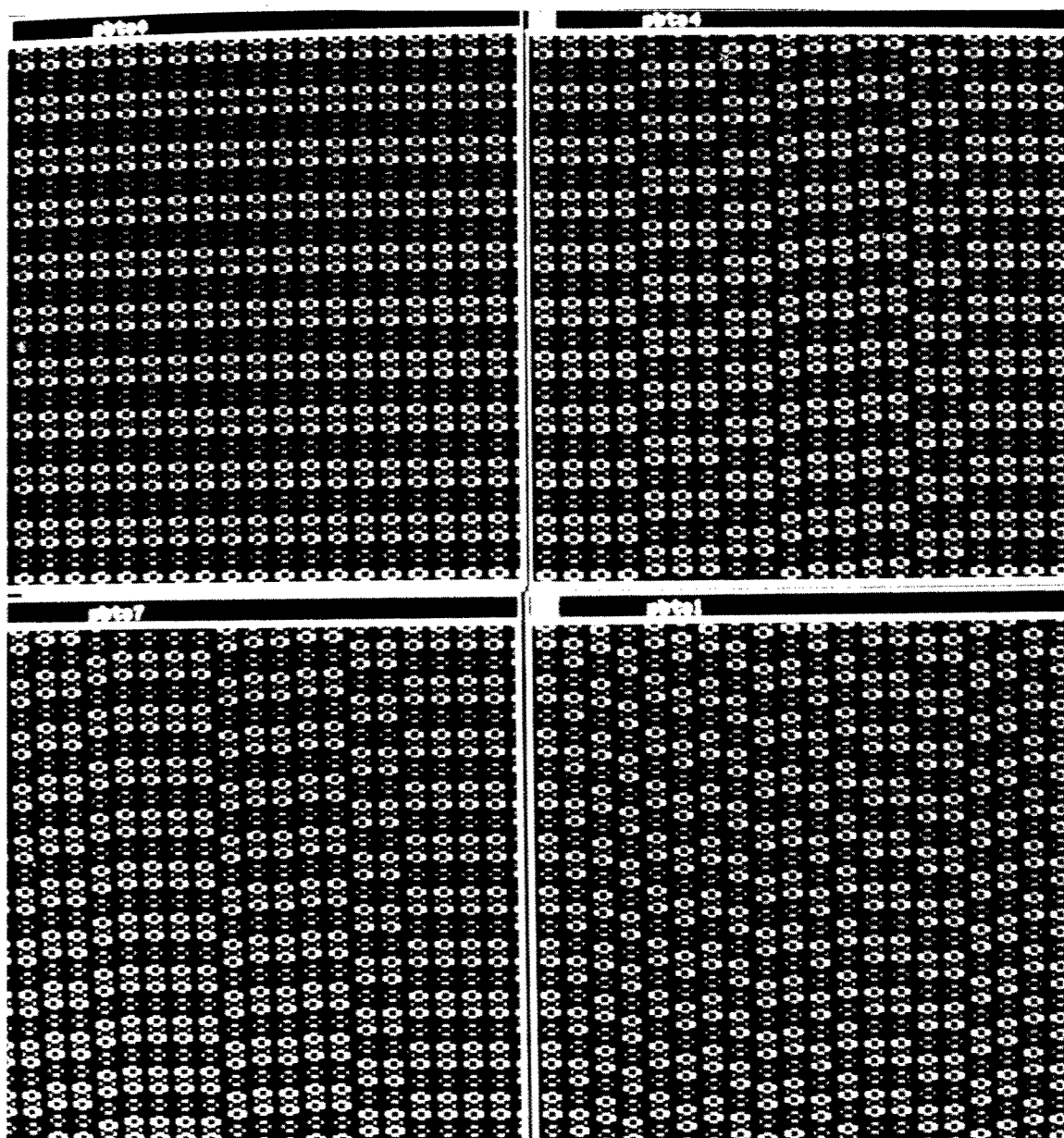


Figure 3.9: Models of PBZT structure showing the effect in real space of an a) 0%, b) 40%, c) 70%, and d) 100% probability of encountering complete axial disorder between laterally adjacent PBZT molecules.

One of the inherent problems with scattering techniques is that they require some sort of structural model in order to predict the scattering behavior of the object to compare with the experimental data. For crystalline materials this usually involves assuming a population of some sort of characteristic defects within an ideal, infinite, three-dimensional crystal lattice. It is not always possible to establish whether such defects are realistic since scattering techniques typically average over large sample volumes. Also, it is possible to predict quite similar scattering behavior from many distinctly different types of defect model.

Here, we have established by HREM imaging the validity of a defect model which involves large, local axial misregistry between laterally well ordered PBZT molecules. For detailed structural comparison, imaging techniques do not provide enough statistics to insure good averaging over the many possible contributions to the overall structure so that images must be thought of as providing "specific" rather than "general" information about sample structure. However, once a valid defect model has support by direct imaging, detailed comparison can be made by using model calculations which describe the disorder and the probability of this defect to occur. With the HREM images as evidence for the validity of defects characterized by large local fluctuations in

molecular packing, we further investigated the predictions of similar disorder models in describing the scattering of fibers of PBZT.

D. Discussion

1. Models for Disorder in Polymer Fibers

For uniaxial fiber samples it is convenient to describe the scattering distribution in cylindrical coordinates with the function $I(R, l/c, \psi_a)$, where l/c is the distance along the c^* axis, R the perpendicular distance from the c^* axis, and ψ_a the azimuthal angle. For cylindrically symmetric samples (fiber symmetry), we have the averaged intensity at a position $(R, l/c)$ along a layer line by averaging over all of the azimuthal angles ψ_a :

$$\langle I(R, l/c) \rangle = 1/2\pi \int_0^{2\pi} /f/{}^2 Z(R, \psi_a, l/c) d\psi_a \quad (3.1)$$

The term $/f/{}^2$ is the form factor corresponding to an individual molecule. The factor Z is the lattice function and has three contributions for each of the three basis vectors a_i of the lattice:

$$Z(R, \psi_a, 1/c) = Z_1 \cdot Z_2 \cdot Z_3 \quad (3.2)$$

The function Z is given by (Hosemann and Bagchi, 1962):

$$Z_i = (1 - /F_i/2) / (1 + /F_i/2 - 2/F_i / \cos(2\pi k \cdot a_i)) \quad (3.3)$$

The $/F_i/$ represent the statistical amplitudes determined by the Fourier transform of the cell-edge statistics $H_i(x)$ describing the deviation of the disordered lattice from the perfectly ordered case. The statistics $H_i(x)$ are defined such that

$$a_i = \int x H_i(x) d^3x \quad (3.4)$$

The statistical amplitudes $/F_i/$ describe the amount of crystalline ordering present in the sample. When all the $/F_i/=1$, the sample is perfectly ordered and the lattice function approaches a series of delta functions at k vectors equal to the nodes of the reciprocal lattice ($1/a_i$). When all the $/F_i/=0$, the lattice function becomes equal to one and the scattering becomes that of the spherically averaged molecular transform (i.e, gas-like scattering from the motif).

If PBZT exhibited complete axial misregistry then the $|F_i|$ corresponding to the lateral directions ($i=1$ and $i=2$) would equal zero and therefore the lattice functions Z_1 and Z_2 would equal one. In this case the distribution of scattering on each layer line would simply be that of the cylindrically averaged molecular transform. The detailed nature of the intensity distribution on the layer lines gives subtle information about the specific nature of the ordering between PBZT molecules. Several different models for predicting scattering behavior for disordered systems are available. First, we will discuss the paracrystalline model (Hosemann and Bagchi, 1962). Later, we will discuss a model involving a statistical probability of encountering random axial shifts between laterally adjacent molecules. The probability of encountering this random axial shift disorder can be different for different lateral directions.

2. Paracrystalline Lattice Fluctuations

The paracrystalline model is a perturbation model which incorporates the deviations of the actual lattice from an "ideal" lattice. In a perfect crystal, all of the lattice vectors \mathbf{a}_i defined as the vector between one lattice site and the next in the i direction are equivalent. The mental exercise of taking all of the actual lattice vectors \mathbf{a}_i in the sample and translating them back to a common origin would give a single end point. In a real sample with distortions

and defects, the \mathbf{a}_i 's are not equivalent and there would be a cloud of points surrounding the neighboring lattice site representing all of the different locations of the nearest neighbor motif.

This operation can be carried out for each of the three basis vectors \mathbf{a}_i describing the lattice of the material. Hosemann describes the cloud of vector end-points by assuming that they can be described well by Gaussian functions centered on the ideal crystal lattice points. Hence, it is possible to estimate the width of the distribution by a parameter representing the breadth of the cloud of end-points. This parameter is called the fluctuation tensor $\mathbf{T}_{jk}(i)$. There will be three independent fluctuation tensors for each of the three basis vectors \mathbf{a}_i .

When the cell-edge statistics are approximated by Gaussian functions, the statistical amplitudes $/F_i/$ depend on the scattering vector \mathbf{k} by the relation:

$$/F_i/ = \exp\{-2\pi^2 \mathbf{k} \cdot \mathbf{T}(i) \cdot \mathbf{k}\} \quad (3.5)$$

where \mathbf{T} is the fluctuation tensor with components $\mathbf{T}_{jk}(i) = \Delta_{jk}^2(i)$. $\Delta_{jk}(i)$ corresponds to the fluctuation of the basis vector \mathbf{a}_i in terms of the coordinate system (j, k) which in general may or may not be simply related to the crystal or cartesian coordinate systems. From equation 3.5,

it is apparent that the statistical amplitudes $/F_i/$ are predicted to be equal to one (ordered) at low scattering angle ($k=0$), and decay in a Gaussian fashion to zero (disordered) at a rate that depends on both k and T . The larger the components of fluctuation T are in a given direction k , the faster $/F_i/$ will decay from one to zero in that direction.

The effect of these fluctuations in the lattice is to decrease the intensity of and broaden the line width of the sharp Bragg reflections which would normally be observed in a perfect crystal. The intensity decreases and the width increases with increasing scattering vector. The breadth of the diffraction peaks dk are predicted to increase as the fourth power of scattering vector k :

$$(dk)^2 = (1/L)^2 + \pi^4 \Delta^4 k^4 \quad (3.6)$$

where Δ^2 is the appropriate component of the fluctuation tensor T and L is the crystallite size (Schultz, 1974). Equation 3.6 shows that the fluctuation tensor T as well as the crystallite size L can be obtained from the slope and intercept of a plot of the width of diffraction peaks dk as a function of k^4 .

Another method of estimating T is to determine the value of the scattering vector k for which it is no longer to

possible to observe discrete crystalline reflections in the scattering pattern. Hosemann showed (1962) that it is no longer possible to observe discrete reflections when the reciprocal lattice points are outside an "limiting ellipsoid of reflexion" where the value of $|F_i|$ becomes equal to 0.1. From equation 3.5 we see that the boundary of this ellipsoid is given by the condition:

$$(k \cdot T \cdot k) = 0.12 \quad (3.7)$$

This equation gives a means of estimating the fluctuation tensor T for reflections which become unresolvable at a scattering vector k . It is important to recall that there is a different fluctuation tensor $T(i)$ for each of the unit cell vectors a_i , and therefore there are three different limiting ellipsoids of reflexion centered at the origin of the diffraction pattern. The boundaries of a particular limiting ellipsoid can be determined by examining where on the diffraction pattern the corresponding component of a reflection becomes indistinguishable from the background. For example, if $T(1)$ is of interest, then it is necessary to investigate the streaking of reflections in the (100) direction. In our analysis we assumed that the fluctuation tensors $T(i)$ are approximately given by three diagonal components parallel to the lattice directions a_1 , a_2 , and a_3 .

From the PBZT SAED pattern it is possible to estimate the value of k at which different families of reflections become unresolvable. From these measurements and equation 3.7 the fluctuation tensors can be determined.

Consider first the fluctuation tensor associated with \mathbf{a}_3 , the unit cell vector along the chain. The corresponding direction in reciprocal space is the \mathbf{c}^* direction along the meridian. The components of $\mathbf{T}(\mathbf{3})$ are given by the scattering vectors at which it is no longer possible to resolve discrete layer lines in the \mathbf{a}^* , \mathbf{b}^* , and \mathbf{c}^* directions. For example, the component $\Delta_{33}(\mathbf{3})$ is given by the position on the meridian at which layer lines broaden and fade into the background. In PBZT SAED patterns it is possible to see up to 17 orders of layer line reflections along the meridian. This means that k_{max} is at least $17/1.25 = 14 \text{ nm}^{-1}$, so that from equation 3.7 $\Delta_{33}(\mathbf{3})$ is 0.02 nm. The components $\Delta_{11}(\mathbf{3})$ and $\Delta_{22}(\mathbf{3})$ are given by the points in the \mathbf{a}^* and \mathbf{b}^* directions at which the layer lines are no longer well defined. Because of the fiber symmetry of the sample it is not possible to distinguish the value of $\Delta_{11}(\mathbf{3})$ and $\Delta_{22}(\mathbf{3})$ from the diffraction pattern. In the analysis of the paracrystalline structure of PPV (Granier, Thomas, and Karasz, 1988) it was assumed that $\Delta_{11}(\mathbf{3})$ and $\Delta_{22}(\mathbf{3})$ were approximately zero since layer lines are usually assumed to be sharp and nearly infinite in extent. However, close examination of PBZT diffraction patterns shows that layer

lines become indistinguishable from the background in the \mathbf{a}^* and \mathbf{b}^* directions at finite scattering vectors. In fact, the layer lines vanish in the lateral directions at a scattering vector of approximately 3 nm^{-1} , giving a value of 0.12 for $\Delta_{11}(3)$ and $\Delta_{22}(3)$.

For the components of the fluctuation tensors for other unit cell vectors \mathbf{a}_1 and \mathbf{a}_2 , it is necessary to examine where in the diffraction pattern the (100) and (010) components of reflections become indistinguishable. Examination of the PBZT SAED pattern shows that the (h00) equatorial reflections can be seen up to the (300), corresponding to a scattering vector \mathbf{k}_{max} of 6 nm^{-1} and $\Delta_{11}(1)$ of 0.06 nm. The (0k0) reflections can be seen up to (030), corresponding to a scattering vector k_{max} of 9 nm^{-1} and $\Delta_{22}(2)$ of 0.04 nm. The fiber symmetry of the pattern makes it difficult to separate $\Delta_{11}(2)$ and $\Delta_{22}(1)$ from the data on the equator, therefore we follow the example of Granier et al. and assume $\Delta_{11}(2) = \Delta_{11}(1)$ and $\Delta_{22}(2) = \Delta_{22}(1)$.

The values of $\Delta_{33}(1)$ and $\Delta_{33}(2)$ are given by how far along the meridian it is possible to see discrete (h0l) and (0kl) reflections on the layer lines, respectively. From the SAED data it is not possible to index either spacing even on the first layer line, therefore \mathbf{k}_{max} is less than 0.8 nm^{-1} and thus $\Delta_{33}(1)$ and $\Delta_{33}(2)$ must be greater than 0.43 nm.

The values of the components of the fluctuation tensors $T(i)$ determined in this way are summarized in Table 3.2. Note that the high degree of axial disorder is manifested as the high values of $\Delta_{33}(1)$ and $\Delta_{33}(2)$. The geometry of $\Delta_{11}(3)$ and $\Delta_{22}(3)$ suggests that they are sensitive to the misorientation of the chain along the fiber axis. This is reasonable, for if chains are highly aligned, then the layer lines are flat and extended. A schematic drawing of the relationship between the unit cell vectors a_1 and a_3 of PBZT and the fluctuation tensors $T(1)$ and $T(3)$ is shown in Figure 3.10.

3. Statistical Disorder

The paracrystalline model discussed above assumes a homogeneous disorder in which each chain is displaced an average amount from its neighbor. The amount of this fluctuation is given by the size of the fluctuation tensors $T(i)$. For perfect crystals the $T(i)$ are zero.

Another disorder model is to assume there is some probability for adjacent chains to either be in perfect axial registry or to be completely misregistered. We term this the statistical disorder model. In this case $f_i = (1 - \alpha_s)$ where α_s is the probability of encountering misregistry in a given direction. Likewise, $(1 - \alpha_s)$ is the probability of adjacent molecules being in perfect registry. This disorder model

Table 3.2

Fluctuation Tensors of PBZT from the
Hosemann Paracrystallinity Model

direction 3: chain axis (c)
direction 2: lateral packing (b)
direction 1: lateral packing (a)

Tensor Component	k_{\max} (nm^{-1})	Δ (nm)
$\Delta_{11}(1)$	6	0.06
$\Delta_{22}(1)$	9	0.04
$\Delta_{33}(1)$	0.8	0.43
$\Delta_{11}(2)$	6	0.06
$\Delta_{22}(2)$	9	0.04
$\Delta_{33}(2)$	0.8	0.43
$\Delta_{11}(3)$	3	0.12
$\Delta_{22}(3)$	3	0.12
$\Delta_{33}(3)$	14	0.02

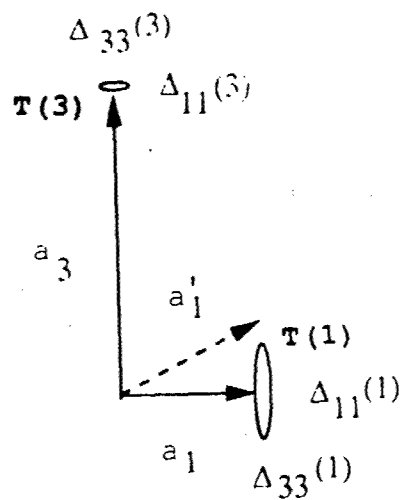


Figure 3.10: Schematic of the paracrystalline fluctuation tensors for PBZT in the \mathbf{a}_1 - \mathbf{a}_3 plane. The fluctuation tensor associated with the direction \mathbf{a}_1 is $\mathbf{T}(1)$, and is characterized by the dimensions $\Delta_{11}(1)$ in the \mathbf{a}_1 direction and $\Delta_{33}(1)$ in the \mathbf{a}_3 direction. Likewise, the fluctuation tensor for \mathbf{a}_3 is $\mathbf{T}(3)$, characterized by dimensions $\Delta_{11}(3)$ in the \mathbf{a}_1 direction and $\Delta_{33}(3)$ in the \mathbf{a}_3 direction.

differs from the paracrystalline model in that for a given orientation of the scattering vector \mathbf{k} the parameter $|F_i|$ does not depend on the magnitude of \mathbf{k} . The model has an advantage in that it requires only a choice for the type of axial registry (the position of the neighboring chain along the c axis) and the probability for that registry to occur. In this way, the scattering behavior can be calculated with a minimum number of adjustable parameters.

With this statistical disorder model it is possible to predict the intensity of scattering along layer lines in a fiber diffraction pattern. By varying the probability of encountering axial disorder in this manner it is possible to observe an evolution from completely streaked layer lines to a three-dimensionally crystalline structure.

Figure 3.11 shows the predicted scattering patterns for PBZT with a different probability for encountering axial misregistry between neighboring monomer units. Figure 3.11a shows the case of complete axial disorder, and therefore this corresponds to the molecular transform of PBZT. Note that the calculation predicts that there should be a strong intensity of scattering on the meridian at the sixth order layer line. Examination of the experimental data (Figure 3.3) shows that the sixth layer line is clearly split into separate peaks off the meridian. Also, there is a

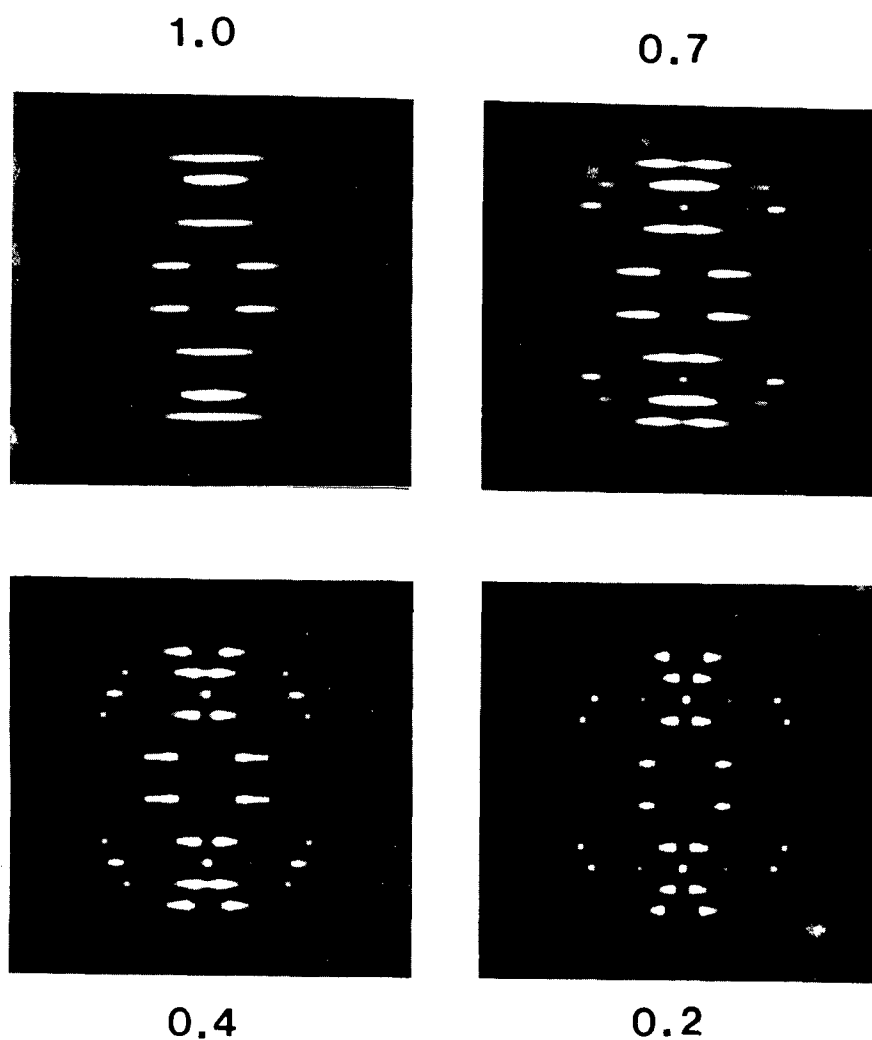


Figure 3.11: Simulated SAED patterns (shown up to layer line six) for PBZT using a triclinic unit cell and a) 100%, b) 70%, c) 40%, d) 20% probability of encountering complete axial disorder between molecules. These should be compared with the experimental data in Figure 3.3. Note that the experimentally observed splitting of scattered intensity near the meridian on $l=6$ is not predicted in the molecular transform.

fluctuation in intensity on $l=5$ which is not predicted by the molecular transform. In order to model the intensity on the layer lines we have found it necessary to consider a new unit cell for PBZT which involves regular placement along the c -axis between laterally adjacent PBZT molecules.

In the calculations shown in Figure 3.11 a unit cell involving an axial translation of the PBZT molecule along the c -direction of 0.31 nm ($1/4 c$) in the a -direction and an axial translation of -0.31 nm ($1/4 c$) in the b -direction was used. A graphical comparison of this model with SAED data is presented in Figure 3.12 for the sixth order layer line. Note that the molecular transform of PBZT ($\alpha_s=1.0$) has a local maximum of intensity on the meridian, whereas experimentally there is a noticeable off-axis peak in the intensity distribution. The best fit to the data clearly involves a probability of axial disorder somewhere between 70% and 100%.

It would be best to investigate the fit of the predicted scattering intensity on all of the observable layer lines. This is most important for low order layer lines where the effect of the paracrystalline nature of the disorder has the least smearing effect on the lattice factor. The predominance of inelastic scattering at low angles in SAED precludes a quantitative investigation in this regime using the data of Figure 3.3. Future work using energy-filtered

Layer Line 6

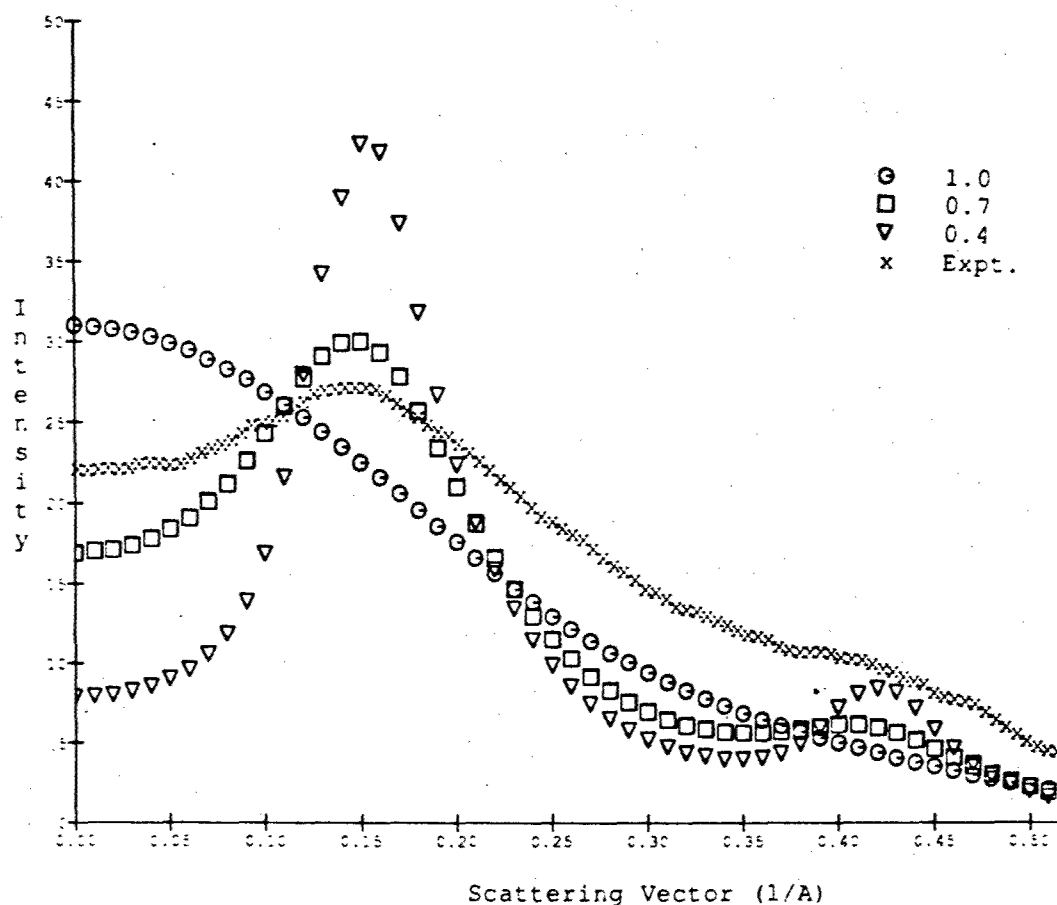


Figure 3.12: Comparison between SAED data for the sixth layer line in heat treated PBZT and theoretical predictions using a triclinic unit cell and a disorder model with different probabilities of encountering complete axial disorder between adjacent molecules. The data indicates that best fit is obtained with a probability of encountering complete axial disorder approximately 80% of the time.

SAED and quantitative WAXS should be useful in further analysis of the scattering on lower order layer lines.

It has been shown that regular axial translations between laterally neighboring molecules are necessary in order to best fit the experimental distribution of layer line scattering intensity. T. Granier (1989, private communication) has investigated in more detail the predictions of this disorder model to experimentally obtained PBZT scattering. In Granier's analysis the data used was WAXS scattering taken by A. Fratini and W. W. Adams and plotted by J. Minter (T. Granier, private communication). The refinement considered different axial translations between PBZT chains in the a and b packing directions. This preserves the projection of the unit cell in the c direction. The analysis varied the axial shift in the a and b direction in order to minimize the difference between the computed and experimental diffraction patterns for layer lines 1 to 9. The search procedure was refined with the SIMPLEX method for function minimization (Nelder and Mead, 1965). Although the refinement indicated that there were minima for several placements of the chain along the axial direction, the best fit was found for a unit cell using an axial translation of +0.33 nm between neighboring PBZT molecules in the a direction and -0.15 nm in the b direction. Specifically, the new triclinic unit cell is:

$a' = 0.681 \text{ nm}$	$\alpha' = 112.6 \text{ degrees}$
$b' = 0.392 \text{ nm}$	$\beta' = 61.0 \text{ degrees}$
$c = 1.249 \text{ nm}$	$\gamma = 95.5 \text{ degrees}$

The space group is $P1$, with one chain per cell. The density is 1.65 gms/cm^3 . Using this unit cell, the best fit to the data was obtained with an 82% probability of encountering axial disorder in the a direction and a 74% probability of encountering axial disorder in the b direction.

The relationship of the $a1'$ axis of this triclinic unit cell to the $a1$ axis of the monoclinic cell is shown in Figure 3.10. Graphic displays of the position of the PBZT molecule in this unit cell indicate that sulfur atoms on one molecule become "locked in" between the two pendant hydrogens on the phenyl ring of a neighboring PBZT molecule (Granier, private communication).

With this unit cell in mind, it is useful to reexamine the HREM images presented earlier. If this unit cell is appropriate for describing the limited three-dimensional crystallinity which occurs in PBZT fibers, then it might be expected that the (001) fringes should be a preferential angle to the fiber axis. Close examination of figure 3.7 shows that there are indeed regions where the (001) fringes make measurable angles with respect to the fiber axis, but the angle of orientation is not particularly uniform. In one

region near the middle and bottom of the figure the (001) fringes make an angle of 83 degrees with the fiber axis. This corresponds to a regular axial shift of 0.07 nm between molecules packed in the a direction.

E. Conclusions

HREM images of heat treated PBZT fiber show well oriented crystallites exhibiting 0.59 nm (100) and 0.36 nm (010) fringes characteristic of the lateral packing between molecules. The fringes map the local orientation of the molecular axis, enabling the precise determination of the orientation distribution. The standard deviation of the crystallite orientation is 1.3 degrees in a 200 nm x 300 nm region, giving a Hermans-Stein orientation parameter f of better than 0.999. Experimentally significant, local variations in orientation do occur and may be as large as 7 degrees.

The HREM images allow detailed investigation of the size and shape of PBZT crystallites. The crystallites were generally compact in shape and limited in extent. The observed size distribution is reasonably broad, with crystalline regions detected as small as 4 nm and as large as 22 nm in the lateral direction and as small as 5 nm and as large as 40 nm in the axial direction. The average lateral

size was found to be 10.4 ± 4.3 nm, and the average axial size was 17.2 ± 8.0 nm. These crystallites are substantially smaller in the axial direction than the size of the average PBZT molecule (100 nm).

Underfocusing the objective lens enables the 1.24 nm (001) reflection to be more clearly resolved. HREM images of the (001) planes show meandering fringes characteristic of the high degree of axial disorder between neighboring molecules. Large lateral mismatches between (001) ordered zones confirms the applicability of a model involving a large, local axial shift disorder.

Model calculations using a statistical disorder model can be used to fit the experimentally obtained SAED patterns. The best agreement with experimental data is obtained by considering a new triclinic unit cell with a high (80%) probability of encountering axial shift disorder between neighboring molecules.

In general, these new findings are quite consistent with our previous understanding of PBZT morphology. Obviously, HREM imaging has shown itself to be a useful and highly complementary technique for the detailed structural analysis of polymer solids.

Although our mental picture of PBZT morphology in the solid state is now detailed, it is not necessarily complete. Future refinements of our model of PBZT ultrastructure might benefit from a more complete simulation of PBZT scattering behavior over the entire Ewald sphere rather than merely on individual layer lines. Also, a quantitative comparison between the contrast experimentally observed in HREM images and that predicted by different disorder models would be of interest. This second goal may require higher magnification images than it has yet been possible to obtain so that the negatives can be scanned directly by a microdensitometer.

CHAPTER IV: ULTRASTRUCTURE OF CIS-PBZO

As discussed in Chapter I, PBZT and PBZO are polymers of considerable interest for high performance applications. Historically, more effort has been expended in refining the spinning and processing steps for PBZT fiber because it was originally easier to obtain higher molecular weight PBZT than PBZO. However, recent advances in synthetic techniques (Wolfe, Sybert, and Sybert, 1985) have made it possible to reproducibly obtain high molecular weight PBZO. PBZO is now under commercial development by Dow Chemical company. It is therefore reasonable to expect an expanded interest in the relationship between structure and properties of PBZO fiber.

In this chapter the ultrastructure of cis-PBZO fiber will be investigated by WAXS, SAED, DF, and HREM. The morphology was examined as a function of post-spinning heat treatment of the PBZO fiber. Also, the structure of PBZO critically point dried from the "as-spun" wet state was examined for comparison with as-spun and tension heat treated fiber.

In this study we address the details of WAXS and SAED scattering of PBZO fiber. We examine the experimentally observed scattering on the meridian and on lower layer lines and compare these with model predictions. The observation of

"single crystal" texturing in SAED of thin PBZO fiber fragments has enabled the unambiguous indexing of localized scattering corresponding to the development of three-dimensional crystalline ordering. We find that best fit of the experimentally observed scattering intensity at intermediate scattering angles is provided by a unit cell involving a regular axial shift of $1/4$ c between PBZO molecules close packed "edge-to-edge" at a distance of 0.55 nm in the a direction. At higher scattering angles the intensity is described by the PBZO molecular transform.

HREM imaging has provided information about the size, shape, and relative orientation of crystalline domains in PBZO as well as the nature of molecular packing within these domains. We compare the size and shape of the crystallites determined by HREM with those determined by DF. Although quantitative studies by either DF or HREM are plagued by problems of sufficient statistics, from our results we find that there is quite good agreement in the crystallite sizes and size distributions determined by the two techniques. We reconfirm previous results which indicate a relatively broad crystallite size but an experimentally significant tendency for PBZO crystals to grow more in the lateral than axial direction after tensioned heat treatment.

The truly unique aspect of HREM is the ability to visualize and subsequently characterize specific types of local

defects in microstructures. In particular, we were able to obtain evidence for different types of grain boundaries and dislocation structures between and within PBZO crystallites. We discuss the structure of an edge dislocation imaged within a PBZO crystallite which has both the direction of the dislocation as well as direction of the Burger's vector perpendicular to the axis of molecular orientation. Observations of grain boundary defects are discussed in more detail in Chapter VI.

A. Introduction

The structure of PBZO fiber was first studied by WAXS by Won Choe and Kim (1981). The PBZO used was spun from an 8.6 % by weight solution of PBZO with an inherent viscosity of 2.8 dl/gm in a solvent of 97.5/2.5 MSA/CSA and was coagulated in a 70/30 H₂O/MSA bath. The WAXS pattern of the as-spun fiber showed good orientation, with two strong equatorial reflections at spacings of 0.555 nm and 0.335 nm and weak scattering on the first and third layer lines (1.135 nm) along the fiber direction.

Model calculations using an empirical molecular orbital approach for the interactions between cis-PBZO molecules (Bhaumik, Welsh, Jaffe, and Mark, 1981) showed that there is a minimum in the energetic interactions between neighboring

PBZO monomers at a characteristic axial shift of 0.2 nm for molecules packed side by side (0.62 nm apart) and at 0.3 nm for molecules packed face to face (0.35 nm apart). However, the energy troughs as a function of relative axial position were shallow (3 kcal/mole; 5 kT) so it might be expected that PBZO molecules would exhibit axial disorder in the solid state as does PBZT (Chapter III).

As discussed in Chapter III for trans-PBZT, Bhaumik et al. did not investigate the effect of different internal conformations of the cis-PBZO molecule. As for PBZT, the energetics of the interactions between neighboring PBZO molecules might be quite sensitive to internal rotations of the heterocyclic group about the chain axis. For cis-PBZO, the interactions between neighboring molecules may be more sensitive to such internal rotations because of the chemical dipole induced within the heterocyclic ring by the different electronegativities of nitrogen and oxygen. For "trans" arrangements these dipoles are in opposite directions and tend to locally cancel. In the "cis" arrangement the dipoles are both in the same direction and locally add. This makes the local net dipole of a "cis" monomer stronger, so therefore the intermolecular interactions should be longer range.

The crystal structure of PBZO was first deduced from WAXS scattering (Fratini and Adams, 1985). A primitive,

monoclinic unit cell was found with parameters ($a=0.565$, $b=0.358$ nm, $c=1.174$ nm, $\alpha=90$, $\beta=90$, $\gamma=102.5$ degrees). This unit cell gives a density of 1.64 gm/cm^3 which is not much different from that observed experimentally (1.56 gm/cm^3). Also, it explains the expected close packings of PBZO molecules "side-to-side" at 0.56 nm in the a direction and "face-to-face" at 0.36 nm in the b direction.

The microstructure of PBZO was studied in detail by Adams et al. (1986) and by Krause et al. (1988). They investigated PBZO with an intrinsic viscosity of 24 dl/g spun from solutions of 13.8 weight % in poly(phosphoric acid). The fibers were heat treated under tension in air at 450 C at an extension ratio of 3.0% with a residence time of 30 seconds. In these studies WAXS, SAXS, SEM, BF, and DF were used.

WAXS and SAED scattering patterns of PBZO fiber indicated strong equatorial reflections and layer line scattering consistent with the high degree of orientation and good lateral packing of the PBZO molecules. The development of three-dimensional crystallinity as evidenced by the development of localized scattering on upper order layer lines was noted in both studies (Adams et al. (1986), Krause et al. (1988)). Adams et al. (1986) suggested that the primitive unit cell of Fratini and Adams (1985) was consistent with WAXS diffractometer data, but a detailed

comparison of the predicted scattering intensity from this unit cell with that obtained experimentally was not presented. In particular, the strong reflections on the second order layer line corresponding to the development of three-dimensional crystallinity were not indexed in terms of this unit cell assignment.

Another feature in the scattering behavior of PBZO which is apparent from the data of Adams et al. (1986) and Krause et al. (1988) but which has not received attention is the notable lack of scattering intensity at the meridian on the second order layer line. Such a lack of scattering intensity may be explained either by a systematic absence due to symmetry in the lattice factor or the presence of a weak molecular transform at this scattering angle.

SAED studies showed that the relative intensity of the first and second equatorial reflections was sensitive to the region of sample investigated (Krause, et al., 1988). This is indicative of a domain structure formed from texturing within the PBZO fiber. Azimuthal scans of the equatorial reflections (Adams et al, 1986) indicated a misorientation of 6 degrees in the as-spun case and 4 degrees in the heat-treated case in both WAXS and SAED, confirming that misorientation was present down to very local size scales in the fiber.

Scatter plots of the crystal sizes observed in equatorial DF showed a rather broad distribution in both axial and lateral size (Adams et al., 1986). The mean crystal dimensions were seen to increase in both the lateral and axial directions, but the ratio of the average axial size to average lateral size of the crystallites decreased from 0.90 to 0.55 after heat treatment. Apparently, the growth of the PBZO crystallites in the axial direction is not as extensive as growth in the lateral direction. This is in contrast to heat treated PBZT, where crystallites have an average axial size to average lateral size ratio of 1.7 (Chapter III).

SAXS patterns of heat treated PBZO fiber exhibit a weak four-point pattern (Adams et al., 1986; Adams and Grubb, 1988). These results indicate the development of periodic fluctuations in electron density at specific angles to the fiber axis. Similar four-point patterns have been seen in SAXS of fibers of ABPBO, a semi-flexible polymer which shows well developed three-dimensional crystallinity. This behavior is in sharp contrast to heat treated PBZT which does not exhibit four-point SAXS behavior (Minter, 1982). Adams et al. (1986) propose a model of tilted lamellar shaped crystallites to explain this four-point SAXS behavior, but it is known from DF that such lamellar crystallites do not exist in PBZO. A more detailed explanation of the four-point SAXS

scattering in terms of specific morphological features present in PBZO and absent in PBZT has not yet been advanced.

The first HREM study of PBZO fiber was recently published by Adams et al. (1989). The fiber used was spun from anisotropic solution in PPA and coagulated in water. The intrinsic viscosity and solution concentration were not reported. After washing in water and drying in air, the fiber was heat treated under tension in a nitrogen atmosphere at 550 C. The critical dose J_c was reported to be 0.2 C/cm^2 for 200 kV electrons. This is somewhat less than that for PBZT (1.6 C/cm^2 at 100 kV), but is still two orders of magnitude better than polyethylene.

The 0.55 nm fringes were clearly visible in the HREM image, with orientation of the molecules in the direction of the fiber maintained over large regions of the micrograph. Evidence for 0.33 nm fringes was seen in the optical transform, but these fringes were difficult to resolve on the micrograph. The sizes, shapes, and relative positions of different PBZO crystallites could be detected (of size approximately $5 \text{ nm} \times 10 \text{ nm}$), but the limited field of view made statistically significant values difficult to establish. A defective region was shown where the 0.55 nm fringes lined up properly on one side of the image but did not line up properly on the other side. Although this data suggests the presence of a dislocation within the PBZO crystallite, a

specific model which explained the structure of the defect was not presented.

More recent attempts to refine the unit cell of crystalline PBZO have focused on the use of a non-primitive unit cell with ($a=1.104$, $b=0.346$, $c=1.206$ nm, $\alpha=90$, $\beta=90$, and $\gamma=91.5$) (Fratini and Adams, 1988, private communication). The placement of the second molecule in this non-primitive cell has been postulated to be at $(1/2, 0, 1/2)$, which corresponds to a regular translation of $1/2$ c for molecules close-packed in the a direction. However, we will show later that this placement of the second chain does not explain the observed distribution of scattering intensity on the second order layer line.

Here, we present WAXS and SAED data of PBZO fiber as a function of heat treatment. Thin sections of PBZO film were found to exhibit orientation texturing. SAED patterns obtained from these regions enabled the assignment of specific hkl indexing to localized reflections off the meridian on the second order layer line using a non-primitive unit cell with a regular axial registry of $1/4$ c between molecules close-packed in the a direction. We compare the intensity of scattering predicted by the proposed unit cell as well as several other reasonable alternative unit cells with that experimentally observed.

We present HREM data of PBZO both as a function of heat treatment and of a fiber prepared by removing the coagulant (water) by critical point drying. The sizes and shapes of the crystallites seen in HREM will be compared with data from DF imaging. We confirmed the earlier observation that PBZO crystallites tend to grow more in the lateral direction than axially.

We saw several interesting types of defects in these images and will describe the highlights of these results. In this chapter we will discuss an image which contains a edge dislocation which has both the dislocation direction and the Burger's vector perpendicular to the molecular axis. Lattice images near compressive deformation zones will be presented in Chapter V. More detailed comparison of HREM images of PBZO with grain boundary defect models will be presented in Chapter VI.

B. Experimental

The cis-PBZO fiber used in this study was spun by Dow Chemical company (H. Ledbetter, 1987) and provided to us by W. W. Adams of WPAFB. The samples received were as-spun (AS), heat treated at 600 C (HT 600) and heat treated at 665 C (HT 665). The mechanical properties of the material as reported by Dow Chemical are listed in Table 4.1.

Table 4.1

Characteristics of PBZO Fiber

as Reported by H. Ledbetter, Dow Chemical
to W. Wade Adams, WPAFB

Designation (Dow Code)	HT C	Color	Modulus GPa	Strength GPa	Elong %
AS-383-C8601037-69E	AS	yellow	165	4.3	2.8
HT-383-C8700357-8A	600	orange	317	4.9	1.7
HT-383-C8700357-8B	665	purple	289	3.0	1.2

Fiber samples were wound on small (10 mm) cardboard supports and placed in a Cu Ka X-ray beam and WAXS patterns obtained of the corresponding bundles. Samples for TEM study were prepared by the detachment replication procedure described in detail in Chapter II.

The critical point dried fiber was prepared by starting with PBZO fiber which had been spun and left in the wet state. The wet PBZO fiber was spun by H. Chuah (UDRI) and also provided by W. Wade Adams of WPAFB. The water in the samples was slowly exchanged with acetone by stepping through baths of 0%, 25%, 75%, and 100% acetone respectively for one hour in each bath. After complete exchange the fibers were soaked in acetone for 24 hours.

The acetone-swollen fiber was then placed in a Polaron E 3000 critical point drying apparatus which consists of a pressure vessel with a water jacket for temperature control. The chamber was sealed and slowly filled with liquid CO₂ at 25 C and 900 psi. After flushing with CO₂ for five minutes to remove residual acetone, the chamber was filled with CO₂ and held under pressure for one hour to fully impregnate the fiber. Then the temperature was slowly raised while the pressure was maintained. During this process the CO₂ slowly loses its meniscus as it passes over the triple point. At the elevated temperature the pressure (now 1200 psi) was

slowly released and the dried fiber finally removed from the apparatus. After critical point drying some of the fiber sample was exposed to an untensioned heat treatment of 600 C for 45 seconds under a nitrogen atmosphere.

C. Results

1. WAXS and SAED Scattering

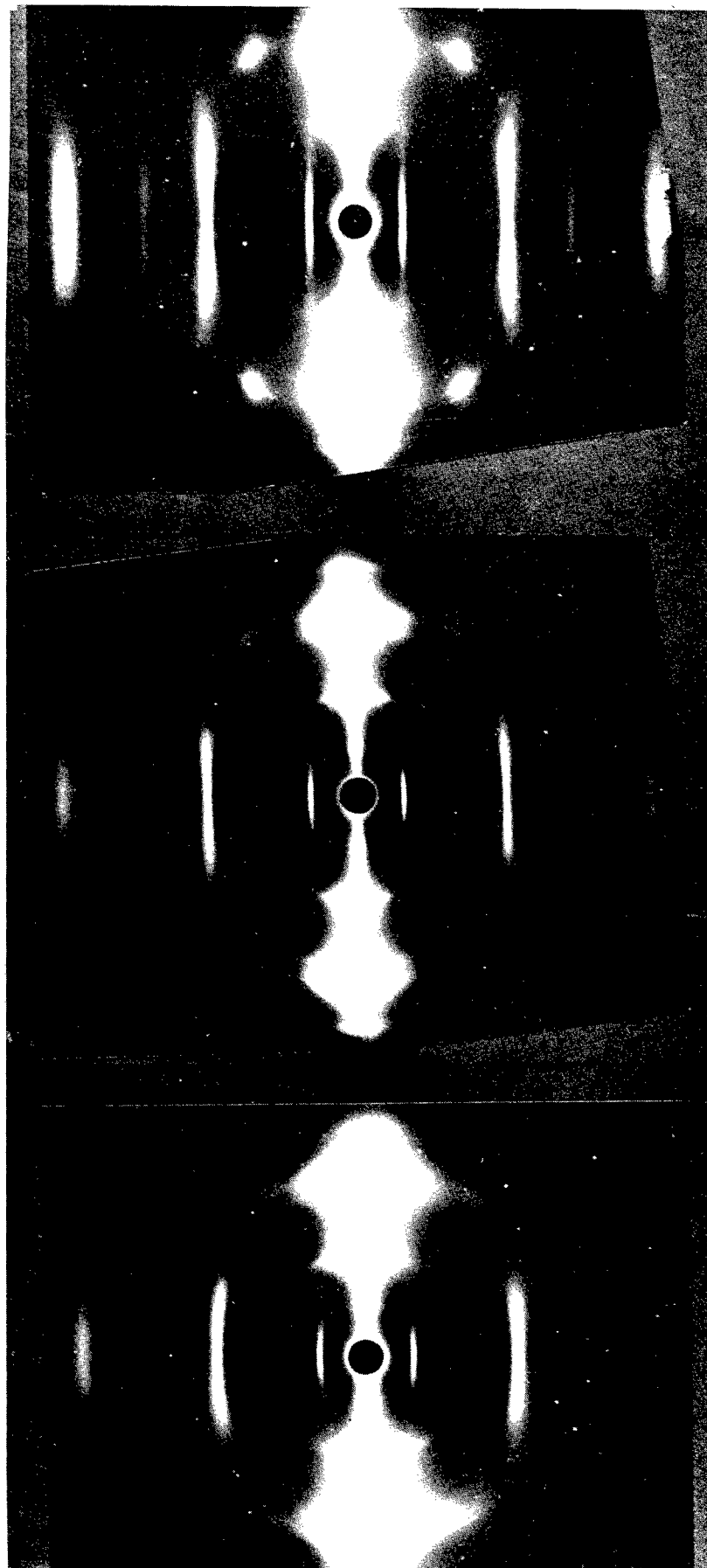
Figure 4.1 shows WAXS patterns of fiber bundles of PBZO as a function of heat treatment. A striking feature of the WAXS patterns is the strong off-meridion reflection on the second order layer line which becomes more intense and localized with increasing heat treatment. This reflection is indicative of 3-D crystallinity in the heat treated PBZO material. This reflection was also observed in the studies by Adams et al. (1986) and Krause et al. (1988).

It can also be noted from Figure 4.1 that the PBZO WAXS patterns do NOT exhibit strong scattering on the meridian on the second order layer line. Furthermore, the scattering on the first layer line is much broader in the lateral direction than the strong reflection on the second order layer line.

Figure 4.2 shows plots of the WAXS data obtained by scanning the negatives with a Optronics P-1000

Figure 4.1: WAXS of PBZO fiber bundles as a function of heat treatment. The patterns exhibit strong equatorial reflections indicative of good lateral packing, and layer lines indicative of high molecular orientation and a certain degree of disorder between molecules. A striking feature is a sharp off-meridional reflection on the second layer line which becomes more prominent after heat treatment. This reflection indicates the development of three-dimensional crystalline ordering.

PBZO Wide Angle X-ray Scattering

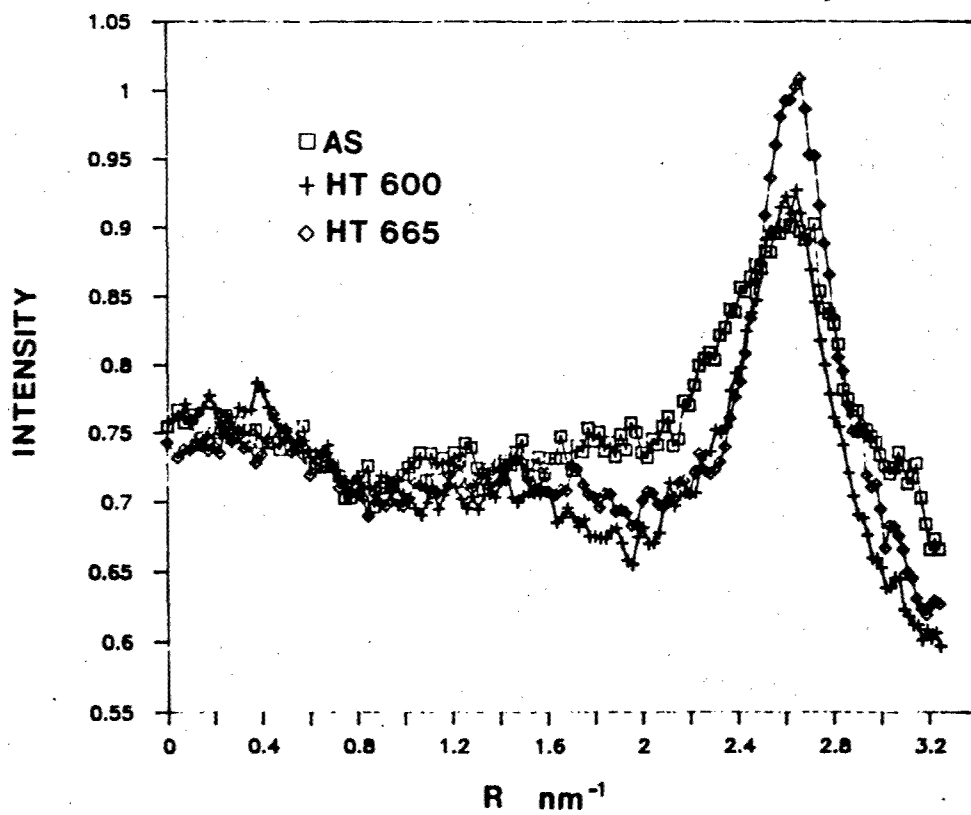
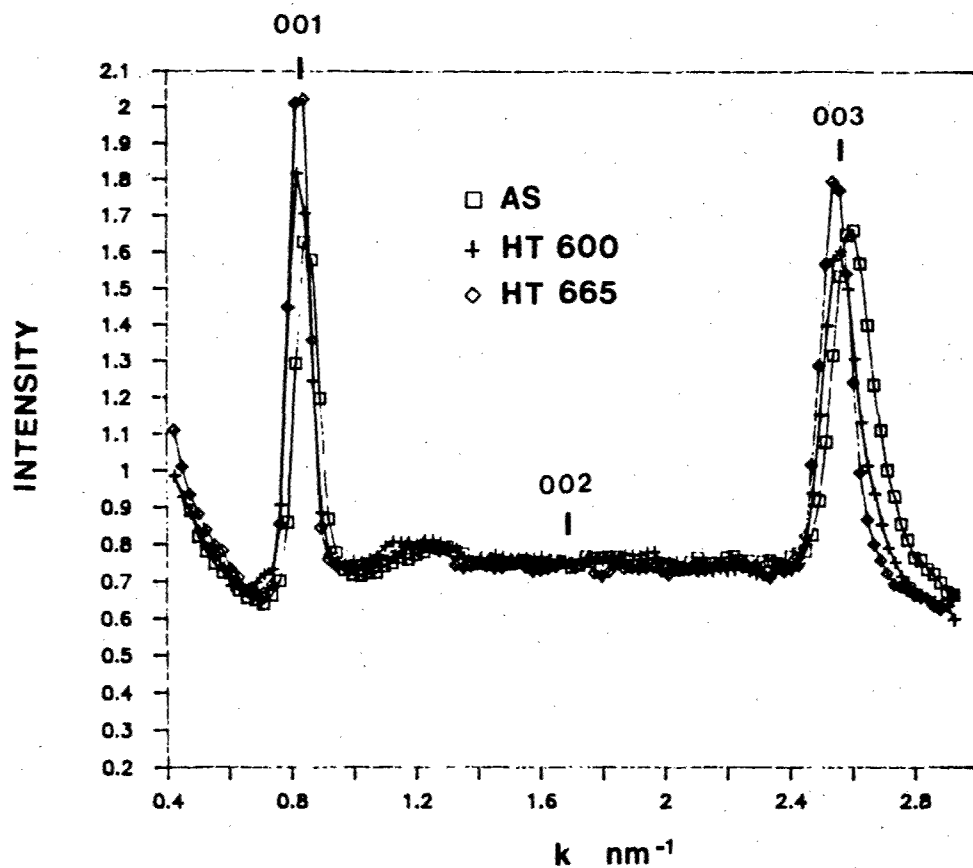


As Spun

HT 600 C

HT 665 C

Figure 4.2: Densitometer scans of the WAXS data presented in Figure 4.1. a) Meridional scan showing the average WAXS intensity in a rectangular window of width 0.8 nm^{-1} oriented along the fiber axis, plotted as a function of magnitude of the scattering vector k . b) Scan of the second order layer line, again using a rectangular window of width 0.8 nm^{-1} centered about the layer line, plotted as a function of the cylindrical reciprocal lattice coordinate R .



microdensitometer. The data were obtained by averaging the intensity within a rectangular window of width 0.8 nm^{-1} oriented along both the meridian and the second order layer line. Figure 4.2a shows scans along the meridian plotted as a function of scattering vector k . Figure 4.2b shows scans along the second layer line, plotted as a function of R , the cylindrical coordinate of the reciprocal lattice corresponding to the projection of the scattering vector k on the equatorial plane. Note in Figure 4.2a the strong peaks corresponding to the (001) and (003) layer lines. During heat treatment the peaks narrow and move in slightly. This is indicative of an increase in the crystalline ordering along the chain and a small increase in the c dimension. Also note that any scattering at (002) is very weak (in fact absent to within the background level). In Figure 4.2b the increase in intensity and localization of the strong peak at a position R of 2.6 nm^{-1} with heat treatment is evident.

Figure 4.3 shows schematic drawings of SAED patterns of thin sections of PBZO. As in the study by Krause et al. (1988), it was found that during SAED observation of PBZO fiber fragments the relative intensity of the first and second equatorial reflections was not constant, indicating again that orientation texturing was present. While studying different regions of PBZO fiber fragments by SAED it was noted that the strong off-axis reflections on the second order layer line and the first and fourth equatorial

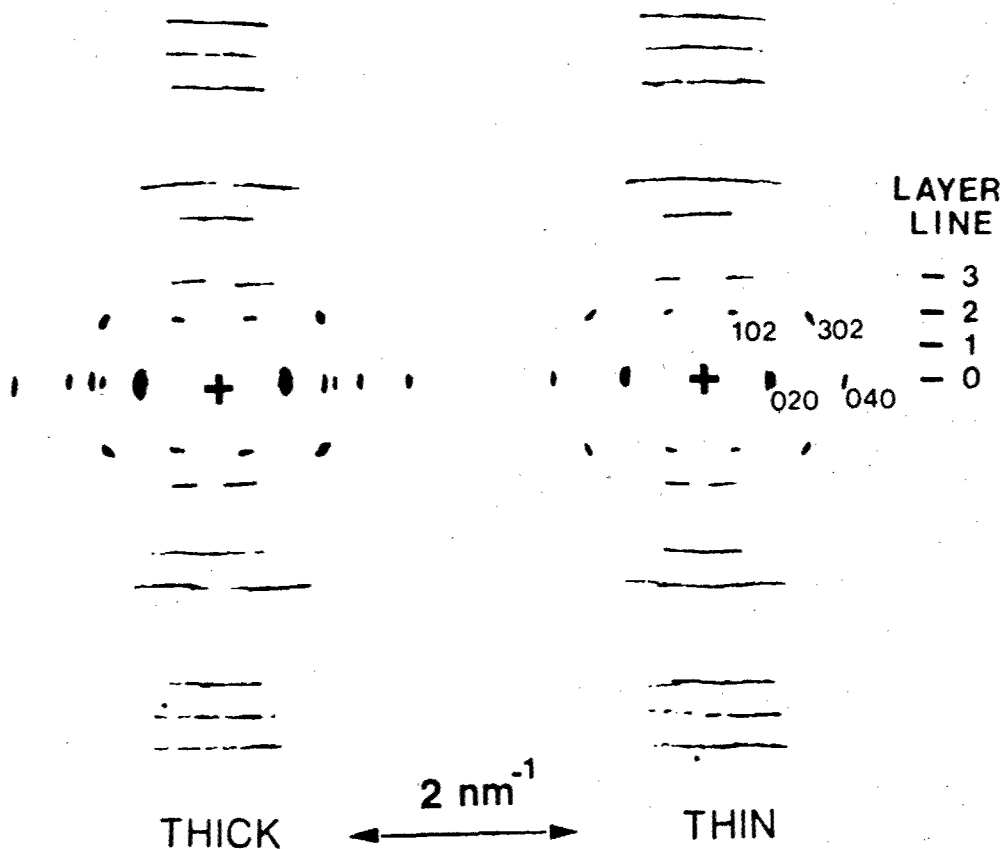


Figure 4.3: SAED patterns of PBZO from thick (a) and thin (b) fiber fragments. In some very thin sections it was possible to observe only the (200) and (400) equatorial reflections corresponding to "single crystal" texturing about the [010] zone axis. It was observed that whenever the (200) and (400) were visible, the localized reflections on the second layer line were also seen. This means it is possible to unambiguously index these reflections as (102) and (302), respectively. The (302) reflection corresponds to that seen in the WAXS patterns (Figure 4.1)

reflections, corresponding to first and second orders of the 0.55 nm "side-to-side" spacing, were always visible at the same time. Furthermore, it was possible to locate extremely thin sections of PBZO fiber fragments in which the texturing was so strong that the first and fourth equatorial reflections were present, but the second and third reflections were completely missing. Figure 4.3 shows schematics of SAED patterns from thick and thin sections of PBZO. In thick sections all of the equatorial reflections are visible and the SAED patterns correspond to the WAXS data presented in Figure 4.1. However, in the thinnest sections only the (h00) set of reflections were seen on the equator. Since the (001) direction is in the fiber direction, this indicates "single crystal" texturing in the thin regions about the [010] zone axis. Nevertheless, in these thin sections there remained localized scattering on the second layer line.

These observations prove that the off-axis reflections on the second order layer line are in the crystal zone containing the 0.55 nm "side-to-side" packing direction. This means that these reflections represent regular ordering between PBZO molecules in the a direction.

Further inspection of the PBZO SAED scattering pattern shows that the localized reflections on the second layer line correspond to intermediate positions of the strong equatorial

reflections. Specifically, the reflections on $l=2$ occur at positions corresponding to (102) and (302) when the first and fourth equatorial reflections are indexed as (200) and (400). This indexing scheme requires a non-primitive PBZO unit cell with two chains per lattice site. Although the (102) reflection could be seen in SAED, this reflection was not strong in the WAXS patterns.

The intense (302) reflections indicate that PBZO molecules laterally closed-packed at 0.55 nm have a tendency to align with relative axial shifts of $3/4 c$, the repeat distance along the chain axis. Since the PBZO molecules are rigid and highly oriented, an axial translation of $3/4 c$ is equivalent to an axial translation of $-1/4 c$.

With this assignment for the localized scattered intensity in mind, it is useful to reexamine the WAXS patterns in Figure 4.1. Notice that while the (302) reflection on the second layer line is strong, there is diffuse streaking on the first layer line. How could it be possible to have streaking on $l=1$ if there are distinct reflections on $l=2$?

Figure 4.4 shows several different models of axial registry between neighboring PBZO molecules. Figure 4.4a shows a model with the neighboring chain at a shift of $0 c$. Figure 4.4b shows the neighboring chain at a shift of $1/2 c$,

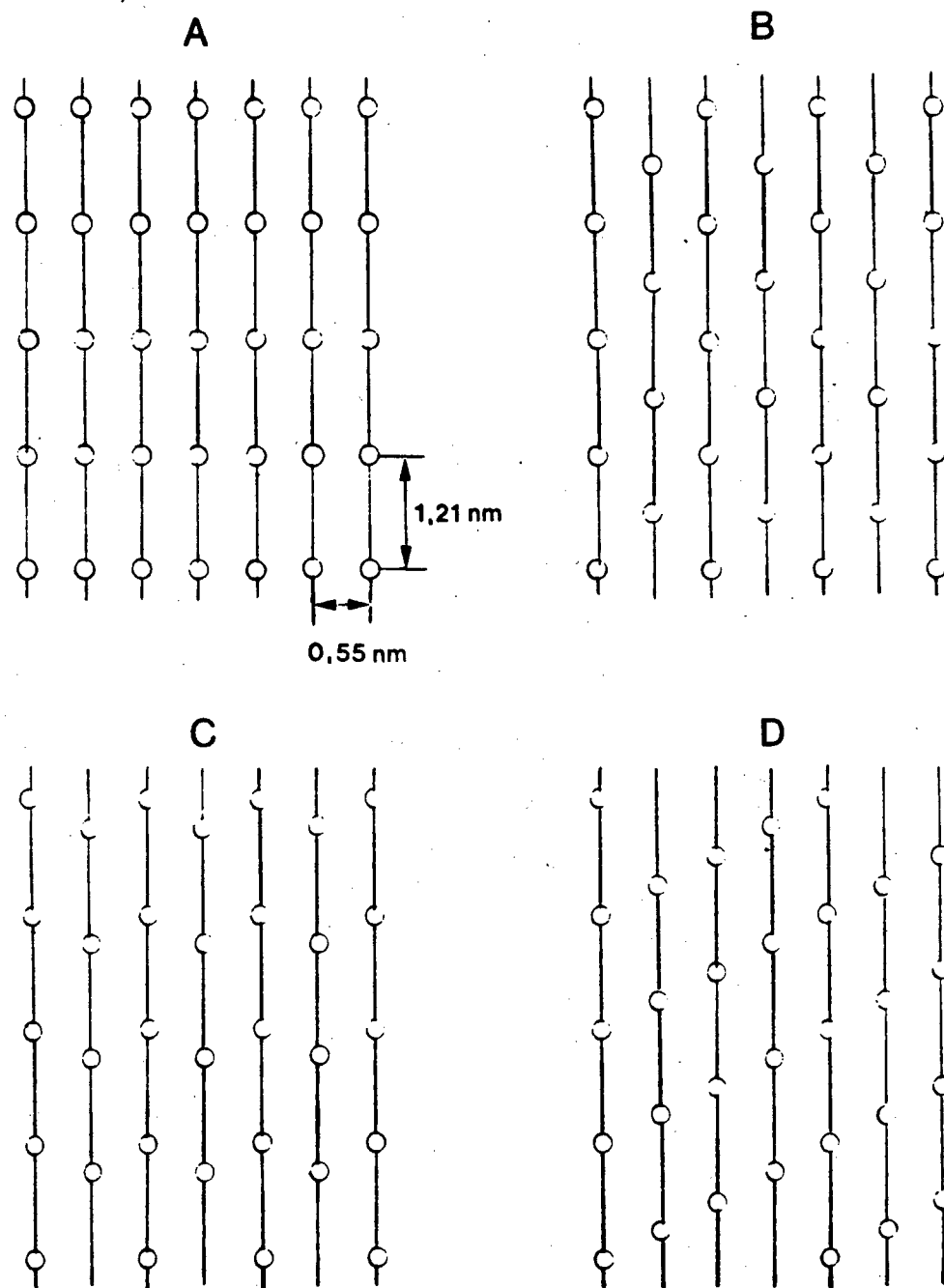


Figure 4.4: Models of different types of regular axial registry between PBZO molecules in the a direction. a) Axial shift of $0\ c$; b) Axial shift of $1/2\ c$; c) Axial shifts of $+1/4\ c$ and $-1/4\ c$; and d) Axial shift of $+1/4\ c$.

as proposed by Fratini and Adams. Figure 4.4c shows a strictly alternating model with axial shifts of $+1/4 c$ and $-1/4 c$. Figure 4.4d shows a model with a regular placement of $+1/4 c$.

Figure 4.5 shows the corresponding predictions of each of these models on the scattering behavior of PBZO. Note that only models C and D which have regular placement of $1/4 c$ between neighboring PBZO molecules correctly predict the experimentally observed scattering behavior on the second layer line with reflections at (102) and (302).

In WAXS patterns of PBZO, there is streaking on the first layer line, yet there are localized reflections on $l=2$. There are two plausible explanations for this observation. First, it may be that there is a strong tendency for $1/4 c$ registry to occur, but that there is a high probability for this registry to be either $+1/4 c$ or $-1/4 c$. This means that the actual structure would be comprised of domains of variable width of type C and type D. Such a structure is reasonable because of the low energy of axial shift misregistry (by analogy with PBZT, Chapter III). Such a regular type of disorder would induce streaking on odd layer lines but would retain localized scattering on the even ones. A schematic comparing the expected diffraction pattern from such a model and that experimentally observed is shown in Figure 4.6.

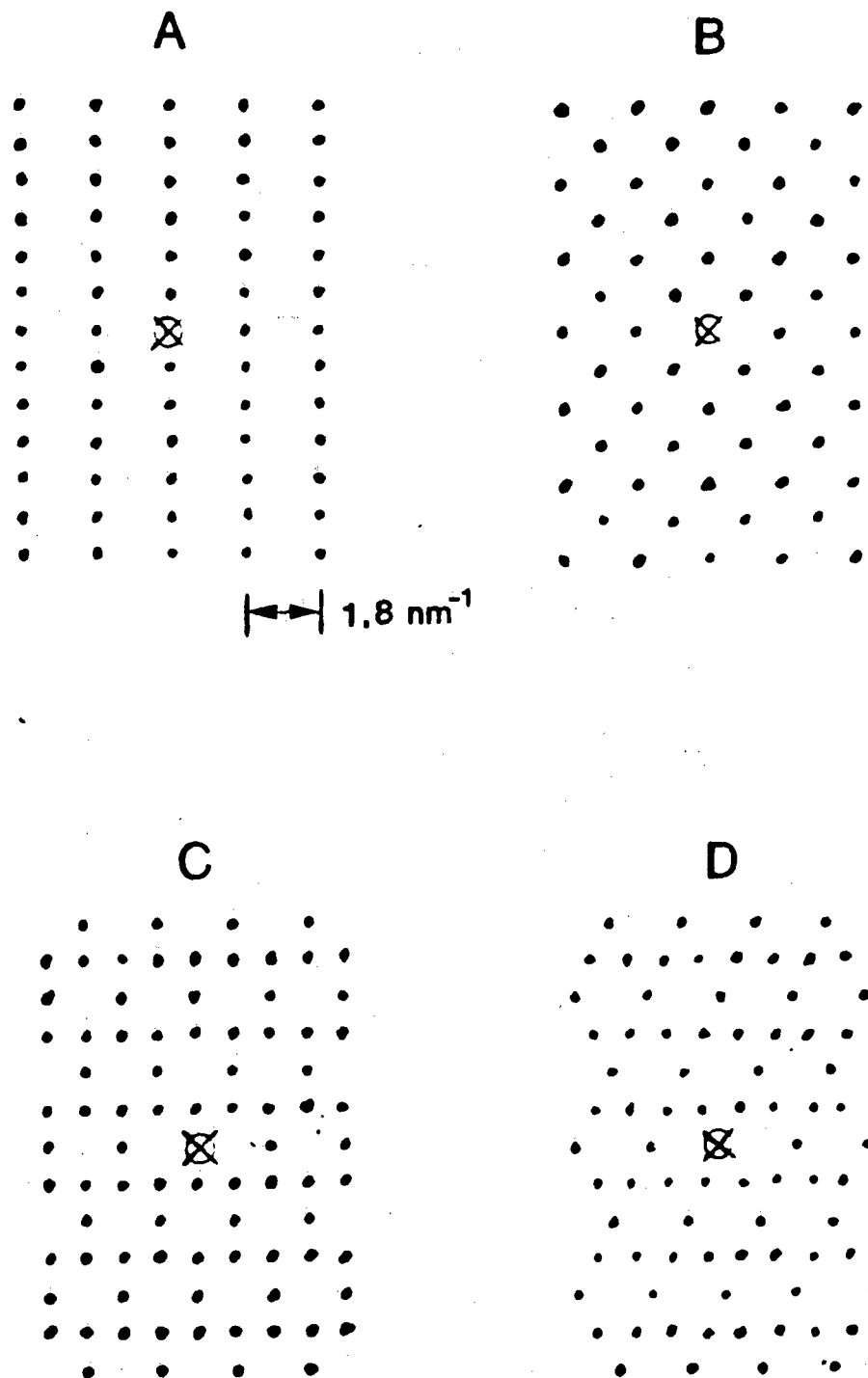
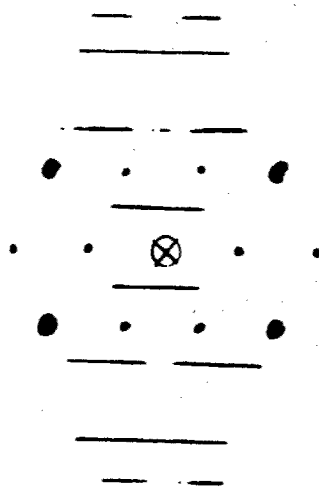
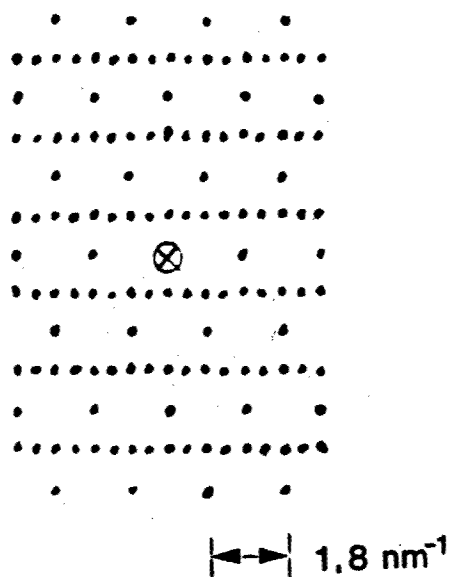


Figure 4.5: Reciprocal lattices corresponding to the axial shift models of Figure 4.4. a) Axial shift of 0 c ; b) Axial shift of $1/2 \text{ c}$, c) Axial shifts of $+1/4 \text{ c}$ and $-1/4 \text{ c}$; and d) Axial shift of $+1/4 \text{ c}$.

C + D



DATA

Figure 4.6: Combined pattern using both models C and D. The reflections are coincident on even layer lines, but interdigitated on odd layer lines. This suggests that a model having regular $+1/4 \text{ c}$ and $-1/4 \text{ c}$ shifts between neighboring molecules would exhibit localized reflections on $l=2$ but would show streaking on $l=1$.

Another possibility is that the streaking on the first layer line occurs because planes of PBZO chain which are highly axially ordered in the **a** direction are highly disordered between chains in adjacent planes in the **b** direction. It is possible to distinguish between these two models by examining the distribution of intensity on the first layer line in single crystal textured zones. If streaking persists on $l=1$ for single crystal textured regions in the [010] zone, then this confirms the model with regular $1/4$ **c** registry with the registry occurring randomly "up" and "down" along **c**. Unfortunately, the predominance of inelastic scattering makes analysis of the details of scattering at low scattering angles ($k=0.8 \text{ nm}^{-1}$ for $l=1$) difficult by conventional SAED. Future studies using energy-filtered SAED would be useful to resolve this question. WAXS requires the use of large samples so it is not possible to distinguish between **a** and **b** axis disorder in a uniaxially symmetric fiber. WAXS would be useful if it were possible to induce single crystal texturing in large fibers, perhaps by rolling deformation.

A convenient method to analyze interchain associations is to calculate the expected intensity of scattering on the meridian. The intensity of scattering on the meridian is related to the distribution of electron density on planes which are perpendicular to the fiber axis. For a highly

oriented, axially rigid molecule, internal rotations of chain segments about the chain axis do not change the distribution of electron density on planes which are perpendicular to the chain axis. Therefore such rotations will not change the intensity of diffraction exactly on the meridian. However, the scattering intensity on the meridian IS sensitive to regular interchain correlations.

Table 4.2 shows the experimentally obtained intensity of meridional WAXS scattering in PBZO obtained on a diffractometer (Adams, et al., 1986). To compare this data with calculations of molecular structure factors, it is necessary to correct for the Polarization factor $P=1/2(1+\cos^2 2\theta)$ and Lorentz factor $L = 1/\sin \theta \cos \theta$, where θ is the Bragg scattering angle (Alexander, 1969). The suitably corrected values are also listed in Table 4.2.

Compared with this experimental data is the calculated intensity of the molecular transform on the meridian for PBZO. Three models were considered in this calculation. First, the form factor of a single PBZO molecule; second, the form factor of a dimer with the second chain at a shift of $1/4 c$, and third, the form factor of a dimer with the second chain at $1/2 c$. A proportionality factor was used to find the best fit (using an R-factor type error criterion) between the experimentally obtained WAXS intensity data (given in relative units) and the model calculation.

Table 4.2

Scattering Intensity Predictions on the Meridion
for PBZO using Molecular Transform

Index	WAXS Expt.	WAXS Corr.	One Molecule	Two 1/4c Molecules	Two 1/2c Molecules
(00 0)	>100				
(00 1)	30	2.1	3.2	2.9	0.3
(00 2)	5	0.7	28.0	0.2	65.1
(00 3)	28	5.6	0.9	4.2	1.4
(00 4)	17	4.8	0.2	0.9	0.8
(00 5)	100	37.9	95.7	80.2	2.0
(00 6)	25	12.1	107.3	1.6	231.0
(00 7)	9	5.3	6.1	6.6	1.5
(00 8)	7	5.0	1.7	0.5	0.5
(00 9)	37	31.6	25.4	30.8	0.9
(00 10)	42	40.1	42.1	1.1	74.7
(00 11)	41	40.9	35.4	40.5	0.5

Figure 4.7 compares the experimentally obtained and calculated scattering intensity on the meridian for PBZO. Note that the dimer model with a $1/4\ c$ axial translation fits the data best for layer lines 7 and lower, whereas the single molecule transform fits the data best at higher scattering angles (layer lines 7 and higher). The model with a dimer having a relative shift of $1/2\ c$ did not fit the data well at all.

Figure 4.8 shows the intensity of the molecular transform on layer lines 1 and 2 for a single PBZO chain and for a PBZO dimer with a relative axial shift of $1/4\ c$. The experimentally obtained WAXS scattering on layer line 2 was shown previously in Figure 4.2b. As noted in the earlier calculation, a single PBZO molecule is predicted to have strong scattering at the meridian on the second layer line. Experimentally, there is little or no scattering at the meridian on the second layer line (Figure 4.2b). It follows that the experimentally observed lack of scattering on the meridian at $l=2$ is due to regular interchain axial registry. The molecular transform of a dimer with a relative axial shift of $1/4\ c$ has only weak scattering on the meridian at $l=2$ (Figure 4.7b).

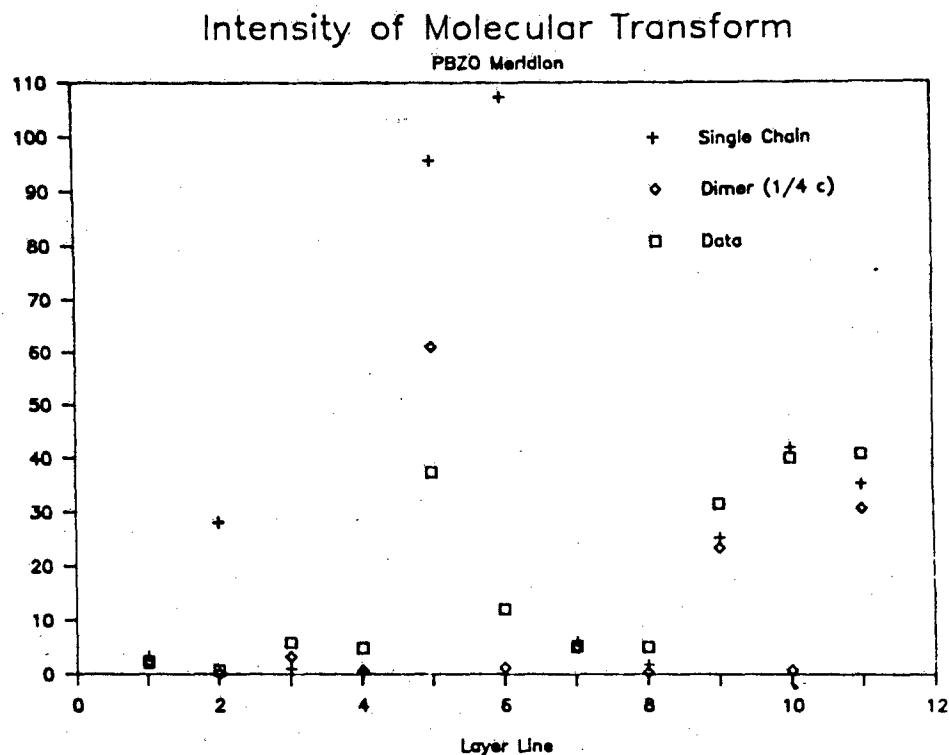


Figure 4.7: Comparison of model calculations of meridional scattering intensity for PBZO and that obtained experimentally by WAXS. At lower scattering angles (layer lines 1-7) the data is fit best by the molecular transform of a dimer with a regular axial shift of $1/4$ c. At higher angles (layer lines 7 and above) the data is fit best by the molecular transform of a single PBZO molecule.

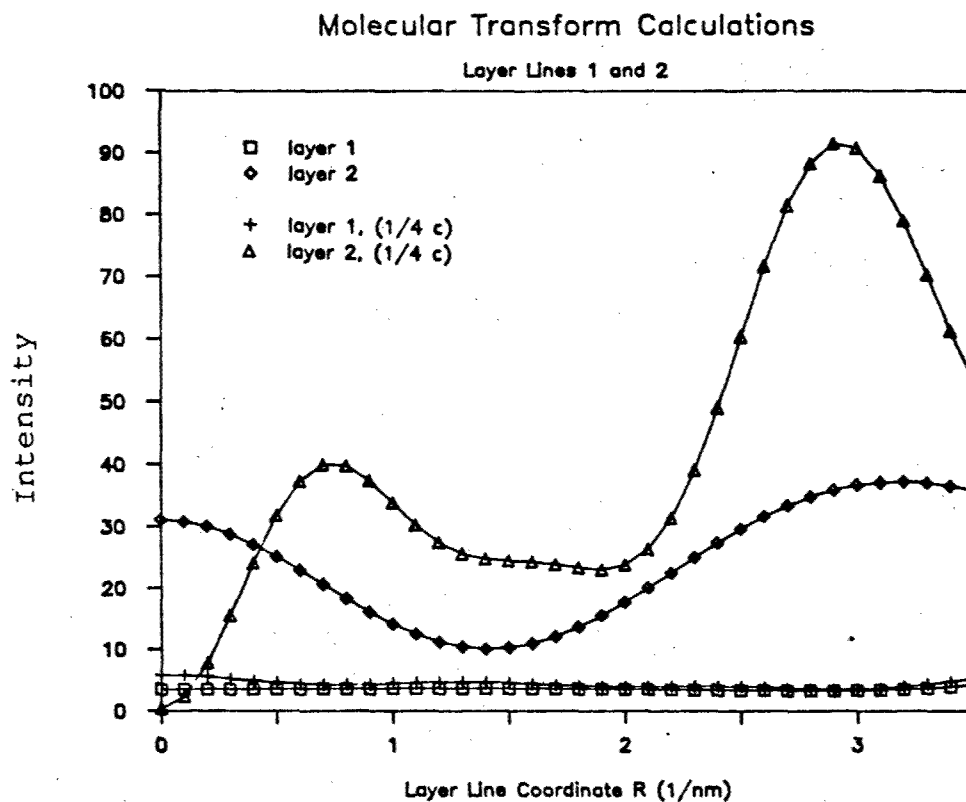


Figure 4.8: Molecular transforms of a single PBZO chain and a PBZO dimer with a relative axial shift of $1/4 c$ on layer lines 1 and 2. In the molecular transform of the single PBZO chain there is a peak of intensity on the meridian on $l=2$ which is not observed experimentally (Figure 4.2b). In the molecular transform of the PBZO dimer there is weak scattering near the meridian as well as a peak at $R=2.6 \text{ nm}^{-1}$, as seen experimentally in WAXS (Figure 4.2b).

From these calculations we can conclude that it is not possible to explain the experimental lack of scattering on the second layer line from the molecular transform. This lack of scattering on $l=2$ is apparently arising from regular interchain axial registry at a position of $1/4 c$.

It is possible to investigate the structure of PBZO fiber by examining the intensity of reflections determined from different PBZO unit cells using the Multislice formalism (Chapter II). Table 4.3 shows the intensity of (hkl) reflections on the meridian and on the second order layer line for different choices of the PBZO unit cell. The unit cells used in Table 4.3 correspond to those shown earlier in Figure 4.4.

Note that the best fit to the meridional intensity at low angles occurs for model C ($1/4$ up, $1/4$ down), whereas the best fit for higher scattering angles is from model A (no axial shift). Model D shows more absences on the meridian than is experimentally observed. The intensity on the second layer line is fit best with model C, but model D also shows the right absences.

Summarizing our results, we find that it is not possible to explain the scattering behavior of PBZO at low scattering angles (less than 6 nm^{-1}) from the molecular transform of a single PBZO molecule. Because of the extended chain,

Table 4.3

Scattering Intensity Predictions

for PBZO using Multislice Program

and Different Choices for the PBZO Unit Cell (Figure 4.4)

Meridion

Unit Cell:	A	B	C	D	WAXS
(00 0)	92.86	92.86	92.86	92.86	>100
(00 1)	0.10	x	0.05	x	30
(00 2)	1.51	1.51	x	x	5
(00 3)	0.22	x	0.11	x	28
(00 4)	0.09	0.09	0.09	0.09	17
(00 5)	2.34	x	1.17	x	100
(00 6)	2.04	2.04	x	x	25
(00 7)	0.01	x	0.00	x	9
(00 8)	0.03	0.03	0.03	0.03	7
(00 9)	0.83	x	0.42	x	37
(00 10)	0.74	0.74	x	x	42
(00 11)	0.98	x	0.49	x	41
(00 12)	0.00	0.00	0.00	0.00	

Second Layer Line

Unit Cell:	A	B	C	D	WAXS, SAED
(002)	1.51	1.51	x	x	x
(102)	x	x	0.43	0.28	weak
(-102)	x	x	0.38	0.36	weak
(202)	0.24	0.24	x	x	x
(-202)	0.32	0.32	x	x	x
(302)	x	x	1.42	0.40	strng
(-302)	x	x	1.32	0.67	strng
(402)	1.14	1.14	x	x	x
(-402)	1.11	1.11	x	x	x
(502)	x	x	0.47	0.44	
(-502)	x	x	0.37	0.70	

colinear structure of PBZO, the scattering intensity along the meridian should be insensitive to rotations of the phenyl or heterocyclic group about the chain axis. Therefore, it appears necessary to explain the scattering intensity observed in terms of regular axial associations between PBZO molecules.

We find that the molecular transform of a "dimer" consisting of two PBZO molecules at a relative axial translation of $1/4 c$ explains well the scattering intensity along the meridian at scattering vectors of less than 6 nm^{-1} . For higher angles the data fit better to the molecular transform of a single PBZO molecule.

These conclusions are supported by Multislice calculations using different choices for the PBZO unit cell. Along the meridian, the scattering at low angles is fit best by unit cell C involving both $+1/4 c$ and $-1/4 c$ axial translations between neighboring molecules. Above 6 nm^{-1} (layer line 7), the experimental data is fit best with a unit cell having no axial shift (and therefore no systematic absences along the meridian, as in the molecular transform).

The molecular structure of PBZO consistent with our scattering data is one based on unit cell C with regular axial shifts of both $+1/4 c$ and $-1/4 c$ between neighboring PBZO molecules in the a direction. The projection of this

unit cell in the b-direction showing the relative axial shifts of $+1/4 c$ and $-1/4 c$ was presented earlier (Figure 2.4). As is apparent from Figure 2.4, the $1/4 c$ placement allows the pendant hydrogens in the middle of the heterocyclic group to fit into gaps created by five-membered rings on the heterocyclic groups of neighboring PBZO molecules.

Unit cell C corresponds to the monoclinic space group Pc (No. 7). It contains a symmetry element consisting of a glide plane oriented perpendicular to c with a glide vector of $a/2$. The unit cell parameters are $a=1.196$ nm, $b=0.3540$ nm, $c=1.205$ nm, $\gamma=101.2$ degrees with two repeat units per cell. The calculated density is 1.66 gms/cm³.

From this analysis we can state that a model involving regular axial shifts of $1/4 c$ between PBZO molecules close packed "edge-to-edge" in the a direction is consistent with our WAXS and SAED data. The streaking which can be seen on upper order layer lines and the fit of the meridional scattering to the molecular transform at high scattering angle is evidence that there is still a substantial amount of axial shift disorder in PBZO. One possibility presented here is that there is regular placement of neighboring PBZO molecules at $1/4 c$ but there is disorder in terms of whether the placement will be at $+1/4 c$ or at $-1/4 c$. The precise characterization of this shift disorder will benefit from

higer resolution HREM images than obtained in this study (imaging the 0.32 nm (302) spacing would be most revealing), as well as more thorough comparison of model to better scattering data from quantitative scans of PBZO layer lines with an X-Ray diffractometer.

2. HREM

The total end point dose (TEPD) J_e of PBZO for 200 kV electrons was determined to be 0.8 C/cm^2 from the fading of the (200) reflection in the SAED pattern. This compares with the critical dose J_c of 0.2 C/cm^2 determined by Adams et al. (1989). During irradiation, the intensity and sharpness of the (001) meriodional reflections persisted even after the loss of sharp crystalline reflections on the equator, with the TEPD of the (003) reflection determined to be approximately 1.6 C/cm^2 . This indicates that the damage mechanism involves the disruption of packing between molecules rather than the scission and reorientation of bonds along the fiber axis. This behavior is similar to that seen in PBZT and other oriented polymers and is consistent with the weak secondary forces between molecules and the strong covalent bonds along the polymer backbone.

It was possible to obtain HREM images of the 0.55 nm (200) and 0.34 nm (010) lattice spacings in fibers of PBZO with various amounts of heat treatment.

Figure 4.9 is an HREM image of a detached fragment of a PBZO as-spun fiber. The crystallites are small but all are highly oriented with respect to one another. The optical transform of the image is inset. Careful inspection shows that there are regions in the image which have low contrast intensity fluctuations which are axially oriented, corresponding to weak lateral ordering between molecules on a very local scale.

Figure 4.10 is an image of a PBZO HT 600 fiber. Again, the crystallites are all highly oriented. However, in the heat treated fiber the crystallites have a distinctly larger mean size. In some HREM images of heat treated PBZO it was possible to find areas which were dominated by (200) fringes, with little or no evidence for (010) fringes. This suggests that these were regions exhibiting "single crystal" orientation texturing like that seen in SAED. Figure 4.11 is an image of such a domain.

In PBZO HT 665 domains which were rather large in the lateral direction were sometimes seen. One such domain is shown in Figure 4.12. These results support the DF studies of Adams et al. (1986) and Krause (1988) which showed a tendency for PBZO crystals to grow more in the lateral than axial direction.

Figure 4.9: HREM image of As-Spun PBZO. The crystallites are small and compact, but are all highly oriented. The optical transform is inset showing both the 0.55 nm (200) and 0.34 nm (010) spacings. A slight indication for the 1.1 nm (001) layer line is also seen.

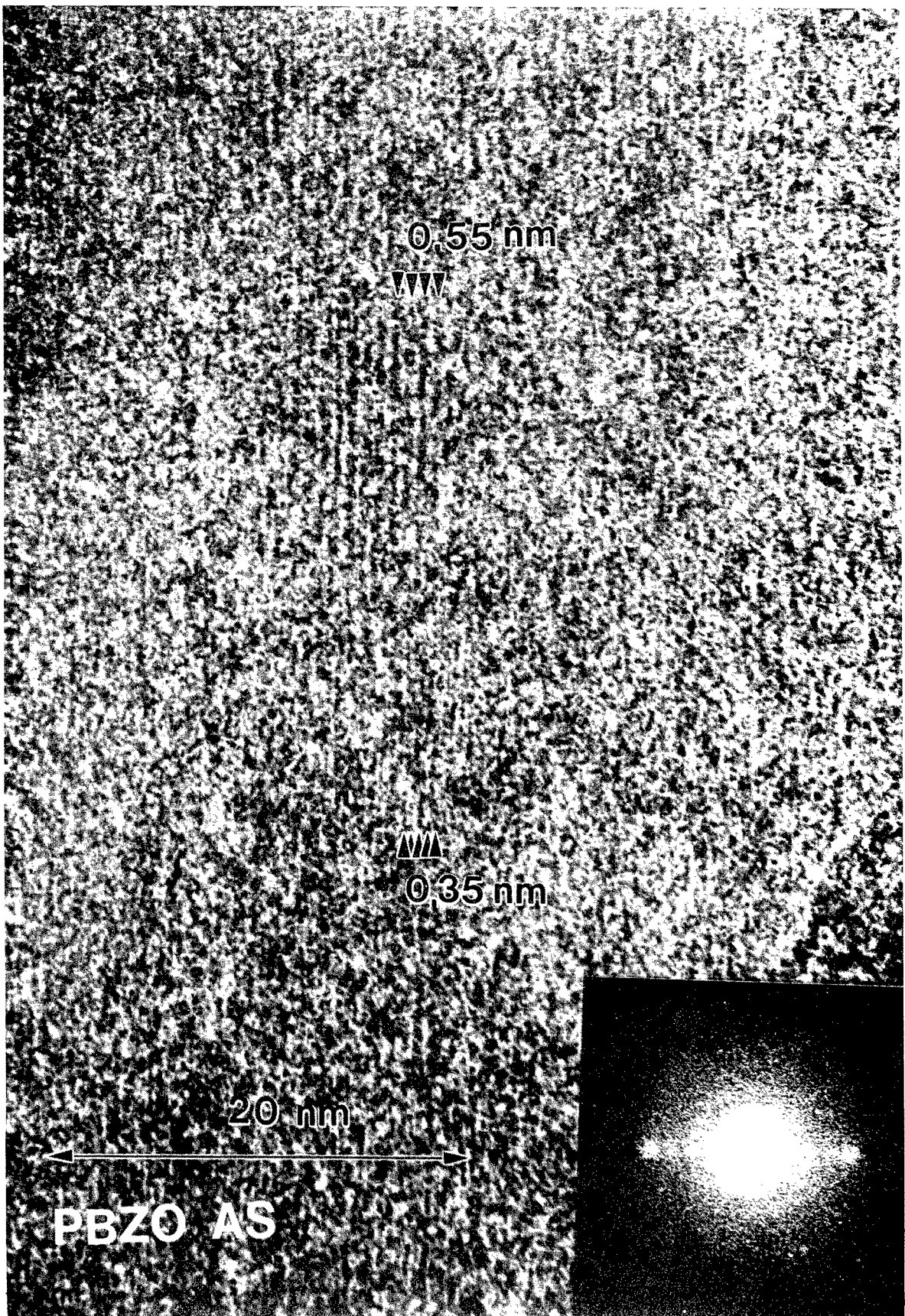
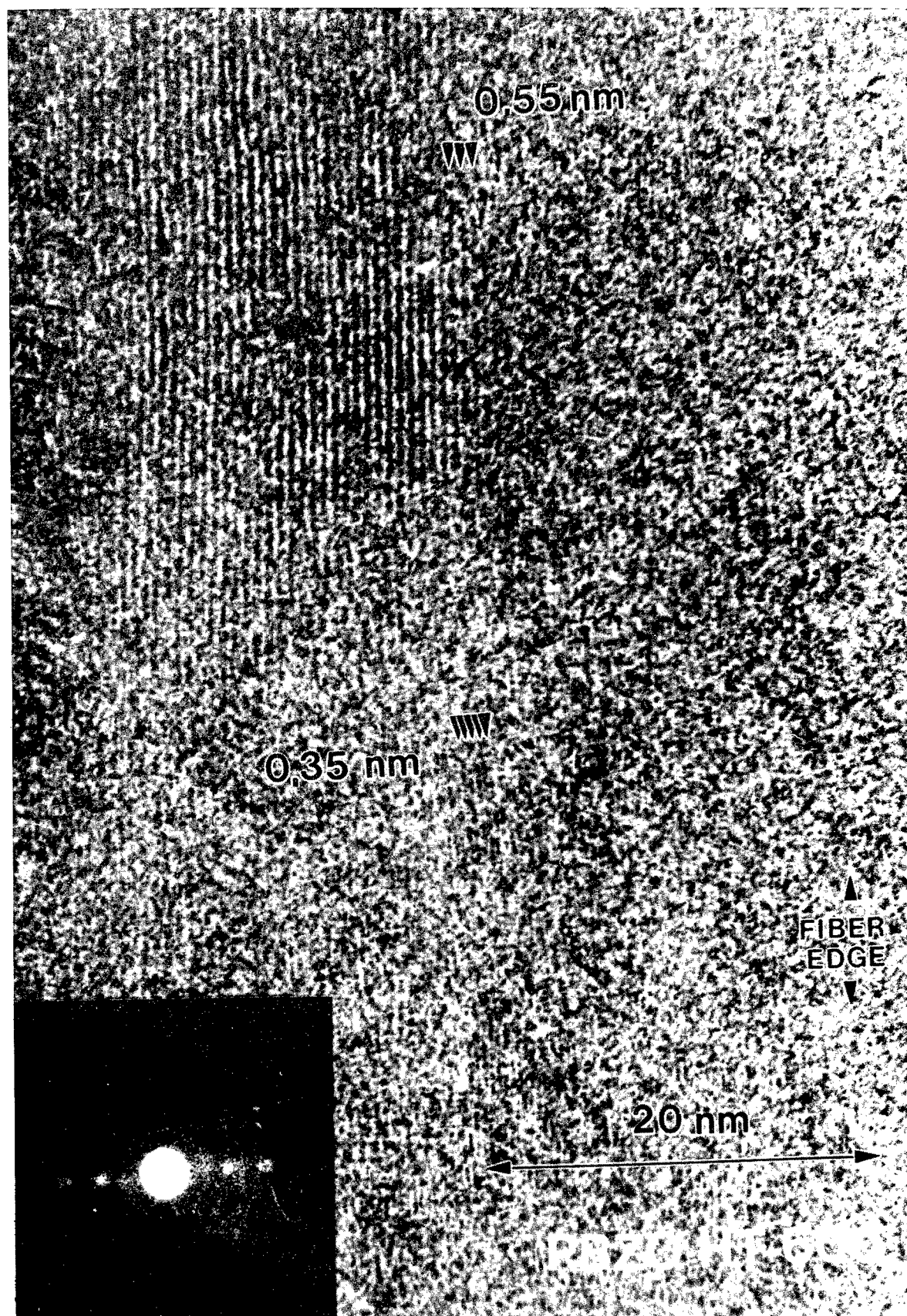


Figure 4.10: HREM image of PBZO HT 600. As for the As-Spun fiber, the crystallites are all highly oriented. However, in this heat-treated sample the crystallites are of a larger mean diameter. The optical diffraction pattern is inset.



71

Figure 4.11: HREM image of a PBZO HT 600 fiber fragment showing a region with a high population of (200) fringes, supporting SAED data which showed "single crystal" orientation texturing in thin sections. The optical diffraction pattern shows only the (200) reflections.

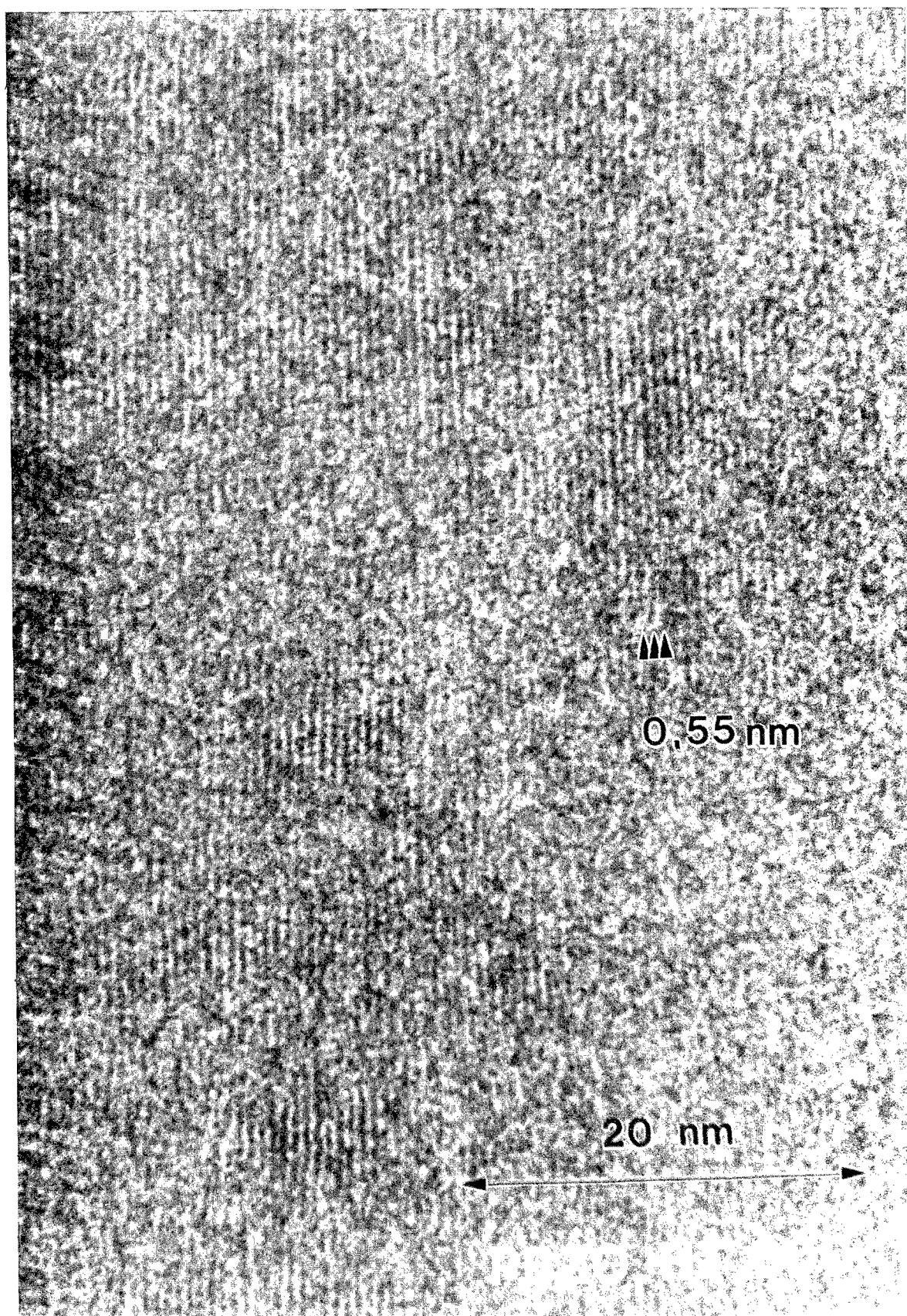
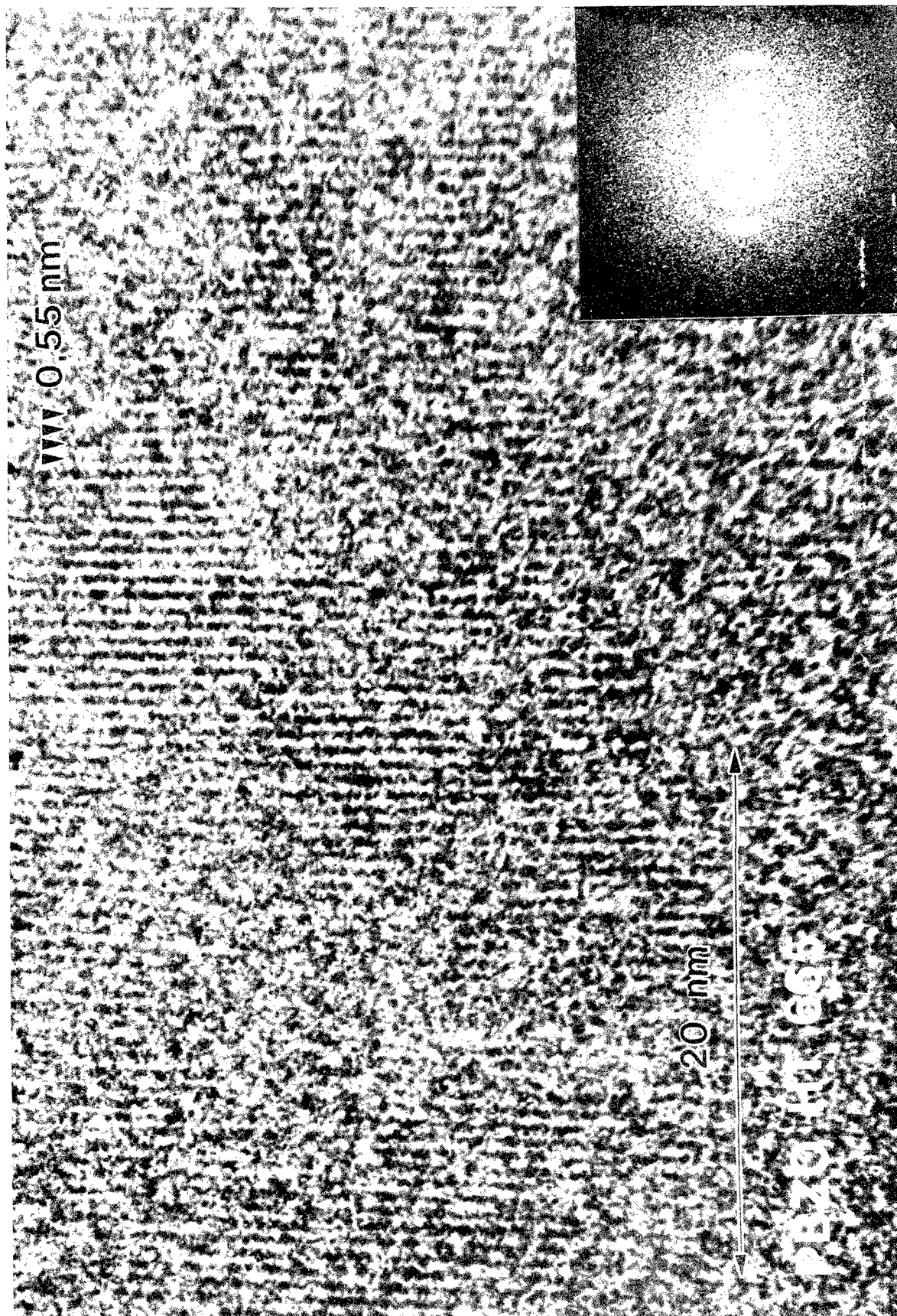


Figure 4.12: HREM image of PBZO HT 665 showing a domain which has grown quite large in the lateral direction. The optical diffraction pattern is inset.

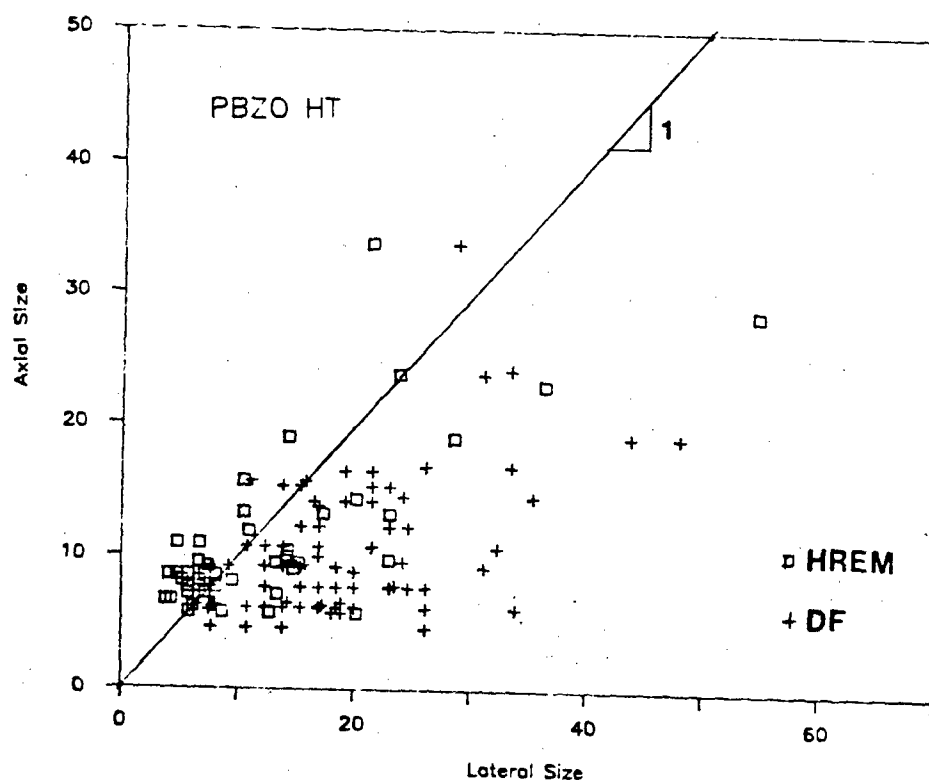
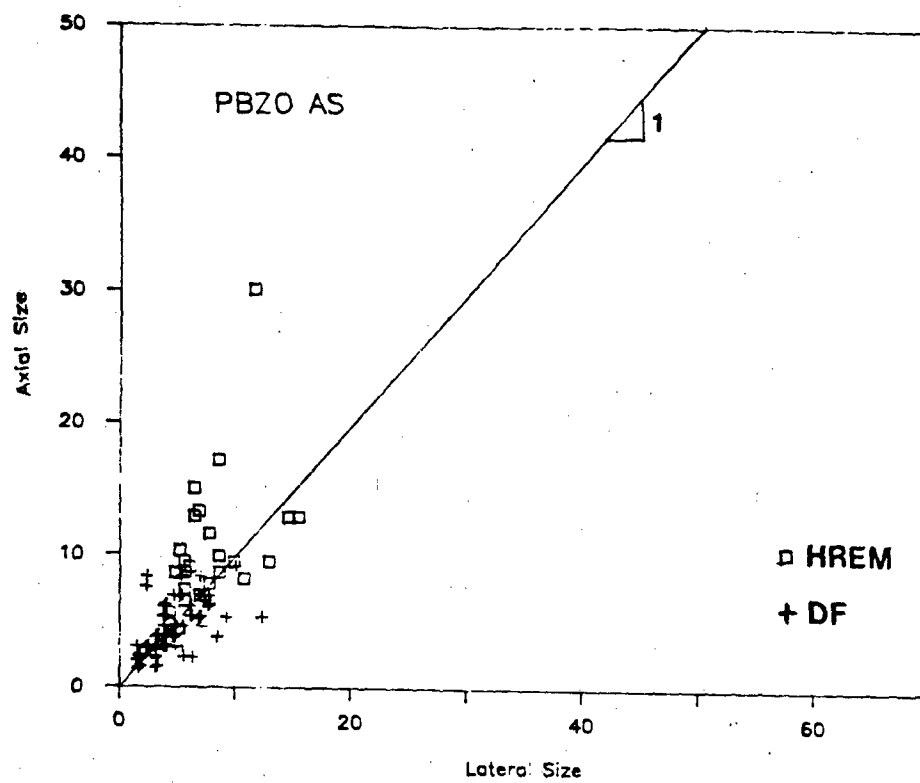


From the HREM images it was possible to characterize the local orientation distribution of the PBZO molecular axis as a function of heat treatment. The results of such measurements were presented in previous chapter (Table 3.1). It can be seen that like PBZT, PBZO is highly oriented on a local scale. However, measurable deviations do exist; there is a standard deviation of about 1.3 degrees of misorientation in all of the PBZO fibers studied. The amount of misorientation measured by HREM does not change significantly with heat treatment. The Hermanns-Stein orientation function is over 0.999 for all of the fiber samples. The orientation frequency distributions for the PBZO samples were previously presented and compared with PBZT in Figure 3.5. The orientation distributions are all indicative of uniform, uniaxial orientation.

In order to analyze the crystallite sizes, shapes, and orientations from these images, several enlargements were made of each sample and the boundaries of the fringe domains were determined by eye. The domains of fringes thus determined were relatively compact and limited in extent. No systematic "rhombohedral" or other unique shapes were seen. The maximum sizes of the domains determined in this way were measured in both the axial and lateral directions.

Figure 4.13 shows a plot of the crystal sizes in a) as-spun PBZO fiber, and b) heat-treated PBZO fiber as determined

Figure 4.13: a) Crystallite size and shape distribution in as spun PBZO as determined by HREM. Results from DF measurements from this study and from the study of Adams et al. (1986) are also shown. b) Crystallite size and shape distribution in heat treated PBZO as determined by HREM. Results from DF measurements from this study and from the study of Adams et al. (1986) are also shown.



by both HREM and DF. The DF data shown was collected both in this study and in the study by Adams et al. (1986). The HREM and DF data are in general agreement, although some of the DF measurements indicate smaller crystallites than those observed by HREM. This may be due to statistical fluctuation problems inherent in DF imaging (Roche and Thomas, 1980), as well as a difficulty in establishing the boundaries of small crystals on HREM image enlargements.

From these plots it is possible to measure the average lateral and axial crystallite size as a function of heat treatment. These results are shown in Table 4.4. As suggested from Figure 4.13, the crystals grow both in the lateral and axial directions, although growth in the lateral direction is more extensive since the lateral dimensions are larger for the same heat treatment. It is interesting to note that the average crystallite size determined for as-spun PBZO from HREM imaging (7.8-10.2 nm) is somewhat larger than that determined using DF images by Adams et al. (1986) and Krause et al. (5.2-5.4 nm). This discrepancy may reflect the fact that it is not possible to distinguish what are truly crystallites and what are statistical intensity fluctuations in DF imaging. It might also indicate the fact that it is difficult to resolve small fringe patterns on low dose HREM images.

Table 4.4

Crystallite Sizes (in nm)
as Determined From HREM Images

Fiber	Nobs	Axial Direction				Lateral Direction			
		min	max	avg	sd	min	max	avg	sd
PBZT HT	46	6.2	40.5	17.2	8.0	4.3	22.4	10.4	4.0
PBZO AS	30	4.3	15.4	10.2	5.0	4.3	10.2	7.8	3.0
PBZO HT 600	35	3.8	21.4	10.2	5.4	6.2	33.8	10.9	7.2
PBZO HT 665	10	7.2	28.6	14.2	7.4	7.2	54.8	19.4	13.3

It is also possible to measure an effective crystallite size from the broadening of spots in the optical transforms of the HREM images. As in a normal diffraction experiment, the average size of the crystallites is proportional to $D=1/k_d$, where k_d is the full width at half maximum of the optical diffraction spot. The area selected with the laser beam for these measurements corresponded to a region of approximately 150 nm in diameter. The results obtained are summarized in Table 4.5. Note that the effective size of the crystallites determined by this method does not increase substantially with heat treatment. Also, the calculated crystallite sizes are significantly lower than that actually observed in the images. This shows that the crystallites have an amount of internal disorder which causes their optical diffraction spots to broaden.

Evident in some of the optical transforms of HREM images of PBZO was diffuse scattering on the 1.2 nm (001) first layer line. This confirms that as in PBZT, there is a significant amount of axial disorder between neighboring molecules. Unfortunately, it has not yet been possible to obtain high quality images of the axial shift disorder in PBZO like those obtained for PBZT in Chapter III.

The true power of HREM imaging is in providing information about defect structures at a local level. In an HREM image of PBZO HT 600 a large crystallite exhibited one more

Table 4.6 5

Crystallite Sizes from
Optical Diffraction Patterns

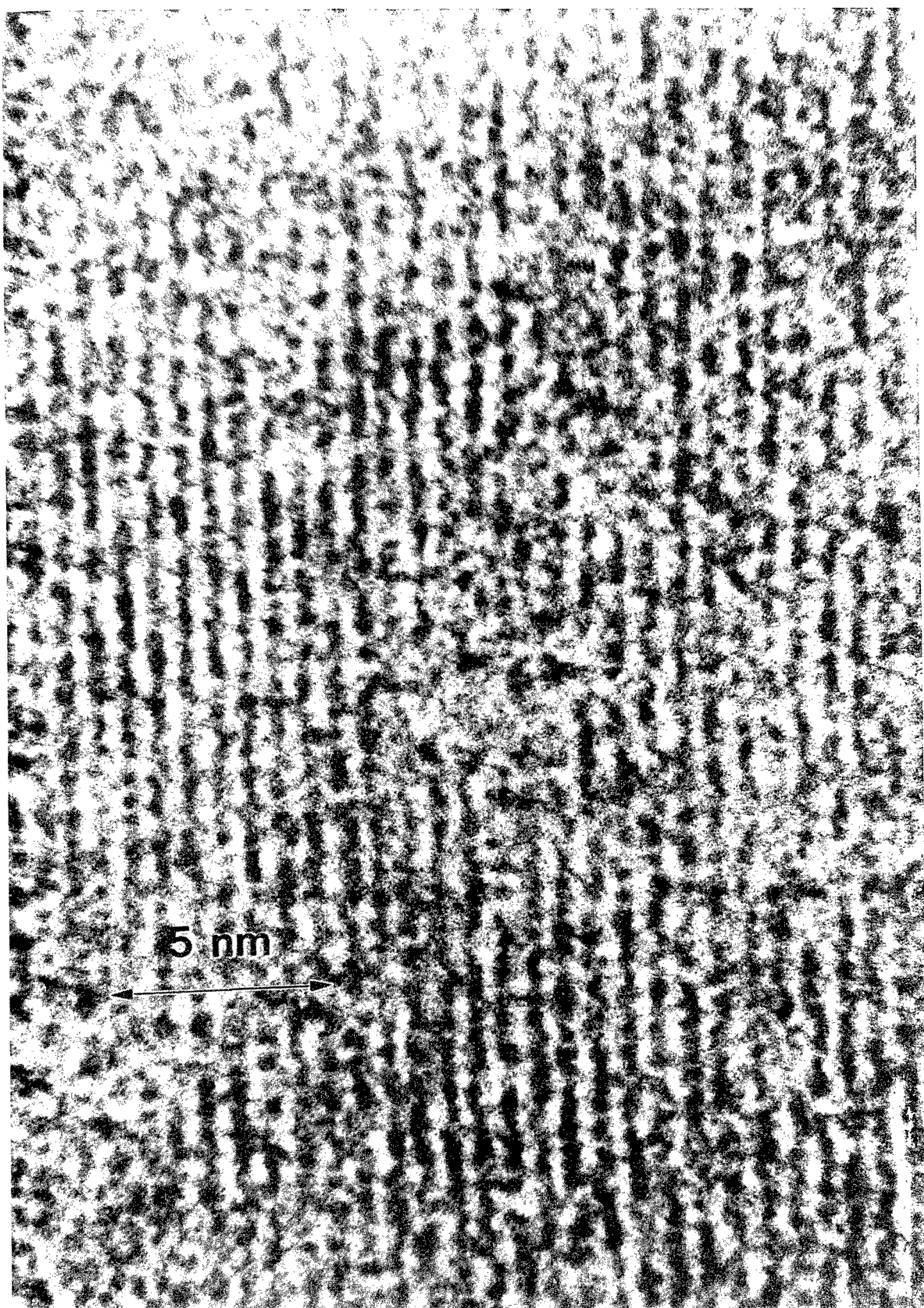
Sample	Equatorial		Layer Line	
	Lateral (nm)	Axial (nm)	Lateral (nm)	Axial (nm)
PBZT	4.6	4.0	1.0	22.8
PBZO AS	2.6	3.0	0.9	13.7
PBZO 600	3.9	3.9		
PBZO 665	4.8	2.4	0.8	19.6
PBZO CPD	5.5	0.7		

(200) plane coming in from the top axial boundary than leaving from bottom axial boundary. This is direct evidence for an edge dislocation within the PBZO crystal. An enlarged view of this defect is shown in Figure 4.14. Both the Burger's vector (0.55 nm in the [100] direction) and the direction of the dislocation (approximately parallel to the [010] beam direction) are perpendicular to the fiber axis.

Figure 4.15 shows an arrangement of a layer of PBZO molecules that could explain the molecular packing which generated this image. If the structure given by this model (Figure 4.15) was repeated on every layer within the thin PBZO section, the position of the dislocation core would be precisely determined. Such a model does not seem physically reasonable, since it would require the mutual segregation of a number of chain ends which were all oriented in the same direction. In fact, the image does not show a well defined dislocation core region. Note that incorporation of the dislocation requires an amount of tilt to be induced in one section of the crystal. Close inspection of the HREM image, accomplished by viewing the micrograph at a glancing angle in the direction of the fringes, shows that similar tilting of the PBZO lattice occurs near the actual defect.

Such an edge dislocation may serve as a nucleus for fracture or for the segregation of solvents and other impurities. Also, it may facilitate or frustrate certain

Figure 4.14: High magnification view of an HREM image of PBZO HT 600 showing a region containing an edge dislocation. The direction of the dislocation is approximately parallel to the $[010]$ viewing direction, and the Burger's vector is 0.55 nm in the $[010]$ direction, corresponding to an extra (100) plane. The location of the dislocation is best determined by viewing the image from a glancing angle along the direction of the fringes.



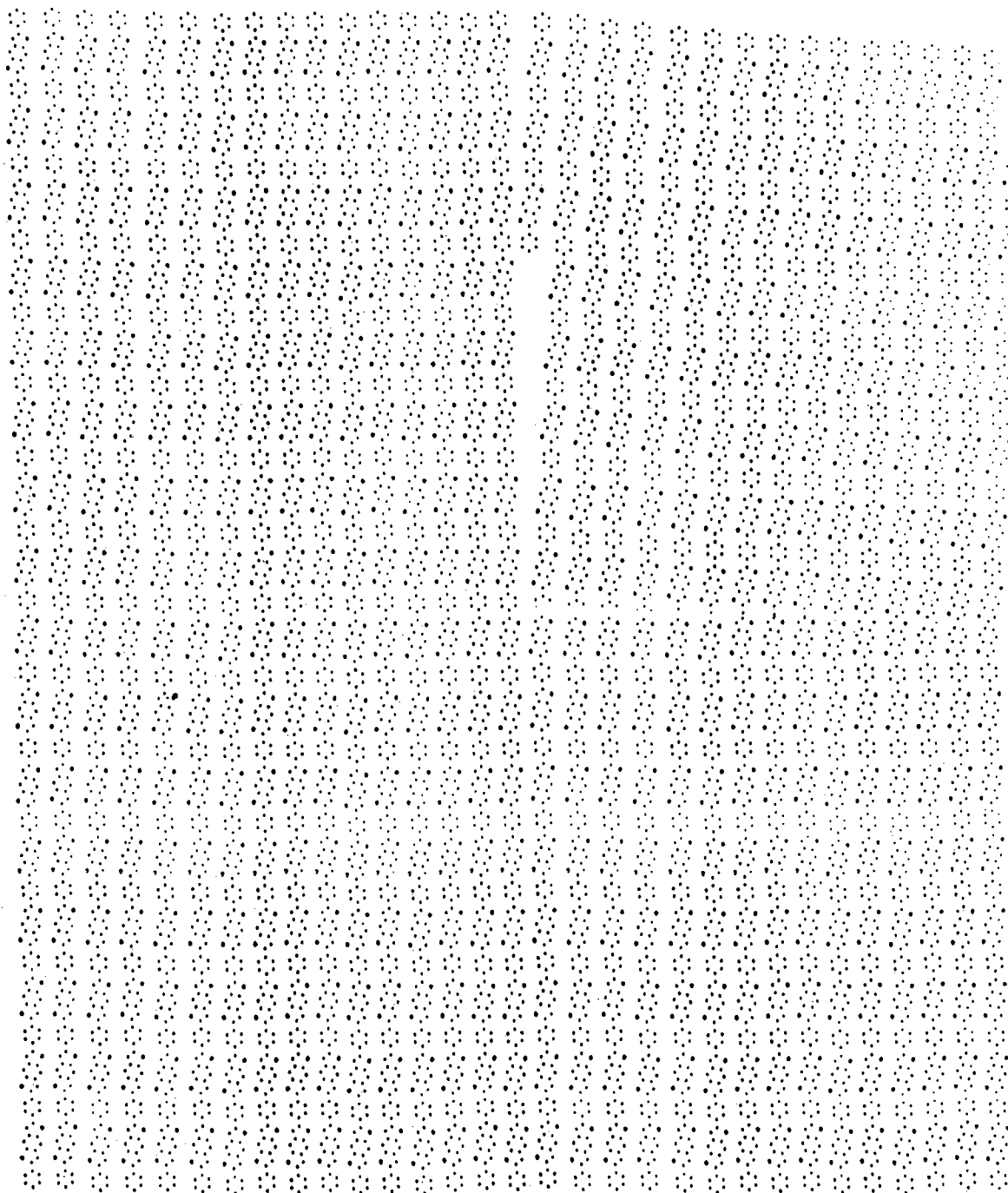


Figure 4.15: Model of an extra (100) plane which would explain the image in Figure 4.14. The lack of a well defined dislocation core in the image suggests the direction of the dislocation is not well determined.

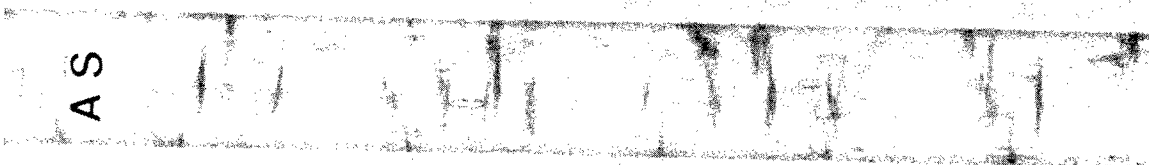
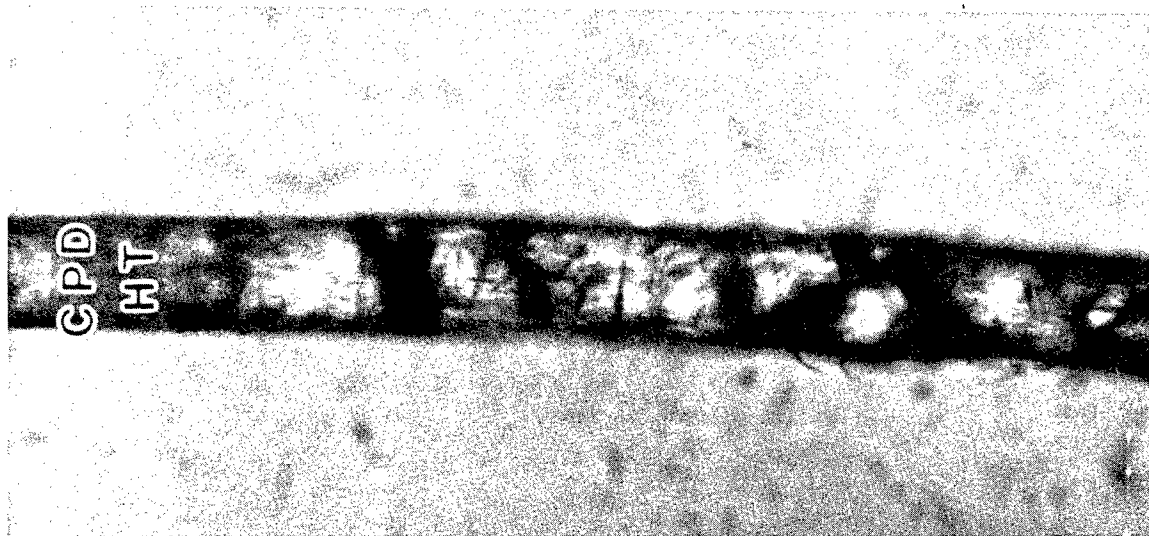
slip systems of the PBZO crystallite during shear deformation. Since the Burger's vector and the dislocation orientation are both perpendicular to the chain axis, it is difficult to envision simple molecular mechanisms for the motion of this dislocation without involving covalent bond bending or climb of an entire plane of molecules.

Images containing crystals with internal dislocation defects were uncommon. This is apparently because the average crystals are so small that most of the disorder is taken up in the grain boundary regions. Most of the PBZO crystals seemed more or less "perfect", yet close inspection of the images shows that the lattice orientation within certain crystals undergoes subtle fluctuations.

3. Critically Point Dried PBZO Fiber

Figure 4.16 is a series of optical micrographs of the wet PBZO fiber, the critical point dried fiber (CPD), and the critical point dried and heat treated fiber (CPD HT). Note that there is some shrinkage of the fiber during the critical point drying procedure. Table 4.6 shows the diameter of the fiber measured from OM observation and with a micrometer. The values determined by the micrometer are slightly lower than those seen in OM, perhaps due to sample compression during the measurement.

Figure 4.16: Optical micrographs of a) wet PBZO fiber, b) Critically Point Dried PBZO fiber, and c) Critically Point Dried and Heat Treated PBZO fiber.



100 μm

Table 4.7
PBZO Fiber Diameters during
Critical Point Drying

Fiber	OM Diameter microns	Micrometer Diameter microns
Wet AS	50-60	48
CPD	42-50	38
CPD-HT	35-40	28

It is of interest to note that "kinks" observed on the surface of wet PBZO fiber are approximately perpendicular to the fiber axis. These kinks were induced merely by sample manipulation. This orientation is quite different from the kink orientation seen in the dried fiber (Chapter V). Also note that the CPD and CPD HT fiber shows darkening due to kink bands which have formed across the entire fiber, but these kinks are not as sharp and well defined as those in tensioned dried fiber (Chapter V). Also observed in Figure 4.16 are small (5 μm) indentations of unknown origin on the fiber surface in the axial direction.

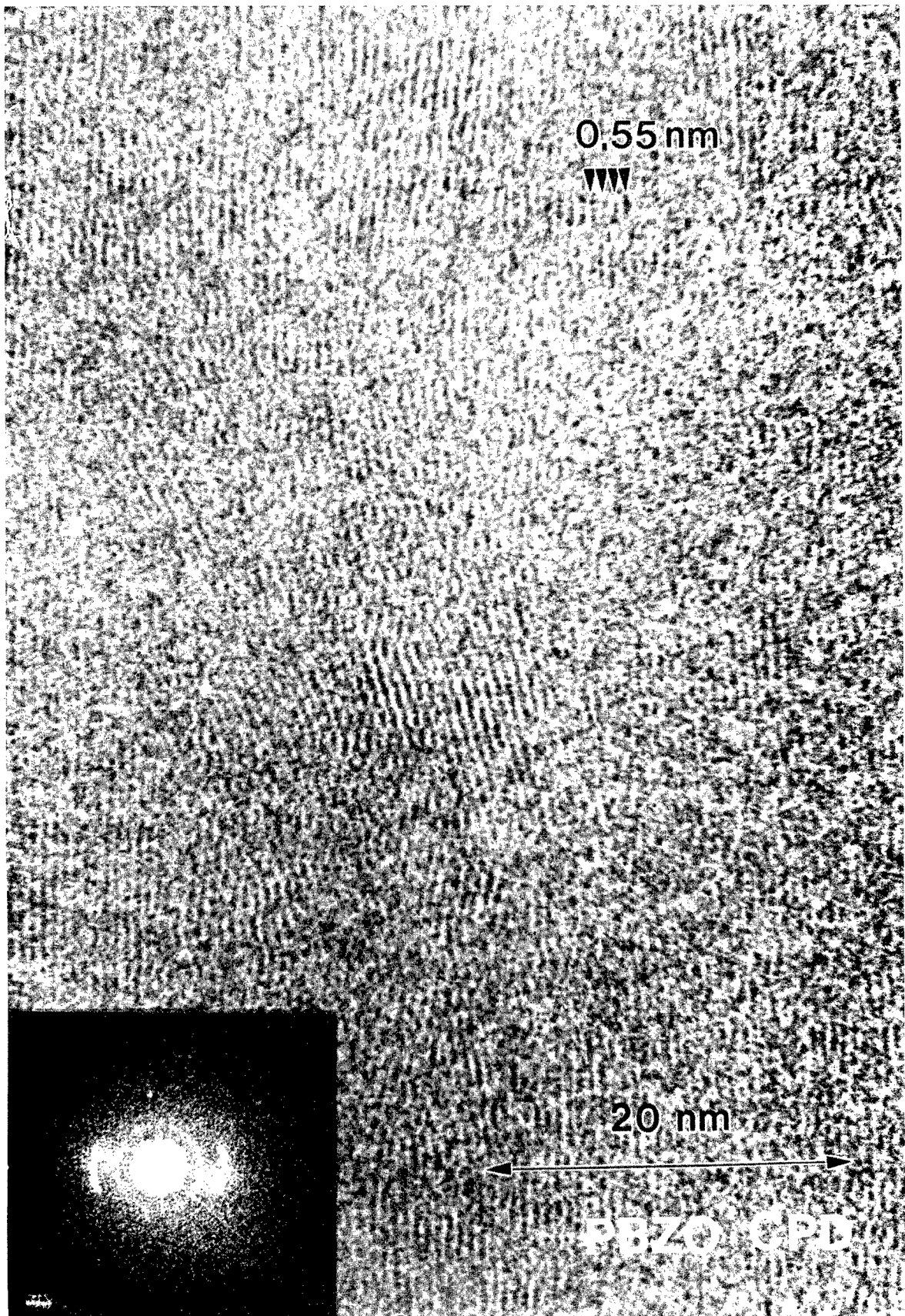
Figure 4.17 is a DF micrograph of a detached fragment of the CPD HT fiber. The misorientation within the fiber is immediately evident during DF observation as crystallites from a given region of a sample come into the Bragg condition for many different positions of the aperture or beam tilt. This is in sharp contrast to fibrous PBZO where the objective aperture must be strictly perpendicular to the fiber axis for crystallites to be observed. Regions of the fragment which have apparently undergone compressive deformation are seen in Figure 4.17, but the "kink bands" in these CPD samples are not as sharply distinguished as in those in fragments from dried fiber (Chapter V).

An HREM image of the CPD HT fiber is shown in Figure 4.18. Note the relative lack of orientation as com-

Figure 4.17: DF image of CPD HT fiber. The CPD fiber shows considerably more misorientation than even the as-spun fiber. The boundaries between the kinked and the unkinked regions are not nearly as distinct as those in tensioned dried fiber (Chapter V).



Figure 4.18: HREM image of CPD HT fiber. Note the dramatic amount of molecular misorientation which is immediately apparent. An area exhibiting two different orientations of the molecular axis in the center of this image provides direct evidence for a lateral chain rotation boundary (Chapter VI).



pared to the fiber samples. Analysis of the orientation distribution (Table 3.1) shows that the CPD fiber shows considerably more misorientation (7.86 degrees S.D.) than as-spun or heat treated PBZO.

The origin of this misorientation apparently comes from a partial collapse of the PBZO microfibrillar network as the water is removed. These results emphasize why it is important to maintain tension on the fiber during drying so that this misorientation does not occur. When the microfibrillar network collapses, it is reasonable to imagine that there are some microfibrils which are not able to pack together well as they become closer to one another. Without applied tension, microfibrils which are joined to other microfibrils at Y-junctions will be forced to misorient in order to accomodate one other as the collapse proceeds. In fact, it is well known that if tension is not placed on the fiber during drying the stresses will become large enough for the fiber to develop a high density of kinks.

It was not possible to completely preserve the "open" nature of the PBZO microfibrillar network by critical point drying. The images shown have evidence for overlapping grains indicative of superposition within the thickness of the film. These images of overlapping crystals emphasize that projection problems are always a concern in HREM images and that thin sections are extremely important for reliable

image interpretation. Nevertheless, this image provides direct evidence for a lateral chain rotation boundary between PBZO crystallites. These boundaries will be discussed in more detail in Chapter VI.

D. Discussion

It is of interest to compare the results about crystal size, size distributions, and shape for PBZT and PBZO with those for other materials. Theories and experimental data for normal grain growth in pure, single phase systems have recently been reviewed by Atkinson (1988). Recent insight about the details of grain growth have been provided by 2-D Monte Carlo simulations (Anderson, Srolovitz, Grest, and Sahni, 1984) which enable specific aspects about the grain size and shape distribution to be analyzed (Srolovitz, Anderson, Sahni, and Grest, 1984).

The computer simulations show a frequency-grain size distribution which is peaked near the average grain size R_a (Srolovitz, et al., 1984). The maximum grain size R_{max} is approximately $2.5 R_a$, and the minimum size is about $0.1 R_a$. Analysis of the growth rate of each grain as a function of size R/R_a shows that for grains larger than R_a the growth rate $d(R/R_a)/dt$ is randomly distributed about zero, whereas for small grains the rate becomes strongly negative. This

indicates that small grains have a strong tendency to decrease in size, whereas large grains are both increasing and decreasing in size in a more or less random fashion.

The breadth of the crystal size distributions seen in HREM and DF for PBZT and PBZO are in general agreement with these results. However, the chain connectivity and extremely anisotropic nature of grain boundary energies suggest that the dynamics and energetics of grain boundaries in polymer solids will be significantly different than those of metals and oxides. Further investigations which provide more information about the nature of grain growth in polymeric solids is important to further elucidate the differences between metallic, ionic, and covalently bonded solids.

Initial 2-D Monte Carlo simulations have shown that grain boundary energy anisotropy causes broadening of the crystal size distribution, giving rise to a microstructure with large grains and extended regions of small grains (Grest, Srolovitz, and Anderson, 1985). This anisotropy was also observed to decrease the grain growth kinetics, and to give rise to grains with preferential shapes. Also, grain boundary anisotropy caused intergrain orientation correlations, but these correlations were limited to a few times R_a for the potentials used (Grest et al., 1985).

It is appropriate to discuss here an observation which was NOT made in this study which might have been expected. The SAXS patterns by Adams and Grubb (1988) confirm that PBZO fiber has a tendency to develop periodic fluctuations in electron density at specific angles to the fiber axis. The characteristic dimensions of the four-point patterns is on the order of 8 nm, and the diffuse regions of diffracted SAXS intensity make an angle of approximately 57 degrees with the fiber axis (Adams et al., 1986).

This characteristic dimension of the SAXS scattering (8 nm) corresponds with the average size of a PBZO crystallite (10 nm). Therefore, it seems reasonable that the four-point SAXS patterns arise from arrangements of crystallites which have a preferential shape. In particular, it seems apparent that axial grain boundaries of PBZO crystallites have a propensity to orient themselves at specific angles to the fiber axis. From WAXS, we found that there were sharp reflections due to good packing in (302) planes. Notably, these strong (302) reflections make an angle of 57 degrees with the fiber axis. This suggests that the (302) planes may have a dominant role in the origin of the four-point pattern. A specific model is that the (302) planes often serve as axial grain boundaries for PBZO crystallites. A model of such a PBZO crystallite with (302) faces is shown in Figure 4.19. Calculations of the shape transform of such a crystallite shows a four-point pattern

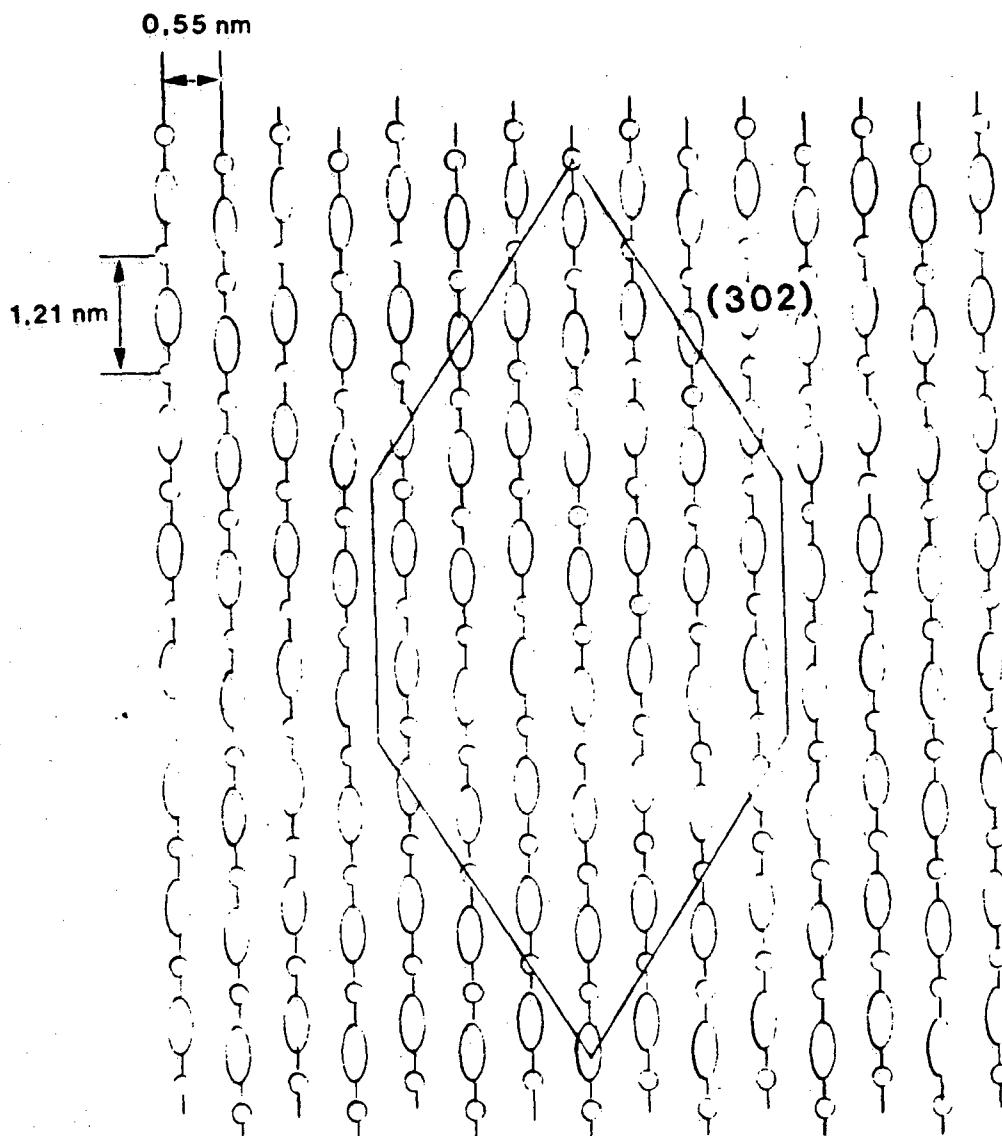


Figure 4.19: Model to explain the origin of the four-point SAXS pattern in terms of crystallites with axial chain invariant boundaries (Chapter VI). The planes which describe the boundaries of the PBZO crystallites are the (302) planes whose WAXS reflections were seen to sharpen and increase in intensity after heat treatment (Figure 4.2b).

which is similar to that of the PBZO SAXS data. The question is, why aren't such regular grain boundary shapes visible in HREM and DF studies?

A reasonable explanation for the lack of observation of crystallites with a unique shape by HREM is that the axial grain boundaries are simply not localized and flat enough to give interpretable projections. Another is that the orientation of the boundary is such that to be visualized properly it is necessary to project the crystallite in a direction which does not correspond to a good viewing direction where "fringes" can be seen. Another reason might be that we simply have not yet obtained enough images to find a region of the sample in which the supposed characteristic shape of the PBZO crystallites can be clearly seen.

It should be noted that it IS possible to find "rhombohedral" shaped crystallites in PPTA thin films. A recent study by Roche, Allen, Gabara, and Cox (1989, submitted) showed rhombohedral crystals for PPTA/Sulfuric acid solutions which were sheared and then slowly coagulated by exposure to atmospheric moisture. The axial boundaries of the crystallites observed in OM and TEM were inclined at a significant angle (approximately 55 degrees) to the axis of orientation of the PPTA molecules. It was thought that these structures were representative of a crystal solvate phase which formed during slow coagulation. Although a physical

explanation for the rhombohedral shapes was not discussed, they apparently arise because of low energy axial grain boundaries which prefer to form at specific orientations with the molecular axis.

E. Conclusions

WAXS and SAED patterns of PBZO show an increase in three-dimensional crystallinity as a function of heat treatment. There is a strong off-axis reflection on the second order layer line which increases in intensity and becomes more localized as the fibers are heat treated.

SAED of PBZO showed that thin sections could exhibit texturing indicative of a preferential orientation of the (010) direction parallel to the electron beam. This corresponds to a tendency for the molecule to lie "flat" in the plane of the film. This phenomena enabled the strong off-axis reflections to be indexed as (302), corresponding to regular axial registry of $1/4$ c between molecules in the (100) direction.

The unit cell proposed for PBZO corresponds to the monoclinic space group **Pc** (No. 7). The unit cell parameters are $a=1.196$ nm, $b=0.3540$ nm, $c=1.205$ nm, $\gamma=101.2$ degrees with

two repeat units per cell. The calculated density is 1.66 gms/cm³.

HREM images of PBZO show 0.55 nm and 0.35 nm fringes corresponding to the closest lateral packing between molecules. The orientation distributions are again determined, with a standard deviation of approximately 1.3 degrees. The amount of misorientation determined by HREM does not vary significantly as a function of heat treatment.

Crystallite sizes determined by HREM are consistent with earlier observations by DF that PBZO crystallites grow more in the lateral than the axial directions. The results of crystallite size measurements determined by HREM and DF measurements were compared directly. It was shown that crystallite sizes determined by HREM were slightly larger than those determined by DF, indicating that either DF is sensitive to small fluctuations in structure which are not due to crystalline ordering, or that it is difficult to distinguish regions of small crystalline ordering in low dose HREM images by eye.

Crystallite sizes determined by the breadth of spots in the optical transform were systematically smaller than those determined directly from HREM images. This suggests that the crystallites have disorder within them that causes the

optical diffraction spots to smear more than can be attributed simply to crystallite size.

Evidence for an edge dislocation defect oriented in the [010] direction with a Burger's vector of [100] was observed within a PBZO crystallite. This type of edge dislocation is unique in that both the dislocation direction and Burger's vector are perpendicular to the primary axis of orientation. Such a defect could be formed by the mutual segregation of a number of similarly oriented chain ends along the dislocation line.

CHAPTER V: MICROMECHANISMS OF COMPRESSIVE PLASTIC DEFORMATION IN RIGID-ROD POLYMER FIBERS

As discussed in Chapter I, the tensile moduli and strengths of rigid-rod polymer fibers are excellent. Theoretical predictions of PBZT and PBZO modulus have been obtained by Adams et al. (1987) and by Weirshke (1988) using semi-empirical quantum mechanical (Minimum Neglect of Differential Overlap) methods. The theoretically predicted moduli of trans-PBZT and cis-PBZO are 605 and 730 GPa, respectively (Weirshke, 1988). The PBZO HT 600 used in this study has a tensile modulus of 317 GPa (Table 4.1), showing that nearly 50% of the theoretically predicted modulus has now been obtained experimentally. Likewise, the tensile strength (4.9 GPa for PBZO HT 600) is excellent. For PBZT, tensile moduli of 330 GPa and tensile strengths of 4.2 GPa have been observed. However, both PBZO and PBZT fibers are about a factor of 10 weaker in compression, with failure occurring by strain localization into kink bands.

This problem has become a severe limitation for the application of rigid-rod polymers in structural components. Hence, a deeper understanding of the molecular motions involved in kinking is a critical concern for future success in the design and processing of high strength, high modulus polymer fibers.

This chapter provides a detailed study of kink bands in rigid-rod polymer fibers. We investigate the morphology of kinking using DF and HREM imaging as well the thermodynamics of kink formation by quantitative measurements of kinking in fibers during compressive plastic deformation. We discuss a model for kinking which involves the nucleation and growth of a kink across a fiber and describe the molecular motions involved in this deformation process. The kink band is envisioned to be a region of shear deformation separated from the undeformed part of the sample by high angle axial chain rotation grain boundaries and partial edge dislocations. The information and insight about the molecular mechanisms and energetics of kinking obtained by this study should prove valuable to those interested in improving the limited compressive strength of these materials.

A. Introduction

The concept of kinking as a deformation mechanism was introduced by Orowan (1942). Both deformation twinning and kinking involve the shear of a local region of material within an originally undeformed sample. Kinking is distinct from deformation twinning, however, in that the lattice inside the sheared zone need not be a mirror image of the undeformed structure. Likewise, the boundary between the kinked and unkinked regions need not be a crystallographic

plane. Orowan proposed a geometric relationship describing the likely angles for kinking based on the argument that the angle of rotation should preserve lateral interactions between glide planes. Orowan's paper concerned kinks which had formed completely across the sample and did not elaborate on how such a deformation structure might nucleate and subsequently grow in an initially undeformed sample.

Frank and Stroh (1952) developed a theory of kinking which considered the stability of a lenticular shaped kink in an isotropic, continuous, linearly elastic medium. The boundary of the kink was envisioned to be formed from a number of edge dislocations. The energy of the kink was rationalized in terms of the macroscopic stress field of the dislocations, a microscopic stress field characteristic of the dislocation cores, and the energy released during the shear deformation involved in kinking. Frank and Stroh predicted that for a given applied shear stress there was a critical size L for kink stability. Kinks larger than L could reduce the energy of the system by growing. The model predicts that the shear stress τ required to make a kink of size L propagate in a medium of shear modulus G is given by

$$\tau = G (g b/2 L)^{1/2}$$

(5.1)

where \mathbf{b} is the Burger's vector of the dislocations along the kink boundary and \mathbf{g} is the shear strain within the kink. Although this analysis treats only the energetic stability of kinks which have somehow already formed, it is possible to imagine that there will always be some "effective" kink nucleus size which is determined by local defects and other structural fluctuations.

Argon developed a theory for the initiation of kinks in oriented composites (1972). His analysis considered the stress necessary to induce a shear collapse instability. The instability occurs because a compressive stress along the orientation direction causes locally misaligned elements to experience a relative shear stress which depends on the misorientation angle ϕ_0 . The model calculated the stress necessary to propagate a region of shear collapse across the sample. The change in elastic energy near the kink-collapse nucleus was modeled with a pair of edge dislocations. At the onset of the instability, Argon predicted that the stress would be given simply by

$$\sigma_c = \tau_s / \phi_0 \quad (5.2)$$

where τ_s is the plastic shear strength of the matrix.

Kink band formation is a general observation in the compressive failure of oriented polymers. Zaukelies (1962)

was the first to document kinking during compression of oriented polymers. He studied kinks in highly oriented nylon 6,6 and nylon 6,10 fibers by OM and BF TEM of surface replicas of cleaved samples and interpreted his results in terms of specific slip systems based on close packed directions in the polymer unit cell. He envisioned the structure of the semicrystalline polymer fiber as essentially a large, highly defective single crystal. The kinks were laterally broad (up to 1 mm) and limited in axial extent (less than 2 μm , sometimes as small as 150 nm). The interface between kinked and unkinked material was sharp (thickness less than 50 nm). Double orientation induced by rolling the sample caused the kinks to form only in directions consistent with slip on (010) planes. Observations of singly oriented fibers showed the kinks to make a uniform angle with the orientation direction but with a random distribution about the fiber axis.

Zaukelies did not consider the questions of kink nucleation and growth. Nevertheless, the observation that kinks form at specific angles with respect to the fiber axis in singly oriented fibers suggests that the nucleation of a kink specifies the angle of kinking which then grows by forcing crystallites to cooperatively deform in a manner which preserves the initial orientation of the deformation band.

Seto and Tajima studied kink bands in oriented polyethylene (PE) by OM, BF TEM of surface replicas, WAXS, and SAXS (1966). Again, kinks were found to form at characteristic angles. The angle of kinking was found to depend on prior heat treatment as well as the temperature of deformation. The angle of the kink boundary with respect to the fiber axis was 52 degrees at room temperature, but decreased to 48 degrees when the PE had been annealed at 80 C for 30 minutes. For samples deformed at low temperatures, an angle of 72 degrees was observed. The boundary between the kinked and unkinked material was sharp (approximately 50 nm). Like Zaukelies, Seto and Tajima found that crystalline slip was useful in understanding the deformation processes involved in kinking. WAXS confirmed that rotation of the chain axis occurred during kinking. SAXS scattering showed that reorientation of the PE lamellae was occurring within the kink band region due to interlamellar slip along the c-axis.

Robertson (1969) found that kinks form easily in oriented crystalline polymers (PE and isotactic polypropylene (PP)), but were not present in oriented glassy polymers. A BF surface replica image of a propagating kink front in PE showed that the included angle of the kink was very small (0.5 degrees). During deformation, the kinks were observed to lengthen by the tip "shooting forward", accompanied by widening of the kink without an apparent change in the ori-

entation of fibrils within the kink. Kinks initiated at stress concentrations such as the sample clamps, and could be induced to occur at deliberate flaws. It was suggested that kink initiation involved the formation of "S-shaped curves" due to shear stresses followed by strain localization involving collapse of fibrils below a critical radius of curvature. It was proposed that the structural features which promote kink formation were the resistance of the oriented fibrils to length changes and the easy slip between fibrils.

Shigematsu, Imada, and Takayanagi (1975) studied further the morphology of kinks in oriented PE and were able to distinguish between the contributions due to uniform c-axis shear and intercrystalline slip by measuring both the angle of chain axis rotation as well as the resulting orientation of crystalline lamellae within the kink. From the observed angle of chain rotation (70-75 degrees), inclination of the kink boundary (50-55 degrees), and angle between lamellae and chain axis within the kink (55-60 degrees), it was concluded that both mechanisms must be involved in the deformation process and that the relative contributions of each might depend on deformation temperature.

Attenburrow and Basset (1979) investigated kinking during a study of the compliances and failure modes of chain-extended PE and found that the angle between the chain axis

and lamellae within the kink was consistent with a uniform c axis shear deformation. Some of the kink bands were observed to be very small in axial extent, approaching nearly the lamellar thickness (50 nm). The uniformity of shear within the kink band as compared to conventional PE was rationalized in terms of the decreased shear resistance of the lamellar crystals in the chain extended material.

From these studies it is apparent that lamellar organization in PE restricts the uniformity of shear deformation in compression. The deformation in oriented lamellar PE is characterized by "blocky" shear, whereas the extended chain conformation of PE facilitates "fine" shear.

The largest known polymer single crystals (up to 1 mm size or larger) are prepared from solid-state polymerization of large crystals of monomer. Typical examples include polymeric sulphur nitride (SN)_x and polymerized diacetylenes. Because of their unique method of synthesis, such single crystal polymers have quite different microstructures than polymers prepared by more traditional synthetic and processing routes.

Young and Baughman (1978) studied shear-induced martensitic phase transformations in polymeric sulphur nitride (SN)_x and found that a conventional deformation twinning model explained well the geometry of the process. Petermann

and Schultz (1979) studied kinking in (SN)x in more detail by BF, DF, and SAED. As in the other cases discussed so far, the kinks were laterally broad (usually crossing the entire sample) and of limited axial extent (200 nm), with sharp boundaries (50 nm) between kinked and unkinked material. It was observed that there was a considerable amount of voiding and fibrillation within (SN)x kink bands. Petermann and Shultz developed a model involving the nucleation and growth of kinks through the action of defects moving from "sources" to "sinks" corresponding to local regions of tension and compression, respectively. These defects were presumed to represent regions of local internal conformational changes within the polymer chains. Such a mechanism does not seem likely to successfully explain the origin of PBZO and PBZT kinks, since internal conformational changes are not reasonable given the fully extended chain structure.

Deformation twinning has also been useful in describing the geometry of local deformation zones in single crystals of poly(diacetylene) (Young, Bloor, Batchelder, and Hubble, (1978); Young, Dulniak, Batchelder, and Bloor, (1979); Robinson, Yeung, Galiotis, Young, and Batchelder, (1986)). The geometry of twinning is shown in Figure 5.1. It is possible to characterize the geometry of a twin by defining the directions n_1 , n_2 and planes K_1 and K_2 (Reed-Hill, 1973). The applicability of twinning models to polymer crystals was shown by Bevis (1978) who incorporated the influence of

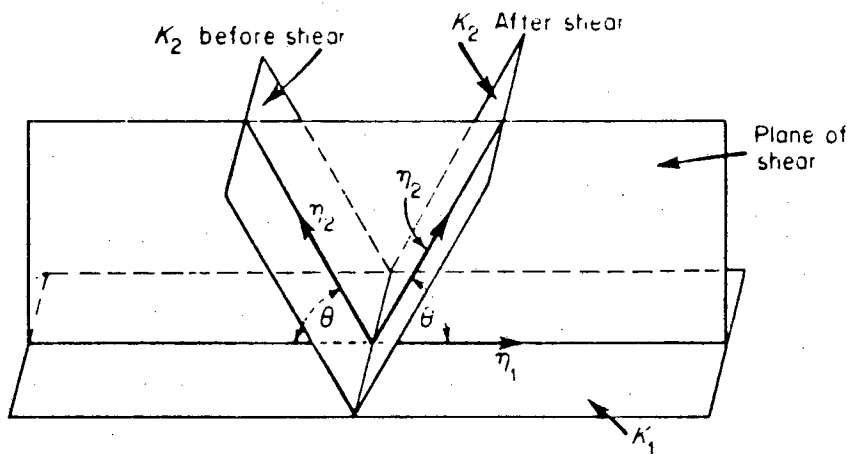


Figure 5.1: Schematic of the geometry of twinning. The twin is characterized by directions n_1 (the shear direction) and n_2 (the intersection of the plane of shear with K_2), and the planes K_1 (the twinning plane) and K_2 (the second undistorted plane). Adapted from Reed-Hill (1973).

molecular connectivity by drawing a distinction between chain axis invariant and chain axis rotation twins. Chain axis invariant twins preserve the orientation of the chain axis and therefore do not require bending of chains at the twin interface. Chain axis rotation twins do require a rotation of the chain and therefore are expected to be of higher energy. For chain axis invariant twins, the chain axis lies in the K_1 plane. For chain axis rotation twins, the chain axis is in the plane K_2 .

Young et al. (1978) examined deformation twins in cleaved crystals of poly(diacetylene) by SEM. The twins were laterally broad (100 μm or more), limited in axial extent (1-10 μm), and had sharp boundaries (to the limit of the SEM, approximately 10 nm). The twinning planes were determined from the observed angle of deformation and the known crystallographic index of the crystal cleavage face. It was found that several different twinning modes were possible in the polydiacetylene TSHD including twins with $K_1=(012)$ and (212) as well as possibly $(2\bar{1}2)$ and (202) . However in polyDCHD only twins with $K_1=(2\bar{1}2)$ were seen (1986). This was explained in terms of the packing of the planar backbone and bulky side groups which limit the possible slip systems in the polyDCHD material.

It was noted by Young et al. (1978, 1979) that if the boundary of a deformation twin is not strictly parallel to K_1

then the boundary is necessarily incoherent, and therefore requires a distribution of dislocations to accommodate this deviation. It was proposed that the boundary of a lenticular shaped deformation twin can be envisioned as a number of edge dislocations separated by chain tilt grain boundaries. The stresses introduced into the material by such a dislocation array were correlated with cracks parallel to the [001] direction which were often seen in the poly(diacetylene) matrix near deformation twins.

The morphology of kinks in a semi-rigid polymer fiber PPTA (Kevlar) was studied by Takahashi, Miura, and Sakuri (1983). The kinks were introduced by axial compression of a cylindrical block of 2-hydroxypropyl methacrylate in which PPTA fibers were embedded. Deformed fibers were removed by treating with dimethyl sulfoxide. The morphology of the kinks was studied by OM, WAXS, BF, DF, and SAED. It was found that kinking occurs primarily by (200) [001] slip corresponding to shear between hydrogen bonded planes of molecules. It was also observed that there was non-uniformity of strain within the kink band, as well as sharp (50 nm) boundaries between the kink and the undeformed fiber. Because of the cylindrically symmetric orientation of the hydrogen bonded planes in PPTA fiber, (200) [001] slip leads to helical kinks which wind their way along the PPTA fiber (DeTeresa, Allen, Farris, and Porter, 1984). DeTeresa (1986)

found that kinking PPTA (3% compressive strain) caused only a small loss in tensile strength.

Kinks have long been known to be characteristic of compressive failure in rigid-rod polymers (Allen et al., 1981) and have also been seen in PBZT-epoxy composites (Cohen and Thomas, 1988).

DeTeresa investigated the behavior of high performance fibers in compression and was able to devise a bending beam experiment to characterize the critical strain for kink initiation (DeTeresa 1986; DeTeresa, Porter, and Farris, 1988). Allen (1988) has used visual inspection for kinks in failed fiber to develop an elastic recoil test for determining the compressive failure stress.

A model for the onset of kink formation in terms of an elastic buckling instability in polymer fibers has been presented (DeTeresa, Porter, and Farris, 1985). This model predicts a correlation of compressive strength with longitudinal shear modulus of the fibre, which has experimental support from data for several high performance fiber materials including PBZT, PPTA, and graphite (DeTeresa et al., 1988). Allen (1988) has investigated the stress dependence of the torsional modulus of several polymer fibers and finds in general that it increases with applied tension, suggesting

an instability in compression when the applied stress would cause the torsional modulus to become equal to zero.

DeTeresa et al. (1988) comment that the model proposed by Argon (equation 5.2) does not seem consistent with the observation that the compressive strengths of PBZT and Kevlar are not particularly sensitive to the overall fiber orientation (Allen, private communication). Also, the Argon model predicts a drastic reduction in compressive strength for small changes in misorientation. This sensitivity is not observed experimentally in compressive strength tests of fiber composites with different amount of misorientation (DeTeresa, private communication). However, since kink initiation is a local process, it is still possible that it is not the overall orientation but the fiber orientation distribution that is important. Careful tests of the relationship between compressive strength and the details of molecular orientation distributions have yet to be performed.

In SEM studies of PBZT (Allen, 1983) and PBZO (Adams, Vezie, and Krause, 1988) evidence for kink bands is often seen on fiber surfaces. Inspection of these images showed that the kinks often occur in bundles, making it difficult to distinguish between single and multiple kink bands. The kinks were laterally broad (as large as the sample) and the boundaries between kinked and unkinked fiber was sharp to the resolution limit of the SEM (approximately 20 nm). Sometimes

small, apparently individual kinks were noted which were limited in axial extent (as small as 200 nm). At times, abrupt surface features indicative of large, local plastic deformation and the lateral, outward "extrusion" of material were seen.

From these studies, we can summarize several consistent features about kinking in oriented polymers. The kinks are laterally very broad (at times as wide as the sample) yet limited in axial extent (less than 2 μm). The interface between the kinked and unkinked regions is very sharp (approximately 50 nm), but detailed information about the deformation close to the kink boundary in all of the past studies has been limited by the resolution of conventional characterization techniques.

In PPTA, most of the tensile strength of the fiber is maintained after kinks have been introduced (DeTeresa, 1985). This suggests that bond bending or reorientation is involved at the kink boundary rather than chain breakage. Tanner, Dhingra, and Pigliacampi (1986) have postulated that the kinking process in PPTA can be explained by a trans-to-cis conformational change of an individual PPTA molecule. Such a local conformational change may very well be involved in formation of the PPTA kink boundary and for determining PPTA kink boundary angles which are of relatively low energy. However, this mechanism says little about the cooperative

nature of the deformation process. Likewise, it does not explain how kinks can grow at specified angles even when the local orientation of the crystallites is such that easy trans-cis conformational changes are not possible to accommodate the strain. Finally, there are no such easy conformational changes in the rigid polymers PBZT and PBZO.

Because of the outstanding questions about kinking mechanisms and because of the particular technological and scientific interest of this problem, we initiated this work to systematically examine the ultrastructure and thermodynamics of kinks in rigid-rod polymer fibers. We wished to determine how the unique nature of molecular packing in these materials influenced the resulting kink morphology. Also, we wished to understand better how materials comprised of highly oriented, completely stiff molecules could generate deformation zones in which there was a great deal of plastic strain.

In the following sections we investigate the molecular mechanisms of deformation which accompany compressive failure in rigid-rod polymer fibers. In particular, our use of HREM provides a powerful tool for obtaining previously unavailable information about structural evolution near and within kink bands.

B. Experimental

The fibers used in this study were heat-treated PBZT (Aftech II) and PBZO AS, HT 600, and HT 665. These samples were previously discussed in Chapters III and IV. Samples could be kinked in one of three ways. Kinks may sometimes form simply from sample manipulation. Many kinks may be purposely introduced due to uniform compression during thermoplastic matrix shrinkage (for example, nylon crystallized from formic acid solution) (DeTeresa, Farris, and Porter, 1982). Kinks may be purposely introduced by floating the fibers in water and exposing the suspension to a Branson Sonifer 185 cell disrupter (20 kHz, 25 watt oscillation for 5 minutes).

The morphology of the kinks was investigated by OM, BF, DF, SAED, and HREM. Samples for EM were prepared by the detachment replication technique described in detail in Chapter II.

C. Results

Figure 5.2 shows OM micrographs of kinks in various heat treated PBZO fibers. The kinks shown in Figure 5.2 were produced by sample manipulation. The kinks visible in OM were at a well defined angle to the fiber axis. Table 5.1 shows the angle θ of the kink boundary with respect to the

Figure 5.2: Optical micrographs of kinks in PBZO fibers: (A) As Spun, (B) HT 600, and (C) HT 665. The angle Θ is defined as the angle between the boundary of the kink and the fiber axis.

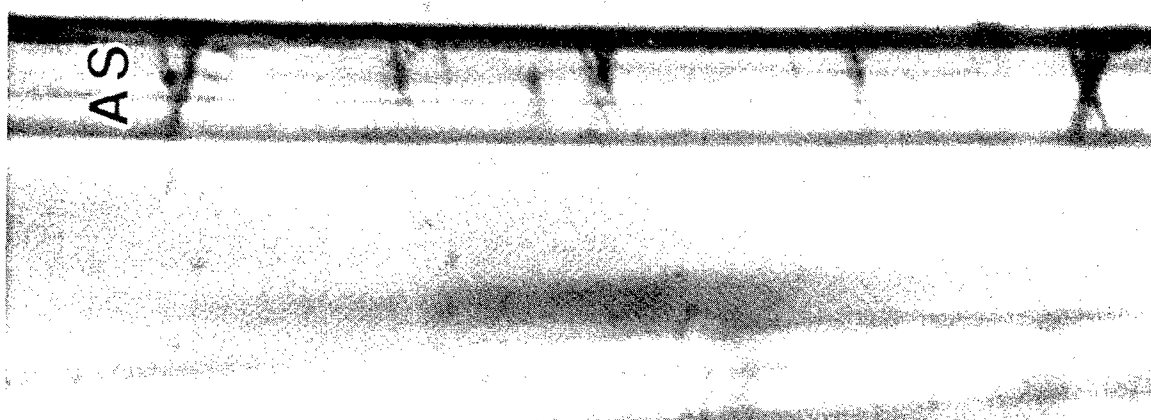
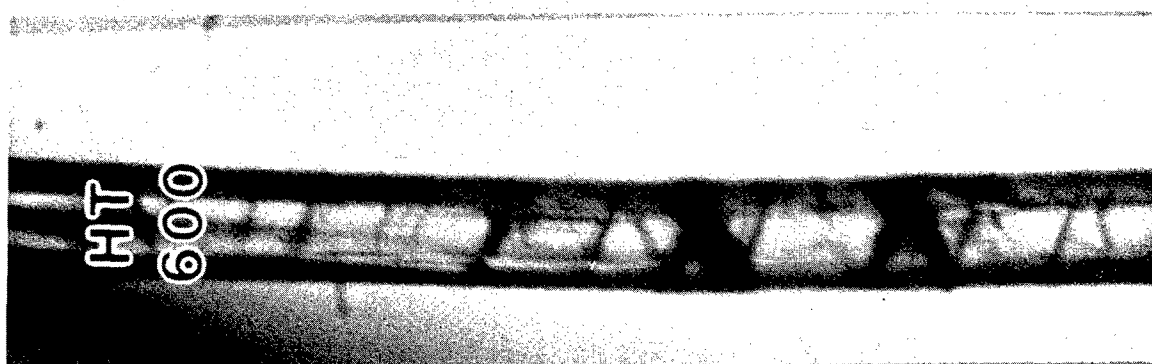
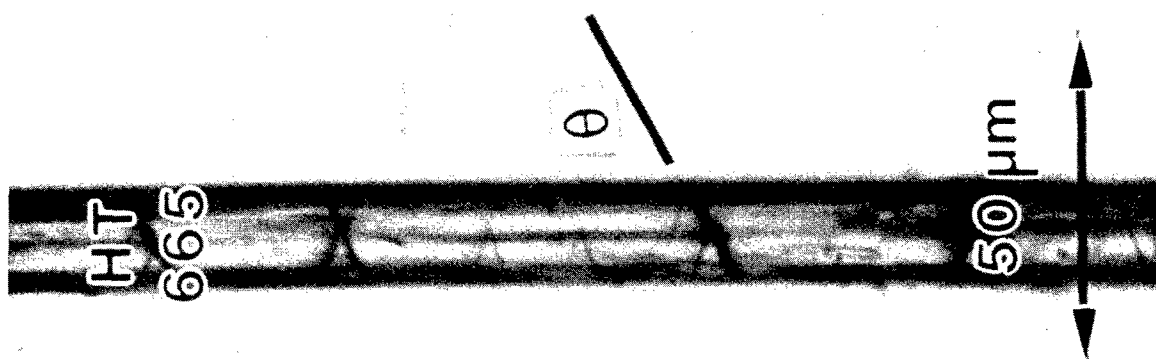


Table 5.1

Angle of Kink With Respect to Fiber Axis
From Optical Microscopy

Fiber	Angle	S.D.
PBZT	72.6	7.8
PBZO As Spun	75.4	2.6
PBZO HT 600	68.6	4.8
PBZO HT 665	66.4	4.0

fiber axis for PBZO as a function of heat treatment. These numbers were obtained by averaging over at least 25 kinks for each material. There seems to be a slight tendency for the angle of kinking in PBZO to decrease with heat treatment.

Kinks were often observed during TEM investigation of PBZT and PBZO fiber fragments. All of the kinks observed by TEM were found to have at least one lateral edge extend completely to a free surface of the fiber fragment. This strongly suggests that kinks initiate at the fiber surface and then grow in towards the body of the fiber. Figure 5.3 shows a DF image of a kink in PBZO HT 600 using the first two equatorial reflections. Bright areas in this image correspond to regions of the sample (PBZO crystallites) that are scattering electrons into the objective aperture. From the position of the aperture in this experiment, these bright regions correspond to areas which have good lateral packing and are oriented in the fiber direction. By moving the objective aperture or rotating the sample during DF imaging it was confirmed that the material within kink bands was misoriented but remained crystalline. This was also confirmed by SAED and by HREM imaging. Note that in Figure 5.3 the kink is dark, indicating that the molecules within the kink band have undergone a large change in orientation.

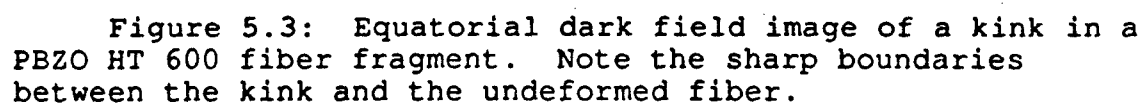
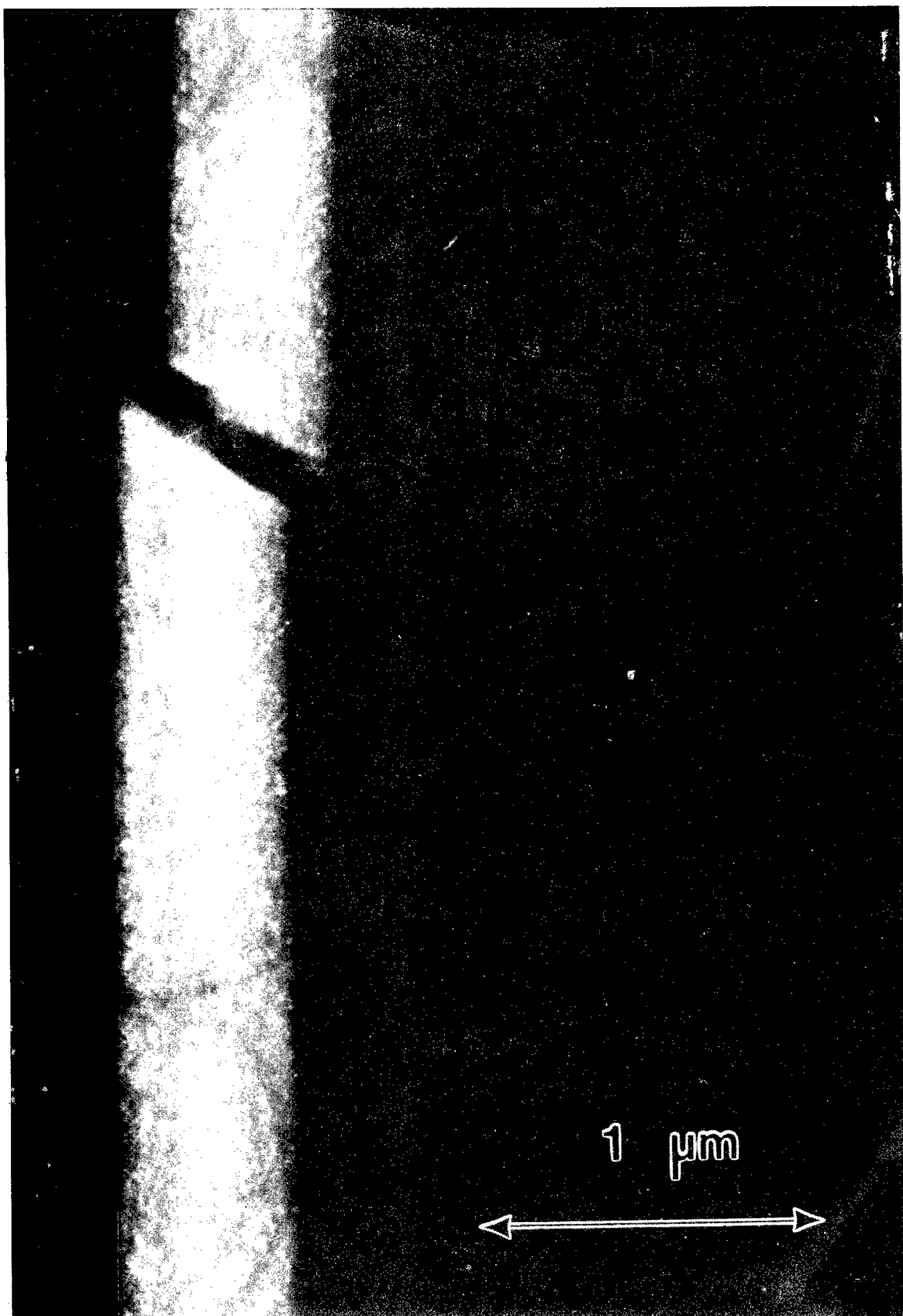
The image area is mostly blank, representing the dark field of the micrograph where the fiber would be visible. The text at the bottom describes the content of this image.

Figure 5.3: Equatorial dark field image of a kink in a PBZO HT 600 fiber fragment. Note the sharp boundaries between the kink and the undeformed fiber.



From Figure 5.3, note the sharp boundaries (10 nm or less) between the kink and the undeformed fiber. Viewing the image from the side shows that the upper boundary is very straight (fluctuations ± 20 nm from a line) across the fiber whereas the lower boundary is more meandering (fluctuations ± 60 nm). Most of the kinks observed by EM had propagated all of the way across the fiber fragment as in Figure 5.3. Figure 5.4 shows another equatorial DF of PBZO HT 600 in which there is a kink which has not yet propagated across the full thickness of the fiber fragment. The size of this kink in the direction of the fiber axis is about 30-50 nm. There is also a kink "bundle" at the bottom of this image where several kinks exist in a local region. Note that the kinks seem to adopt preferred orientations with respect to the fiber axis. The measured angle (67 degrees) corresponds well with that observed by OM.

Careful inspection of the kink which has propagated part way across the fiber shows different features for the upper boundary (where the local deformation is away from the body of the fiber) and lower boundary (where the local deformation is toward the body of the fiber). The change in contrast at the upper boundary is sharp (changing from bright to dark in 6 nm), whereas the change in contrast at the lower boundary is more diffuse (changing from bright to dark in 15 nm). Since the contrast in this image is related to the local orientation of the PBZO molecules, these results imply that

Figure 5.4: Equatorial dark field image of a kink in PBZO HT 600 in which a kink has not propagated all of the way across the fiber fragment. Near the bottom of the figure is a "bundle" in which several kinks exist in the same region. The DF image contrast shows that the upper boundary of the isolated kink is "sharp" (bending in 6 nm), while the lower boundary is more "diffuse" (bending in 15 nm). The size of the kink in the axial direction (30-50 nm) is much less than the average size of a PBZO molecule (100 nm).



the misorientation angle as a function of distance along the fiber is more discontinuous at the upper kink boundary than at the lower.

Another characteristic type of kinking which was identified was an S-shaped configuration. One such instance of this type of kink in PBZO HT 600 C is shown in Figure 5.5. The common features of these S-shaped kinks include a stripe of axially oriented material in the center of the kink (A) as well as extremely localized bending as evidenced by 10-20 nm bands of equatorial DF contrast near the edge of the fiber (B).

Kink bands in PBZT and PBZO usually appeared to be of uniform density. However, fibers of PBZO were sometimes observed to exhibit fibrillation and void formation inside the kink band. This is similar to that seen in (SN)x by Schultz and Petermann (1979). A BF example of such a fibrillated kink is shown in Figure 5.6. The formation of elongated voids within the kink is easily noted (A). Also, the boundary region between areas which can be considered as belonging to the kinked and unkinked regions of the fiber is remarkably sharp (less than 0.5 nm) (B). The irradiation of the electron beam caused the fibrillated kink to "open up" slightly during the exposure, as evidenced by rotational drift about a point centered near the kink (C). Lattice

Figure 5.5: Equatorial Dark Field image of an S-shaped kink in PBZO HT 600. The characteristic features of these type of kinks include a stripe of axially oriented material (A) as well as localized buckling near the fiber edge (B).

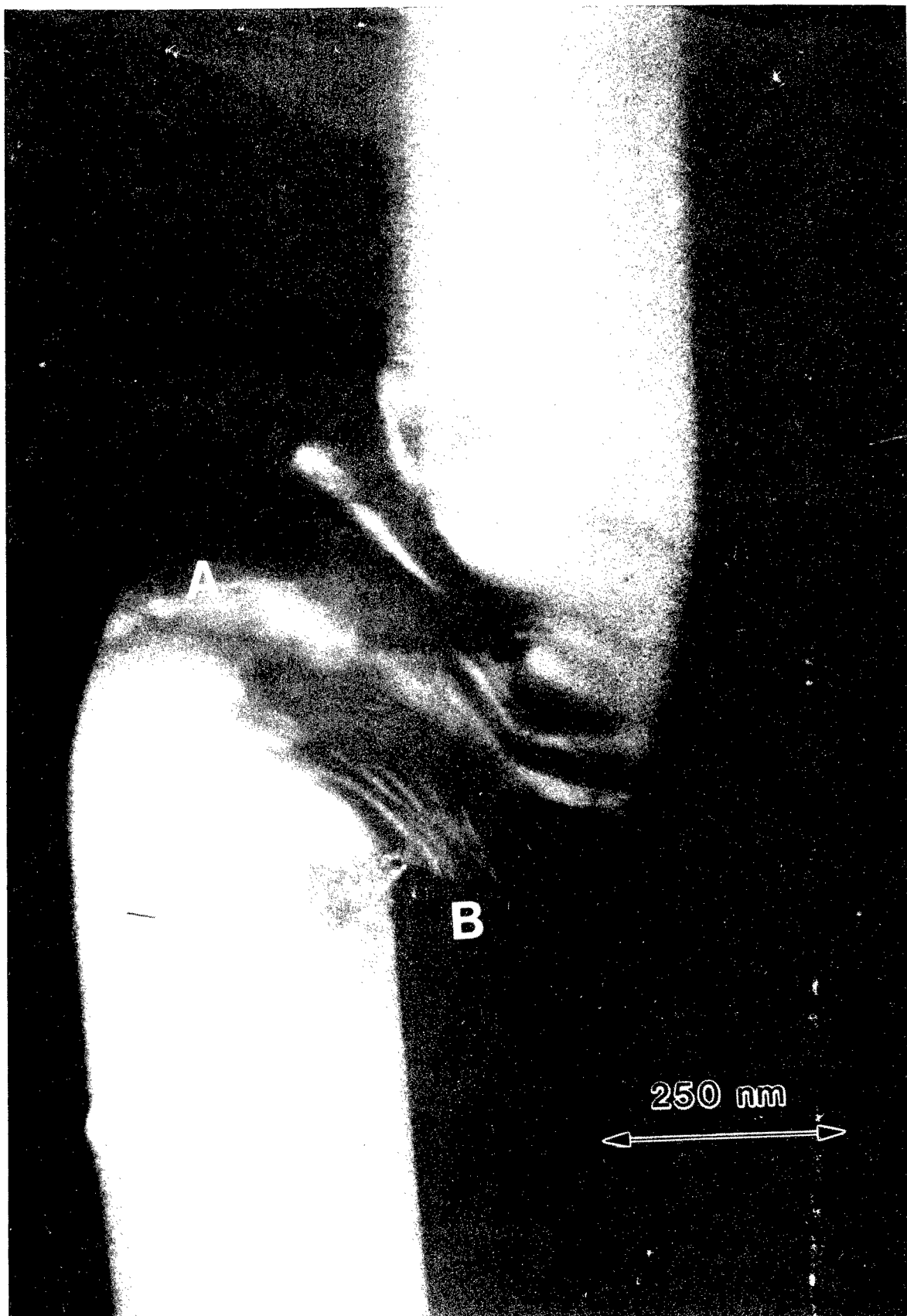
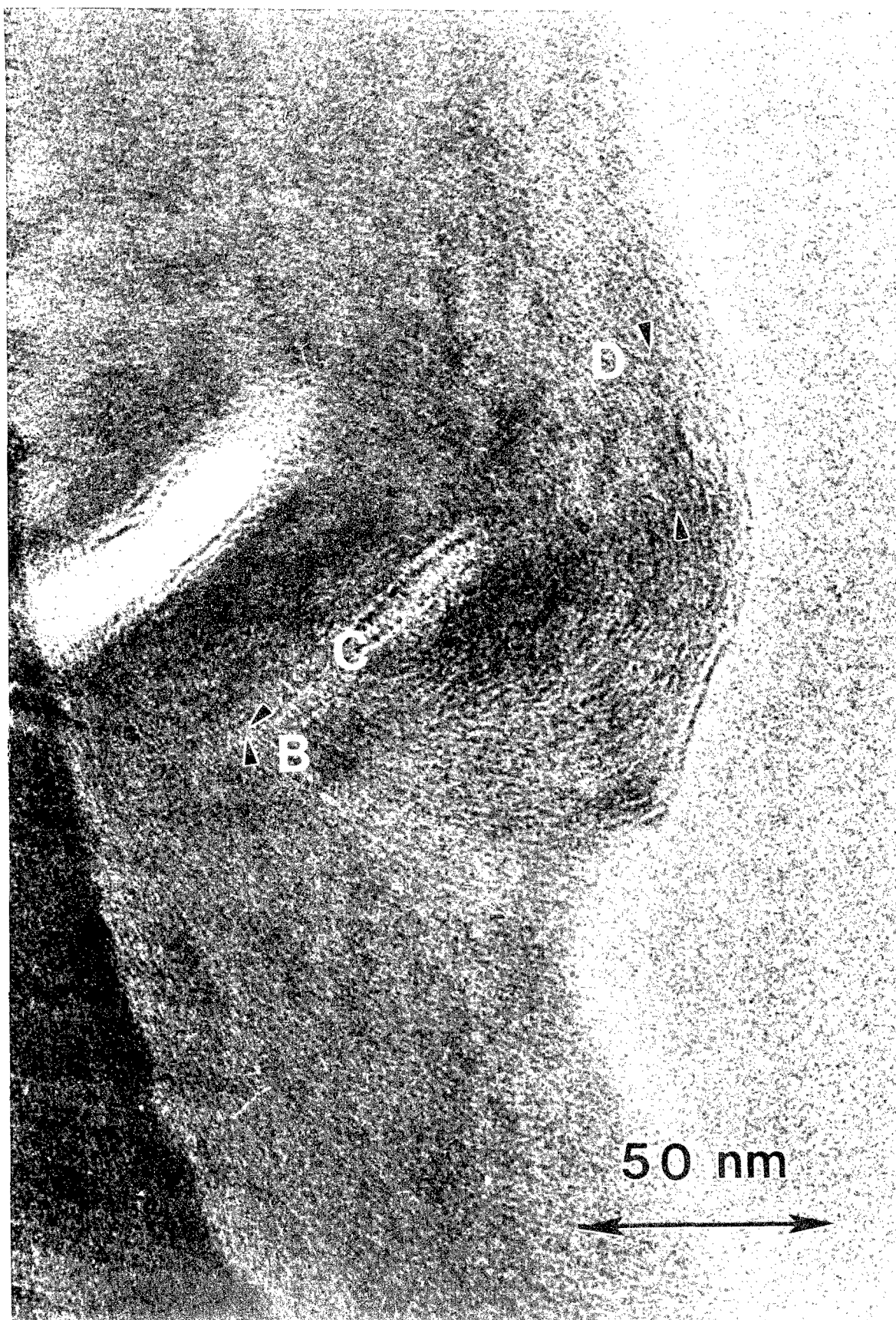


Figure 5.6: Fibrillated kink in PBZO HT 665. Elongated voids can be seen within the kink (A). The boundary region between kinked and unkinked material (B) is very sharp (less than 0.5 nm). Irradiation caused a slight opening of the kink during the exposure (C). Lattice resolution of the 0.5 nm (100) planes can be discerned near the edge of the fiber (D).



resolution of the 0.55 nm (100) planes can be discerned in a region near the very edge of the fiber (D).

Figure 5.7 is a tracing of an HREM lattice image of a kink band in PBZT. The orientation of the diffracting crystallites may be determined precisely and is shown with 20 nm long dashes as a function of position. Again, there is evidence for a sharp variation in contrast near the boundary of the kink where the deformation is away from the body of the fiber (A), while the boundary corresponding to deformation towards the fiber is more diffuse (B). In this BF image the contrast changes due to mass thickness effects, suggesting that there is material "extrusion" or "bulging" at the upper surface of the kink where the deformation is away from the body of the fiber.

Figure 5.8 is an HREM lattice image of a kink band in PBZO HT 665 C. The edge of the fiber fragment is to the right as in the previous micrographs. The arrows on top and bottom indicate the molecular direction in the undeformed regions of fiber on either side of the kink. Several striking features of the deformation process are visible. The local heterogeneity of the kinking strain is obvious. A tilt boundary corresponding to an abrupt change in molecular orientation (38 degrees over a distance of about 0.5 nm) is seen (A). Other features such as a local curvature of the PBZO lattice are apparent (B). Finally, note the abrupt

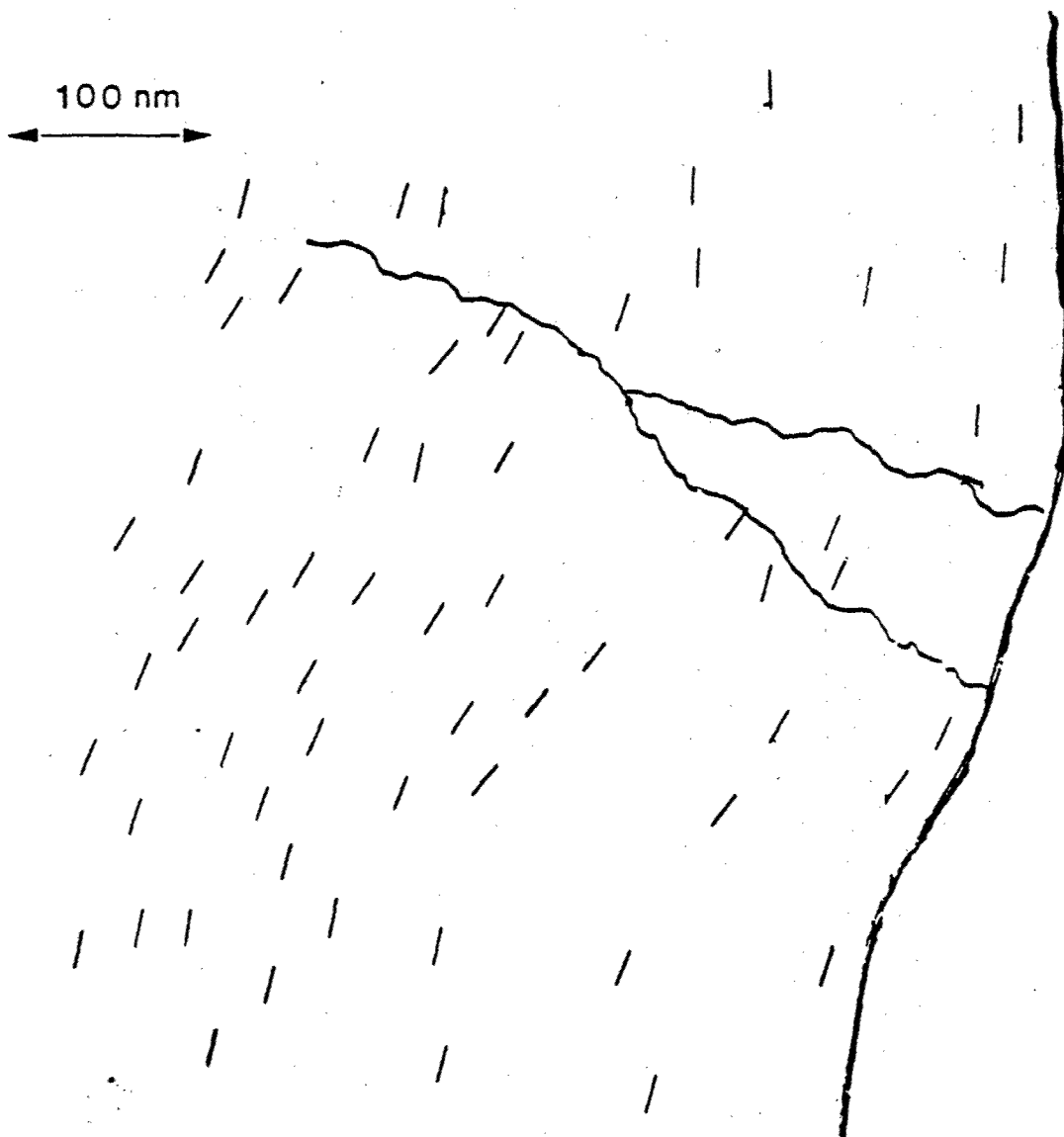
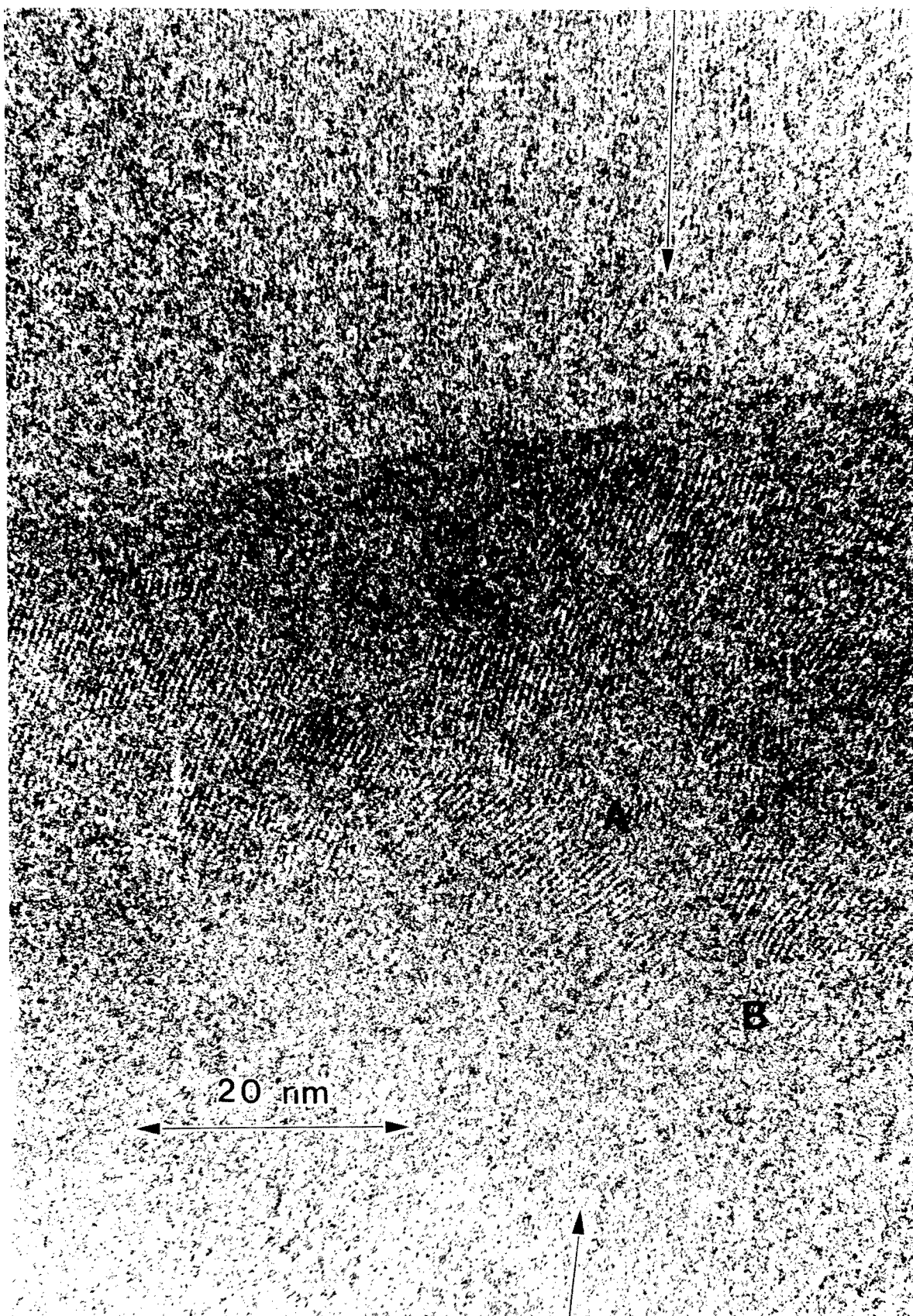


Figure 5.7: Sketch of a HREM image of PBZT showing the orientation of 0.59 (100) or 0.36 (010) lattice fringes as a function of position. The edge of the fiber as well as sharp surface features are drawn as solid lines.

Figure 5.8: HREM image of a kink in PBZO HT 665. The heterogeneous nature of deformation within the kink is evident. Sharp, high angle tilt boundaries are seen (A). Evidence for local bending of the PBZO lattice is noted (B). The nearest edge of the fiber fragment is to the right. Sharp variations in mass thickness contrast are seen on the upper boundary where the deformation is toward the edge of the fiber.



change and sharp contrast variation at the upper edge of the kink (C). This feature is again indicative of a local change in the thickness, indicative of a lateral failure causing material to be "extruded" at the upper boundary.

From these and similar images it is possible to measure the geometrical features pertaining to the kink deformation process. Figure 5.9 shows a plot of the number of occurrences of kinks in PBZO with a particular dimension in the direction of the fiber axis. Note that there is a strong tendency to form kinks in the 20-30 nm size range. These TEM results suggest that only the smallest features in SEM images of fiber surfaces are due to individual kinks, and that kinks observed in OM are due to kinks or kink bundles which have grown to a substantial size in order to cause significant scattering of light.

D. Discussion

In this section we will first review the implications of our morphological observations in terms of the geometry of kinking in rigid-polymers. We will then discuss a model for estimating the stress distribution around a propagating kink in terms of partial dislocations, and will interpret our experimental data in terms of this analysis. Finally, we will present a detailed molecular mechanism for the ini-

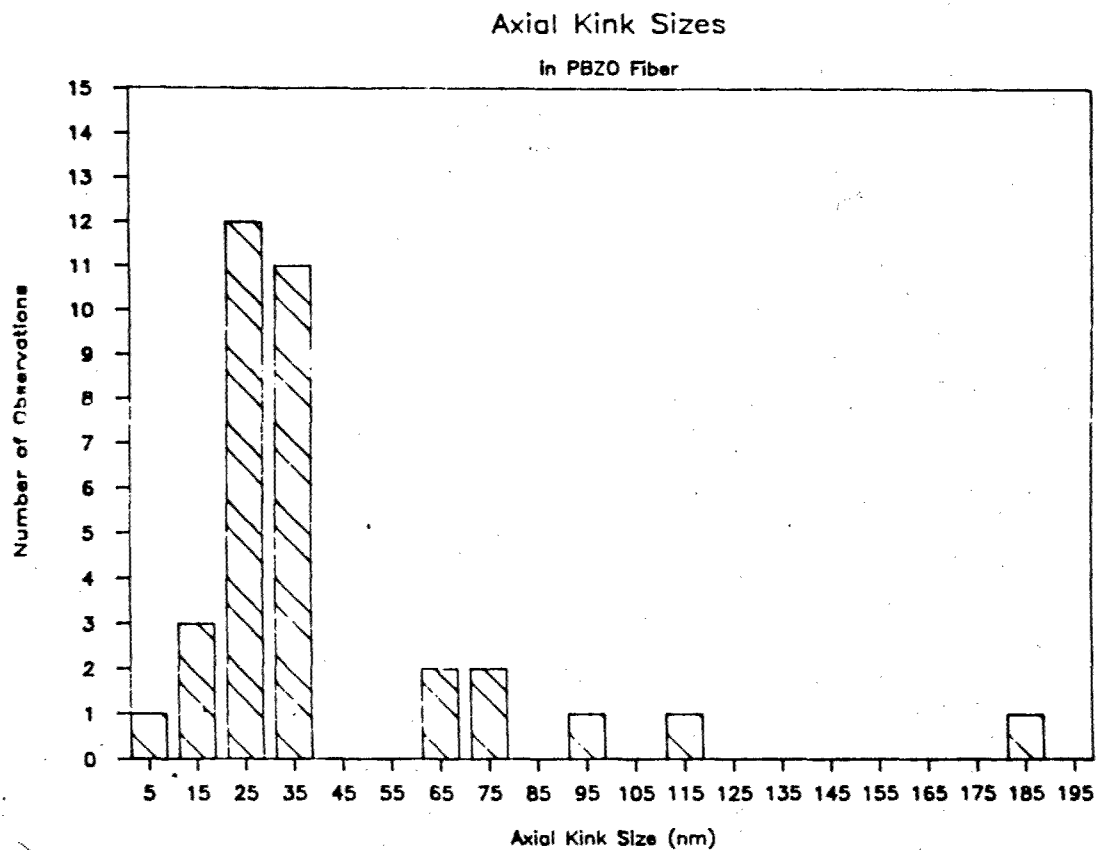


Figure 5.9: Histogram of the frequency of observation of a kink of a given axial size in DF images of PBZO. There is a strong tendency to form kinks in the 20-30 nm size range.

tiation and propagation of kink bands in rigid-rod polymers. From the insight provided by our new understanding of plastic deformation we are able to suggest several possible schemes for modifying microstructure and thereby improving the compressive strength of rigid-rod polymer fibers.

Our results indicate that kinks tend to be much smaller in the direction of the fiber axis (20-30 nm) than an average molecule (100-200 nm). Sharp, high angle tilt boundaries between adjacent crystals have been directly imaged within kink bands by HREM. These experimental observations confirm that a local a cooperative bending and/or breaking of covalently bonded polymer molecules is involved in kinking. The strain within the kink is not homogeneous; local crystallite misorientation, fibrillation, and bending of the lattice have all been detected.

The fact that there is a characteristic angle of kinking suggests an analogy of between kinking in these fibers and that of deformation twinning in atomic crystals. Let us now examine further this relationship in terms of the known unit cell of rigid-rod polymers. Referring again to Figure 5.1, K_1 is the twinning plane and represents the boundary between the kinked and unkinked regions of the fiber. n_1 , called the shear direction, lies in K_1 and is perpendicular to the second undistorted plane K_2 . The plane perpendicular to K_1

and K_2 is S , the shear plane. The intersection of S with K_2 is n_2 .

In rigid rod crystals the easy slip systems are those which involve sliding parallel to the molecular axis. These slip planes are of general index $\{hk0\}$. Likewise, in the kinking of fibers the direction of slip is along the fiber direction. Since K_2 is the undistorted plane which is rotated during deformation, it follows that K_2 belongs in the $\{hk0\}$ family and n_2 is in the direction $[001]$ along the chain axis. It is obvious the K_1 and n_1 are not parallel to $[001]$, but from the observed angle of kinking (Table 5.1), it is not possible to index K_1 and n_1 with small integer indices. In Table 5.2 some possible indexing for the observed kink geometry is presented using low index planes for the undistorted plane K_2 .

From the experimentally observed geometry and the large amount of shift disorder present in these fibers (Chapter III), it is apparent that the observed values of K_1 do not correspond to well defined planes of crystallographic order, nor is n_1 a high symmetry direction. This is not particularly surprising since the deformation twinning model is appropriate for large single crystals, whereas the structure of PBZT and PBZO consists of small (10 nm) crystallites with a random orientation about the chain axis.

Table 5.2

Possible Deformation Twinning Systems to
explain kinking in rigid-rod polymers

Material	Angle	g	K ₁	K ₂	n ₂
PBZT	72.6	0.627	(1 0 7) (0 1 13)	(1 0 0) (0 1 0)	[0 0 1] [0 0 1]
PBZO:					
AS	75.4	0.521	(1 0 8) (0 1 13)	(1 0 0) (0 1 0)	[0 0 1] [0 0 1]
HT 600	68.6	0.784	(1 0 6) (0 1 9)	(1 0 0) (0 1 0)	[0 0 1] [0 0 1]
HT 665	66.4	0.874	(1 0 5) (0 1 9)	(1 0 0) (0 1 0)	[0 0 1] [0 0 1]

The stress field which is present around a kink which has not propagated fully across a fiber may be envisioned by considering the accommodation strain required to incorporate a kink with non-parallel edges. Figure 5.10 shows a fiber before and after a wedge of material undergoes a uniform shear. Note that the material near the edge of the wedge which deforms away from the body of the fiber is dilated and therefore should be in relative tension. The lower edge of the wedge is compressed and therefore would be in relative compression.

An useful means of describing the strain field around a propagating kink or deformation twin is in terms of partial dislocations. The edge dislocations involved in kinking or twinning are "partial" because the Burger's vectors do not necessarily correspond to a full translation of the lattice. Also, they deform but do not disrupt the continuity of the lattice. The use of dislocations to accomodate the strains near twins was described first by Vladimirkii (1947). Frank and van der Merwe (1949) described these as "dislocations of second order". The Burger's vector of the dislocation lies in the twin boundary, which is also the glide plane. Olson and Cohen have suggested the name "coherency glide dislocations" to recognize the important fact that lattice is deformed yet retains its connectivity (1986). A similar dislocation is the partial edge dislocation attributed to Shockley which occurs at a stacking fault termination within

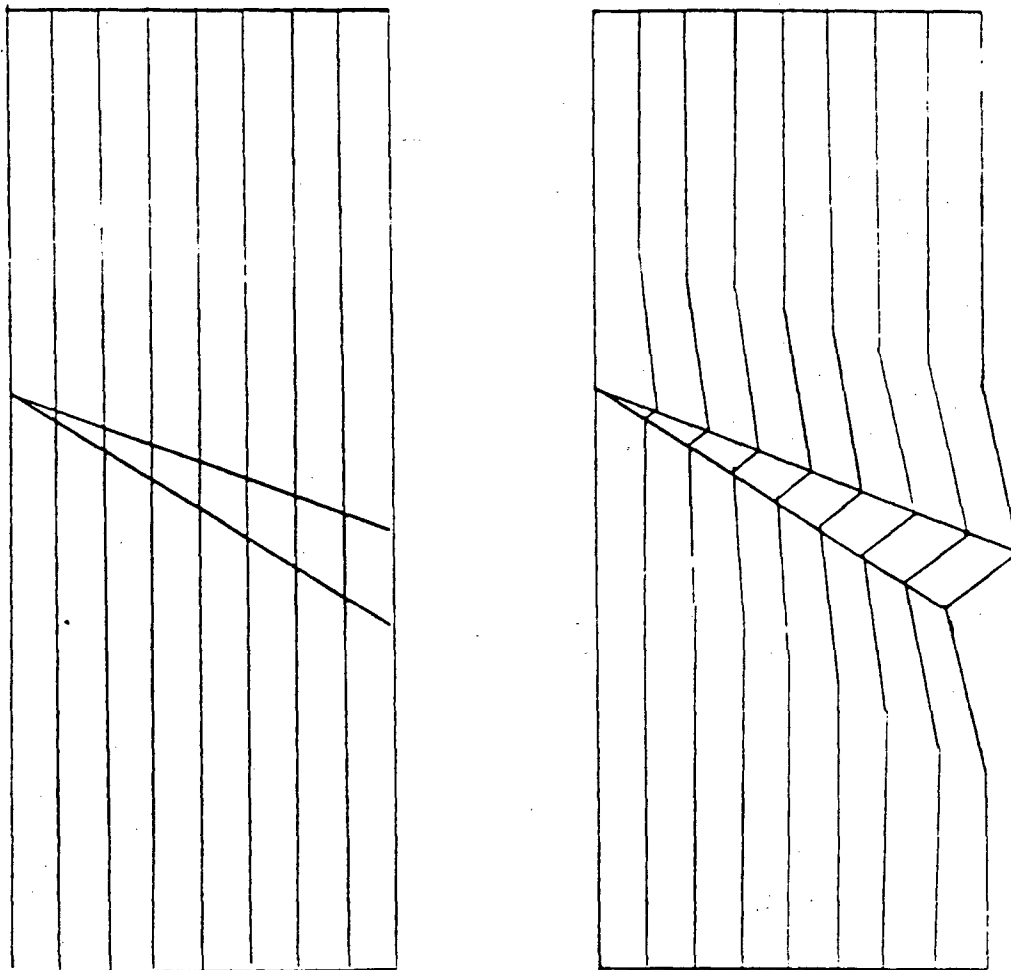


Figure 5.10: Schematic diagram illustrating the geometry of kinking. The drawing shows the case in which the crystalline packing is perfectly maintained after deformation and the boundaries of the kink band are not parallel to one another. In order to accomodate the kink band the upper boundary must deform away from the interior of the fiber, whereas the lower boundary must deform toward the fiber. This implies that the upper boundary would be in relative tension, whereas the lower boundary would be in relative compression.

a crystal (Hull, 1975, Kosevich 1979). The role of dislocations in twinning and their relationship to twin geometry has been described by Kosevich and Boiko (1971) and by Kosevich (1979).

Figure 5.11 shows a model of fiber containing several partial edge dislocations. These dislocations represent the local strain dilation above and compression below the kink front as it propagates across the fiber. The Burger's vectors of the edge dislocations are pointing toward the interior of the fiber, representing the shear strain which would be necessary to return the deformed region back to its originally undeformed configuration. This is the amount of shear induced as a dislocation passes an originally undeformed area. Using this model, kink formation in rigid-rod polymer fibers may be considered as the nucleation and subsequent propagation of a bundle of partial edge dislocations of like sign across the body of the fiber. As shown in Figure 5.10, the strain field around the dislocation bundle is expected to be dilational on top of the bundle (as drawn) and compressional on the bottom.

In the model shown in Figure 5.11, the dislocations are separated by sharp, coherent tilt boundaries across which the rigid-rod polymers undergo a large, local change in orientation. This deformation will require a local bending and/or breaking of a rigid-rod polymer molecule. This model

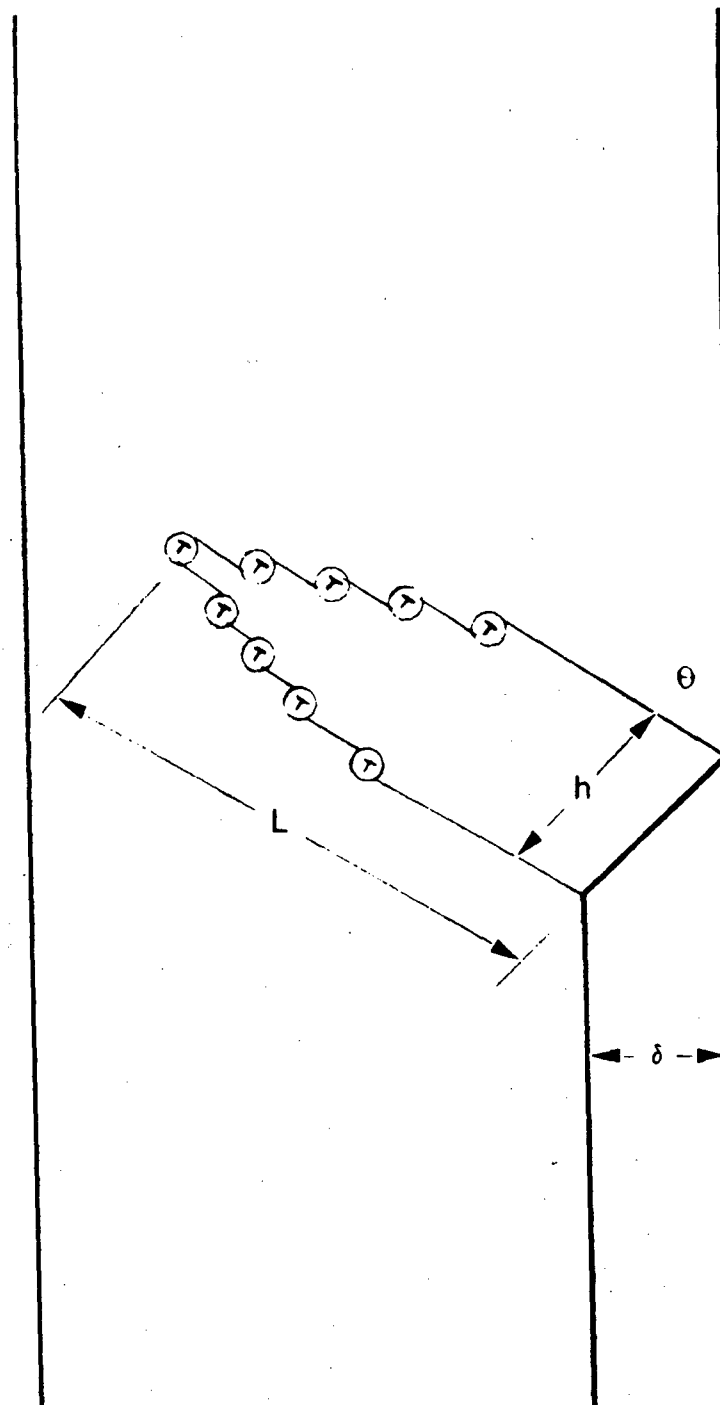


Figure 5.11: Schematic of the partial dislocation model of kink formation and propagation. The mechanism involves the formation of a bundle of dislocations which propagate across the sample. The number of dislocations in a given kink can be determined from the observed kink geometry if the Burger's vector is known or if one is assumed.

is similar to that proposed by Young et al. (1978, 1979) for deformation twinning in poly(diacetylene). It is important to note, however, that the partial edge dislocations involved in kinking of axially disordered fibers do not seem to be well-formed and localized as they are in materials with large crystals.

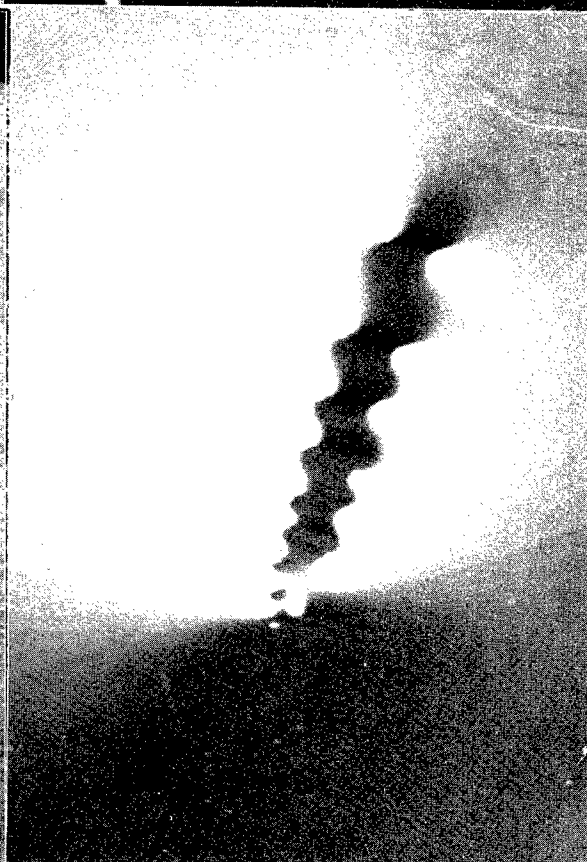
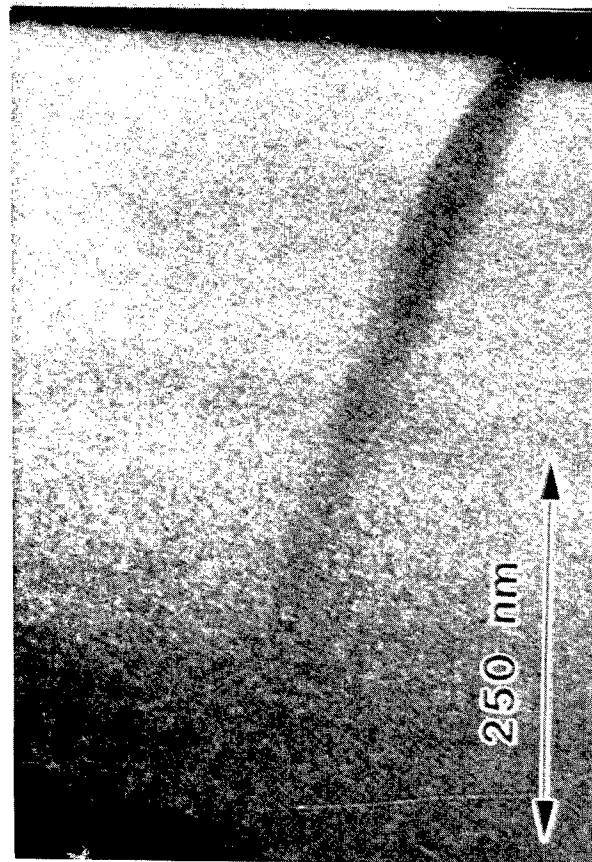
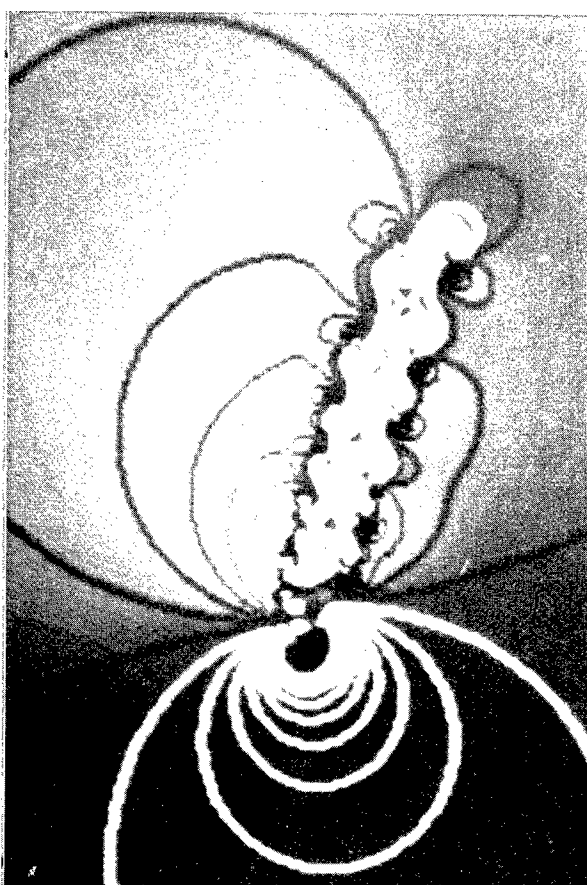
An important point to understand is that it is not necessary to have a well-defined crystal lattice in order to have a dislocation. The Burger's vector of a dislocation in a continuous substance is defined by the path integral of the elastic displacement around the dislocation direction (Hirth and Lothe, 1982). Dislocations can be used to describe any inhomogeneous strain distribution, but this representation is not necessarily unique (Hull, 1975). Future work should clarify the applicability of dislocation models in partially disordered systems and compare these dislocations with those in systems with much more developed order.

By analogy with deformation twinning, the strains characterizing the shape of the kink at the surface are indicative of the number of dislocations present within the sample interior, as long as the dislocation geometry is known or assumed (Kosevich and Boiko, 1971). From Figure 5.11, the amount of lateral strain is d and the size of the kink in the direction of the fiber is h . The number of dislocations involved in making such a kink is given by $h=N a$ and $d=N b$,

where a is the projection of the Burgers' vector in the direction of the fiber axis and b is the projection of the Burger's vector perpendicular to the fiber axis. From the kink in Figure 5.4 we measure $d=14$ nm and $h=32$ nm. This gives a ratio $h/d = a/b = 2.3$. The characteristic dimension along the axis of the fiber is $d_{001} = 1.24$ nm, the monomer repeat distance. If this number is used as a , this gives $b = 0.55$ nm. This is close to a lateral spacing between neighboring molecules, namely $d_{100} = 0.59$ nm. Using these values as the characteristic size for the Burger's vectors comprising the kink gives $N=25$. Hence, the kink in Figure 5.4 may be modeled as a propagating bundle of 25 partial dislocations with $a=1.24$ nm and $b=0.59$ nm.

It is possible to use this dislocation model to estimate the form of the stress field around a propagating kink band. Figure 5.12a shows the partial kink from Figure 5.4 and the positions of the dislocations determined with an extended Burgers vector of $a' = 5a = 6.2$ nm. This larger value for the Burgers vector roughly corresponds to the resolution of the dark field image in Figure 5.4. Using a larger value for the Burgers vector simply enables us to rescale the problem to consider a fewer number of dislocations. Whereas before there were 25 dislocations with the choice of $a=1.24$ nm, with $a'=6.2$ nm there should be a net of 5 large dislocations in this kink. The positions of these dislocations were determined by finding the intersections of lines perpendicular to

Figure 5.12: Dislocation stress model. (a) Detail from Figure 5.4 showing the kink which had not propagated completely across the fiber. (b) Positions of the dislocations determined using $b=6.2$ nm. (c) The hydrostatic component of the stress field around the kink using the dislocation model. Here, hydrostatic tension is in white and compression is in black. (d) Iso-stress contour lines. Note the compressive side is curving down toward the body of the fiber.



the edge of the kink with the kink boundary (Figure 5.12b). During this exercise it was found that the kink had propagated down and into the fiber far enough so that it was necessary to include a second set of dislocations of opposite sign at the bottom of the kink. Hence, the outline of the kink in Figure 5.12a can be described by 11 edge dislocations with the Burger's vectors pointing toward the interior of the fiber on the upper side of the kink, and 6 edge dislocations with the Burger's vectors pointing toward the outer surface of the fiber on the lower side of the kink.

The stress field around an edge dislocation in an isotropic medium oriented with the Burgers vector parallel to the x -axis and the direction of the dislocation parallel to the y -axis is given by the following equations (Hirth and Lothe, 1982):

$$\sigma_{xx} = -C y (3x^2 + y^2) / (x^2 + y^2)^2 \quad (5.3)$$

$$\sigma_{yy} = C y (x^2 - y^2) / (x^2 + y^2)^2 \quad (5.4)$$

$$\sigma_{xy} = C x (x^2 - y^2) / (x^2 + y^2)^2 \quad (5.5)$$

$$C = G b / (2\pi (1 - \nu)) \quad (5.6)$$

where \mathbf{x} and \mathbf{y} are the positions around the kink, G is the shear modulus, b is magnitude of the Burger's vector, and ν is Poisson's ratio.

These formulae are appropriate only for isotropic, linearly elastic media with localized dislocations. Obviously, the highly anisotropic nature of PBZO and PBZT makes it necessary to seek a rigorous solution to the stress and strain distribution near a kink with anisotropic dislocation theory (Steeds and Willis, 1979). Rigorous solutions to problems in anisotropic elasticity theory may lead to results which are non-intuitive (R. Farris, private communication). However, our interest here is in establishing the general form of the stress field around a propagating kink in terms of a simple dislocation model. This naive approach provides a helpful understanding of the micromechanisms of kink nucleation and propagation. The success of this method provides an impetus for future studies where more realistic aspects of known material behavior can be incorporated.

The stress field around the dislocation array for the kink in Figure 5.12a was solved numerically by assuming linear elastic behavior. The stress field of the sample was determined by the linear superposition of the individual stress fields generated by each dislocation. The result of this calculation is shown in Figure 5.12c where the

hydrostatic component of the stress field ($\sigma_{xx} + \sigma_{yy}$) is shown as a function of position around the kink. The image is dark where the material is predicted to be in local hydrostatic compression and light where there is local hydrostatic tension. Contours of constant hydrostatic pressure drawn at intervals of 0.1 G are shown in Figure 5.12d.

It is apparent that from Figures 5.12c and 5.12d that there is a region of hydrostatic tension on the upper side of the kink and hydrostatic compression on the lower side of the kink. The kink has migrated noticeably toward the compressive side, curving away from its initial trajectory.

The "sharp" and "smooth" image contrast features of the kink previously mentioned can now be rationalized in terms of this stress distribution around the kink and the asymmetric nature of the intermolecular potential function. Figure 5.13 shows a plot of a typical intermolecular potential function (Van Vlack, 1983). In compression, the energy simply increases as the repulsive forces act to resist strain, and there is no instability. However, in tension an instability occurs at a point when the effective modulus (the curvature of the energy-position function) becomes zero.

If such an instability does occur, then the deformation band might become pinned on the tensile boundary when

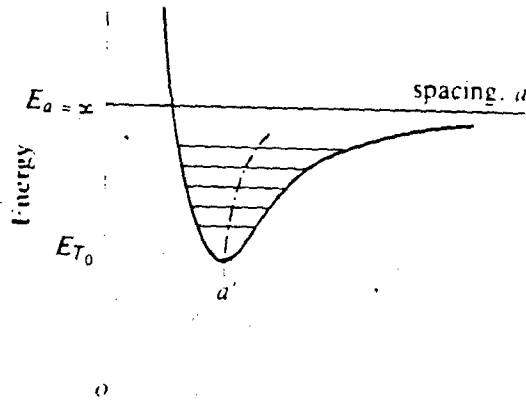


Figure 5.13: Schematic of an asymmetric potential well. In compression there is no instability, but in tension there is a point where the modulus becomes zero. Adapted from Van Vlack (1983).

adjacent molecules split apart in the lateral direction. The kink would then grow by propagation toward the compressive side. Similar indications of growth in the compressive direction can be seen in more macroscopic kinks of carbon fiber composites observed by OM (Evans and Adler, 1978), and evidence for axial splitting is seen in deformation twins of poly(diacetylene) (Young et al., 1978; Young et al., 1979). Lateral splitting in PBZO is evident within the kink band in Figure 5.6, and is sometimes visible by SEM near kink bands (Adams, Vezie, and Krause, 1988).

It does not seem likely that the dislocations move smoothly across the fiber during the deformation process. The glide planes involved correspond to the K_1 planes of the deformation twinning model discussed earlier, which were found to be non-crystallographic and oriented at an oblique angle to the covalently bonded fiber axis. Therefore, it seems reasonable that dislocation glide will be severely hindered in the lateral direction. A more realistic model than uniform glide is the irregular nucleation of dislocation "packets" in the region preceding the kink boundary. As noted earlier, the curvature of the kink toward the compressive side suggests that these dislocations preferentially nucleate in pairs of opposite sign on the compressive side of the propagating kink front. This mechanism of growth may explain why some fully grown kinks show one kink boundary

which is sharp and well formed, while the other is more irregular (see for example, Figure 5.3).

Besides the problem of restricted dislocation glide, a further complication is the non-uniformity of shear strain which is possible within the kink. Figure 5.8 shows that while crystallinity is maintained after kinking, the strain within the kink is very non-uniform. We interpret this to mean that not every K_2 plane within the kink band undergoes the same amount of shear with respect to its neighbors. In other words, the shear within the kink is "blocky" rather than "fine" shear. This is certainly the case in the PBZO fiber which was seen to exhibit fibrillation within the kink band (Figure 5.6). This non-uniformity of shear strain is reasonable given the polycrystalline nature and small crystallite size (approximately 10 nm (Chapters III and IV)) which leads to a high abundance of lateral and axial grain boundary defects. Axial Chain Invariant (ACI) grain boundaries (Chapter VI) will involve the intertwining of polymer molecules and therefore may be particularly resistant to shear deformation.

For rigid-rod polymers in tension the tensile breaking stress is about 4 GPa and the modulus is about 400 GPa, or $\sigma/E=10^{-2}$. If we assume that the shear stress τ and shear modulus G which control kinking have the same ratio, we obtain a value of the critical kink dimension L from the

Frank and Strohm model equal to 1.5 microns using $b = 0.5$ nm. The corresponding width of the kink is given by the Frank and Strohm model by the relation $w = Ls/Gg$, which in our case would be 25 nm. From the histogram of kink dimensions (Figure 5.9), we see that this is in good agreement with our experimental observations.

The validity of dislocation models like those discussed here in understanding the plastic deformation behavior of disordered systems has been discussed by Argon (1981). In crystalline solids, plastic deformation occurs by the familiar mechanism of dislocation motion. Dislocation sources usually are not widely and uniformly distributed and therefore the deformation always becomes localized. The mechanism of plasticity in disordered media such as metallic glasses is proposed to involve a set of local shear transformations having a distribution of free energy barriers which depend on the free volume distribution. The difference is that structural disorder severely hinders easy dislocation motion; therefore the material can support higher loads and becomes more "activated", that is, it is possible to nucleate new sources of deformation more uniformly throughout the material than in the crystalline case.

In kinking of rigid-rod polymer fibers we seem to be somewhere between these two extremes. The orientation of the molecule along the fiber provides for easy slip along the

[001] direction, but the high axial disorder, fiber symmetry, and small crystallite size mean that the local defect concentration is much higher than in materials with larger crystals. These local constraints serve to provide an increased resistance to deformation that enables the nucleation of new dislocations at the propagating kink front. Hence, we have a deformation process that becomes localized because of the ability of the fiber to slip along its axis and form a kink band, but the propagation of the kink band is hindered by the disorder perpendicular to the fiber axis and therefore involves the activation of new sources of deformation at the leading edge of the kink.

To summarize, a model for the micromechanisms of kink deformation in rigid-rod polymer fibers is presented. First, there is an initiation step which involves nucleation of a bundle of edge dislocations which delineate a region of shear deformation which extends to the edge of the fiber. The driving force for the nucleation of these dislocations is the reduction in matrix strain energy caused by the shear strain along the kink boundaries. Once this nucleus is formed, the angle of kinking is defined. Subsequent propagation of the kink involves the cooperative rotation of subsegments of neighboring polymer molecules as the kink front moves past. Instabilities occur on the tensile side of the kink front which impair dislocation motion and promote propagation of the kink toward the compressive side of the deformation zone.

With this model of the molecular motions involved in compressive deformation of polymer fibers in mind, it is useful to consider possible routes for improving the compressive strength of these materials. We reconfirm the conclusion of the buckling instability model which says it is important to improve the shear modulus. We also find that modifications which make it harder for kinks to initiate, such as surface hardening, would be useful. Such a scheme might involve the crosslinking or partial graphitization or oxidation of the sample surface.

Since we have established that local, sharp bending of molecules is involved in kinking, molecular structures such as "ladders" and "sheets" which are even more difficult to bend than PBZT and PBZO molecules are of interest. Also, modifications which improve shear resistance will increase the amount of energy required to shear the material within the kink, and therefore will decrease the amount of energy available for kink propagation. An example might be a molecule which becomes somehow "twisted" or "intertwined" with its neighbors.

The axial disorder and small crystallite size in these materials means that the inherent kink nucleus size is probably already quite small. Dramatic improvements in crystallite size and ordering will be useful if they can serve to

improve lateral interactions, but the formation of very large PBZT or PBZO crystals may facilitate easy slip and therefore make kinking easier. Similar arguments hold for crystal shape. Long, thin crystals should restrict the glide of dislocations across the fiber but will facilitate axial slip, whereas short, oblate crystals should restrict axial slip but may make it easier for lateral dislocation glide.

Similar arguments can be made about other schemes for trying to hinder dislocation motion across the fiber and therefore disrupt kink propagation. A possibility might involve the placement of a second phase or perhaps local crosslinking to act as dislocation obstacles. Such microstructural modifications will be successful only if they do not serve as kink initiation sites.

Another problem with large PBZT and PBZO crystallites is that this might promote the preferential segregation of chain ends to the crystal boundaries. This could have a deleterious impact on mechanical properties due to the presence of well-defined flaws which would serve as kink nucleation sites in compression and as pre-cracks in tension. This argument can be extended further to consider the importance of the molecular weight distribution. If the polydispersity of the molecules was small, then any tendency for chain ends to segregate would be repeated all the way down the fiber axis. A broad distribution in molecular length

makes it possible for these flaws to be more randomly distributed and therefore of lesser importance.

As a final note, it should be mentioned that the formation of kink bands is not necessarily a "bad" characteristic. Kinks serve to absorb a substantial amount of energy and therefore enable high performance fibers to be well suited for applications where toughness is a primary concern. It should be kept in mind that modifications to improve compressive strength will be most useful if they can increase the stress required for kink initiation yet still allow the deformation to precede by kinking without causing fracture once the instability occurs. In this way, we will have obtained a material which is simultaneously strong, stiff, and tough.

E. Quantitative Observations of Kinking

This section will outline an experimental study of the plastic response of rigid-rod polymer fibers under axial compression. In particular, the linear density of kink formation will be determined as a function of plastic strain. This will enable an estimation of the energy involved in creating these deformation zones in polymer fibers.

1. Thermodynamics of Kinking

Consider a system consisting of a fiber subjected to a uniform axial compressive load as in Figure 5.14. After the strain reaches a critical amount, kinks are observed to initiate within the fiber. As the amount of strain applied to the fiber increases, more and more kinks appear.

In this analysis, it will be assumed that the material behaves in a purely elastic-plastic behavior. The fiber is assumed to respond linearly up to the yield point and then undergo plastic deformation at the yield stress. For PBZT, the critical strain to initiate kinking $\epsilon_c = 0.001$, the critical kinking stress is $\sigma_c = 400$ MPa.

The total energy density at the yield point is the area under the stress-strain curve:

$$E_c = 1/2 \sigma \epsilon_c \quad (5.7)$$

We will assume that the fiber is able to withstand this amount of energy density without kinking. All extra energy put into the fiber by the action of external stresses past this energy density is used to make kinks. Some of this extra energy will be stored as an internal energy change, the rest will be dissipated to the surroundings. The amount of excess energy density increase for ϵ_p past ϵ_c is:

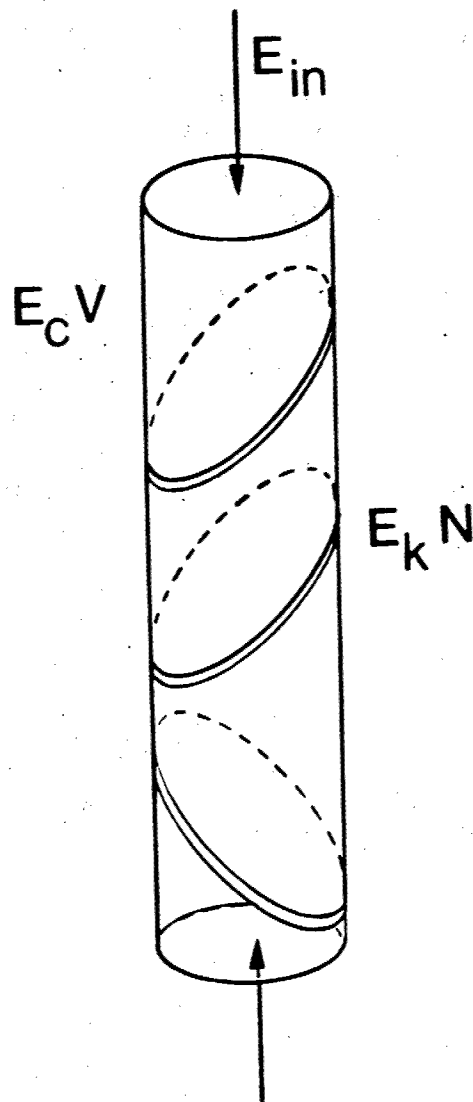


Figure 5.14: Energy balance of a fiber in compression. The energy in (E_{in}) is stored as elastic energy until the material reaches the stress required to form kinks. Further stressing either causes more kinks to initiate or causes already formed kinks to grow.

$$E_e = \sigma_c \epsilon_p \quad (5.8)$$

with assumption of ideal plasticity. The total excess energy in the fiber is then:

$$E_t = E_e V \quad (5.9)$$

where the volume V is given by

$$V = A_0 l \quad (5.10)$$

with A_0 the cross-sectional area of the fiber and l its length. If the strain ϵ_p causes N kinks, then the energy used per kink is:

$$E_k = E_t / N \quad (5.11)$$

If the number density $\rho(\epsilon_p)$ of kinks which occur per unit length of fiber for a given plastic strain ϵ_p is known, then the total number of kinks in a given length l of fiber with plastic strain ϵ_p is:

$$N = \rho(\epsilon_p) l \quad (5.12)$$

The energy per kink can be expressed as a surface energy by dividing by the area per kink:

$$E_s = E_k / A$$

(5.13)

The area of a kink boundary is related to the cross-sectional area of the fiber by the relation:

$$A = A_0 / \sin(\Theta)$$

(5.14)

where Θ is the angle of the kink boundary with respect to the fiber axis (Figure 5.2). Hence, by combining the above equations we obtain the surface energy of a kink:

$$E_s = \sigma_c \epsilon_p \sin(\Theta) / \rho(\epsilon_p)$$

(5.15)

This equation shows that fewer kinks will be initiated per unit of plastic strain if they are more energetically costly to produce. Likewise, it predicts that the function $\rho(\epsilon_p)$ depends only on the critical stress and the surface energy of the kink and not the area of the fiber.

2. Experimental

The geometry used in this study has been used previously by DeTeresa et al. (1988) to investigate ϵ_c , the critical strain for kink initiation. The fiber is bonded with Krylon acrylic spray to a clear tensile bar which is then subjected to a known strain. The bent configuration is observed in the

optical microscope and the critical strain for kink formation determined by observation. In this study we extended the experiment by counting the number of kinks observed as a function of strain above the yield point.

The strain within the bent beam configuration (Figure 5.15) is given by

$$\epsilon(d) = 3tv/2L^2(1-d/L) \quad (5.16)$$

where t is the thickness of the beam, v is the diameter of the wedge used to deflect the beam, L is the position of the wedge under the beam, and d is the distance from the metal clamping plate. The strain varies linearly with d from a maximum value of $3tv/2L^2$ at the clamping plate to zero beyond the wedge.

The number of kinks as a function of distance was determined by securing the sample holder on an optical microscope with a calibrated sample translation stage. The sample was observed before and after straining so that kinks which may have been present before the experiment could be accounted for. The density of kinks seen before straining was low (less than 1 kink/mm) so that this did not pose a serious problem. The reproducibility of feature detection and distance measurement by this technique was found to be excellent.

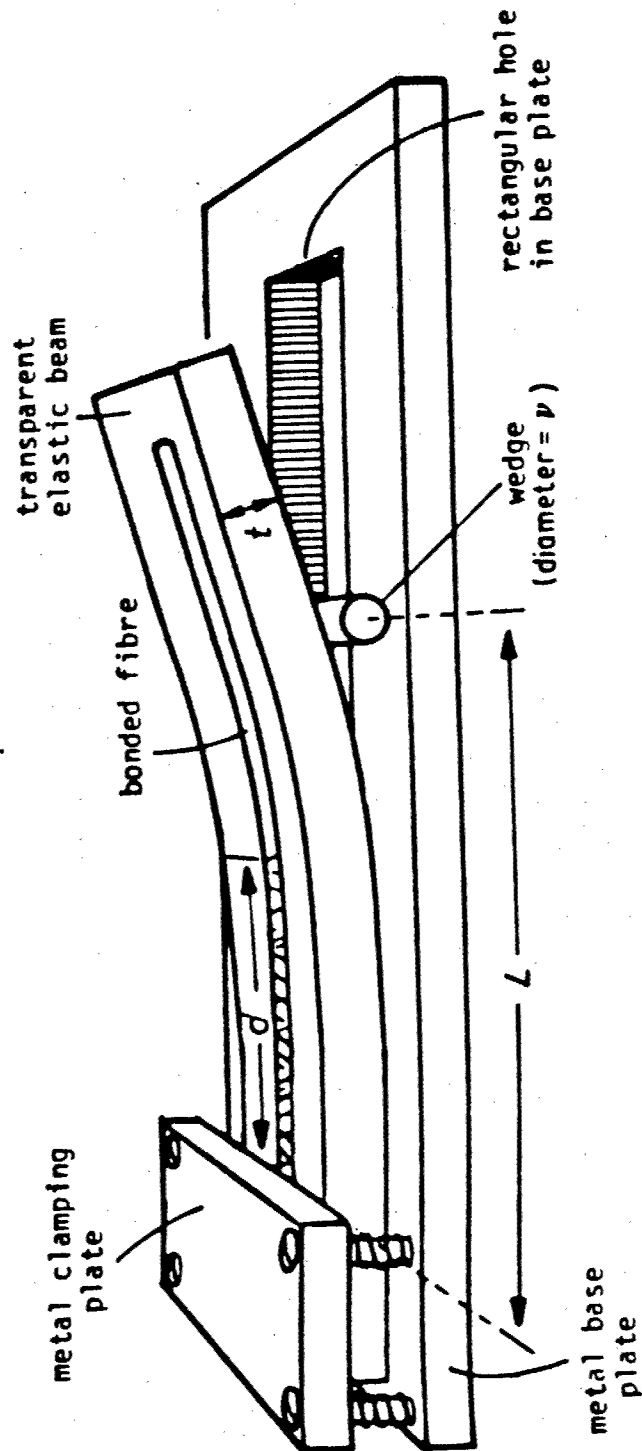


Figure 5.15: Experimental configuration used by DeTeresa (1985) to study the critical strain necessary for kink initiation.

In TEM we found that individual kinks can be quite small (20-30 nm) in the axial direction. During OM investigation of the deformation of originally unkinked fiber we found that kinks initiate at relatively large separations from one another so that they can be easily distinguished. That kinks are visible in OM at all implies that we are apparently imaging kink "bundles" which occur as a number of kinks grow together across the fiber in a local region.

Takahashi, Miura, and Sakuri (1983) presented OM and SEM data of a PPTA fiber that had been kinked to a strain of 20% in compression while held in a resin matrix. The OM and SEM images are similar in appearance, indicating that the linear density of kinks observed in OM is reasonably consistent with that determined by SEM. However, it should be kept in mind that kink densities measured by OM can only represent only a lower bound on the actual number of individual kinks present, and should be thought of as indicative of the number of kink "bundles" rather than of individual kinks.

A experimentally obtained plot of the total number of kinks visible in OM N_t vs x is shown in Figure 5.16. Note that past a critical strain the number of kinks observed goes up dramatically.

Total Kinks as a Function of Position

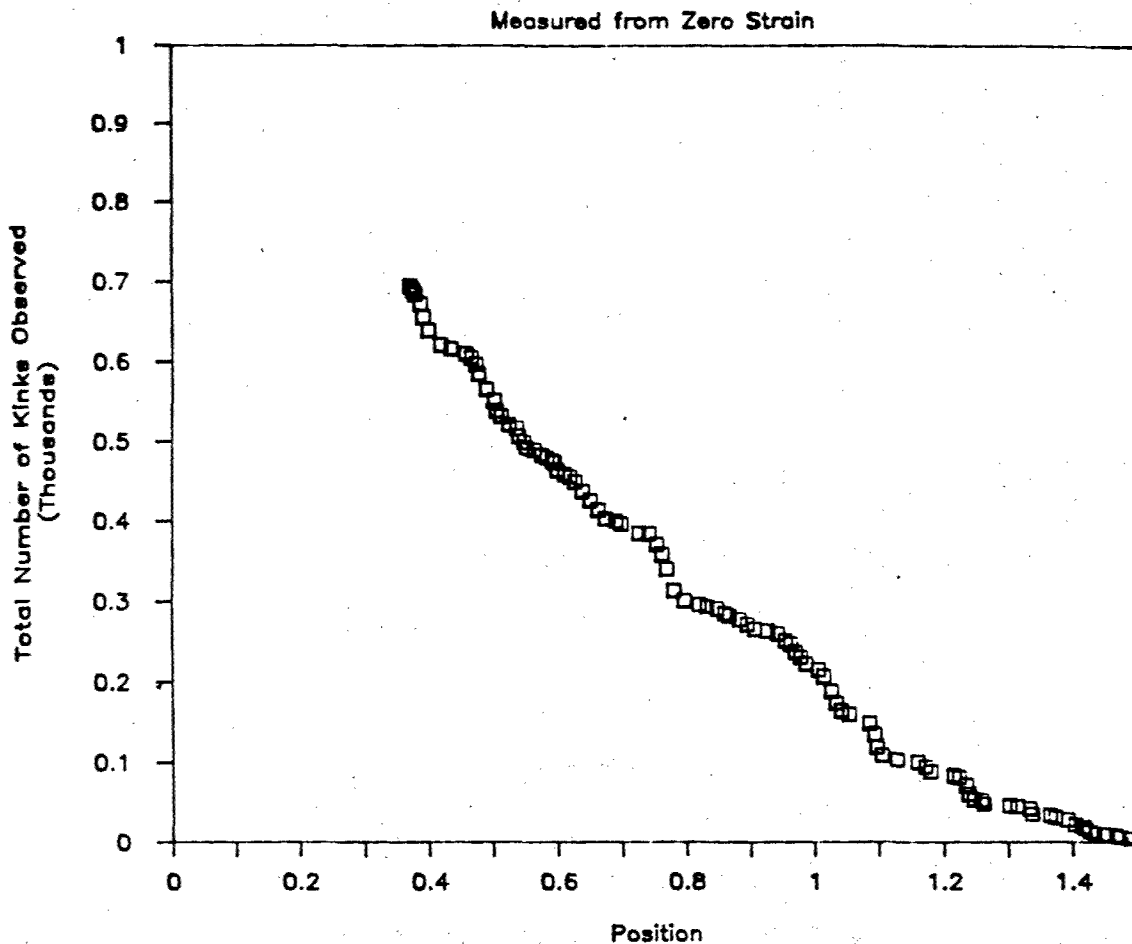


Figure 5.16: Typical plot of the total number of kinks N_t seen in the optical microscope vs. position x along the fiber. The strain is the highest at $x=0$. The curve was generated by starting at large x and then counting the number of visible kinks as a function of distance. After reaching the critical yield strain the number of visible kinks increases dramatically. The density of kinks induced as a function of strain is found by taking the derivative of this curve with respect to x .

Although the experimentally measured quantity was N_t vs x , we wished to obtain $\rho(\epsilon_p)$, the density of kinks as a function of uniform strain. However, in this experiment the strain was not uniform. If the strain is uniform, then the total number of kinks observed at position x would be

$$N_t = \int_0^x \rho(\epsilon) dx \quad (5.17)$$

Since ϵ was now a function of x , in our case we have:

$$N_t = \int_0^x \rho(\epsilon(x)) dx \quad (5.18)$$

Hence, the desired function can be obtained by taking the derivative of the experimentally measured $N_t(x)$ with respect to x . This gives the function $\rho(\epsilon(x))$. It would be of interest to compare the results of the experiments described in this chapter where $\epsilon(x)$ varies with a jig in which $\epsilon(x)$ was constant.

3. Results

Figure 5.17 shows the density of kinks per mm of fiber $\rho(\epsilon)$ as a function of applied strain for PBZO as a function of heat treatment and for Kevlar 49. Note that the strain to initiate kinking is much lower for PBZO (0.001) than for

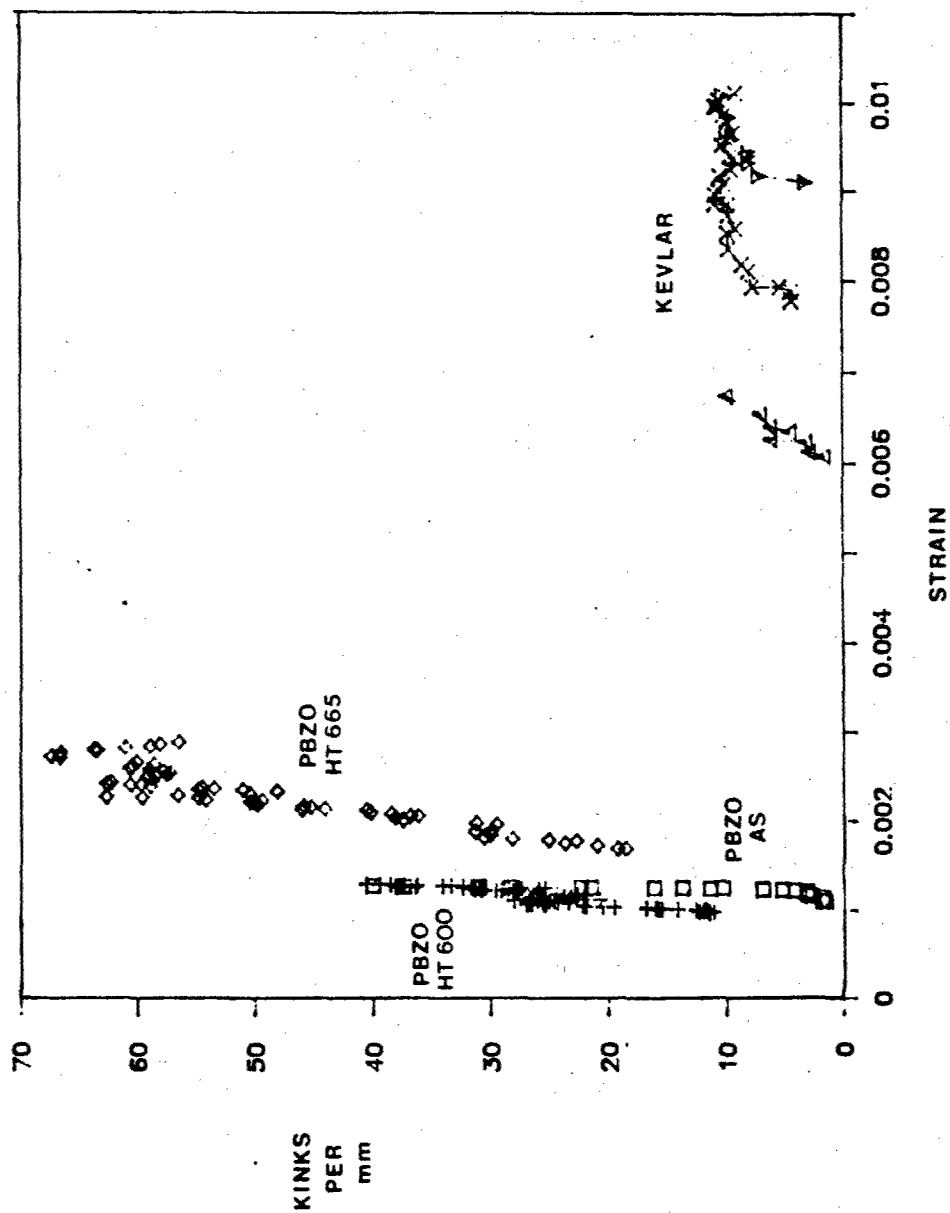


Figure 5.17: Plots of the density of kinks $\rho(\epsilon)$ vs. strain ϵ for PBZO as a function of heat treatment and for PPTA.

Kevlar 49 (0.005). Note also that the Kevlar 49 data seems to level off while in PBZO the kink density keeps increasing. This is apparently due to a transition for PPTA from kink initiation to kink growth at higher plastic strain. From the initial slopes of these curves it is possible to estimate the energy required to form kinks from the analysis given above. In this calculation the stress to initiate kinks was assumed to be $0.1 \sigma_t$, the breaking stress in tension. Table 5.3 summarizes these results.

The values of the surface energy of a kink obtained by this method (2000-7000 dyne/cm) are much larger than the normal surface tensions of organic liquids (20 dyne/cm). In fact, they are larger than the surface energies of typical solids (for Si(111), $E_s = 1240$ dyne/cm) (Swalin, 1972).

From theoretical studies of the buckling instability of isolated PBZO molecules, it was found that an energy of 5 kcal/mole was required to initiate strain localization in compression (S. Weirschke, 1988). Given the cross section of the PBZO molecule (0.2 nm^2), this corresponds to a surface energy of 160 dyne/cm. Since each kink will have at least two surfaces, this would give a minimum surface energy of 320 dyne/cm for purely elastic bending of the polymer chain.

Note again that the experimentally determined energy is more than an order of magnitude higher than this amount

Table 5.3

Kink Density Results

Fiber	ϵ_c $\%$	Kinks/mm $\epsilon=.001$	S.D.	Surface Energy dyne/cm
PBZO AS	0.11	184	39	2200
PBZO HT 600	0.08	66	4	6900
PBZO HT 665	0.10	38	2	7200

(2000-8000 dyne/cm). As mentioned earlier, the actual density of kinks should be higher than that determined in OM since each kink visible in OM likely consists of a kink bundle.

These results suggest that there is a great deal of the energy dissipated during kinking. This energy may be released as heat to the surroundings during the shear deformation, or may be stored as multiple bending of molecules within the kink bundle. Also, it may be that the theoretical calculation on single chains significantly underestimates the energy required to bend arrays of molecules to large angles.

F. Conclusions

We have established by low dose HREM imaging that sharp, localized bending occurs during kinking in rigid-rod polymer fibers. The characteristic dimension of kinks in the direction of the molecular axis is often much smaller than the average size of each molecule. We have observed large angle changes in molecular orientation (40 degrees) at very sharp (0.5 nm) tilt boundaries. We therefore conclude that local bending and/or breaking of covalent bonds is involved in the formation of kink bands in rigid-rod polymers.

A stress analysis of a propagating kink using partial dislocations indicates regions of local hydrostatic tension and compression near the kink front. The kinks exhibit "sharp" changes in orientation and material density on the tensile side of the kink, whereas the compressive side is more "diffuse". The kinks curve as they grow, moving down toward the compressive side of the boundary. We interpret these results in terms of lateral instabilities involving splitting failure due to the asymmetric nature of the intermolecular potential and the tensile nature of the local hydrostatic stress state.

A quantitative analysis of the plastic deformation of PBZO fibers by OM enabled an estimation of the energy required to form a kink bundle. It was found that for PBZO the density of kink bundles formed for a given increment of plastic strain decreased with increasing heat treatment. This means that it requires more energy to form kink bundles in the heat treated material. The surface energies for kink bundles are high (2000-7000 dyne/cm).

CHAPTER VI: GRAIN BOUNDARIES IN EXTENDED CHAIN POLYMERS

A. Introduction

By definition, a grain boundary is the interface between two adjacent crystalline domains. The study of the structure and energetics of grain boundaries in metallic and ionic crystals is well developed (Atkinson, 1988; Sutton and Baluffi, 1987; Sass, 1986). However, in crystals of long-chain covalently bonded molecules (like polymers) grain boundaries are not nearly so well understood.

The reasons for this lack of understanding are several. Polymer solids are a younger class of material and details of structure-property relationships have been less well investigated than metals and ceramics. Also, the organic composition of most polymer solids makes structural characterization of defects difficult at high resolution because of the sensitivity to electron irradiation. Finally, the large amount of disorder typical in polymer microstructures makes generalizations about specific "defect" features difficult. Despite these limitations, the study of grain boundaries in polymers is important because the crystallites are often extremely small (typically 10 nm), so that the amount of material which is residing in grain boundary regions makes up a substantial fraction of the sample volume.

Studies of grain boundary microstructure in metallic and inorganic crystals has benefited from the application of High Resolution Electron Microscopy (HREM) techniques (Buseck, Cowley and Eyring, 1988). Recent advances in HREM at low electron doses, made possible by stable high voltage instrumentation, advances in sample preparation, and careful attention to instrument operation (Chapter II), have now made it feasible to obtain images of grain boundary structures in certain polymers. However, the lack of theoretical studies on the structure and energetics of grain boundaries in polymers means that it is difficult to compare experimentally obtained HREM images with possible models for grain boundary structure. Also, the role of grain boundaries in determining material properties is not well established.

The HREM work discussed in Chapters (III-V) of this thesis has enabled the direct visualization of different types of grain boundaries between crystallites in rigid-rod polymers. The chain connectivity present in these systems has important implications for the structure and energetics of the grain boundaries which are observed. Here, we present a classification scheme for understanding the different types of grain boundaries in polymer solids. This simple analysis makes a distinction between grain boundaries that are parallel to the chain (lateral boundaries) and those which are not (axial boundaries). Also, it considers whether the

chain axes in the two crystallites are parallel (chain invariant boundaries), or not (chain rotation boundaries).

In the following section we will outline basic aspects of the theory of grain boundary geometry. We will then point out how the orientation of the chain axes in the neighboring crystals is important in determining the structure and energetics of these boundaries, and how this leads us to the proposed classification scheme. Finally, we will discuss each of the four types of grain boundaries (lateral chain invariant, lateral chain rotation, axial chain invariant, and axial chain rotation) in terms of their expected structure and energetics in polymer solids. We will speculate about the conditions necessary for the different types of grain boundaries to form, and will describe plausible molecular mechanisms which could facilitate their growth. When possible, we will present examples of these different kinds of grain boundaries from microstructures of the rigid-rod polymers PBZT and PBZO investigated in this thesis.

B. Grain Boundary Geometry

Grain boundaries are regions between two adjacent crystalline domains. The study of grain boundaries in metallic and ionic crystals is greatly developed. Of particular importance in understanding the energetics of grain bound-

aries is their geometry and atomic (or molecular) level structure. The structure of grain boundaries and interfaces is given by the O-lattice theory presented by Bollman (1970). Here, we review the essential features of the O-lattice approach in order to develop an understanding of the structure of a general grain boundary. We will then discuss questions of grain boundary energetics based on this structural understanding.

The positions of a site in space near the two crystals is given by the position vector \mathbf{x} . A convenient coordinate system for describing the vector \mathbf{x} is the crystal coordinate system defined by the unit cell vectors \mathbf{a}_1 , \mathbf{b}_1 , and \mathbf{c}_1 and some arbitrary origin. In this case, the coordinates of the endpoint of a given vector \mathbf{x} are (x_a, x_b, x_c) , where the x_i are the coordinates in terms of the unit cell basis vectors \mathbf{a}_1 , \mathbf{b}_1 , and \mathbf{c}_1 . For a given point, the first set of integers lower than (x_a, x_b, x_c) are termed the external coordinates, and the position of the point with respect to the external coordinate position the internal coordinates. For example, for the point $(3.53, 4.20, -5.29)$ the external coordinates are $(3, 4, -6)$ and the internal coordinates are $(0.53, 0.20, 0.61)$. The internal coordinates are always between 0 and 1.

Near this first crystal is a second crystal (2) which can be described by three unit cell vectors of its own \mathbf{a}_2 , \mathbf{b}_2 , and \mathbf{c}_2 . Every position in space can be described either by

the coordinate system of crystal 1 or the coordinate system of crystal 2. The relationship between the two coordinates systems is given by:

$$\mathbf{x}(1) = \mathbf{A} \mathbf{x}(2) \quad (6.1)$$

where \mathbf{A} is a transformation matrix. \mathbf{A} is a general affine transformation (perhaps stretch and/or rotation) which describes the relation between the two lattices (1) and (2).

For a given transformation matrix \mathbf{A} , certain points in space will have the same internal coordinates for both lattice 1 and lattice 2. The specific positions of these points of equivalence will depend on the transformation matrix \mathbf{A} . Such points are termed the "0-points", and represent coincidences between sites with the same internal coordinates. These points make a three-dimensional "0-lattice". When the values of the internal coordinates are equal to (0,0,0), the 0-lattice points correspond to lattice sites. In this special case the 0-lattice is a "coincidence site lattice" (CSL). In the general case, it is not necessary that the "0-points" be located precisely at lattice sites.

The geometry of grain boundaries is therefore determined by finding the transformation \mathbf{A} which relates crystal (1) to crystal (2), and then finding the orientation of the boundary with respect to the two crystals. This means that an

arbitrary grain boundary has five free parameters (the three rotation axes of A and the two rotation axes of the grain boundary plane). For rotations of an angle Θ about the z axis, A is given by:

$$A = \begin{pmatrix} \cos \Theta & -\sin \Theta & 0 \\ \sin \Theta & \cos \Theta & 0 \\ 0 & 0 & 1 \end{pmatrix} \quad (6.2)$$

The vectors $x(0)$ describing the 0-lattice are given by the relation

$$(I - A^{-1}) x(0) = b(1) \quad (6.3)$$

where I is the unit matrix and $b(1)$ are the translation vectors of lattice (1).

The formation of a grain boundary using the 0-lattice proceeds as follows. First determine the transformation matrix A required to transform lattice (1) into lattice (2). This defines the position of the 0-lattice (which is three-dimensional). Next, place the boundary between the two crystals in the orientation and position desired. Ideally, the boundary should pass through as many 0-lattice positions as possible. Now fill the lattice sites with atoms on either side of the boundary. The 0-lattice will describe the

repeating nature of the atomic arrangement in the region where lattice (1) stops and lattice (2) begins.

At high rotation angles the transformation **A** may cause next nearest neighbors to move closer to a given atom than the original nearest neighbor. It is possible to have several different choices for **A** depending on which neighbor is considered. In general, the new nearest neighbors are given by that choice of **A** for which the determinant of $|\mathbf{I} - \mathbf{A}^{-1}|$ has the smallest absolute value.

The 0-lattice theory has been very useful in describing the geometry and structure of crystalline interfaces (Sass, 1986; Carter and Sass, 1981). However, the theory is strictly a geometrical scheme and says little about the energetics of a given boundary other than qualitative arguments that 0-lattices with small unit cell volumes "should" have lower energy since then there will be a higher population density of equivalence sites on the grain boundary.

Sutton and Balluffi (1987) have recently reviewed the ability of several geometric criteria of grain boundary structure to provide good estimates of low boundary energies in metals and ionic crystals. These criteria included (1) low reciprocal volume density of coincidence sites; (2) high planar density of coincidence sites, **G**; (3) high **G** at constant interplanar spacing, **d**; (4) large **d**; and (5) high

density of "locked-in" rows of atoms. They came to the conclusion that in general, there was no particularly notable criterion which could reliably give estimates of low energy boundaries from a simple geometrical framework. Only criterion (3) seemed to have useful predictive ability for determining low energy grain boundaries, and even here was found to hold only for metal/metal or ionic/ionic boundaries, not metal/ionic boundaries. They concluded that any useful understanding of the energy of interfaces must take into account the details of molecular bonding and local relaxations at the boundary, and that simplistic geometric considerations were of limited applicability.

As reviewed by Sutton and Balluffi (1987), the general features of low grain boundary energy depend on the specific nature of bonding in the solid under consideration. For metals it is necessary to have an atomic coordination number for atoms within the grain as close as possible as that in the perfect crystal (Vitek, Sutton, Smith, and Pond, 1980). In ionic solids low interfacial energy requires that no nearest neighbor ions have the same valence (Duffy and Tasker, 1985). In tetrahedrally coordinated covalently bonded solids grain boundary structures are such that they minimize the number of "dangling bonds" near the grain boundary (Sutton and Balluffi, 1987).

In polymer solids the bonding is extremely anisotropic, with covalent bonding along the chain and van der Waals or hydrogen bonding between chains. Therefore we expect that the surface energetics of grain boundaries will depend critically on the local orientation of the chain axis. We believe that geometrical considerations of grain boundaries in polymers which take into account the role of chain connectivity on the local orientation of the crystals and the grain boundary itself will be useful in determining the energetics of the the boundary. Also, considerations of chain connectivity and topology will be of particular importance for developing models for the local molecular motions involved in grain growth. It is our goal in this chapter to provide a conceptual outline of the importance of chain connectivity on the structure, energetics, and mobility of grain boundaries in covalently bonded molecular solids. Where possible, we will correlate these ideas with HREM images of grain boundaries in the rigid-rod polymers PBZT and PBZO studied in this thesis.

C. Grain Boundaries in Polymers

We now extend our discussion to concern crystalline domains which have a well-defined direction defined by c_1 . In polymers, this direction c_1 is easily associated with the direction of the chain axis. Chain connectivity along c_1

makes geometrical constructions which involve c_1 of particular importance, because the strength of the molecular bonding along the chain axis (covalent bonding) is often two orders of magnitude stronger than the interactions between molecules (van der Waals or hydrogen bonding). Besides this well-defined direction c_1 are two other vectors a_1 and b_1 which represent the unit cell vectors required to define the crystalline lattice.

Consider now a neighboring domain with unit cell vectors a_2 , b_2 , and c_2 . How do the different possible orientations of this second crystal and the choice of the plane of the grain boundary affect the expected structure and energetics of the grain boundary which results?

The understanding of the role of molecular connectivity and chemical topology on the structure and energetics of defects in molecular solids is still in its infancy. Bevis (1978) considered the role of chain connectivity on the expected structures of twin boundaries in polymers, and drew a distinction between "chain-axis invariant" and "chain-axis rotation" twins, distinguished by whether the chain axis in the crystals on either side of the twin boundary were parallel or not.

Here we extend the initial analysis of Bevis, which concerned only twins, to the more general case of an arbi-

trary grain boundary. We suggest that a second important and obvious geometrical parameter in classifying grain boundaries in polymer crystals is the orientation of the grain boundary with respect to the molecular direction.

With this model we are able to classify all of the different conceivable grain boundaries in molecular crystals into four distinct categories.

As shown by Bevis (1978), the orientations of the second crystal can be separated into two distinct classes:

I. The directions c_1 and c_2 are parallel.

(Chain Axis Invariant)

II. The directions c_1 and c_2 are not parallel.

(Chain Axis Rotation)

In the perfect crystal, the chain directions c_1 and c_2 are parallel. Hence, we expect chain axis invariant grain boundaries will be of lower energy than chain axis rotation boundaries.

The second important geometrical parameter is the orientation of the boundary separating the two crystallites. Again, we expect two obvious classification schemes:

III. The plane of the boundary is parallel to both c_1 and c_2 .

(Lateral Boundary)

IV. The plane of the boundary is not parallel to either c_1 or c_2 or both.

(Axial Boundary)

An axial boundary will necessarily be of higher energy than a lateral boundary because the bonds along the chain axis are much stronger than those in other directions.

With this simple construction it is possible to classify the different types of boundary between crystallites containing well defined directions c_1 and c_2 into four categories. These are 1) lateral chain invariant (LCI), 2) lateral chain rotation (LCR), 3) axial chain invariant (ACI), and 4) axial chain rotation (ACR) grain boundaries.

Figure 6.1 shows a schematic of the four different types of grain boundaries. The following discussion details the important features of each of these different kinds of grain boundary. The boundaries are presented in the general order of lowest energy to highest energy. In each class we will examine the questions of structure, energetics, and mechanisms of formation and growth of the grain boundary. We will provide examples of physical situations in which each

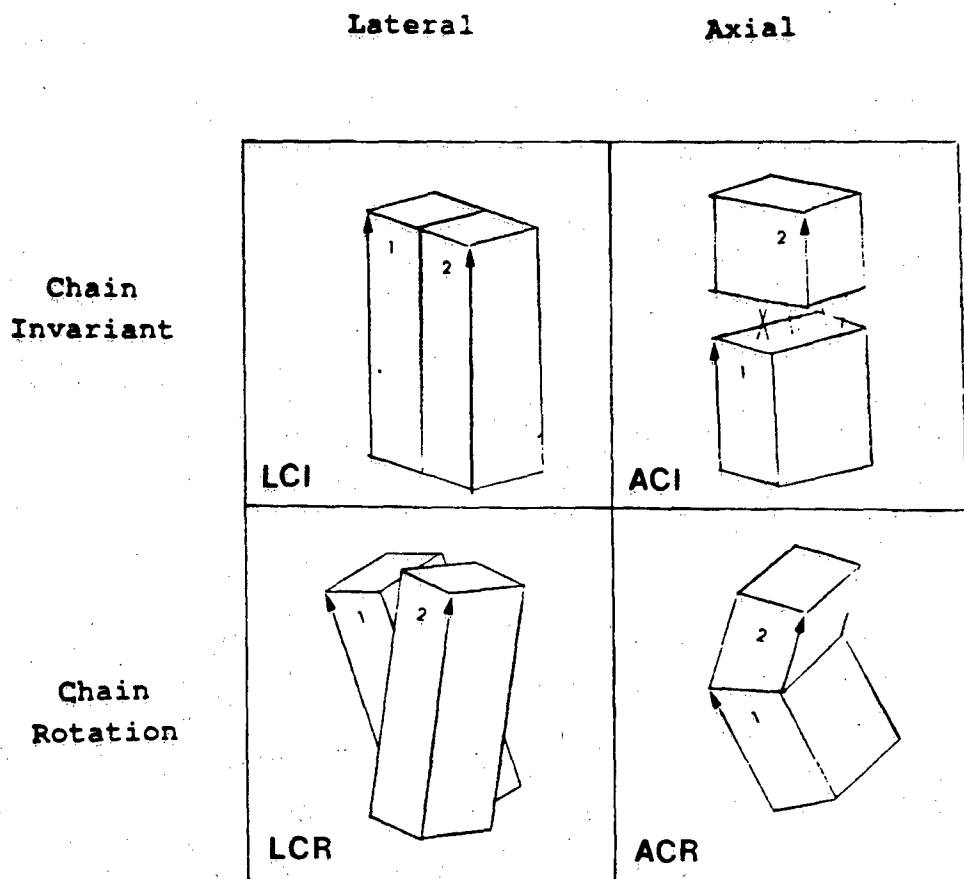


Figure 6.1: The four different types of grain boundaries which are possible between crystals which have a well defined directions c_1 and c_2 (denoted by arrows). In polymers c_1 is associated with the direction of the covalently bonded chain axis. If directions c_1 are the same in both crystals, then the boundary is a "chain invariant" boundary, otherwise it is "chain rotation" boundary. If the boundary plane is parallel to c_1 and c_2 , then it is a "lateral boundary", otherwise it is an "axial boundary". Therefore, there are four types of boundary: 1) lateral chain invariant (LCI), 2) lateral chain rotation (LCR), 3) axial chain invariant (ACI), and 4) axial chain rotation (ACR).

type of boundary might be particularly important in controlling the macroscopic properties of the polymer solid.

1. Lateral Chain Invariant (LCI) Boundaries

A LCI boundary (Figure 6.1a) does not disrupt the chain axis. Also, it preserves chain orientation. LCI boundaries should have the lowest energy of the four types. In fact, in some polymers (like the PBZT and PBZO studied in this thesis), there is a high degree of axial shift disorder within the crystallite itself, emphasizing how easy it is for molecular misregistry to occur along an LCI boundary.

Figure 6.2 shows a schematic view down the chain axis of a microfibril of rigid rod polymer. The crystallites within the microfibril are separated from one another by LCI grain boundaries.

Since LCI boundaries do not disrupt the orientation or the continuity of the chain axis, they should be of relatively low energy. Within the class of lateral chain invariant boundaries, different energies might exist if the lateral bonding was unique in different directions. Such is the case in PPTA which has hydrogen bonding in certain crystallographic directions and van der Waals bonding in others (Northolt, 1974).

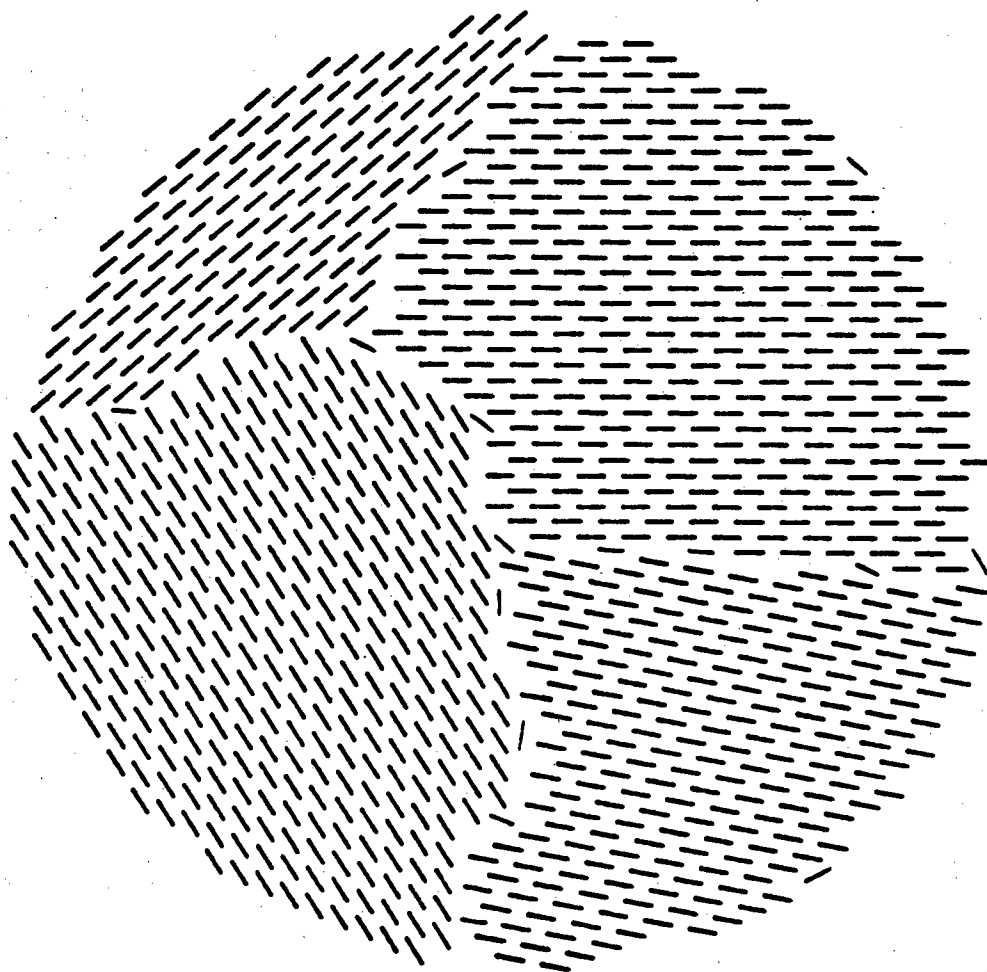


Figure 6.2 Schematic diagram of a cross section of an individual microfibril in a rigid-rod polymer fiber projected down the chain axis. The microfibril shown has four crystallites which meet at lateral chain invariant (LCI) boundaries. LCI boundaries are of relatively low energy because they do not require conformational changes or bending of the rigid-rod polymer backbone.

It is reasonable to imagine that an LCI boundary could form during grain growth from an initially oriented yet non-crystalline polymer solid. Slip would be easily managed by relative motion of one crystallite with respect to the other along the LCI boundary.

Growth twins seen in PPX (Pradere and Thomas, 1989) as well as antiphase boundaries in syndiotactic polystyrene (Pradere and Thomas, 1989) are examples of LCI boundaries which occur during the normal growth of a polymer single crystal. Recent studies of polyethylene crystals by Scanning Tunneling Microscopy have shown that overgrowths caused by screw dislocations at crystal edges have steep lateral edges and are forced to the top of the lamellar crystallites in discrete plateaus, suggesting that the shear across LCI boundaries occurs as the PE crystals flatten from solution onto the STM substrate (Piner, Reifenberger, Martin, Thomas, and Apkarian, 1989).

The movement of an LCI boundary might occur by the local reorientation of an internal segment of the polymer chain about the chain axis. This would involve the motion of a twist defect (represented by a local conformational change from the orientation of crystal (1) to the orientation of crystal (2)) along the length of a molecule positioned at the grain boundary interface. A schematic drawing of such a

molecular mechanism of LCI grain growth is shown in Figure 6.3.

The uniformity of deformation which is mitigated by LCI boundary slip will be determined by how often this slip occurs. Adams, Yang and Thomas (1986) have distinguished between "blocky" and "fine" slip in the deformation of polyethylene. Essentially, this scheme considers how often an LCI grain boundary participates in the shear deformation process. If only a few boundaries are activated then the slip is "blocky", but if many or all of the boundaries experience deformation then the slip is "fine".

LCI grain boundary slip also an important deformation mechanism in the kinking of rigid rod polymers (Chapter V), and in the deformation twinning of polydiacetylene single crystals (Young et al., 1979).

2. Lateral Chain Rotation (LCR) Boundaries

LCR boundaries do not require interference with the chain axis and therefore should also be of relatively low energy. However, the rotation of the crystallites should cause these types of boundaries to be of higher energy than the LCI boundary. This will be particularly true if the matching faces of the two crystals do not correspond to low-index planes. In this case there will be a number of "furrows" on

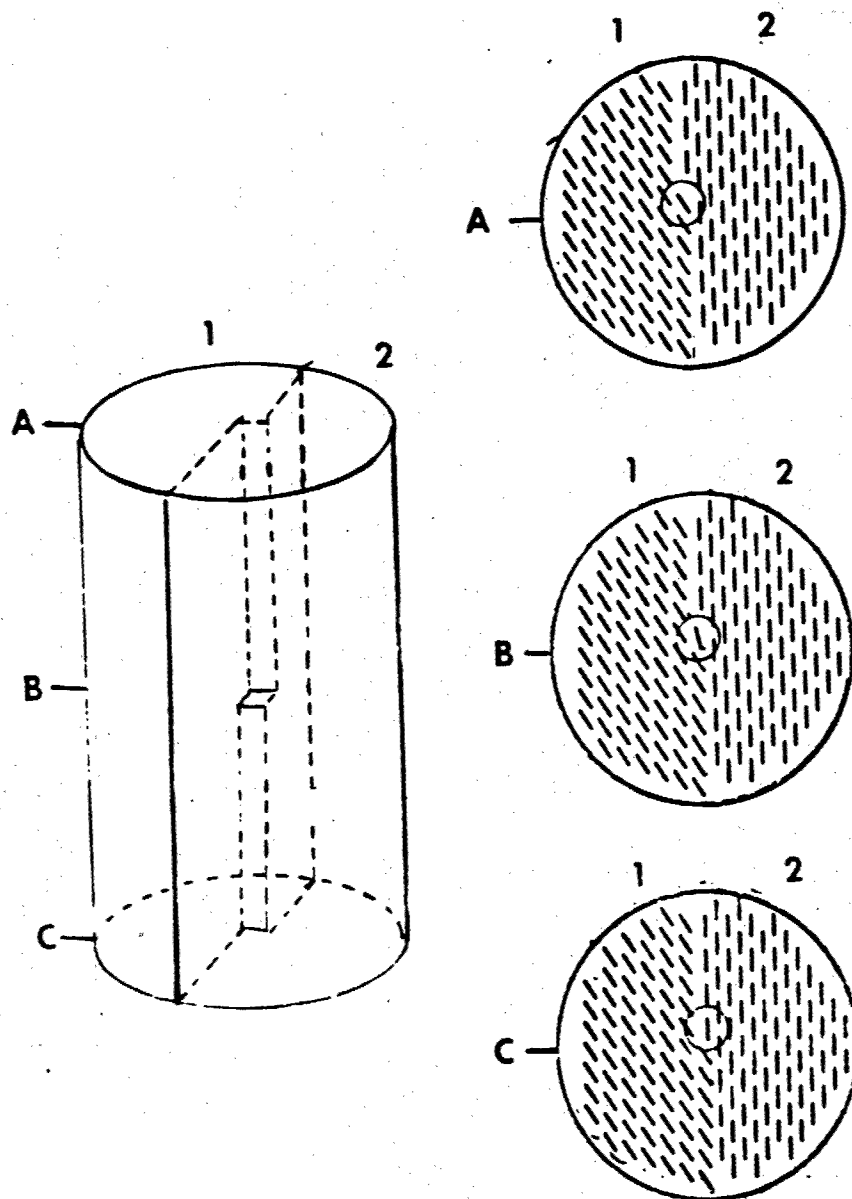


Figure 6.3: Schematic diagram of a plausible mechanism for grain growth by LCI boundary migration. The mechanism consists of the axial motion of an internal twist about the axis of a chain from the orientation of crystallite (1) to that of crystallite (2). The twist defect is envisioned to move along the backbone of the molecule. The diagram shows sections on planes above (A), at (B), and below (C) the twist defect. If the twist defect moves up, then crystal (2) will grow laterally and crystal (1) will shrink. If it moves down, then crystal (1) will grow laterally and crystal (2) will shrink.

the the surface which will give rise to voids between the crystallites.

An LCR boundary could be thought of as a "lateral twist" boundary. It is possible to imagine a "lateral tilt" grain boundary which would be formed by tilting the axes of crystals toward or away from one another. Such a boundary was described by Predecki and Statton (1966) and was postulated to occur by the cooperative segregation of chain ends to a lateral surface of a polymer crystallite. However, the boundary thus created is no longer parallel to c_1 AND c_2 and therefore is not a "lateral" chain rotation boundary as per our definition. Rather, it is an "axial" chain rotation boundary where the angle between the grain boundary plane and chain axis is low.

A LCR grain boundary is shown in Figure 6.4. Note that rotation about this boundary changes the orientation between the crystallites. A specific example of an LCR boundary was seen earlier in this thesis in an HREM image of a critically point dried PBZO (Chapter 4). An enlargement of this region is shown in Figure 6.5. Figure 6.6 shows a molecular interpretation of the structure which is generally consistent with the HREM image contrast. The crystallites are oriented at a significant angle (27 degrees) to one another and meet each other on lateral (010) crystal faces.

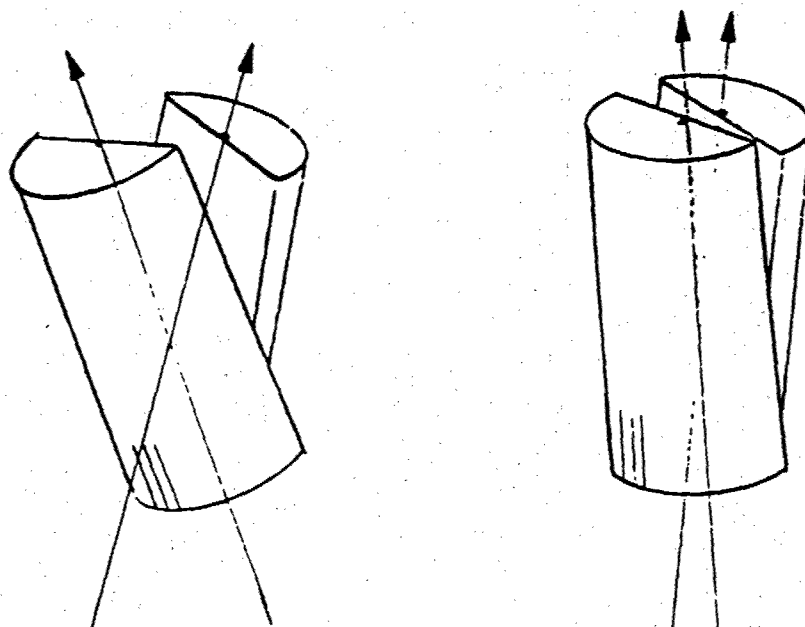
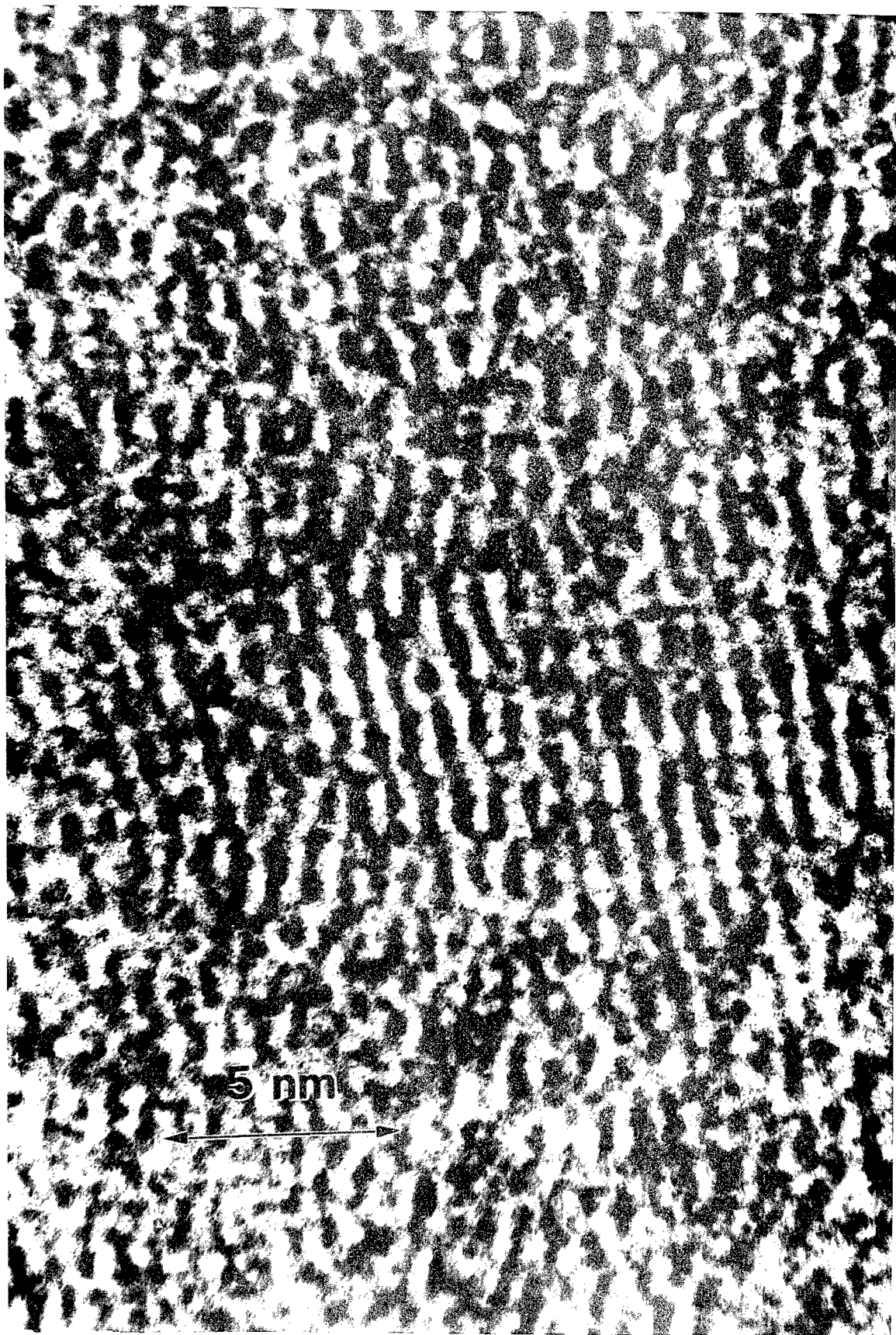


Figure 6.4: Schematic diagram of a lateral chain rotation (LCR) boundary between neighboring polymer crystallites. Twist of the crystallites about the boundary will change the molecular orientation.

Figure 6.5: Enlargement of an HREM image of a LCR boundary in critically point dried PBZO fiber. The image shows two crystallites with different orientations of the chain axis (27 degrees) laterally superposed within the thickness of the thin (approximately 20 nm) sample.



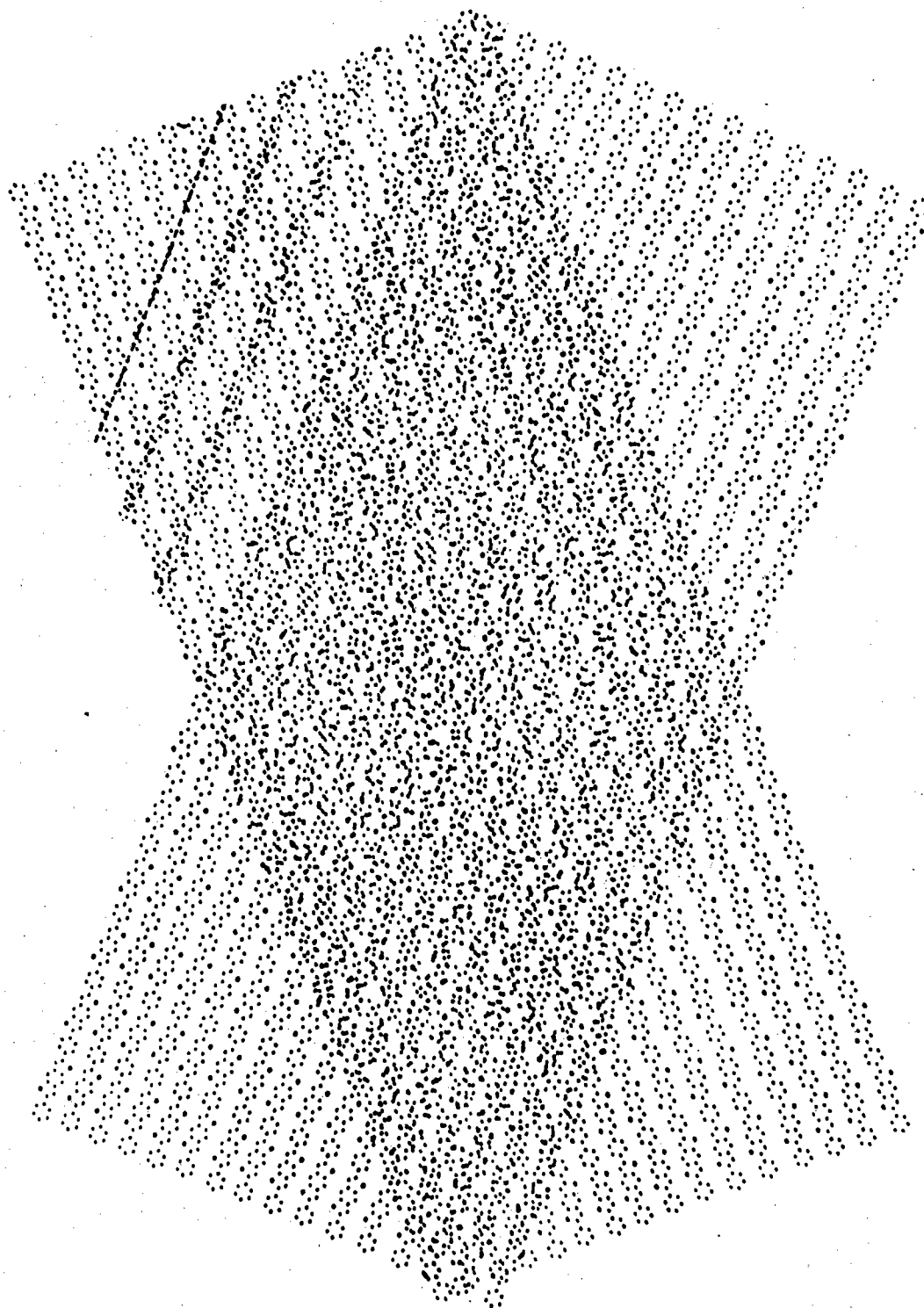


Figure 6.6: Molecular interpretation consistent with the contrast seen in Figure 6.5: The molecules in the two crystallites are highly misoriented. The crystallites meet on (010) lateral crystal faces.

The growth of a LCR boundary poses some severe geometrical problems. It does not seem possible for such a boundary to move without a substantial reorientation of a large amount of material at the grain boundary. One possible mechanism for a LCR boundary to move is to have both of the neighboring crystallites oriented properly so that chain rotation at the boundary can occur. In other words, the LCR boundary must be first converted into a LCI boundary in order to move by the simple chain axis twist defect mechanism discussed earlier (Figure 6.3). This may be a major reason why the application of tensile stress is so important in successful post-processing heat treatment of rigid-rod polymer fibers (Allen, 1983).

An alternative mechanism for the growth of a LCR boundary might be the formation and subsequent propagation of a "bend" along the axis of a polymer molecule. Although this mechanism does not involve the cooperative motion of a large number of molecules, it does require slip of the polymer perpendicular to its axis of orientation (Figure 6.7). Whether such a mechanism is feasible will depend on how much energy it costs to make such a "bend" within the polymer of interest.

LCR boundaries may be prolific in films of rigid-rod polymers which are not highly oriented. During deformation of thin films of unoriented rigid-rod polymers, it was

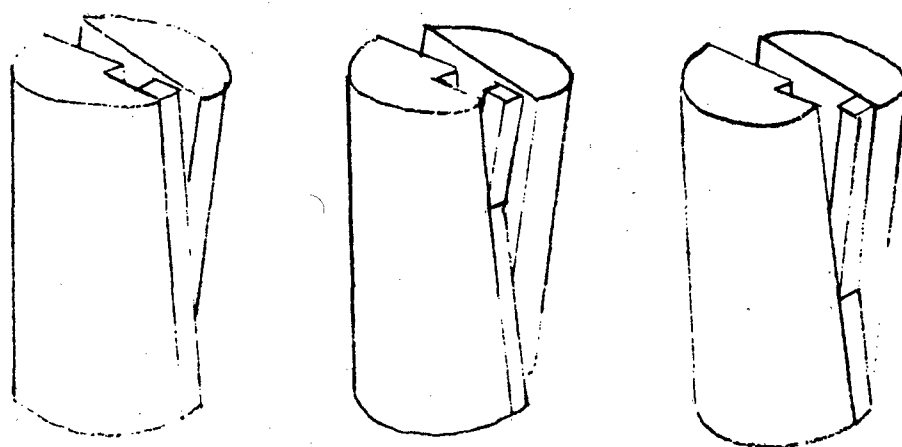


Figure 6.7: Possible mechanism for grain growth at an LCR boundary involving the propagation an internal molecular kink along the boundary and the cooperative lateral motion of a segment of the molecule. Another feasible mechanism for LCR growth is to reorient the grains so that the LCR boundary becomes an LCI boundary, and then grow by the mechanism proposed in Figure 6.3.

Figure 6.8: OM and SEM views of a region from an isotropic thin film of PBZT deposited on a deformable substrate and then deformed in uniaxial tension. The sample mostly cracks perpendicular to the stress but sometimes exhibits localized regions of birefringence at 55 degrees to the tensile direction. Since PBZT is a stiff molecule, it seems necessary to explain this shear instability in terms of a lateral slip mechanism similar to that shown schematically in Figure 6.5.



observed that bands of shear deformation as evidenced by local areas of birefringence in OM could sometimes be seen at angles to the direction of applied deformation. Such an area of local deformation is shown in Figure 6.8. It seems that a reasonable mechanism to explain this mode of deformation is by LCR boundary slip between locally misoriented rigid molecules or microfibrils.

3. Axial Chain Invariant (ACI) Boundaries

ACI boundaries involve two crystallites with parallel chain axes. In a sample with a very high molecular weight chain ends are very dilute, so it will be necessary to maintain chain flux across such a boundary. This will require each chain to twist as it crosses the boundary, and will require many chains to both twist and translate.

The maintainance of chain flux means that it is necessary to connect chain sites in crystal (1) with others in crystal (2). The specific manner in which the chains minimize their energy in such a "braided" structure will depend on the details of the internal conformations available to the polymer of interest. Figure 6.9 shows a microfibril of a rigid-rod polymer which has several ACI boundaries between crystallites.

From the geometry of an ACI grain boundary model it is possible to calculate the amount of induced misorientation expected by maintaining flux across the boundary. All other factors being equal, a reasonable model for an axial chain invariant boundary with known crystal boundary conditions is one which minimizes the projections of the required misorientation on the boundary plane. In other words, the boundary will require the least energy when the amount of induced misorientation is the least.

The amount of misorientation and the specific solution to the energy minimization problem will be sensitive to the cross-section characteristics (size and shape), as well as the specific internal conformational changes available to the molecule under study.

The structure of a typical example of an ACI grain boundary seen from the top is shown in the Figure 6.10. The structure is such that all of the chains are required to twist, some are required to both twist and translate. The actual structure will depend on the details of the molecular architecture and the ability of the molecule to thread its way through the boundary. In this specific example, the unit cell of PBZT is used. The orientation of crystal (1) is such that the [010] direction is oriented forward, enabling the 0.59 nm (100) planes to be viewed. Crystal (2) is oriented with the [100] direction forward, enabling the 0.36 nm (010)

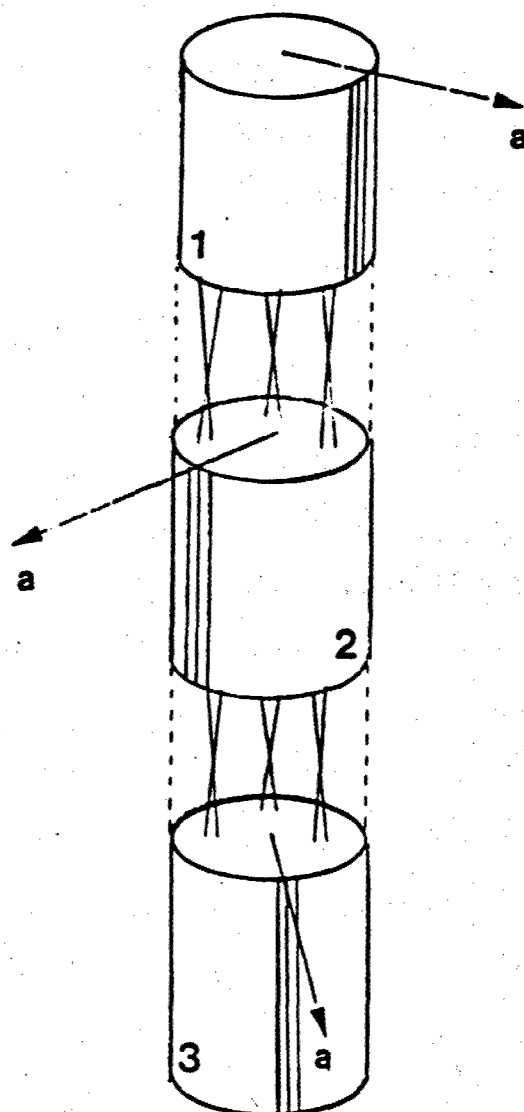
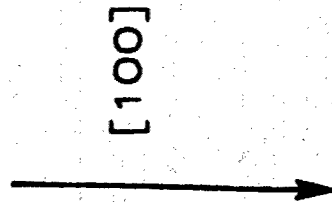
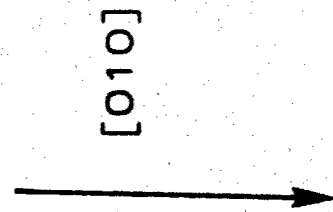
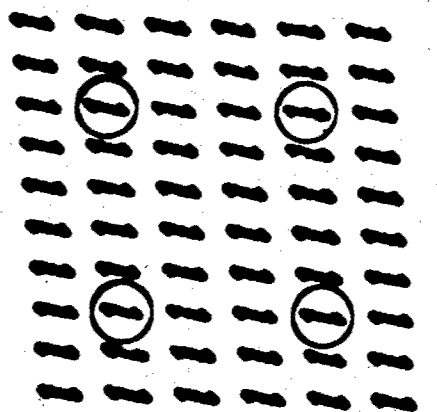
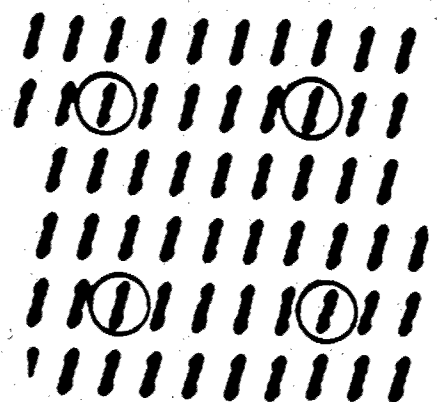
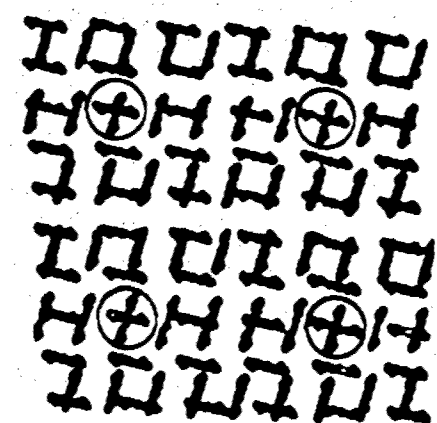


Figure 6.9: Microfibril consisting of three crystallites in axial registry separated by ACI grain boundaries. The c directions in each crystallite are along the microfibrillar axis. The a directions are oriented in different directions. The molecules are long enough to pass completely through the ACI boundaries. Each molecule must twist as it passes through the boundary, some are required to both twist and translate. The ACI boundaries are thus considered to be a region of lower density in which the molecules become slightly intertwined and entangled.

Figure 6.10: View of a specific ACI boundary in PBZT as seen from the top. This boundary separates a crystallite with the $[100]$ direction pointing forward from one with the $[010]$ direction pointing forward. The structure of the boundary can be considered from a unit cell of the 0-lattice whose sites are given approximately by the circles. The molecules at the circled positions have only to twist as they pass through the boundary, the other chains have to both twist and translate.



planes to be seen. The chains circled are only required to twist as they pass through the boundary, whereas the other chains are required to both twist and translate.

One of the insights provided by the 0-lattice theory is that it emphasizes that most of the essential physics of grain boundaries can be revealed by considering only a unit cell of the 0-lattice and not the entire boundary. This greatly simplifies the calculations of grain boundary structure and energetics, which in general would require an infinitely large interface.

Figure 6.11 shows an image from PBZT which provides experimental support for an ACI grain boundary (Boudet et al., 1987). The image shows a transverse view of a crystallite with 0.59 nm (100) planes directly meeting another crystallite with 0.36 (010) planes along the molecular axis. This image is consistent with the model presented in Figure 6.10. Note that unlike metallic grain boundaries which are sharp (0.2-0.5 nm), this boundary is more diffuse (4-5 nm). Figure 6.12 shows a molecular model corresponding to the image in Figure 6.11.

ACI boundaries will inevitably be of lower density than the perfect crystallites because of lateral packing problems as the molecules twist and entangle. It is reasonable to expect that ACI boundaries will therefore act as places for

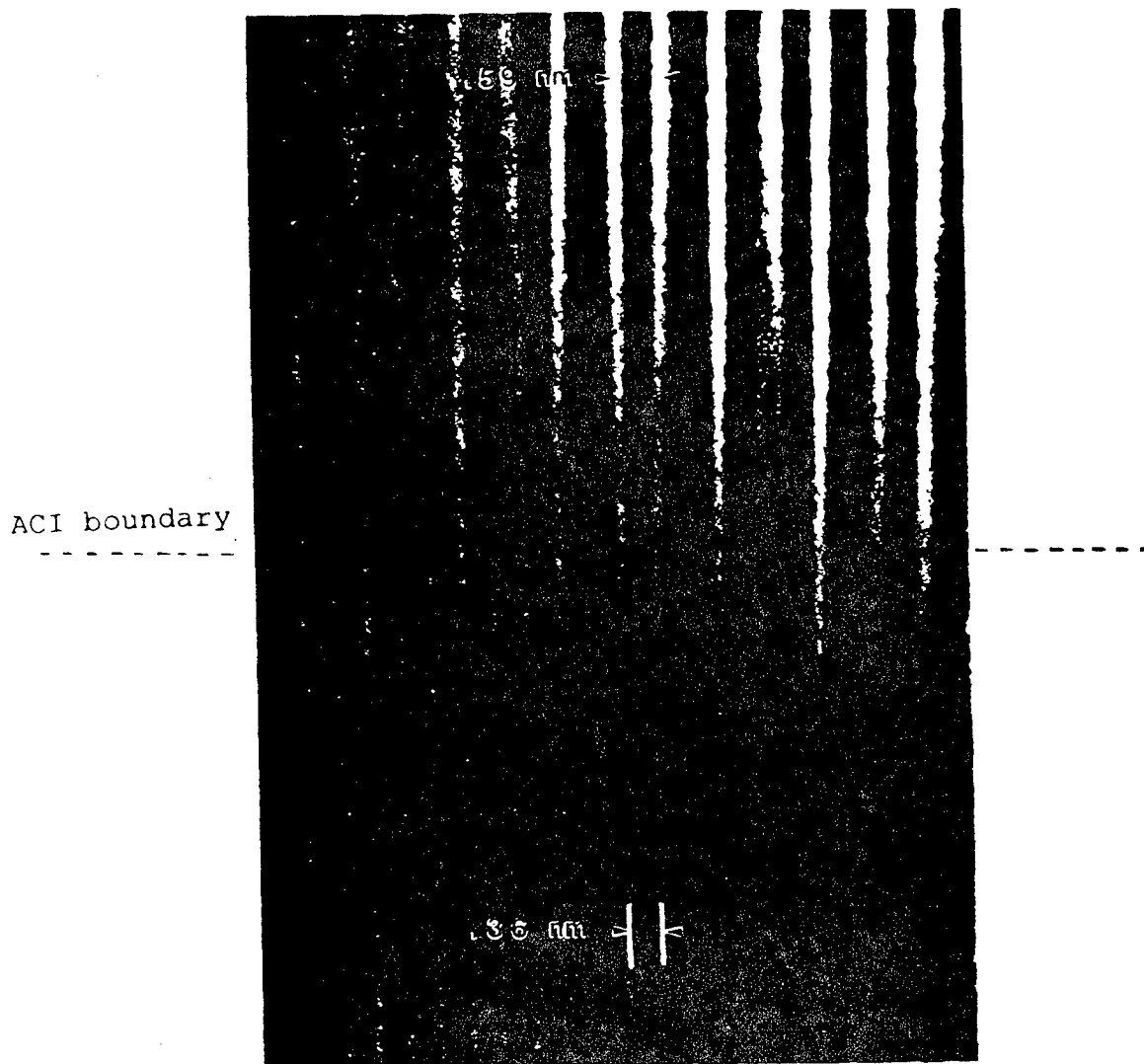


Figure 6.11: HREM Image showing 0.59 nm (100) fringes meeting 0.36 nm (010) fringes in the axial direction (Boudet et al., 1987). The boundary region is in the center of the figure. The transition from sharp 0.59 nm fringes to sharp 0.36 occurs over a distance of about 5 nm in the axial direction.

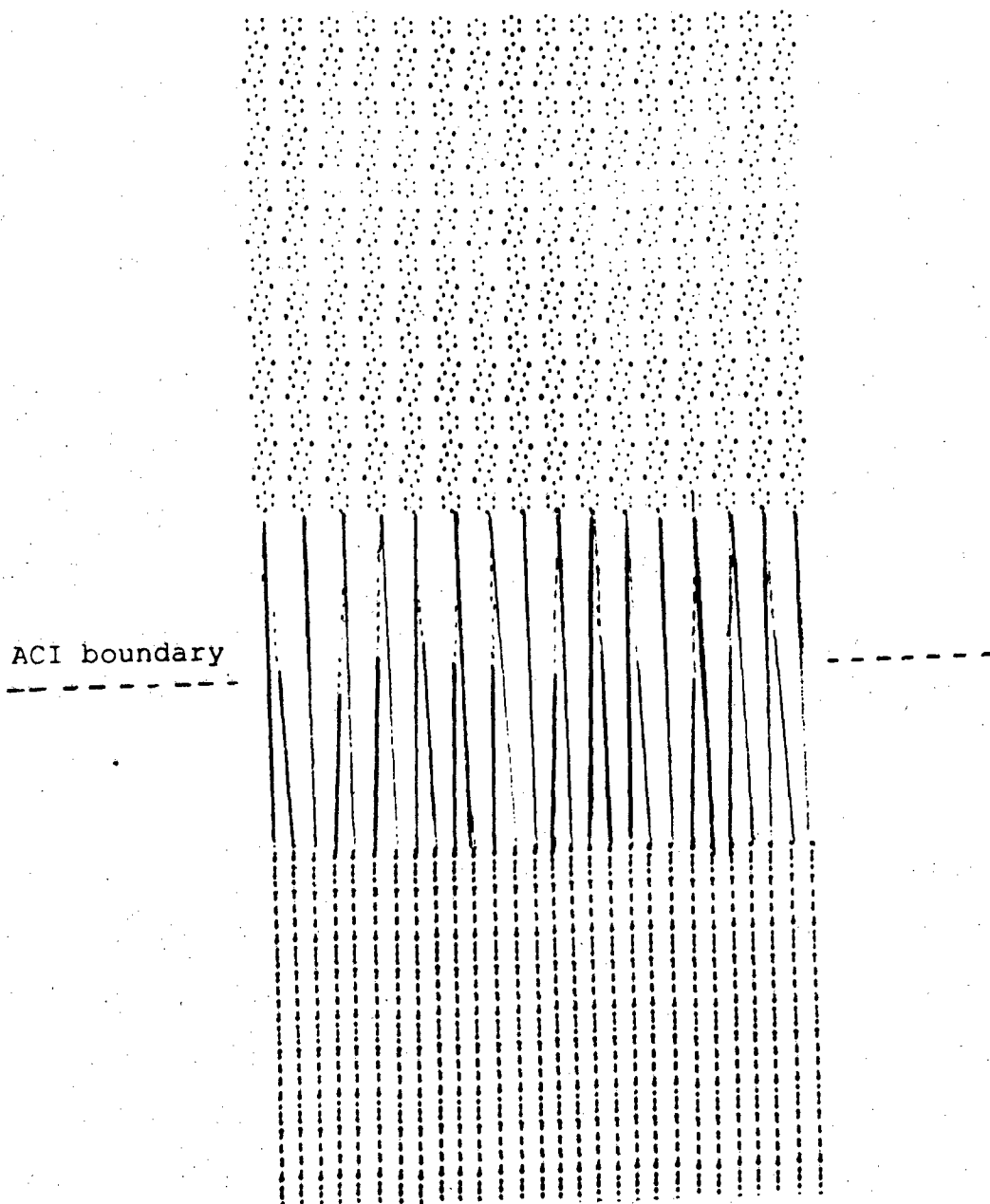


Figure 6.12: Molecular interpretation of Figure 6.11 showing both the two crystallites in axial registry with one crystallite oriented so the molecules are seen "edge-to-edge" and the other "face-to-face". The axial width of the boundary is on the order of 5 nm, which is much larger than is typical for most metallic and inorganic crystals. This is apparently due to the packing problems within the boundary imposed by the long chain connectivity of the polymer molecules.

the initiation of failure and the segregation of solvents or liquids from the environment. Also, it seems reasonable that chain ends will be able to reduce the free energy of the system if they can find their way to a boundary of this sort rather than getting stuck inside a perfect crystal.

The growth of an ACI boundary might occur by the simultaneous reorientation of a number of small segments near the grain boundary. When the boundary is very twisted and entangled, this might be difficult to accomplish. However, the energy of an ACI boundary should be quite high so there will be a substantial driving force to eliminate it.

ACI boundaries maintain good chain orientation and therefore should retain the high modulus and strength of oriented fibers. However, the misorientation which is necessarily induced within the boundary region may explain the deviation between theoretically predicted and experimentally obtained values for modulus in these materials. Theoretical predictions (Northolt and van Artsen, 1978) have shown that misorientation can account for a substantial decrease in the modulus of an oriented fiber.

With this structure of ACI boundaries in mind, it is possible to see why the modulus of a rigid-rod fiber depends on stress (Eby, 1988). As the fibers are placed in axial tension, the molecules which are twisted together in ACI

boundaries will laterally interact more strongly and therefore resist further deformation. Likewise, the tendency for an ACI boundary to misorient during heating may be a reasonable explanation for the low and even negative values of the axial thermal expansion coefficient in rigid-rod polymer fibers.

As discussed in Chapter IV, the presence of four-point SAXS scattering in PBZO may be due to the formation of low energy ACI boundaries which occur at specific angles to the fiber axis. The model presented in Figure 4.19 was that specific, low energy ACI boundaries in PBZO occur parallel to (302) planes. These (302) planes give rise to strong WAXS and SAED diffraction spots.

Similar "axially invariant" boundaries may occur in other, entirely different physical situations. For instance, in superconductors there is a regime in magnetic field-temperature space in which the superconducting current confines itself into a discrete "flux lattice". The presence of this "lattice" can be easily seen by decoration experiments (Khurana, 1989). The stiffness of the interacting lines of current is dictated by the temperature and applied field. The lower the temperature and higher the field the stiffer the lines of current become (D. R. Nelson, 1988).

It has been shown that fluctuations in flux line stiffness cause there to be a regime where there is a stable "entangled flux liquid" in which some of the lines of current become intertwined (D. R. Nelson, 1989). If such a phase were quenched into a region of the phase diagram where it was more favorable to disentangle (by raising the field or lowering the temperature), it is reasonable to expect that some of the entanglements might become trapped and then forced into discrete grain boundaries between locally mis-oriented "flux crystallites". However, the axial 6-fold symmetry of the flux lattice means that it will require only as much as a 30 degree axial rotation of the grain in order to eliminate the grain boundary.

4. Axial Chain Rotation (ACR) Boundaries

In ACR boundaries the chain axes in the two crystallites are not parallel to one another. Also, the boundary is not parallel to the chain axes.

ACR boundaries are the most general type of grain boundary between two crystallites with a well defined chain axis. Since the boundary is not parallel to the chain axes of the crystallites, this will require the chains to bend as they pass from one crystallite orientation to the other.

ACR boundaries might form by growth, in which case the boundary would be characterized by array of chain ends, bends, or some other sort of defect structure which describes the way in which the change in orientation between the crystallites is accomodated. Also, ACR boundaries might be induced by applied deformation; in which case the boundary would consist of local set of bends or conformational changes which occurred as one crystal sheared with respect to the other.

An example of an ACR boundary seen in PBZO is shown in Figure 6.13. This image appeared within a kink band and shows a sharp angle change (38 degrees) in the chain axis orientation over a small distance (0.5 nm). Figure 6.14 shows a molecular interpretation of this image, which requires significant covalent bond bending of molecules at the boundary plane.

As mentioned before, "lateral tilt" boundaries are really of the ACR type, where the angle between the grain boundary and the crystal axes is small. Here, the segregation of chain ends to the boundary serves to accomodate the local rotation between crystallites.

Like ACI boundaries, ACR boundaries will also inevitably serve as locations for defect and second phase segregation. They may serve as fracture initiation sites as well. If the

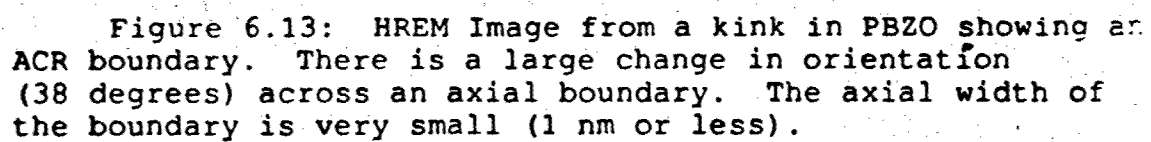
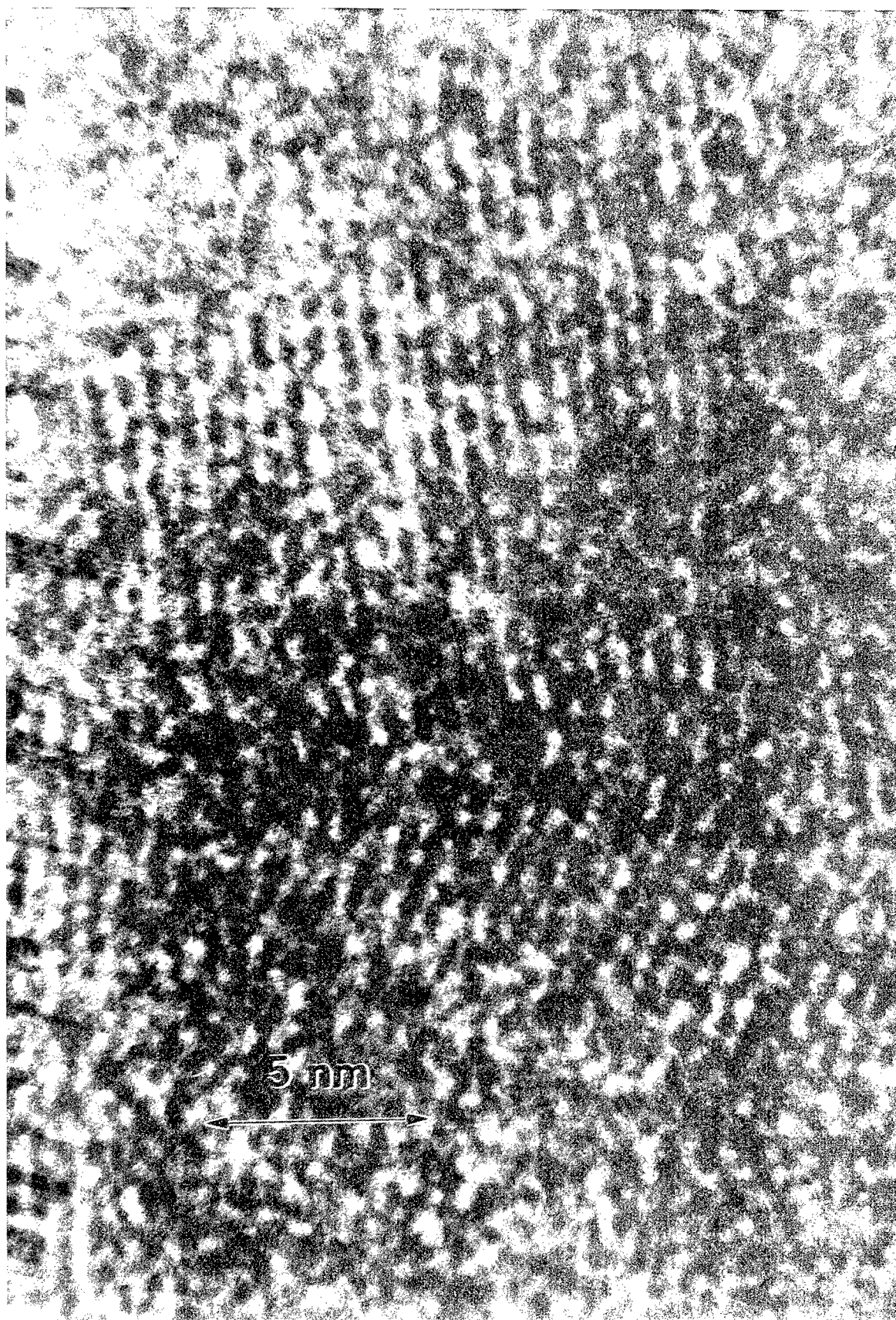
The image is a high-resolution transmission electron micrograph (HREM) showing a kink in a perovskite-based ferroelectric material (PBZO). The kink is characterized by a sharp change in the orientation of the atomic columns, which is visible as a discontinuity in the lattice fringes. The axial boundary of the kink is very narrow, with a width of 1 nm or less. The orientation change across the boundary is 38 degrees.

Figure 6.13: HREM Image from a kink in PBZO showing an ACR boundary. There is a large change in orientation (38 degrees) across an axial boundary. The axial width of the boundary is very small (1 nm or less).



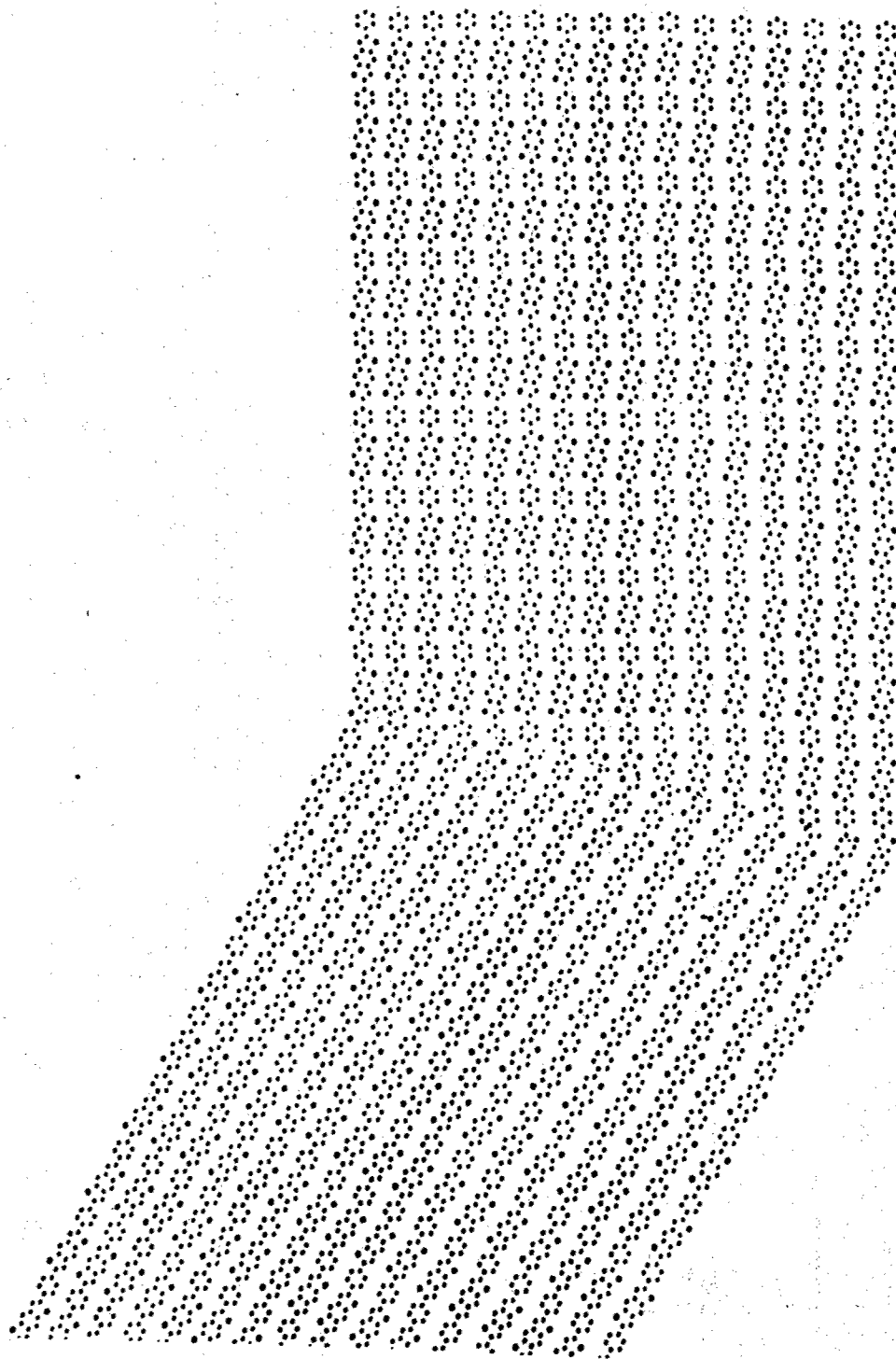


Figure 6.14: Molecular interpretation of Figure 6.13 which is consistent with the experimental HREM contrast. The molecules undergo a sharp bend as they change from one orientation to the other across the boundary. This would require the bending of covalent bonds in each polymer which passes through the ACR boundary.

molecular bending in the ACR boundary is sharp, the bonds may be "activated" and therefore more prone to chemical attack.

The motion of ACR boundaries will require not only the internal reorientation of molecular segments at the boundary about their own axes, but will require an additional bending of the molecular axis in order to accomodate the misorientation between crystallites.

ACR boundaries have also been seen in poly(parapheylene vinylene) (PPV) (Masse et al., 1989), where HREM studies have shown a change in chain orientation between small PPV crystallites packed along the axial direction. PPV conducts electricity when properly doped with AsF_5 . The structure of axial grain boundaries may be particularly important in determining the nature of charge transfer along the chain axis in this novel material.

D. Conclusions

Grain boundaries between neighboring crystals of extended chain polymers have been classified into four types depending on the orientation of the chain axes and the position of the boundary. This scheme recognizes the unique influence of one-dimensional covalent bonding on grain boundary structures in polymer solids. In increasing order of relative energy, these types are lateral chain invariant

(LCI), lateral chain rotation (LCR), axial chain invariant, (ACI), and axial chain rotation (ACR) grain boundaries. It is expected that the precise nature of each of these types of boundary will depend on the specific system of interest. Experimental evidence for each of these boundaries were described from the literature and from the work in this thesis. This simple approach illustrates the important way in which macromolecular architecture modifies traditional concepts of defect structure and energetics.

CHAPTER VII: CONCLUDING REMARKS AND FUTURE WORK

This chapter provides an overview of the major conclusions for each chapter, followed by some speculations about future avenues of research which should provide profitable areas for further investigation.

A. Chapter III: PBZT Ultrastructure

The observation of PBZT crystals over large areas of fiber fragments at high resolution has enabled the size and shape distribution for these crystallites to be obtained. We find that heat treated PBZT fiber is highly oriented, with the orientation over a 200 x 300 nm region exhibiting less than a 1.3 degree standard deviation in orientation (Hermans-Stein orientation parameter greater than 0.999). However, the maximum-minimum angle seen was 7 degrees, indicating that significant local misorientations can and do exist.

Plots of the crystallite lateral and axial sizes indicate that the PBZT crystals are in general compact, but are systematically larger in the axial than the transverse direction. The average lateral size was found to be 10 +/- 4 nm, and the average axial size was 17 +/- 8 nm.

We have also been able to image in real space the nature of axial shift disorder in PBZT fiber. The limited amount of

three-dimensional crystallinity present in PBZT is manifested in HREM imaging as undulating (001) lines which run at different angles to the edge of the PBZT fiber fragment.

These images have prompted the study of the distribution of scattering intensity of PBZT layer lines. We found that the molecular transform (indicative of complete axial disorder) is not as good an approximation to the experimental layer line data as a model using a triclinic PBZT unit cell with a high probability (80%) of encountering axial misregistry between neighboring molecules in the a and b directions. The optimum unit cell for PBZT is space group P1, $a=0.681$ nm, $b=0.392$ nm, $c=1.249$ nm, $\alpha=112.6$ degrees, $\beta=61.0$ degrees, and $\gamma=95.5$ degrees, with a density of 1.65 gms/cm³.

One area which is of immediate concern for understanding these results is a more detailed analysis of the inter-molecular energetics for both PBZT and PBZO. The preliminary study by Welsh et al. (1981) should now be extended in full detail to more critically assess the potential energy surface between PBZT and PBZO molecules.

It would be useful to calculate and compare the scattering from both the paracrystalline and stacking fault disorder models using the unit cell proposed by Granier. This

would be best done by getting higher quality scattered intensity data along each layer line.

The calculations to date have only concerned themselves with intensity on a layer line. However, the broadening of the layer lines in the meridional direction, as well as the fading of the layer lines in the equatorial direction, has interesting information about the details of molecular disorder. Calculations should proceed which consider all of scattering space.

Again, this comparison should be done using X-Ray or energy filtered SAED in order to avoid the problem with inelastic scattering near the main beam. This scattering obscures low angle SAED data, and makes quantitative studies in this regime of scattering space difficult.

B. Chapter IV: PBZO Ultrastructure

Our observation of single crystal texturing in very thin films of PBZO has enabled the indexing of the PBZO unit cell. We have found that there is a tendency for neighboring molecules to register at a relative axial shift of $1/4 c$, where c is the repeat distance along the chain axis. The unit cell consistent with our data is monoclinic, space group Pc , with $a=1.196$ nm, $b=0.354$ nm, $c=1.205$ nm, $\gamma=101.2$ degrees, and has a density of 1.66 gms/cm³.

We have seen by HREM that the crystallite size increases more in the lateral than the axial direction for PBZO, and have compared these results directly with those obtained by DF.

In PBZO, it would be useful to establish in more detail the nature of the domain texturing seen in SAED. For this purpose, it would be best to have a axial view of the fibrous sample so that the distribution in morphology across the fiber could be investigated. Attempts by Cohen to microtome PBZT have shown that when the fiber is cut across the molecular orientation direction there is a large amount of plastic deformation that occurs as the knife blade is unable to make a sharp cut. It has been found that "molecular" and "in-situ" composites of PBZT and nylon can be microtomed well by cutting at significant angles (45-50 degrees) to the fiber axis (Hwang, et al, 1989). Hence, it may be possible to overcome this limitation by cutting at different angles at liquid nitrogen temperatures.

Future work with higher resolution instruments should make it possible to more clearly resolve the PBZO microstructure and therefore help answer some outstanding questions. It would be obviously very useful if it were possible to resolve the (302) spacings directly. This would give information about the development of three-dimensional

crystallinity, and may help to prove or disprove the suggestion that axial grain boundaries parallel to (302) planes are an adequate explanation for the four-point SAXS behavior. The spacing d_{302} is 0.32 nm, which is very near the ultimate resolution limit of the 200 kV TEM used in this study (Chapter II), but well within the capability of available instruments (0.17 nm).

As for PBZT, it would be useful to obtain better quality data of the distribution of scattering on PBZO layer lines and compare these with disorder models.

C. Chapters III and IV: PBZT and PBZO

An area of possible development which comes to mind from these studies is that of rigid-rod polymer blends. What modifications of structure and properties would occur if it were possible to make miscible solutions of PBZT and PBZO, or PBZT/PPTA and PBZO/PPTA? In this way we could make materials with both hydrogen bonding and rigid-rod character.

Studies of "molecular composites" have shown that it is possible to achieve mixing between PBZT and nylon down to a scale of 4 nm or less (Hwang et al., 1989). Similar intimacy should be possible with PBZT/PPTA, PBZO/PPTA, or PBZT/PBZO blends. Materials in these intermediate composition ranges might have the right amount of heterogeneous microstructure to

successfully block the onset of kink deformation by limiting easy shear and disrupting the motion of the partial dislocations. Therefore, such blends may be of improved compressive strength when compared to the component materials. Heat treatment of these blends would cause not only crystallization and grain growth but also phase separation.

D. Chapter V: Kinking

It would be of interest to establish the dynamics of kink band propagation. A study involving the application of short stress pulses of known duration, similar to that used by Johnston and Gilman to study dislocation motion in LiF, may be appropriate here.

Since it has now been established that covalent bond bending at room temperature is involved in the kinking process, this provides new possibilities for novel chemistry at these activated sites after kinks have been introduced.

Although we have established that crystallinity within the kink is maintained, we have also seen that the deformation can be quite heterogeneous. It would be valuable to quantify further the change in size and shape of the crystalline domains within kink bands with DF imaging and with additional HREM studies. This would be particularly valuable

in a material which shows more axial ordering so that the "fine" versus "blocky" nature of the shear within the kink band could be more accurately understood.

The possible role of dislocations in kinking of oriented polymers is a general question raised by this work which should be addressed in more detail. HREM studies of compressive deformation in systems with larger, more perfect crystals (like poly(diacetylenes)) should be able to characterize the nature of dislocations at incoherent kink boundaries better than in these partly disordered systems.

Another study of interest would be to further characterize the thermodynamics of the deformation process by measuring the change in state of the fiber with a known amount of kinks introduced. This is best done by solution microcalorimetry which would measure the stored enthalpy with respect to a well defined equilibrium state (isotropic solution). Studies of this nature have been used to measure the stored energy of deformation in glassy thermoplastics.

E. Chapter VI: Grain Boundaries

Studies which can further our knowledge about the structure and energetics of grain boundaries will help es-

tablish whether the categorization scheme for grain boundaries in polymers outlined in Chapter VI will be useful.

It would be valuable to investigate with molecular mechanics methods the structure and energetics of the different types of grain boundaries proposed. At the moment, it is only possible to make rough estimates of the energies of these boundaries. Studies such as these may find unique structures which have low energy and therefore might be particularly abundant in the actual fiber.

A material which has particular promise for HREM studies of grain boundary defects is an aromatic polyester which is similar to PPTA (Kevlar) and shows very high degrees of crystallinity (Gardner et al., 1989). The very strong, sharp crystalline reflections in these fibers means that morphological study by HREM should reveal many interesting types of structure and structural defects.

The observation of shear bands in isotropic films of PBZT (Chapter VI) indicates that a local conformation change is probably not a necessary requirement for shear localization, since such a motion does not seem possible for stiff PBZT without involving a local covalent bond bending. The molecular motions involved in shear localization of isotropic PBZT films are not at all clear, and warrant further investigation. This understanding may become particularly

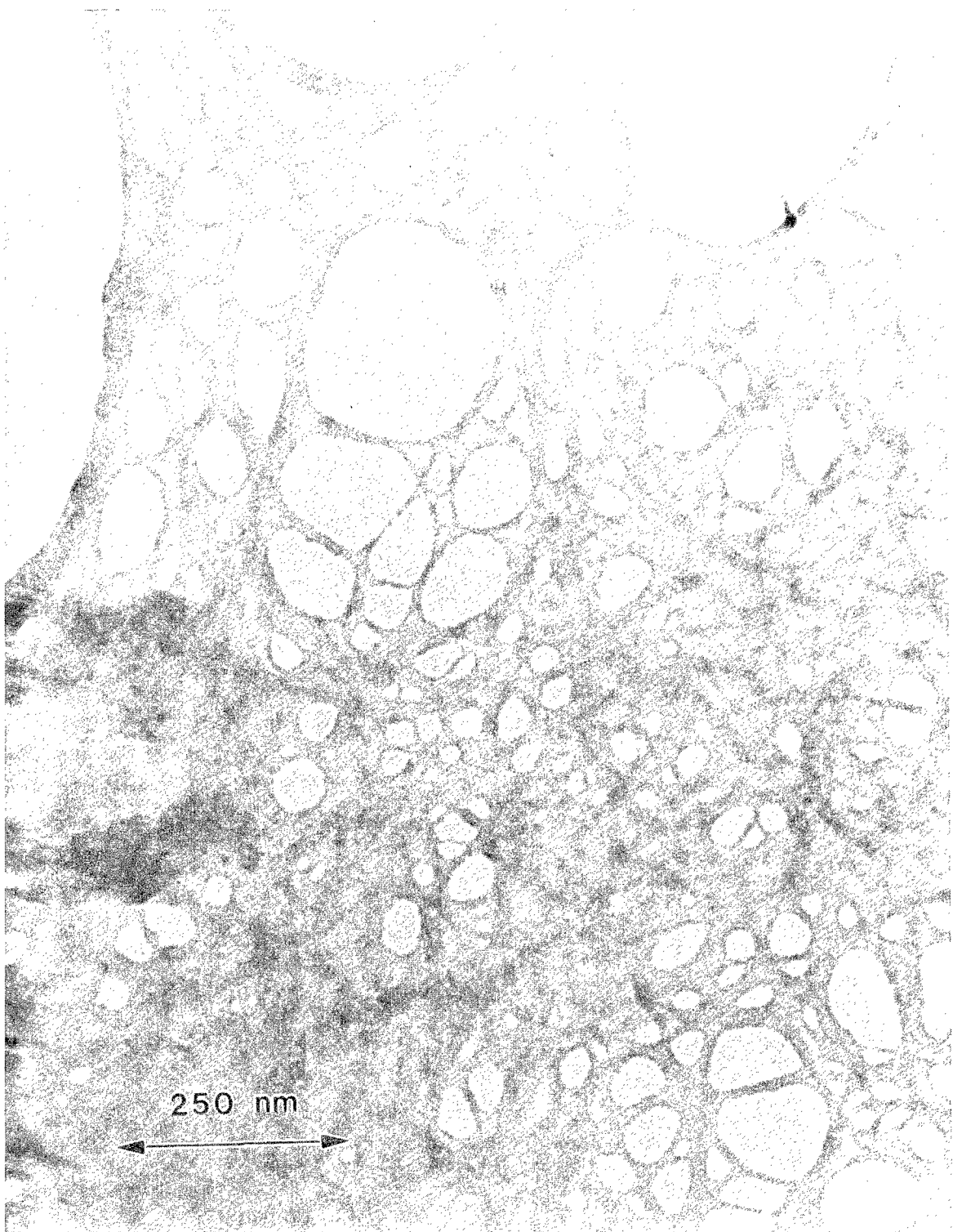


Figure 7.1: Lacy Film of PBZT IV=2.5 dl/gm prepared by floating a 0.135 weight percent solution in MSA onto water.

important for larger, bulk parts which may have a more isotropic orientation of the PBZT molecules.

F. PBZT and PBZO Thin Films and Crystal Solvates

Another area of research which has many fruitful possibilities is that of the structure of PBZT and PBZO thin films. Figure 7.1 shows a film of PBZT made by floating a 0.135 weight % solution in MSA onto water and then lifting the resulting film with a holey carbon grid. The PBZT used to make this film had an intrinsic viscosity of 2.5 dl/gm in MSA at 30 C, corresponding to a molecular weight of 11,000 gms/mole. The PBZT molecules form a film with many very fine holes and junction points. Close inspection suggests that there are no extremely fine holes (less than 20 nm), suggesting that at very small distances the PBZT molecules have enough mobility to minimize surface energy effects. Apparently a free surface provides sufficient energy to force PBZT molecules together enough to overcome their inherent rigidity.

Other geometrical frustration problems might arise as the temperature is raised and the molecules begin to crystallize. The structure of Y-junctions in thin films will be of particular interest, since it is easy to imagine these might be the most stressed areas and locations of initial fracture for materials made from PBZT microfibrillar net-

works, such as "in-situ network" composites (Hwang, et al., 1989).

Also observed in studies of PBZT thin films were crystal solvate phases which formed when dilute PBZT solutions in MSA were slowly exposed to atmospheric moisture. Electron diffraction of these phases showed them to be highly crystalline, with very sharp and distinct diffraction spots (Martin, unpublished). The crystal solvate phases formed from PBZT 0.135 weight percent solution in MSA exhibit d-spacings which cannot be indexed in terms of the known unit cells for crystal solvate phases formed from more concentrated solutions in poly(phosphoric acid) (Cohen, Saruyama, and Thomas, 1989). Optical microscopy of the coagulation behavior of crystal solvate spherulites showed a change in color from orange to yellow when exposed to copious amounts of water, followed by a dramatic collapse of the spherulite just as the water meniscus passes during evaporation.

WAXS experiments have shown that PBZO solutions exist in the crystal solvate phase prior to fiber spinning (Adams and Cohen, private communication). A concern for the future is a detailed understanding of the equilibrium phase diagram for rigid-rod polymer/solvent/non-solvent systems. Such a study will require closed systems in which the amount of non-solvent is carefully controlled.

BIBLIOGRAPHY

- W. W. Adams, Leonid V. Azaroff, A. K. Kulshreshtha, "X-ray Diffraction by a Nematic Polybenzothiazole Fiber", *Zeitschrift fur Kristallographie*, 1150, 321-313, (1980).
- W. W. Adams, T. Grieshop, T. Helminak, M. Hunsaker, J. F. O'Brien, M. Altieri, S. J. Bai, M. Brandt, A. V. Fratini, W-F. Hwang, G. E. Price, E. Soloski, T. Haddock, S. J. Krause, and P. G. Lenhert, "Processing, Properties, Structure, and Morphology of PBO and ABPBO Polymer Fibers", AFWAL-TR-86-4011, August (1986).
- W. W. Adams, P. G. Lenhert, J. J. P. Stewart, H. E. Klei, R. K. Eby, H. Jiang, and J. Smith, "Experimental and Theoretical Tensile Modulus of Rigid-Rod Polymers", *Bull. Amer. Phys. Soc.*, 32(3), (1987).
- W. W. Adams and R. K. Eby, "High-Performance Polymer Fibers", *Materials Research Society Bulletin*, XII(8), 22-25, November 16/December 31 (1987).
- W. W. Adams, D. L. Vezie, and S. J. Krause, "Scanning Electron Microscopy Evaluation of PBO Fibers", AFWAL-TR-88-4082, January (1988).
- W. W. Adams, S. Kumar, D. C. Martin, and K. Shimamura, "Lattice Imaging of Poly(p-phenylene benzobisoxazole) Fibre", *Polym. Comm.*, 30, 285-287, (1989).
- W. W. Adams and D. T. Grubb, unpublished results, (1988).
- W. W. Adams, D. Yang, and E. L. Thomas, "Direct Visualization of Microstructural Deformation Processes in Polyethylene", *J. Mat. Sci.*, 21, 2239-2253, (1986).
- S. R. Allen, A. G. Filippov, R. J. Farris, E. L. Thomas, C. P. Wong, G. C. Berry, E. C. Chenevey, "Mechanical Studies of High Strength, High Modulus Poly(p-phenylene benzobisthiazole) Fibers", *Macromol.*, 14, 1135-1138 (1981).
- S. R. Allen, A. G. Filippov, R. J. Farris, and E. L. Thomas, "Structure-Property Relations in Poly(p-phenylene benzobisthiazole) Fibers", Chapter 9 in A. E. Zacharides and R. S. Porter, eds., *The Strength and Stiffness of Polymers*, Marcel Dekker, Inc., New York, (1983).
- S. R. Allen, *Mechanical and Morphological Correlations in Poly(p-phenylene benzobisthiazole) Fibers*, Ph.D. Thesis, University of Massachusetts, Amherst (1983).

S. R. Allen, R. J. Farris, E. L. Thomas, "High Modulus, High Strength Poly(p-phenylene benzobisthiazole) Fibers", J. Mat. Sci., 20, 4583-4592 (1985).

S. R. Allen, "Tensile Recoil Measurement of Compressive Strength for Polymeric High Performance Fibres", J. Mat. Sci., 22, 853, (1987).

S. R. Allen, "Stress-coupling Phenomena in Anisotropic Fibres", Polymer, 29, 1091-1094, (1988).

S. Amelinckx, "High Resolution Electron Microscopy in Materials Science", in Examining the Submicron World, Ralph Feder, J. Wm. McGowan, and Douglas M. Shinozaki, eds., NATO ASI Series, Series B: Physics, Volume 137, Plenum Press, New York, (1986).

M. P. Anderson, D. J. Srolovitz, G. S. Grest, and P. S. Sahni, "Computer Simulation of Grain Growth--I. Kinetics", Acta Metall., 32(5), 783-791, (1984).

A. S. Argon, "Fracture of Composites", in Treatise on Materials Science and Technology, Vol. 1., Academic Press, New York, (1972).

A. S. Argon, "Inelastic Deformation and Fracture in Oxide, Metallic, and Polymeric Glasses", Chapter 3 in Glass Science and Technology, Vol. 5, Academic Press, (1980).

A. S. Argon, "Dislocations in Non-crystalline Media?", in M.F. Ashby, R. Bulloch, C.S. Hartley, and J.P. Hirth, Dislocation Modelling of Physical Systems, Proceedings of the International Conference, Gainesville, FL, June 22-27 1980, Pergamon Press, pg. 393, (1981).

M.F. Ashby, R. Bulloch, C.S. Hartley, and J.P. Hirth, Dislocation Modelling of Physical Systems, Proceedings of the International Conference, Gainesville, FL, June 22-27 1980, Pergamon Press, (1981).

H. V. Atkinson, "Theories of Normal Grain Growth in Pure Single Phase Systems", Acta Metall., 36(3), 469-491, (1988).

G. E. Attenburrow and D. C. Bassett, "Compliances and Failure Modes of Oriented Chain-Extended Polyethylene", J. Mat. Sci. 14, 2679-2687, (1979).

G. A. Bassett and A. Keller, as cited by A. Keller, Kolloid-Z., 231, 386, (1969).

R. H. Baughman, H. Gleiter, and N. Sendfeld, "Deformation and Microstructure of Extended-chain Polydiacetylene Crystals", J. Polym. Sci.: Polym. Phys. Ed., 13, 1871-1879, (1975).

S. C. Bennett, M. G. Dobb, D. J. Johnson, R. Murray, and B. P. Saville, "High Resolution Studies of Electron-Beam Sensitive Polymers", EMAG Proceedings, 329-332, (1975).

G. C. Berry, "Rheological and Rheo-Optical Studies of a Constitutive Equation for Nematogenic Solutions of Rod-like Polymers", Faraday Discuss. Chem. Soc., 79, 141-148, (1985).

G. C. Berry, "Rheological Properties of Nematic Solutions of Rodlike Polymers", Mol. Cryst. Liq. Cryst., (1988).

G. C. Berry, Kazunori Se, and Mohan Srinivasarao, "Rheological, Rheo-Optical and Light Scattering Studies on Nematic Solutions of Poly(1,4-Phenylene-2,6-Benzobisthiazole), Chapter 7 in A. E. Zachariades and R. S. Porter, eds., High Modulus Polymers: Approaches to Design and Development, Marcel Dekker, Inc., New York, pg 195, (1988).

M. Bevis, "Chain-axis Invariant and Chain-axis Rotation Twins in Polymer Crystals", Colloid & Polym. Sci., 256, 234-240, (1978).

S. Bhattacharya, H. H. Chuah, My Dotrong, K. H. Wei, C-S. Wang, D. Vezie, Allan Day, and W. W. Adams, "Rigid-Rod Benzobisthiazole Polymers with Reactive Fluorene Moieties: II. Fiber Processing, Properties, and Morphology", Polym. Mater. Sci. Eng., 60, 512, (1989).

D. Bhaumik, W. J. Welsh, H. H. Jaffe, and J. E. Mark, "Interchain Interactions in Some Benzobisoxazole and Benzobisthiazole Rigid-Rod Polymers", Macromol., 14, 951-953, (1981).

D. Bhaumik and J. E. Mark, "A Theoretical Investigation of Chain Packing and Electronic Band Structure of the Rigid-Rod Polymer Trans-Poly(p-Phenylene Benzobisthiazole) in the Crystalline State", J. Polym. Sci.: Polym. Phys. Ed., 21, 2543-2549, (1983).

V. S. Boiko, "Dislocation Description of Twin Dynamic Behaviour", Phys. Stat. Sol. (b), 55, 477, (1973).

W. Bollman, Crystal Defects and Crystalline Interfaces, Springer-Verlag, Berlin, (1970).

A. Boudet, "Radiation Damage of Polyethylene Single Crystals in Electron Microscopy Between 1 and 2.5 MV. II. The Influence of Temperature", J. Physique, 47, (1986).

A. Boudet, D. C. Martin, and E. L. Thomas, "Observation of High Resolution Lattice Images of Polymer Fibres", Proceedings of the European Symposium on Polymeric Materials, Lyon, France, September 14-18, 1987.

B. Budiansky, "Micromechanics", Comp. & Struct., 16(1-4), 3-12, (1983).

P. R. Buseck, J. M. Cowley, and L. Eyring, "High-Resolution Transmission Electron Microscopy and Associated Techniques", Oxford University Press, Oxford, (1988).

C. B. Carter and S. L. Sass, "Electron Diffraction and Microscopy Techniques for Studying Grain-Boundary Structure", J. the American Ceramic Society, 64(6), 337, June (1981).

H. D. Chanzy, P. Smith, J. -F. Revol, and R. St. John Manley, "High-resolution Electron Microscopy of Ultradrawn Gels of High Molecular Weight Polyethylene", Polymer Comm., 23, 133, (1987).

H. Chanzy, T. Folda, P. Smith, K. Gardner, J. F. Revol, "Lattice Imaging in Poly(tetrafluoroethylene) Single Crystals", J. Mat. Sci., Lett., 5, 1045-1047, (1986).

H. D. Chanzy, P. Smith, and J.-F. Revol, "High Resolution Electron Microscopy of Virgin Poly(tetrafluoroethylene)", J. Mat. Sci., (1987).

S. G. Chu, S. Venkatraman, G. C. Berry Y. Einaga, "Rheological Properties of Rodlike Polymers in Solution, 1. Linear and Non- linear Steady State Behavior", Macromol., 14, 939-946, (1981).

H. H. Chuah, T. Kyu, and T.E. Helminiak, "The Kinetics of Phase Separation of PBT/Nylon 66 Composites", Polym. Mater. Sci. Eng., 56, 58, (1987).

A. Ciferri, W. R. Krigbaum, "Self Assembly of Natural Polymers via Liquid Crystalline Phases", Mol. Cryst. Liq. Cryst., 69, 273-280, (1981).

Y. Cohen and E. L. Thomas, "Structure Formation During Spinning of Poly(p-phenylene benzobisthiazole) Fiber", Polym. Eng. Sci., 25, 1093-1096 (1985).

Y. A. Cohen, "Structure Formation in Solutions of Rigid Polymers Undergoing a Phase Transition", Ph.D. Thesis, University of Massachusetts at Amherst, (1987).

Y. Cohen, H. H. Frost, and E. L. Thomas, "Structure Formation and Phase Transformations in Solutions of Rigid Polymers", Chapter 12 in P. S. Russo, ed., *Reversible Polymeric Gels and Related Systems*, American Chemical Society Symposium Series, (1987).

Y. Cohen and E. L. Thomas, "Formation of Solid Phases by Coagulation of a Monodomain Nematic Solution of Poly(p-Phenylene Benzobisthiazole)", *Mol. Cryst. Liq. Cryst.*, 153, pp. 375-384, (1987).

Y. Cohen and E. L. Thomas, "Microfibrillar Network of a Rigid Rod Polymer. 1. Visualization by Electron Microscopy", *Macromol.*, 21, 433, (1988).

Y. Cohen and E. L. Thomas, "Microfibrillar Network of a Rigid Rod Polymer. 2. Small Angle X-Ray Scattering", *Macromol.*, 21, 436, (1988).

Y. Cohen, Y. Saruyama, and E. L. Thomas, "Crystal-Solvates in the Poly(p-phenylene Benzobisthiazole) / Polyphosphoric Acid / Water System", in preparation, (1989).

D. B. Cotts and G. C. Berry, "Polycondensation of Poly([benzo(1,2-d:5,4,d')bisoxazole -2,6 diyl]1,4 phenylene)", *Macromol.*, 14, 930-934 (1981).

P. M. Cotts and G. C. Berry, "Studies on Dilute Solutions of Rodlike Macroions. II. Electrostatic Effects", *J. Polym. Sci.: Polym. Phys. Ed.*, 21, 1255-1274, (1983).

J. M. Cowley and A. F. Moodie, *Acta Crystallographica*, 10, 609-619, (1957).

J. M. Cowley, Chapters 1-4 in *High Resolution Transmission Electron Microscopy and Associated Techniques*, P. Buseck, J. Cowley, and L. Eyring, eds., Oxford University Press, (1989).

C. R. Crosby, W. C. Ford, F. E. Karasz, K. H. Langley, "Depolarized Light Scattering of a Rigid Macromolecule Poly(p-phenylene benzobisthiazole)", *J. Chem. Phys.*, 75, 4298-4306 (1981).

J. C. Dainty and R. Shaw, "Image Science: Principles, Analysis, and Evaluation of Photographic-type Imaging Processes", Academic Press, London, (1974).

W.C. Dale and E. Baer, "Fibre-buckling in Composite Systems: A Model for the Ultrastructure of Uncalcified Collagen Tissues", *J. Mat. Sci.*, 9, 369-382, (1974).

D. J. DeRosier and A. Klug, "Reconstruction of Three-dimensional Structures from Electron Micrographs", *Nature*, 217, 130-134, (1968).

- S. J. DeTeresa, R. J. Farris, and R. S. Porter, "Behavior of an Aramid Fiber Under Uniform Compression", Polym. Composites, 3(2), 57-58, April (1982).
- S.J. DeTeresa, S.R. Allen, R.J. Farris, and R.S. Porter, "Compressive and Torsional Behaviour of Kevlar 49 Fibre", J. Mat. Sci., 19, 57-72, (1984).
- S. J. DeTeresa, Axial Compressive Strength of High Performance Polymer Fibers, Ph.D. Thesis, University of Massachusetts, Amherst (1986).
- S. J. DeTeresa, R. S. Porter, and R. J. Farris, J. Mat. Sci., 20, 1645, (1985).
- S. J. DeTeresa, Y. Cohen, and R.J. Farris, United Kingdom Patent GB 2195672 A (1988).
- S.J. DeTeresa, R.S. Porter, and R.J. Farris, "Experimental Verification of a Microbuckling Model for the Axial Compressive Failure of High Performance Polymer Fibres", J. Mat. Sci., 23, 1886, (1988).
- M. G. Dobb and R. Murray, "Towards Higher Resolution in Electron Beam Sensitive Specimens of Biological Origin", J. Micros., 101(3), 299-309, (1974).
- M.G. Dobb, D.J. Johnson, and B.P. Saville, J. Polym. Sci., Polym. Phys. Ed., 15, 2201, (1977).
- M. G. Dobb, A. M. Hindeleh, D. J. Johnson, and B. P. Saville, "Lattice Resolution in an Electron-Beam Sensitive Polymer", Nature, 253, 189, (1975).
- D. L. Dorset and F. Zemlin, "Structural Changes in Electron Irradiated Paraffin Crystals at <15K and Their Relevance to Lattice Imaging Experiments", Ultramicroscopy, (1985).
- D. L. Dorset, "Electron Crystallography of n-Paraffins", Institute of Physics Conf. Serv., 78, (1985).
- D. L. Dorset, "Electron Crystal Structure Analysis of Small Organic Molecules", J. Electron Microscopy Technique, 2, 89-128, (1985).
- D. L. Dorset, "Crystal Structure of Lamellar Paraffin Eutectics", Macromol., 19(12), 2965-73, (1986).
- D. L. Dorset and F. Zemlin, "Specimen Movement in Electron-Irradiated Paraffin Crystals--A Model for Initial Beam Damage", Ultramicroscopy, 21(3), pg. 263, (1987).

- D. M. Duffy and P. W. Tasker, *J. Physique Paris*, 46, 64-185, (1985).
- H. Durst and I. G. Voight-Martin, "Direct Imaging of Smectic layers in Side-Chain Liquid Crystal Polymers by High Resolution Electron Microscopy", *Makromol. Chem. Rapid Commun.*, 7, 785-790, (1986).
- R. Eby, private communication, (1988).
- Y. Einaga, G. C. Berry, S. G. Chu, "Rheological Properties of Rodlike Polymers in Solution, 3. Transient and Steady State Studies on Nematic Solutions", *Polym. J.*, 17, 239-251 (1985).
- A. G. Evans and W. F. Adler, "Kinking as a Mode of Structural Degradation in Carbon Fiber Composites", *Acta Metallurgica*, 26, 725-738, 725, (1978).
- B. L. Farmer, S. G. Wierschke, and W. W. Adams, "A Study of the Conformations of Stiff Chain, Rigid Rod, and Substituted Rigid Rod Polymers", submitted to *Polymer*, July (1989).
- S. A. Fawaz, A. N. Palazotto, C.-S. Wang, "Compressive Properties of High Performance Polymeric Fibers", AFWAL-TR-88-4262, March (1989).
- L. Feldman, R. J. Farris, and Edwin L. Thomas, "Mechanical Properties of As-extruded and Heat-treated Poly(p-phenylene benzobisthiazole) Films", *J. Mat. Sci.*, 20, 2719-2726, (1985).
- L. Feldman, A. M. Zihlif, R. J. Farris, and E. L. Thomas, "Temperature and Strain Rate Dependence of the Deformation Behaviour of Poly(paraphenylene benzobisthiazole)", *J. Mat. Sci.*, 22, 1199-1205, (1987).
- P. J. Flory, "Statistical Thermodynamics of Semi-flexible Chain Molecules", *Proc. Roy. Soc. (London)*, A234, 60-73 (1956).
- P. J. Flory, "Phase Equilibria in Solutions of Rigid Particles", *Proc. Roy. Soc. (London)*, A234, 73-89 (1956).
- P. J. Flory, "Molecular Theory of Liquid Crystals", *Adv. Polym. Sci.*, 59, 2-36 (1984).
- F. C. Frank and J. H. van der Merwe, "One-dimensional Dislocations. I. Static Theory", *Proc. Roy. Soc.*, 198, pg. 205, (1949).
- F. C. Frank and A. N. Stroh, "On the Theory of Kinking", *Proc. Roy. Phys. Soc.*, (1952).

F. C. Frank, A. Keller, and A. O'Conner, "Deformation Processes in Polyethylene Interpreted in terms of Crystal Plasticity", *Phil. Mag.*, 3, 64, (1958).

A.V. Fratini and W.W. Adams, *Am. Cryst. Assoc. Abs.*, 13, 72, (1985).

A. V. Fratini, E. M. Cross, J. F. O'Brien, and W. W. Adams, "Structure of Poly (2,5-benzoxazole) (ABPBO) and Poly (2,6-benzothiazole) (ABPBT) by X-Ray Diffraction", *J. Macro. Sci., Phys. Ed.*, B24, 159, (1985-1986).

A. V. Fratini, P. G. Lenhert, T. J. Resch, and W. W. Adams, "Molecular Packing and Crystalline Order in Polybenzobisoxazole and Polybenzobisthiazole Fibers", in *Materials Science and Engineering of Rigid-Rod Polymers*, W. Wade Adams, R. Eby, and D. McLemore, eds., MRS Proceedings, (1989).

E. J. Freise and A. Kelly, "Twinning in Graphite", *Proc. Roy. Soc.*, A264, 269-276, (1961).

H. H. Frost, "Microstructure and Phase Behavior of Poly(para-phenylene benzobisthiazole)/Methane Sulfonic Acid Crystal Solvates", Master's Thesis, *Polym. Sci. and Engineering*, The University of Massachusetts at Amherst, (1984).

J. R. Fryer and D. J. Smith, *Proc. Roy. Soc. London*, A 381, (1982), 225.

J. R. Fryer, "Crystallization and Lattice Resolution of a Straight Chain Paraffin nC₃₆H₇₄ and its Adducts", presented at EMAG, Cambridge, 7-10 September 1981, *Inst. Phys. Conf. Ser.*, No. 61: Chap. 1, 19-22, (1982).

J. R. Fryer, "The Reduction of Radiation Damage in the Electron Microscope", *Ultramicroscopy*, 11, 67-70, (1983).

J. R. Fryer and F. Holland, "High Resolution Electron Microscopy of Molecular Crystals, III. Radiation Processes at Room Temperature", *Proceedings of the Royal Society of London*, A393, 353-369, (1984).

J. R. Fryer, "Radiation Damage in Organic Crystalline Films", *Ultramicroscopy*, 14, 227-236, (1984).

J. R. Fryer, R. A. Hann, and B. L. Eyres, "Single Organic Monolayer Imaging by Electron Microscopy", *Nature*, 313(6001), 382-384, (1985).

J. R. Fryer and David J. Smith, "High Resolution Microscopy of Interfaces in Chlorinated Phthalocyanine Molecular Crystals", *J. Microscopy*, 141, Pt. 1, pp. 3-9, January (1986).

J. R. Fryer, "Intermolecular Structure in Organic Crystals Shown by High Resolution Electron Microscopy", *Molecular Crystals and Liquid Crystals*, 137, 49-65, (1986).

J. R. Fryer and D. L. Dorset, "Direct Imaging of Paracrystalline Phospholipid Structure in the Electron Microscope", *J. Microscopy*, 145(1), 61-68, (1987).

F. E. Fujita and M. Hirabayashi, "High-Resolution Electron Microscopy", in *Microscopic Methods in Metals*, U. Gonser, ed., *Topics in Current Physics*, 40, Springer-Verlag, (1986).

K. H. Gardner, R. R. Matheson, P. Avakian, Y. T. Chin, T.D. Gierke, and H. H. Yang, *J. Polym. Sci., Polym. Phys. Ed.*, 21, 1955, (1983).

K. H. Gardner, R. R. Matheson, P. Avakian, Y. T. Chia, T. D. Gierke, "A Partial Phase Diagram and Crystal Solvate for the Poly(p-phenylene terephthalamide)/Sulfuric Acid System", E.I. du Pont de Nemours and Company, Experimental Station, Wilmington, DE, *Abs. Pap. ACS*, 186(Aug), 37 (1983).

S. Giorgio and R. Kern, "High Resolution Electron Microscopy of Polyethylene and Paraffin Crystals: Stability in the Electron Beam", *J. Polym. Sci.: Polym. Phys. Ed.*, 22, 1931-1951, (1984).

S. Giorgio and R. Kern, "Associations Between Polymer Membranes and Globular Molecules", *Ultramicroscopy*, 21, 251-262, (1987).

G. S. Grest, D. J. Srolovitz, and M. P. Anderson, "Computer Simulation of Grain Growth--IV. Anisotropic Grain Boundary Energies", *Acta Metall.*, 33(3), 509-520, (1985).

D. T. Grubb, "Review: Radiation Damage and Electron Microscopy of Organic Polymers", *J. Mat. Sci.*, 9, 1715-1736, (1974).

N. L. Hancox, "The Compression Strength of Unidirectional Carbon Fibre Reinforced Plastic", *J. Mat. Sci.*, 10, 234-242, (1975).

R. A. Hann, S. K. Gupta, J. R. Fryer, B. L. Eyres, "Electrical and Structural Studies on Copper Tetra-tert-butyl Phthalocyanine Langmuir-Blodgett Films", *Thin Solid Films*, 134, 35-42, (1985).

H. M. Hawthorne and E. Teghtsoonian, "Axial Compression Fracture in Carbon Fibres", *J. Mat. Sci.*, 10, 41-51, (1975).

- R. Henderson, J. M. Baldwin, K. H. Downing, J. Lepault, and F. Zemlin, "Structure of Purple Membrane from Halobacterium Halobium: Recording, Measurement, and Evaluation of Electron Micrographs at 3.5 Å Resolution", *Ultramicroscopy*, 19, 147-178, (1986).
- P. B. Hirsch, A. Howie, R. B. Nicholson, D. W. Pashley, M. J. Whelan, *Electron Microscopy of Thin Crystals*, Butterworth & Co., London, (1965).
- J. P. Hirth and J. Lothe, *Theory of Dislocations*, Second Ed., John Wiley & Sons, New York, (1982).
- R. Hosemann and S. N. Bagchi, *Direct Analysis of Diffraction by Matter*, North-Holland, Amsterdam, (1962).
- B. F. Howell and D. H. Reneker, "Resolution of Polymer Chains by Electron Microscopy", *Polym. Mat. Sci. Eng.*, 56, 725, (1987).
- D. Hull, *Introduction to Dislocations*, 2nd Ed., Pergamon Press, (1975).
- N. P. Huxford, D. J. Eaglesham, and C. J. Humphreys, "Limits on Quantitative Information from High Resolution Electron Microscopy of $\text{YBa}_2\text{Cu}_3\text{O}_7$ Superconductors", *Nature*, 329, 812-813, (1987).
- C. R. Hwang, M. F. Malone, R. J. Farris, D. C. Martin, and E. L. Thomas, "'In-Situ Network' Composite Fibers of PBZT/Nylon", W. W. Adams, R. Eby, and D. McLemore, eds., *Materials Science of Rigid-Rod Polymers*, Materials Research Society Symposia Proceedings, Boston, MA, (1989).
- C. R. Hwang, M. F. Malone, R. J. Farris, D. C. Martin, and E. L. Thomas, "Microstructure and Mechanical Properties of 'In-Situ Network' Composite Fibers of PBZT With Nylon", submitted to *J. Mat. Sci.*, submitted July (1989).
- S. Isoda, M. Tsuji, M. Ohara, A. Kawaguchi, K. Katayama, "Direct Observation of Dislocations in Polymer Single Crystals", *Makromol. Chem., Rapid Comm.*, 4, 141-144 (1983).
- S. Isoda, M. Tsuji, M. Ohara, A. Kawaguchi, and K. Katayama, "Structural Analysis of beta-form Poly(p-xylylene) Starting From a High Resolution Image", *Polymer*, 24, 1155-1160, (1983).
- S. A. Jenekhe and P. O. Johnson, "Solubilization, Solutions, and Processing of Aromatic Heterocyclic Rigid Rod Polymers in Aprotic Organic Solvents: Poly(p-phenylene-2,6-Benzobisthiazole) (PBT)", *Polym. Mater. Sci. Eng.*, 60, 502, (1989).

- S. A. Jenekhe et al., *Macromol.*, 22, 3216-3222, (1989).
- W. G. Johnston and J. J. Gilman, "Dislocation Velocities, Dislocation Densities, and Plastic Flow in Lithium Fluoride Crystals", *J. Appl. Phys.*, 30(2), 129, February (1959).
- W. Jones and J. M. Thomas, "Application of Electron Microscopy to Organic Solid-State Chemistry", *Org. Solid State Chemistry*, 12, 101-124, (1979).
- W. Junhua, P. Ziang, D. Xueli, and Z. Xiao, "A HREM Study on Molecular Images of Poly(phthalocyaninosiloxane)", *J. Polym. Sci.: Part C: Polym. Lett.*, 26, 433-439, (1988).
- K. Katayama, S. Isoda, M. Tsuji, M. Ohara, and A. Kawaguchi, "High Resolution Electron Microscopy of Polymers with Fiber Structure", *Bull. Inst. Chem. Res., Kyoto Univ.*, 62(3), (1984).
- A. Kawaguchi, S. Isoda, J. Petermann, and K. Katayama, "High Resolution Electron Microscopy of (SN)x", *Colloid & Polym. Sci.*, 262, 429-434 (1984).
- A. Kawaguchi and K. Katayama, "Fiber Structure of Poly(p-Phenylene)", *Proceedings of the International Symposium on Fiber Science and Technology*, PI-12, (1986).
- A. Kawaguchi, M. Tsuji, S. Monguchi, A. Uemura, S. Isoda, M. Ohara, J. Petermann, K. Katayama, "Electron Microscopical Studies on p-Polyphenyls", *Bulletin of the Institute for Chemical Research, Kyoto University*, 64(2), (1986).
- J. W. Kauffman and W. George, "Delayed Plastic Flowing in Certain Polyamide Films", *J. Colloid Science*, 6, 450, (1951).
- A. Keller and J. G. Rider, "On the Tensile Behaviour of Oriented Polyethylene", *J. Mat. Sci.*, 1, 389-398, (1966).
- A. Khurana, "High Temperature Supercurrents May Not Be Forever", *Physics Today*, 17, March (1989).
- A. M. Kosevich, "Crystal Dislocations and the Theory of Elasticity", Chapter 1 in *Dislocations in Solids*, F. R. N. Nabarro, ed., Volume 1, North-Holland, (1979).
- A. M. Kosevich and V. S. Boiko, "Dislocation Theory of the Elastic Twinning of Crystals", *Soviet Physics Uspekhi*, 14(3), 286, Nov-Dec 1971.
- S. Kozunori, G. C. Berry, "Nematic Solutions of Rodlike Polymers. 1. Light Scattering from Nematic Solutions with Complex Texture, and Phase Separation in Poor Solvents", accepted for publication in P. S. Russo, ed., *Reversible Gelation in Polymers*, ACS Symp. Series (1987).

S. J. Krause and W. W. Adams, Proc. Electron Micros. Soc. Am., 42, 382, (1984).

S. J. Krause, T. B. Haddock, D. L. Vezie, P. G. Lehnert, W.-F. Hwang, G. E. Price, T. E. Helminiak, J. F. O'Brien, and W. W. Adams, "Morphology and Properties of Rigid-Rod Poly(p-phenylene benzobisoxazole) (PBO) and Stiff-Chain Poly(2,5(6)-benzoxazole) (ABPBO) fibres", Polymer, 29, 1354, August (1988).

O. L. Krivanek, "Practical High-Resolution Electron Microscopy", in High Resolution Transmission Electron Microscopy and Associated Techniques, P. Buseck, J. Cowley, and L. Eyring, eds., Oxford University Press, (1989).

S. Kuga and R. M. Brown Jr., "Lattice Imaging of Ramie Cellulose", Polym. Comm., 28, 311, (1987).

S. Kuga and R. M. Brown, Jr., "Practical Aspects of Lattice Imaging of Cellulose", J. Electron Microscopy Technique, 6:349-356, (1987).

S. Kumar, S. J. Krause, and W. W. Adams, "Electron Beam Damage in High-Temperature Polymers", in Proceedings of the 43rd Annual Meeting of the Electron Microscopy Society of America, San Fransisco Press, Inc., San Fransisco, CA, 84-85, (1985).

S. Kumar, W. W. Adams, and T. E. Helminiak, "Uniaxial Compressive Strength of High Modulus Fibers for Composites", J. Reinforced Plastics and Composites, 7, 108, March (1988).

S. Kumar and T. Helminiak, "Compressive Strength of High Performance Fibers", in W. W. Adams, R.K. Eby, and D. McLemore, eds., Materials Science and Engineering of Rigid-rod Polymers, Mat Res Soc Symp Proc, 134, (1989).

S. Kumar and W. W. Adams, "Electron Beam Damage in High Temperature Polymers", private communication, (1989).

M. Kurokawa and T. Ban, "Slip Deformation in Drawn Polyethylene Films", J. Applied Polym. Sci., 8, 971-983, (1964).

C. C. Lee, S. G. Chu, G. C. Berry, "Studies on Dilute Solutions of Rodlike Macroions, 1. Light Scattering, Densitometry and Cryoscopy", J. Polym. Sci., Polym. Phys. Ed., 21, 1573-1597 (1983).

D. F. Lynch, A. F. Moodie, and M. O'Keefe, "N-Beam Lattice Images: V. The Use of the Charge Density Approximation in the Interpretation of Lattice Images", Acta Cryst., A31, 300, (1975).

S. Marianer and A. R. Bishop, "Frenkel-Kontorova Model with Nonconvex-Interparticle Interactions and Strain Gradients", Physical Review B, 37(16), 9893, (1988).

D. C. Martin and E. L. Thomas, "Analysis and Simulation of High-Resolution Lattice Images of Polymer Fibers", Bulletin of the American Physical Society, March 16-20, 1987.

D. C. Martin, S. D. Hudson, and Edwin L. Thomas, "HREM of Thermotropic Liquid Crystals", Bull. Am. Phys. Soc., 33, (1988).

D. C. Martin and E. L. Thomas, "Observation of Defects in Crystalline Polymers by High Resolution Electron Microscopy", Materials Research Society Bulletin, Volume XII, No. 8, November 16/December 31, 27-37, (1987).

D. C. Martin, A. Boudet, and E. L. Thomas, "Grain Boundary Imaging by Digital Reconstruction of High Resolution Lattice Images in Poly(p-phenylene benzobisthiazole) Fibers", in G. W. Bailey, ed., Proceedings of the Electron Microscopy Society of America, San Fransisco Press, Inc., San Fransisco, CA, pgs 464-465, (1987).

D. C. Martin and E. L. Thomas, "Morphology of Rigid-Rod Polymer Fibers: An Overview", in Materials Science of Rigid-Rod Polymers, W. Wade Adams, R. Eby, and D. McLemore, eds., Materials Research Society Symposia Proceedings, (1989).

D. C. Martin and E. L. Thomas, "Direct Imaging of Compressive Failure Zones in Rigid-Rod Polymer Fibers", in W. W. Adams, R. Eby, and D. McLemore, eds., Materials Science and Engineering of Rigid-Rod Polymers, Materials Research Society Symposia Proceedings, Boston, MA, (1989).

D. C. Martin and E. L. Thomas, "Direct Imaging of Intermolecular Shift Disorder in Fibers of Rigid-Rod Polymers", Bull. Am. Phys. Soc., (1989).

D. C. Martin, T. Granier, A. Boudet, and E. L. Thomas, unpublished, (1989).

D. C. Martin, unpublished results, (1989).

M. A. Masse, D. C. Martin, J. H. Petermann, E. L. Thomas, and F. E. Karasz, "Crystal Morphology in Pristine and Doped Films of Poly(p-phenylene Vinylene)", Journal of Materials Science, accepted, (1989).

R. R. Matheson, Jr., and P.J. Flory, "Statistical Thermodynamics of Mixtures of Semirigid Macromolecules: Chains with Rodlike Sequences at Fixed Locations", Macromolecules, 14, 954-960, (1981).

C. H. McConnell, J. R. Fryer, D. L. Dorset, and F. Zemlin, "Direct Lattice Imaging of Crystalline Paraffins", Inst. Phys. Conf. Ser. No. 78: Chapter 11, presented at EMAG '85, Newcastle upon Tyne, 2-5 September 1985.

J. R. Minter, K. Shimamura, E. L. Thomas, "Microstructural Study of As-Extruded and Heat-Treated Ribbons of Poly(p-phenylene benzobisthiazole)", J. Mater. Sci., 16, 3303-3308 (1981).

J. R. Minter, "Structural Investigations of Fibers and Films of Poly(p-phenylene benzobisthiazole)", Ph.D. Thesis, University of Massachusetts, Amherst (1982).

M. Misra and R. F. Egerton, "Assessment of Electron Irradiation Damage to Biomolecules Using the Patterson Function", J. Microscopy, 139(2), 197-204, (1985).

D. L. Misell and I. D. J. Burdett, "Determination of the Mass Thickness of Biological Sections from Electron Micrographs", J. of Microscopy, 109(2), 171-182, (1977).

A. F. Moodie, "Reciprocity and Shape Functions in Multiple Scattering Diagrams", Z. Naturforsch., 27a, 437, (1972).

P. W. Morgan, "Synthesis and Properties of Aromatic and Extended Chain Polyamides", Macromol., 10, 1381-1390, (1977).

N. F. Mott and H. S. W. Massey, The Theory of Atomic Collisions, 3rd. ed., Clarendon Press, Oxford, 86-112, (1965).

O. A. Nehme, C.A. Gabriel, R.J. Farris, E.L. Thomas, and M.F. Malone, "Microstructural Investigations of PBT/Nylon 6,6 Composites", J. Appl. Polym. Sci., 35, 1955-1965, (1988).

D. R. Nelson, "Vortex Entanglement in High-Tc Superconductors", Phys. Rev. Lett., 60(19), 1973, (1988).

M. G. Northolt, "X-Ray Diffraction Study of Poly(p-phenylene terephthalamide) Fibres", European Polym. Journal, 10, 799-804, (1974).

M. G. Northolt and J. J. Van Aartsen, "Chain Orientation Distribution and Elastic Properties of Poly(p-phenylene terephthalamide), a "Rigid-Rod" Polymer", J. Poly. Sci., Poly. Symp., 58, 283-306, (1977).

J. A. Odell, A. Keller, E. D. T. Atkins, M. J. Miles, "Structural Studies of Poly(p-phenylene benzobisthiazole) Films", J. Mater. Sci., 16, 3309-3318 (1981).

- M. A. O'Keefe, *Electron Image Simulation: A Complementary Processing Technique*, Electron Optical Systems, SEM Inc., Chicago, (1984).
- G. B. Olson and M. Cohen, "Dislocation Theory of Martensitic Phase Transformations", Chapter 37 in *Dislocations in Solids*, F.R.N. Nabarro, ed., Volume 7, North-Holland, (1986).
- E. Orowan, "A Type of Plastic Deformation New in Metals", *Nature*, 149(3788), 643, June 6 (1942).
- A. Ourmazd and J. C. H. Spence, *Nature*, 329, 425-428 (1987).
- M. Panar, P. Avakian, R.C. Blume, K.H. Gardner, T.D. Gierke, and H.H. Yang, "Morphology of PPTA Fibers", *J. Polym. Sci.: Polym. Phys. Ed.*, 21, 1955-1969, (1983).
- P. G. Partridge, "The Crystallography and Deformation Modes of Hexagonal Close-Packed Metals", *Metallurgical Reviews*, Review 118, 169, (1966).
- L.-M. Peng and J. M. Cowley, "Errors Arising from Numerical Use of the Mott Formula in Electron Image Simulation", *Acta Cryst.*, A44, 1-5, (1988).
- J. Petermann and J.M. Schultz, "Deformation and Defects in (SN)x Kink Bands", *J. Mat. Sci.*, 14, 891-896, (1979).
- J. M. Peterson, "Thermal Initiation of Screw Dislocations in Polymer Crystal Platelets", *J. Appl. Phys.*, 37(11), 4047, (1966).
- M. R. Piggott, "A Theoretical Framework for the Compressive Properties of Aligned Fibre Composites", *J. Mat. Sci.*, 16, 2837-2845, (1981).
- R. Piner, R. Reifengerger, D. Martin, E. L. Thomas, and R. P. Apkarian, "A Scanning Tunneling Microscope Study of Single Crystal Polyethylene", to be submitted, (1989).
- L. A. Pottick, S. R. Allen, R. J. Farris, "Force-Temperature Behavior of Rigid Rod Polymeric Fibers", *J. Applied Polym. Sci.*, 29, 3915-3924, (1984).
- L. A. Pottick, R. J. Farris, "Alterations in the Structure and Mechanics of Poly(p-phenylene benzobisthiazole) Fibers due to the Collapse Process During Drying", *TAPPI Proceedings: Nonwovens Symposium*, 85, 65-71 (1985).
- L. A. Pottick, "The Influence of Drying on the Structure and Mechanics of Poly(p-phenylene benzobisthiazole) Fibers", Ph.D. Thesis, University of Massachusetts, Amherst (1986).

P. Pradere, J. F. Revol, and R. St. John Manley, "Domains in Single Crystals of Poly-4-Methyl-Pentene-1", Proceedings of the Electron Microscopy Society of America, Baltimore, MD, August 1987.

P. Pradere, J. F. Revol, and R. St. John Manley, "Computer Averaging of Lattice Images of Poly-4-Methyl-Pentene-1 (P4MP1): Noise Created Artifacts", Proceedings of the Electron Microscopy Society of America, Baltimore, MD, August (1987).

P. Pradere, J.F. Revol, L. Nguyen, and R. St. John Manley, "Lattice Imaging of Poly-4-Methyl-Pentene-1 Single Crystals; Use and Misuse of Fourier Averaging Techniques", submitted to Ultramicroscopy, 1987.

P. Pradere, The University of Massachusetts at Amherst, unpublished (1988).

P. Pradere and E. L. Thomas, "Three-Dimensional Model for Twinning in Polymer Single Crystals with Inclined Chains", Phil. Mag. B, accepted September 19, (1988).

P. Pradere and Edwin L. Thomas, "Shot Noise Simulations of HREM Images of Polymer Crystals", Proc. of EMSA, (1989).

P. Pradere and Edwin L. Thomas, "Antiphase Boundaries and Ordering Defects in Syndiotactic Polystyrene Crystals", submitted to Macromol., July 18, (1989).

P. Predecki and W. O. Statton, "Dislocations Caused by Chain Ends in Crystalline Polymers", J. Appl. Phys., 37(11), 4053, (1966).

R. T. Read and R. J. Young, "Direct Lattice Resolution in Polydiacetylene Single Crystals", J. Mat. Sci., Lett., 16, 2922-2924, (1981).

R. T. Read and R. J. Young, "Radiation Damage and High Resolution Electron Microscopy of Polydiacetylene Crystals", J. Mat. Sci., 19, 327-338, (1984).

R. E. Reed-Hill, Physical Metallurgy Principles, Second Ed., Brooks/Cole Engineering Division, Litton Educational Publishing, Monterey, CA, (1973).

L. Reimer, Transmission Electron Microscopy: Physics of Image Formation and Microanalysis, Springer Series in Optical Sciences, 36, Springer-Verlag, Berlin, (1984).

J.-F. Revol, "Change of the d Spacing in Cellulose Crystals During Lattice Imaging", J. Mat. Sci., Lett., 4, 1347-1349, (1985).

J.-F. Revol and H. Chanzy, "High Resolution Electron Microscopy of Chitin Microfibrils", *Biopolymers*, 25:1599-1601, (1986).

J.-F. Revol and R. St. John Manley, "Lattice Imaging in Polyethylene Single Crystals", *J. Mat. Sci. Lett.*, 5, 249-251, (1986).

J.-F. Revol, "Lattice Imaging of Natural and Synthetic Polymers with a Conventional Transmission Electron Microscope (CTEM)", *Proc. XIth Int. Cong. on Electron Microscopy*, Kyoto, 1743, (1986).

U. Rieck and J. H. Magill, "Lattice Imaging of Polyphosphazene Single Crystals", *Polym. Comm.*, 128, (1987).

N. Rivier, "Statistical Crystallography: Structure of Random Cellular Networks", *Phil. Mag. B*, 52(3), 795-819, (1985).

R. E. Robertson, "Formation of Kink Bands in Oriented Polymers", *J. Polym. Sci.: Part A-2*, 7, 1315-1328 (1969).

I. M. Robinson, P. H. J. Yeung, C. Galiotis, R. J. Young, and D. N. Batchelder, "Stress Induced Twinning of Polydiacetylene Single Crystal Fibres in Composites", *J. Mat. Sci.*, 21, 3440-3444, (1986).

E. J. Roche, T. Takahashi, E. L. Thomas, "Structure of High Modulus Fibers of Poly(p-phenylene benzobisthiazole)", in A. D. French, K. H. Gardner, eds., *Fiber Diffraction Methods*, ACS Symp. Series, 141, 303-313 (1980).

E. J. Roche, S. R. Allen, V. Gabara, and B. Cox, "Thin Film Morphology and Crystal Structure of the Poly(p-phenylene terephthalamide)/Sulfuric Acid System", submitted to *Polymer*, (1989).

P. S. Russo and W. G. Miller, "On the Nature of the Poly(g-benzyl-glutamate)-Dimethylformamide 'Complex Phase'", *Macromol.*, 17, 1324, (1984).

P. S. Russo, S. Siripanyo, M. J. Saunders, and F. E. Karasz, "Observation of a Porous Gel Structure in Poly(p-phenylenebenzobisthiazole)/97% H₂SO₄", *Macromol.*, 19, 2856-2859, (1986).

S. Sasaki, K. Tokuma, and I. Uematsu, *Polym. Bulletin*, 10, 539, (1983).

S. L. Sass, "Grain Boundary Structure", in *Encyclopedia of Mat. Sci. and Eng.*, M. B. Bever, ed., Pergamon Press, (1986).

L. C. Sawyer and D.T. Grubb, *Polymer Microscopy*, Chapman and Hall, New York (1987).

W. O. Saxton, D. J. Smith, and S. J. Erasmus, "Procedures for Focusing, Stigmating, and Alignment in High Resolution Electron Microscopy", J. Micros., 130(2), 187-201, (1983).

O. Scherzer, "The Theoretical Resolution Limit of the Electron Microscope", J. Appl. Phys., 20, 20-29, (1949).

J. M. Schultz, Polymer Materials Science, Prentice-Hall, Inc., New Jersey, (1974).

J. M. Schultz and J. Petermann, "Deformation and Defects in (SN)x: Lattice Strain and Fibrillation", Phil. Mag. A, 40(1), 27-38, (1979).

K. Se and G. C. Berry, "Nematic Solutions of Rodlike Polymers: Light Scattering from Nematic Solutions with Complex Texture and Phase Separation in Poor Solvents", Chapter 10 of Reversible Polymeric Gels and Related Systems, American Chemical Society, (1987).

K. Se and G. C. Berry, "Frank Elastic Constants and Leslie-Ericksen Viscosity Coefficients of Nematic Solutions of a Rodlike Polymer", Mol. Cryst. Liq. Cryst., submitted, (1988).

P. G. Self and M. A. O'Keefe, "Calculation of Diffraction Patterns and Images for Fast Electrons", in High Resolution Transmission Electron Microscopy and Associated Techniques, P. Buseck, J. Cowley, and L. Eyring, eds., Oxford University Press, (1989).

T. Seto and Y. Tajima, "Observation of Kink Bands in Oriented Polyethylene", Japanese J. Appl. Phys., 5(6), 534, June (1966).

D. Y. Shen, G. M. Venkatesh, D. J. Burchell, P. H. C. Shu, and S. L. Hsu, "Spectroscopic Study of Rigid-Rod Polymers. II. Protonation Effect", J. Polym. Sci.: Polym. Phys. Ed., 20, 509-521, (1982).

D. Y. Shen and S. L. Hsu, "Vibrational Spectroscopic Characterization of Rigid Rod Polymers: 3. Microstructural Changes in Stressed Polymers", Polymer, 23, 969, (1982).

A. Shepp, in Imaging Processes and Materials, Neblettes Eighth Ed., J. Sturge, V. Walworth, and A. Shepp, eds., Van Nostrand Reinhold, (1989).

K. Shigematsu, K. Imada, and M. Takayanagi, "Formation of Kink Bands by Compression of the Extrudate of Solid Linear Polyethylene", J. Polym. Sci.: Polym. Phys. Ed., 13, 73-86, (1975).

K. Shimamura, J. R. Minter, and E. L. Thomas, "Lattice Imaging of High Modulus Poly(p-phenylene benzobisthiazole) Fibers", J. Mater. Sci. (Lett.), 2, 54-58 (1983).

J. C. H. Spence, Experimental High Resolution Electron Microscopy, Clarendon Press, Oxford, (1981).

D. J. Srolovitz, M. P. Anderson, P. S. Sanhi, and G. S. Grest, "Computer Simulation of Grain Growth--II. Grain Size Distribution, Topology, and Local Dynamics", Acta Metall., 32(5), 793-802, (1984).

H. Staudinger, Ein-aggregatige Polyoxymethylen-dimethylather [Zweiter Teil, B. II. 4., p. 263, 1932], in "Wissenschaftliche Werk von Herrman Staudinger", p. 919.

J. W. Steeds and J. R. Willis, "Dislocations in Anisotropic Media", Chapter 2 in F. R. N. Nabarro, ed., Dislocations in Solids, North-Holland, (1979).

J. Sturge, V. Walworth, and A. Shepp, "Imaging Processes and Materials: Neblette's Eighth Ed.", Van Nostrand Reinhold, New York, (1989).

J. Sugiyama, H. Harada, Y. Fujiyoshi, and N. Uyeda, "High Resolution Observations of Cellulose Microfibrils", Mokuzai Gakkaishi, 30(1), 98-99, (1984).

J. Sugiyama, H. Harada, Y. Fujiyoshi, and N. Uyeda, "Lattice Images from Ultrathin Sections of Cellulose Microfibrils in the Cell Wall of Valonia Macrophysa Kutz", Planta, 166, 161-168, (1985).

J. Sugiyama, H. Harada, Y. Fujiyoshi, and N. Uyeda, "Observations of Cellulose Microfibrils in Valonia macrophysa by High Resolution Electron Microscopy", Mokuzai Gakkaishi, 31(2), 61-67, (1985).

A. P. Sutton and R. W. Balluffi, "On Geometric Criteria for Low Interfacial Energy", Acta Metall., 35(9), 2177-2201, (1987).

R. A. Swalin, Thermodynamics of Solids, John Wiley & Sons, New York, (1962).

Synoptics, Inc., SEMPER Image Processing Software, Cambridge, England, (1989).

T. Takahashi, M. Miura, and K. Sakuri, "Deformation Band Studies of Axially Compressed Poly(p-phenylene Terephthalamide) Fiber", J. Applied Polym. Sci., 28, 579-586, (1983).

D. Tanner, A. K. Dhingra and J. J. Pigliacampi, J. Metals, "Aramid Fiber Composites for General Engineering", 38, 21, (1986).

E. L. Thomas, "The Defect Structure of Polyethylene Single Crystals", Ph.D. Thesis, Cornell University, (1974).

E. L. Thomas and E. J. Roche, "Critical Evaluation of Electron Microscope Evidence for Order in Glassy Polymers", Polymer, 20, 1413, (1979).

E. L. Thomas, R. J. Farris, S. L. Hsu, S. Allen, A. Filippov, J. Minter, E. Roche, K. Shimamura, T. Takahashi, and G. Venkatesh, US Air Force Technical Report AFWAL-TR-80-4045, vol.III, part I, (1982).

M. Tomita, H. Hashimoto, T. Ikuta, H. Endoh, and Y. Yokota, "Improvement and Application of the Fourier-transformed Pattern From a Small Area of High Resolution Electron Microscope Images", Ultramicroscopy, 16, 9-18, (1985).

M. Tosaka, M. Tsuji, A. Kawaguchi, and K. Katayama, "High-Resolution Observation of Syndiotactic-Polystyrene Single Crystal by Transmission Electron Microscopy", Polym. Preprints, Japan, 37, 1-4, (1988).

H. H. Tsai, Phase Equilibrium and Rheological Studies of Solutions of Rodlike Articulated Polymers and their Mixtures, Ph.D. Thesis, Carnegie-Mellon University, Pittsburgh (1983).

M. Tsuji, S. Isoda, M. Ohara, K. Katayama, and K. Kobayashi, "Construction of Image Processing Systems and Application to the Random Noise Removal in Electron Micrographs", Bulletin of the Institute for Chemical Research, Kyoto University, 55(2), (1977).

M. Tsuji, "Direct Imaging of Molecular Chains in a Poly(p-Xylylene) Single Crystal", Ph.D. Thesis, Laboratory of Polymer Crystals, Institute for Chemical Research, Kyoto University, (1981).

M. Tsuji, S. Isoda, M. Ohara, A. Kawaguchi, and K. Katayama, "Direct Imaging of Molecular Chains in a Poly(p-xylylene) Single Crystal", Polymer, 23, 1568-1574, (1982).

M. Tsuji and R. St. John Manley, "Determination of the Illumination Angle and Defocus Spread in Transmission Electron Microscopy", J. of Microscopy, 130(1), 93-98, (1983).

M. Tsuji, S. K. Roy, and R. St. John Manley, "Direct Lattice Imaging in Single Crystals of Isotactic Polystyrene", Polymer, 25, 1573-1576, (1984).

M. Tsuji, S. K. Roy, and R. St. John Manley, "Lattice Imaging of Radiation-Sensitive Polymer Crystals", J. Polym. Sci.: Polym. Phys. Ed., 23, 1127-1137, (1985).

M. Tsuji, A. Uemura, M. Ohara, A. Kawaguchi, K. Katayama, and J. Petermann, "High Resolution Electron Microscopy of Thin Crystalline Films of Isotactic Polystyrene", Sen-I Gakkaishi, 42(10), 92-95, (1986).

M. Tsuji, S. Moriguchi, K.-J. Ign, A. Kawaguchi, and K. Katayama, "Resolution Limit in Electron Microscopy of Polymer Crystals", Proceedings of the XIth Congress on Electron Microscopy, Kyoto, Japan, 1749-1750, (1986).

M. Tsuji and R. St. John Manley, "One-Dimensional Image Simulation in the Electron Microscopy of Negatively Stained Cellulose Protofibrils", Sen-I Gakkaishi, 42(6), pgs T-323:T-334, (1986).

A. Uemura, S. Isoda, M. Tsuji, M. Ohara, A. Kawaguchi, and K. Katayama, "Morphology of Solution-Grown Crystals and Crystalline Thin Films of Poly(p-Phenylene Sulfide)", Bulletin of the Institute for Chemical Research, Kyoto University, 64(2), 66-77, (1986).

A. Uemura, M. Tsuji, A. Kawaguchi, and K. Katayama, "High-Resolution Electron Microscopy of Solution-grown Crystals of Poly(p-phenylene sulphide)", J. Mat. Sci., 23, 1506-1509, (1988).

P. N. T. Unwin and R. Henderson, "Molecular Structure Determination by Electron Microscopy of Unstained Crystalline Specimens", J. Mol. Biol., 94, 425-440, (1975).

L. H. Van Vlack, Elements of Materials Science and Engineering, (1983).

G. M. Venkatesh, D. Y. Shen, and S. L. Hsu, "Spectroscopic Study of Rigid-Rod Polymers. I. Structures of Model Compounds", J. Polym. Sci.: Polym. Phys. Ed., 19, 1475-1478, (1981).

S. Venkatraman, Studies on the Thermodynamics, Rheological and Rheoptical Properties of a Rigid Rod Polymer in Solution, Ph.D. Thesis, Carnegie-Mellon University, Pittsburgh (1981).

S. Venkatraman, G. C. Berry, Y. Einaga, "Rheological Properties of Rodlike Polymers in Solution, 2. Linear and Non-linear Transient Behavior", J. Polym. Sci., Polym. Phys. Ed., 23, 1275-1295 (1985).

V. Vitek, A. P. Sutton, D. A. Smith, and R. C. Pond, in Grain Boundary Structure and Energetics, R. W. Balluffi, ed., Am Soc. Metals, Metals Park, OH, 115, (1980).

K. V. Vladimirkii, Zh. Eksp. Teor. Fiz., 17, 530, (1947). as quoted in Kosevich and Boiko, (1971).

I. G. Voight-Martin and H. Durst, "High-Resolution Images of Defects in Liquid Crystalline Polymers in the Smectic and Crystalline Phases", Macromol., 22, 168, (1989).

I. G. Voight-Martin, H. Durst, and H. Krug, "High-Resolution Images of Defects in Liquid-Crystalline Polymers: Image Analysis Using Light Diffractometer and Computer Techniques", Macromol., 22, 595-600, (1989).

I. G. Voight-Martin, private communication, (1989).

C. S. Wang, J. Burkett, S. Bhattacharya, H. H. Chuah, and F. E. Arnold, "Disruptive Packing Order Via Bulky Benzobisthiazole Rigid-Rod Polymers", Polym. Mater. Sci. Eng., 60, 767, (1989).

C. W. Weaver and J. G. Williams, "Deformation of a Carbon-Epoxy Composite Under Hydrostatic Pressure", J. Mat. Sci., 10, 1323-1333, (1975).

M. W. Wellman, W.W. Adams, D.R. Wiff, and A.V. Fratini, US Air Force Technical Report AFWAL-TR-79-4184, (1980).

W. J. Welsh, D. Bhaumik, and J.E. Mark, "Phenylene Group Rotations and Nonplanar Conformations in Some cis- and trans-Poly(benzobisoxazoles) and -Poly(benzobisthiazoles)", Macromol., 14, 947-950, (1981).

W. J. Welsh, H. H. Jaffe, N. Kondo, and J. E. Mark, "The Flexibility of Biphenyl and Related Species Utilizable as Molecular Swivels in Rodlike Polymers. A CNDO/2 Analysis", Makromol. Chem., 183, 801-820, (1982).

W. J. Welsh, D. Bhaumik, J. E. Mark, Air Force Technical Report AFML-TR-78-3683. J. Macromol. Sci. Phys., (1981).

W. J. Welsh and J. E. Mark, "Effects of Protonation on the Conformational Characteristics and Geometry of the Rod-like Benzobisoxazole Polymers", Polym. Eng. and Sci., 23(3), 140, (1983).

W. J. Welsh, D. Bhaumik, H. H. Jaffe, and J. E. Mark, "Theoretical Investigations on Some Rigid-Rod Polymers Used as High-Performance Materials", Polym. Eng. and Sci., 24(3), 218, (1984).

S. G. Weirschke, "A Computational Study of the Tensile and Compressive Properties of Ordered Polymers via the Austin Model 1 (AM1) Semi-Empirical Molecular Orbital Method", US Air Force Technical Report AFWAL-TR-88-4201, (1988).

S. M. Wickliffe, M.F. Malone, and R.J. Farris, "Processing and Properties of Poly(p-phenylene benzobisthiazole)/Nylon Fibers", J. Appl. Polym. Sci., 34, 931 (1987).

J. O. Williams and J. M. Thomas, "Lattice Imperfections in Organic Solids, Part I.--Anthracene", Faraday Discussions, (1967).

J. F. Wolfe, B. H. Loo, F. E. Arnold, "Rigid Rod Polymers. 2. Synthesis and Thermal Properties of Para-Aromatic Polyamides with 2,6 Benzobisthiazole Units in the Main Chain", Macromol., 14, 915-920 (1981).

J. F. Wolfe, P.D. Sybert, and J.R. Sybert, US Patent 4 553 693, (1985).

E. Won Choe and S. N. Kim, "Synthesis, Spinning, and Fiber Mechanical Properties of Poly(p-phenylene benzobisoxazole)", Macromol., 14, 920-924, (1981).

C. P. Wong, H. Ohnuma, G. C. Berry, "Properties of Some Rodlike Molecules in Solution", J. Polym Sci., Polym. Symp., 65, 173-192, (1978).

P. H. J. Yeung and R. J. Young, "Direct Imaging of Molecules in Polydiacetylene Single Crystals", Polymer, 27, 202-210, February (1986).

R. J. Young and R. H. Baughman, "Deformation Mechanisms in Polymer Crystals. Part 1: The Geometry of the Stress-induced Phase Change of Polymeric Sulphur Nitride (SN)_x", J. Mat. Sci. 13, 55-61, (1978).

R. J. Young, D. Bloor, D. N. Batchelder, and C. L. Hubble, "Deformation Mechanisms in Polymer Crystals. Part 2: Twinning in Macroscopic Single Crystals of Bis(p-Toluene Sulphonate) Diacetylene Polymer", J. Mat. Sci., 13, 62-71, (1978).

R. J. Young, R. Dulniak, D. N. Batchelder, and D. Bloor, "Twinning in Macroscopic Polymer Single Crystals", J. Polym. Sci.: Polym. Phys. Ed., 17, 1325-1339, (1979).

R. J. Young and P. S. Rainbow, "The Structure of Ferritin Single Crystals in Amphipods", J. Mat. Sci. Lett., 4, 838-842, (1985).

R. J. Young and P. H. J. Yeung, "Molecular Detail in Electron Micrographs of Polymer Crystals", J. Mat. Sci., Lett., 4, (1985).

D. A. Zaukelies, "Observation of Slip in Nylon 66 and 610 and Its Interpretation in Terms of a New Model", J. Appl. Phys., Volume 33(9), 2797, September (1962).

F. Zemlin, E. Reuber, E. Beckmann, E. Zeitler, D. L. Dorset, "Molecular Resolution Electron Micrographs of Monolamellar Paraffin Crystals", Science, 229, 461-462, (1985).

X. Zhou, T. J. Marks, and S. H. Carr, "Topotactic Polymerization Mechanism of Phthalocyaninatogermanium Dihydroxide in the Solid State", Polymeric Materials Science and Engineering, 51, 651, (1984).

X. Zhou, T. J. Marks, and S. H. Carr, "Direct Imaging of the Lattice in Poly(phthalocyaninatogermoxane) Single Crystals", Mol. Cryst. Liq. Cryst., 118, 357-360, (1985).

ADDENDUM:

T. Granier, E. L. Thomas, and F. E. Karasz, "Paracrystalline Structure of Poly(paraphenylene vinylene)," J. Poly. Sci., B: Poly. Phys. Ed. 27, 469-487, (1989).

J. A. Nelder and R. A. Mead, "Simplex Method for Function Minimization," Computer Journal, 308, (1965).